ISSN: 2376-2136 (Print)
ISSN: 2376-2144 (Online)

Trends in Renewable Energy

Volume 4, Issue 2, December 2018

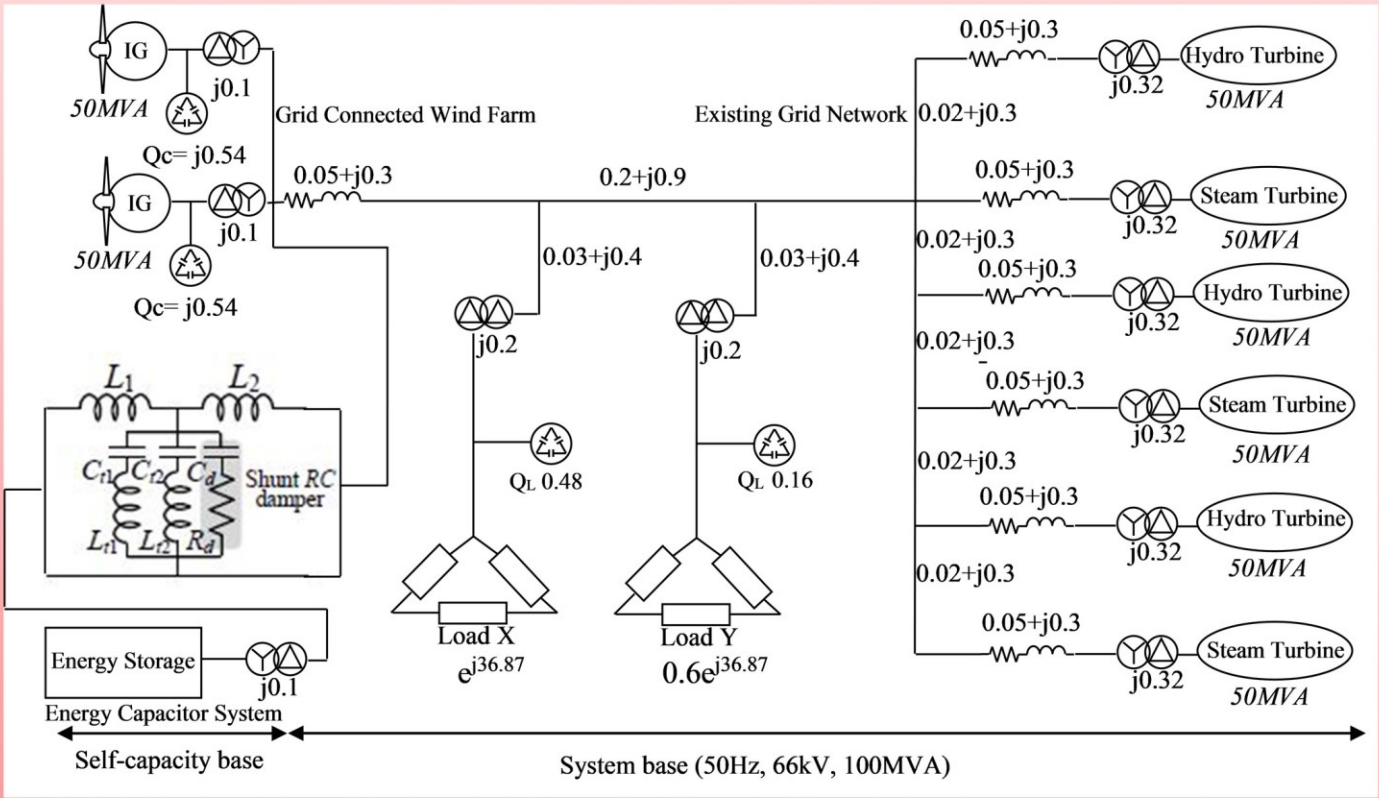

Cover image: a model system of the wind farm, see article by Okedu in this issue.

futureenergysp.com
thefutureenergy.org

Trends in Renewable Energy

ISSN: 2376-2136 (Print) ISSN: 2376-2144 (Online)

http://futureenergysp.com/

Trends in Renewable Energy is an open accessed, peer-reviewed semi-annual journal publishing reviews and research papers in the field of renewable energy technology and science.

The aim of this journal is to provide a communication platform that is run exclusively by scientists working in the renewable energy field. Scope of the journal covers: Bioenergy, Biofuel, Biomass, Bioprocessing, Biorefinery, Biological waste treatment, Catalysis for energy generation, Energy conservation, Energy delivery, Energy resources, Energy storage, Energy transformation, Environmental impact, Feedstock utilization, Future energy development, Green chemistry, Green energy, Microbial products, Physico-chemical process for Biomass, Policy, Pollution, Renewable energy, Smart grid, Thermo-chemical processes for biomass, etc.

The Trends in Renewable Energy publishes the following article types: peer-reviewed reviews, mini-reviews, technical notes, short-form research papers, and original research papers.

The article processing charge (APC), also known as a publication fee, is fully waived for the Trends in Renewable Energy.

Editorial Team of Trends in Renewable Energy

EDITORIAL BOARD

Dr. Ong Huei Ruey	DRB-HICOM University of Automotive, Malaysia
Dr. Miguel Ángel Reyes Belmonte	IMDEA Energy Institute, Spain
Dr. Chitra Venugopal	Associate Professor in Electrical Engineering, University of Trinidad and Tobago, Trinidad
Dr. Amit Kumar Singh	Assistant Prof., Instrumentation & Control Engineering Department, Dr. B.R.A. National Institute of Technology, India
Dr. Suvanjan Bhattacharyya	University of Pretoria, South Africa
Dr. Karunesh Tiwari	Babu Banarasi Das University, India
Dr. Sharadrao A. Vhanalkar	Karmaveer Hire Arts, Science, Commerce and Education College, India
Dr. Prasenjit Chatterjee	Assistant Prof. and Head, MCKV Institute of Engineering, India
Dr. S. Balamurugan	Mindnotix Technologies, India
Dr. Mohammad Nurunnabi	University of Oxford, United Kingdom
Dr. Kenneth Okedu	Caledonian College of Engineering, Oman
Dr. Cheng Zhang	Sr. Materials Engineer, Medtronic, Inc., United States
Dr. Chandani Sharma	Assistant Prof., Department of Electrical Engineering, Graphic Era University, India
Dr. Kashif Irshad	Assistant Prof., Mechanical Engineering Department, King Khalid University, Saudi Arabia
Dr. Abhijit Bhagavatula	Principal Lead Engineer, Southern Company Services, United States
Dr. S. Sathish	Associate Prof., Department of Mechanical Engineering, Hindustan University, India
Mr. A. Avinash	Assistant Prof., KPR Institute of Engineering & Technology, India
Mr. Bindeshwar Singh	Assistant Prof., Kamla Nehru Institute of Technology, India
Dr. Yashar Hashemi	Tehran Regional Electric Company, Iran
Dr. Navanietha Krishnaraj R	South Dakota School of Mines and Technology, United States
Dr. SANDEEP GUPTA	JECRC University, India
Dr. Shwetank Avikal	Graphic Era Hill University, India
Dr. Xianglin Zhai	Poochon Scientific LLC, United States
Dr. Rui Li	Assistant Prof., College of Engineering, China Agricultural University, China
Dr. Adam Elhag Ahmed	National Nutrition Policy Chair, Department of Community Services, College of Applied Medical Sciences, King Saud University, Saudi Arabia
Dr. Jingbo Li	Massachusetts Institute of Technology, United States
Dr. Srikanth Mutnuri	Associate Prof., Department of Biological Sciences, Associate Dean for International Programmes and Collaboration, Birla Institute of Technology & Science, India
Dr. Bashar Malkawi	S.J.D., Associate Prof., College of Law, University of Sharjah, United Arab Emirates
Dr. Simona Silvia Merola	Istituto Motori - National Research Council of Naples, Italy
Dr. Hakan Caliskan	Faculty of Engineering, Department of Mechanical Engineering, Usak University, Turkey

Table of Contents

Volume 4, Issue No. 2, December 2018

Articles

Reviews

Enhancing Frequency of Grid-connected Wind Farm using Energy Capacitor System and Trap RC Shunt Damper Strategies

Kenneth E. Okedu [1,2,*]

1: Department of Electrical and Computer Engineering, National University of Science and Technology, PC 111, Muscat, Sultanate of Oman
2: Department of Electrical and Electronic Engineering, University of Port Harcourt, P.M.B. 5323, Rivers State, Nigeria

Received April 30, 2018; Accepted May 30, 2018; Published June 3, 2018

In this paper, a combination of the conventional energy capacitor system and a proposed two-trap Resistor Capacitor (RC) shunt damper circuitry is used to stabilize a grid network made up of fixed speed wind turbines, steam turbines and hydro turbines. The energy storage system is connected to the terminals of the wind farm and has the capability of stabilizing the grid network during periods of wind speed change. The two-trap damper has the ability to mitigate the mechanical vibration of the wind turbine and increase its output and rotor speed acceleration during disturbances, so the turbine speed is reduced. Simulations were run using Power System Computer Aided Design and Electromagnetic Transient Including DC (PSCAD/EMTDC) environment, for scenarios where grid frequency control was not implemented and when frequency control was employed using the energy storage device. A further investigation was carried out in enhancing the performance of the grid network considering the proposed two-trap shunt DC damper control topology. The results show the improved performance of the variables of the wind turbine and the entire grid network during dynamics, due to the coordinated control strategies of the two-trap RC circuit and the energy capacitor system employed.

Keywords: Wind energy; Wind farm; Frequency; Grid; Wind turbine; Filters; RC damper

Introduction

Recently, the renewable energy technology has received more attention, because it not only has the potential to improve energy security, but also reduces the environmental impact of greenhouse gases. Hence, this type of energy is eco-friendly. The constant penetration of wind farms that are equipped with wind turbines into existing grid connected network, would definitely affect the frequency and stability of the entire power system. Power electronics technology is the main technology that enables the connection of renewable energy sources like wind and solar into the grid system [1-3]. They are used to interface the generated energy into the grid. However, these voltage source converters produce unwanted harmonics. As a result, filters are used to smoothen the output of the network.

With tremendous rise in renewable energy penetration into the grid system, there is bound to be disturbances in the power network. Consequently, the grid network and its

* *Corresponding author:* Okedu.kenneth@Caledonian.edu.om, kenokedu@yahoo.com

Tr Ren Energy, 2018, Vol.4, No.2, 96-110. doi: 10.17737/tre.2018.4.2.0070

control associates are becoming complex by day. The integration of wind power into existing power network causes frequency distortions due to the stochastic nature of the wind. A lot of papers have been presented in the literature regarding frequency control of the grid connected network. Traditionally, the automatic load frequency control can be used to maintain the grid system frequency by variation of the governor set points of the turbines connected to the network [4, 5]. In the literature [6-8], the genetic algorithm strategy was proposed to control the load frequency in a mixed generation system, in order to maintain zero steady state error during grid disturbances. The major shortcoming of this approach is the presence of oscillations in the frequency deviations and a longer time to reach steady state for the power system variables. Another good approach to stabilize the frequency of a grid connected system is the utilization of adaptive notch filters [9-11]. The challenge in using this approach is that the measured signal frequency should remain constant and this is not the case with the use of wind energy system.

Usually, an Inductive Capacitive Inductive (LCL) filter is used to mitigate the switching harmonics emanating from a Voltage Source Converter (VSC) that is connected to the grid network. This is because they offer lower cost and are simple in nature [12]. For this reason, the LCL filter is employed in the integration of renewable sources in grid networks. With recent advancement in power electronics technology, the trap filters have been proposed as a good solution to suppress switching harmonics more than the traditional LCL filters [13]. The trap filter topology are smaller in size with low cost compared to earlier filter strategies.

In order to avoid the risk of instability in the grid connected VSC as a result of resonance in the capacitive and inductive components in the grid, it is necessary to consider damping. However, due to constant changes in the grid network variables, effective damping may not be realized using active damping control strategies alone [14]. Another solution to this problem may be to employ passive damping because it will improve the stability of the system [15], however, there must be large losses to be incurred [16].

Energy storage system can effectively mitigate oscillations in the power system, and hence could be used for frequency regulation. In the literature [17], additional power to achieve control of a grid connected network was provided by both internal and external energy storage devices. In [18], the energy capacitor system was used to stabilize grid voltage system, however, the shunt trap frequency control responses were not considered. Thus, the controllers of the energy capacitor system were not tested for robustness during grid dynamics. Reference [19] considered the use of a small value of series dynamic braking resistor in the stator of the wind turbine to improve the frequency of the power system.

The tripping of wind power generators *i.e.*, grid connected wind turbines is most likely to avoid grid dynamics or transient disturbances [20]. This is not allowed in most countries, based on the recent grid codes. In this paper, the conventional Energy Capacitor System (ECS) technology is used to stabilize grid connected wind power and synchronous turbine systems. The ECS is used to achieve smoothing of the terminals of the distorted wind turbine variables in order to maintain steady supply of power despite the stochastic nature of the wind. In order to enhance the performance of the conventional wind farm frequency control ECS topology, a two-trap Resistor Capacitor (RC) shunt damper is proposed to work in combination with the ECS control system. The proposed two-trap shunt RC damper is used to improve the performance of the wind turbine during grid disturbances. The new control strategy also has the ability to reduce the speed

excursion of the wind turbine and boost the turbine speed during grid dynamics. Besides, the proposed system effectively enhances the reactive power production of the VSC connected ECS external device, thus, improving its performance when there is grid disturbance. These effects would reduce the grid connected VSC losses and improve the overall performance of the system. In addition, the grid codes minimum frequency values stipulated in the operation of wind farms and power systems would be achieved, thus, avoiding the tripping of the wind turbines during grid disturbances. In this work, simulations were run for different scenarios in Power System Computer Aided Design and Electromagnetic Transient Including DC (PSCAD/EMTDC) platform [21]. In the first scenario, no frequency control was employed in the power system. The second scenario considered frequency control of the grid network, using the ECS topology, while the third scenario employs the proposed two-trap shunt RC damper to further enhance the performance of the ECS system. The presented results show the robustness of the proposed control strategy in enhancing the performance of the frequency and some other variables of the grid connected wind farm in the power network.

Model System of Study

The model system of study is shown in Figure 1, where the wind farm is made up of two aggregated wind turbines of total power rating 100 MVA connected to aggregated steam and hydro turbines of 50 MVA each.

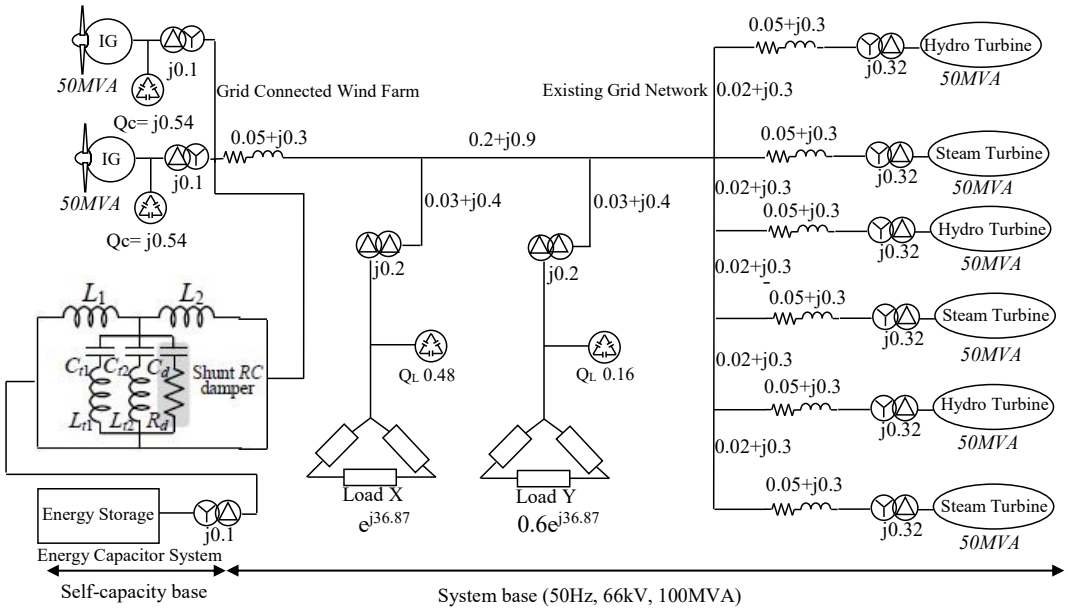

Figure 1. Model system of study

The ECS is connected at the terminals of the wind turbines via the proposed two-trap RC shunt circuitry in the wind farm as shown in Figure 1. Loads X and Y are connected between the bus bar connecting the wind farm and the steam and hydro synchronous generators. The power network is operating at 100 MVA, 66 kV and 50 Hz with the given line parameters. The two-trap shunt RC damper circuitry is connected

between the terminals of the wind turbine and the VSC grid side of the ECS. The parameters of the wind turbine, steam and hydro turbines are given in Table 1. The excitation circuit parameters of the ECS and the proposed two-trap shunt RC damper are given in Tables 2 and 3, respectively.

Table 1. Parameters of the model system turbines

Generator Type	Steam turbine	Hydro turbine	Generator Type	Wind turbine
MVA	200	200	MVA	100
r_a (pu)	0.003	0.003	r1 (pu)	0.01
x_a (pu)	0.102	0.130	x1 (pu)	0.1
X_d (pu)	1.651	1.200	Xmu (pu)	3.5
X_q (pu)	1.590	0.700	r21 (pu)	0.035
X'_d (pu)	0.232	0.300	x21 (pu)	0.030
X'_q (pu)	0.380		r22 (pu)	0.014
X''_d (pu)	0.171	0.220	x22 (pu)	0.098
X''_q (pu)	0.171	0.250		
T'do (sec)	5.900	5.000		
T'qo (sec)	0.535			
T''do(sec)	0.033	0.040		
T''qo(sec)	0.078	0.050		
H (sec)	3.000	2.500		

Table 2. Parameters of the ECS excitation circuit

Parameters	Ratings
DC-link Voltage	6.6 kV
DC-link Capacitor	50,000μF
Device for Power Converter	IGBT
PWM Carrier Frequency	1.05kHz
low pass filter time constant	30 sec

Table 3. Parameters of the two-trap shunt RC damper

Parameters	Ratings
Line Inductor	0.1mH
Filter Capacitor	2.15/0.21μF
Damp Resistor	5.4Ω
DC-link Voltage	6.6 kV
Damp Capacitor	2.35μF
Trap Inductors	0.113/0.3mH

Control Strategy of the FACTS Energy Storage Device

Figure 2 shows the control structure of the grid connected VSC ECS, where a dq to abc transformation is done with an angle thetha that is calculated from the Phase Lock Loop (PLL) of the system. The effective grid voltage is compared with a reference value

of 1.0 pu that is then passed through a Proportional Integral (PI) controller system. The signal is further compared with a signal generator to generate six pulse reference signals, which are used for switching the Insulated Gate Bipolar Transistors (IGBTs) to achieve control of the wind farm system and the entire power network during grid disturbances. Also, the control structure and design for the inbuilt Low Pass Filter (LPF) of the ECS are shown in Figure 2. The reference signals are the grid active power and the wind turbine active power, respectively. The difference of the powers is fed through a PI system whose output is added to a constant gain value to generate signal that is compared with a triangular carrier signal generator. The output is thus used in the switching of the DC chopper circuit unit of the ECS system for charging and discharging limitations. The proposed connected two-trap shunt RC damper increases the mechanical power extracted from the drive train of the aggregated wind generator and reduces its speed excursion during dynamic periods. Also, since mechanical torque is proportional to the square of the stator voltage of the wind turbine, the effect would enhance the fast recovery of the turbine during grid disturbances.

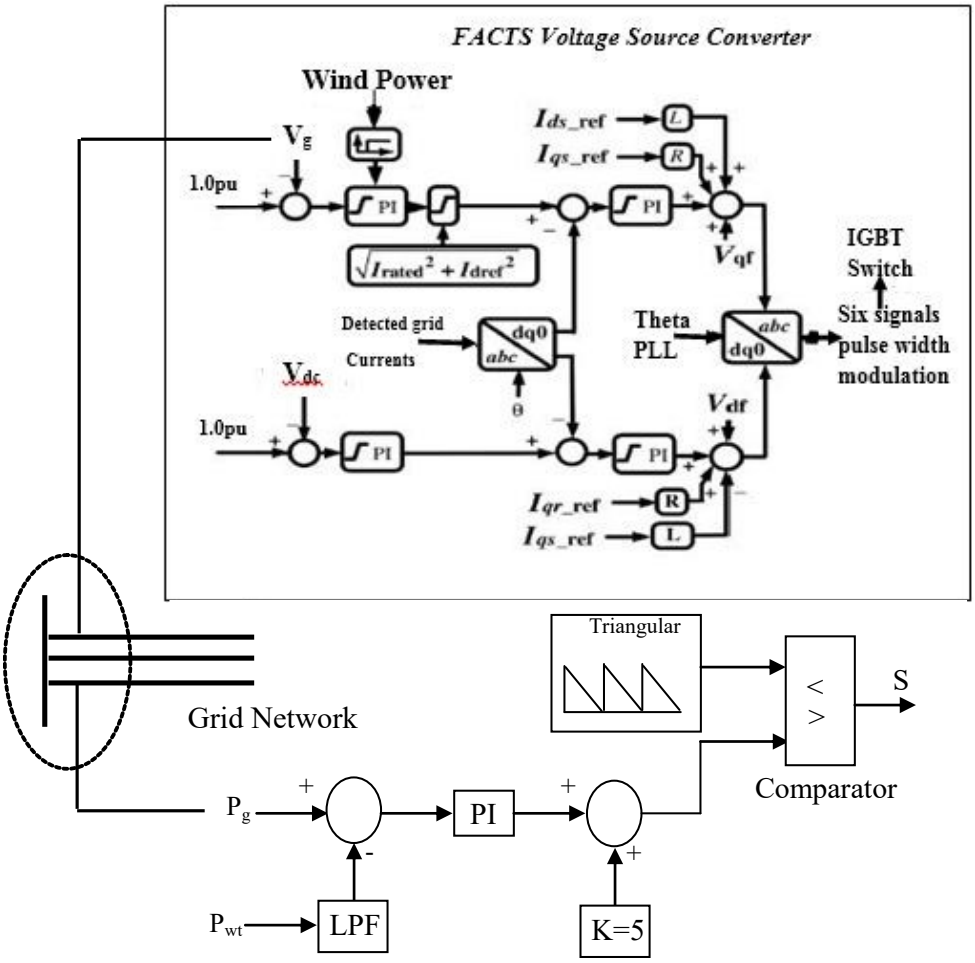

Figure 2. ECS and its associate controls

Space Vector Control of the ECS and the Trap Shunt RC Damper

The control system of the three phase voltage source converter for the ECS shown in Figure 2 is based on space vector transformation. As seen from the figure, the detected three phase currents are i_a, i_b and i_c, which are vectors that are equally spaced in abc clockwise sequence with respect to the grid, which is in stationary abc reference frame as given in equation (1) [22].

$$\begin{bmatrix} i_a \\ i_b \\ i_c \end{bmatrix} = \begin{bmatrix} \hat{I}\cos(\omega t) \\ \hat{I}\cos(\omega t - 2\pi/3) \\ \hat{I}\cos(\omega t + 2\pi/3) \end{bmatrix} \quad (1)$$

The transformation of these vectors into two phase stationary reference frames αβ is shown in Figure 3 and their products are represented with i_α and i_β in the clockwise direction in Figure 4.

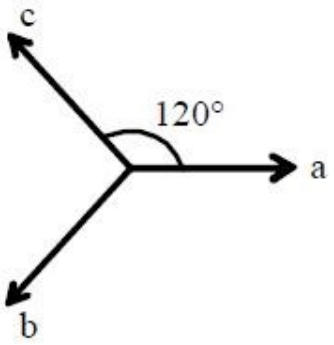

Figure 3. VSC abc stationary frame

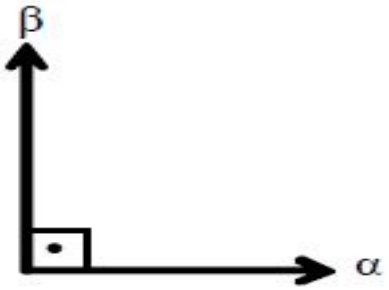

Figure 4. VSC αβ stationary frame

A further decoupling of the abc phase vectors based on the α and β axis results in equation (2) with three unknown variables.

$$\begin{aligned} X_2 i_\alpha &= X_3 i_a + X_3 i_b cos\left(\frac{4\pi}{3}\right) + X_3 i_c cos\left(\frac{2\pi}{3}\right) \\ X_2 i_\beta &= 0 + X_3 i_b sin\left(\frac{4\pi}{3}\right) + X_3 i_c sin\left(\frac{2\pi}{3}\right) \\ X_2 i_0 &= kX_3 i_a + kX_3 i_b + kX_3 i_c \end{aligned} \quad (2)$$

From equation (2), X_2 represents the $\alpha\beta$ frame magnitude, while X_3 represents the components of the abc frame. Putting equation (2) into matrix forms, gives

$$\begin{bmatrix} i_0 \\ i_\alpha \\ i_\beta \end{bmatrix} = \frac{N_3}{N_2} \underbrace{\begin{bmatrix} k & k & k \\ 1 & -1/2 & -1/2 \\ 0 & -\sqrt{3}/2 & -\sqrt{3}/2 \end{bmatrix}}_{[T_{\alpha\beta 0}]} \begin{bmatrix} i_a \\ i_b \\ i_c \end{bmatrix} \quad (3)$$

Considering the orthogonal condition, $[T_{\alpha\beta 0}]^{\cdot}\,[T_{\alpha\beta 0}] = I_{3x3}$, the transformation matrix $[T_{\alpha\beta 0}]$ and X_3/X_2 ratio are computed as shown in equation (4), where $[T_{\alpha\beta 0}]^T$ is the transpose of $[T_{\alpha\beta 0}]$ and I_{3x3} is a 3x3 identity matrix.

$$\begin{bmatrix} i_0 \\ i_\alpha \\ i_\beta \end{bmatrix} = \sqrt{\frac{2}{3}} \begin{bmatrix} 1/\sqrt{2} & 1/\sqrt{2} & 1/\sqrt{2} \\ 1 & -1/2 & -1/2 \\ 0 & \sqrt{3}/2 & -\sqrt{3}/2 \end{bmatrix} \begin{bmatrix} i_a \\ i_b \\ i_c \end{bmatrix} \quad (4)$$

Equation (4) is known as the Clarke transformation and the vectors in both frames are the same, since equation (2) normalizes the transformation. This situation would lead to equation (5)

$$i_\alpha{}^2 + i_\beta{}^2 + i_0{}^2 = i_a{}^2 + i_b{}^2 + i_c{}^2 \quad (5)$$

It should be noted that zero sequence component is not utilized for the remaining transformation analysis, because it is ignored for simplicity. And the matrix would reduce to equation (6).

$$\begin{bmatrix} i_\alpha \\ i_\beta \end{bmatrix} = \sqrt{\frac{2}{3}} \begin{bmatrix} 1 & -1/2 & -1/2 \\ 0 & \sqrt{3}/2 & -\sqrt{3}/2 \end{bmatrix} \begin{bmatrix} i_a \\ i_b \\ i_c \end{bmatrix} \quad (6)$$

If the frequency of rotation of the grid is ω_g, then based on Fig. 5, the variables of the stationary αβ frame can be expressed as equation (7). Also, the variables of the stationary reference frame in equation (6) can be transformed into synchronous frame based on equation (8) with displacement clockwise direction angle θ between the ranges of 0 to2π.

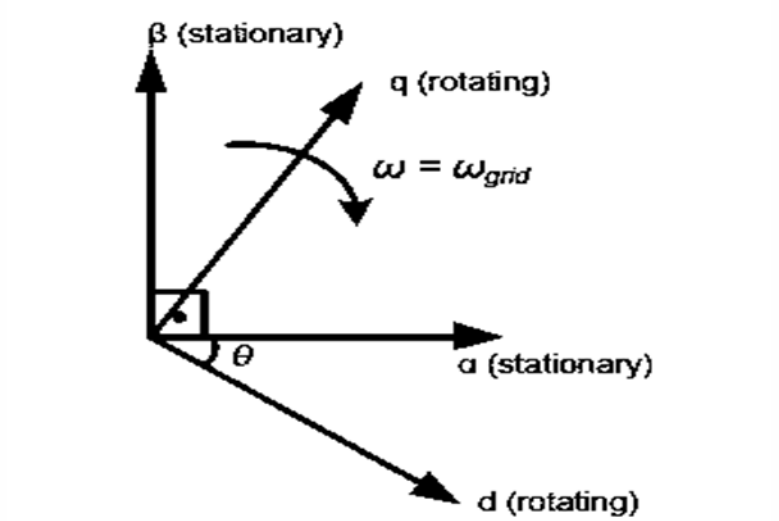

Figure 5. VSC Pulse width modulation vector

$$\underline{i}_{\alpha\beta} = i_\alpha + j\, i_\beta \quad (7)$$

$$\underline{i}_{dq} = \underline{i}_{\alpha\beta}\, e^{j\theta} \qquad \theta = \int \omega\, dt \quad (8)$$

Applying equations (6) to (7) to transform the αβ vectors along the two orthogonal dq axes leads to equation (9), with two unknowns in both equations.

$$\begin{aligned} i_d &= i_\alpha cos\theta + i_\beta \sin\theta \\ i_q &= -i_\alpha sin\theta + i_\beta \cos\theta \end{aligned} \quad (9)$$

The transformation matrix $[T_{dq}]$ helps in representing eqn (9) as eqn (10)

$$\begin{bmatrix} i_d \\ i_q \end{bmatrix} = \underbrace{\begin{bmatrix} cos\,\theta & -sin\theta \\ sin\theta & cos\theta \end{bmatrix}}_{[T_{dq}]} \begin{bmatrix} i_\alpha \\ i_\beta \end{bmatrix} \tag{10}$$

The matrix $[T_{dq}]$ satisfies the condition of orthogonality given by $[T_{dq}]^T[T_{dq}] = I_{2x2}$, where $[T_{dq}]^T$ is the transpose of $[T_{dq}]$ and I_{2x2} is the identity matrix. The transformation expression of equation (10) with an additional sequence component of 0 is known as the Park transformation. The αβ frame to dq frame normalized transformation creates room for the current vector to be the same in both frames of reference, therefore,

$$i_\alpha{}^2 + i_\beta{}^2 = i_d{}^2 + i_q{}^2 \tag{11}$$

From the proposed two-trap shunt RC damper shown in the model system in Figure 1, the mathematical model based on the dq reference frame could be expressed as [22, 23]:

$$\frac{d}{dt}\underline{i}_{g,dq} = \frac{1}{L_{grid} + L_g}\left(\underline{V}_{C_f,dq} - \underline{E}_{grid,dq} - R_{grid}\underline{i}_{g,dq} - j\omega\left(L_{grid} + L_g\right)\underline{i}_{g,dq}\right)$$

$$\frac{d}{dt}\underline{i}_{c,dq} = \frac{1}{L_c}\left(\underline{V}_{c,dq} - \underline{V}_{C_f,dq} - j\omega L_c\underline{i}_{c,dq}\right) \tag{12}$$

$$\frac{d}{dt}\underline{V}_{C_f,dq} = \frac{1}{C_f}\left(\underline{i}_{c,dq} - \underline{i}_{g,dq} - j\omega C_f\underline{V}_{C_f,dq}\right)$$

It is considerably meaningful for the transformation of the mathematical model into the same frame as the current controllers are in dq frame operation. From equation (12),

$\underline{i}_{g,dq}$ is the grid current vector,

$\underline{i}_{c,dq}$ is the converter current vector,

$\underline{v}_{g,dq}$, $\underline{V}_{c,dq}$, and $\underline{V}_{Cf,dq}$ are the grid voltage vector, the converter output voltage vector and the filter capacitor current vector, respectively.

Operating Principle of the Proposed Scheme

From the model system in Figure 1, the proposed two-trap shunt RC damper is used to reduce multiple harmonic frequencies that are basically above the tuning frequency of the filter by using the capacitors and the tuned inductors. The circuit when tuned, resonates at a fundamental frequency, so that the fundamental current flowing into the resistor could be bypassed. Hence, the proposed two-trap filter has the characteristics of low damping losses and better harmonic attenuation, when operating in combination with a grid connected voltage source converter.

The selection of the parameters of the filter is based on [24], which ensures that the harmonics in the connected grid current are lower than the specified values. The performance of the filter is based on the admittance transfer function represented by the grid current to the converter voltage expressed in equation (13) [24, 25].

$$Y_{gc} = \frac{i_g}{V_c}\bigg|_{V_g=0} = \frac{1}{s(L_c+L_g)} \frac{\frac{s^3}{\omega_0\omega_t^2 Q} + \frac{s^2}{\omega_t^2} + (n+1)\frac{s}{\omega_0 Q} + 1}{\frac{s^4}{\omega_0^2\omega_t^2} + \left(\frac{n}{\omega_0^3} + \frac{1}{\omega_0\omega_t^2}\right)\frac{s^3}{Q} + \left(\frac{1}{\omega_0^2} + \frac{1}{\omega_t^2}\right)s^2 + (n+1)\frac{s}{\omega_0 Q} + 1} \tag{13}$$

Equation (13) describes how the modulation control strategy of the harmonic voltage is propagated into the grid current. In equation (13), ω_t is the tuned frequency and ω_0 is the characteristic frequency, and they are expressed in equations (14) and (15), respectively as [26]:

$$\omega_t = \sqrt{\frac{1}{nL_tC_f}} \tag{14}$$

$$\omega_o = \sqrt{\frac{L_c+L_g}{L_cL_gC_f}} \tag{15}$$

The damping effect in the circuit is determined by the quality factor and it depends on the filter components. This is expressed as

$$Q = \frac{R_0}{R_d} \tag{16}$$

$$R_0 = \sqrt{\frac{L_cL_g}{(L_c+L_g)C_f}} \tag{17}$$

Theoretically, a trap filter produces infinite attenuation at the switching frequency, and at frequencies above the switching frequency, the filter attenuation rapidly decreases. Based on the above features and analysis, the two-trap shunt RC damper will give a good damping performance of the variables of a grid connected VSC system during network disturbance.

Evaluation of the Model System Performance

Simulations were run for 600 seconds for dynamic analysis considering the model system in Figure 1 using natural wind speed obtained from Hokkaido Island, Japan as shown in Figure 6. Three scenarios were considered. In the first scenario, no grid frequency control was implemented in the model system. The second scenario uses the conventional energy capacitor system for stability of the grid frequency. In the third scenario, the proposed two-trap shunt RC damper was used to further enhance the performance of the energy capacitor system and the entire power network. Some of the simulation results in PSCAD/EMTDC are discussed as follows for the model system variables.

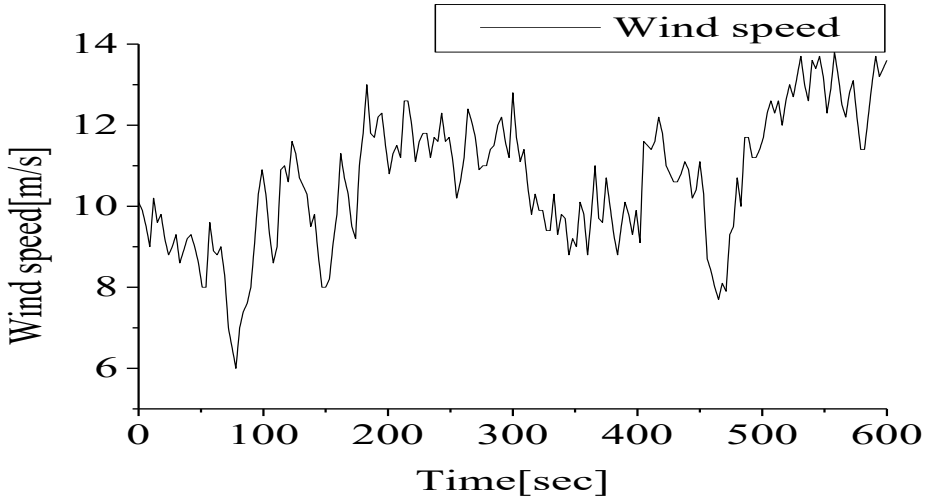

Figure 6. Wind speed data for system analysis

Figure 7 shows the response of the grid frequency considering three scenarios. When no control was implemented, the grid frequency was distorted due to the stochastic nature of the natural wind energy in Figure 6. Hence, the grid codes require the wind farm to be shut down in this case to avoid damage to the power network and utilities connected to it. With the help of the energy capacitor system control strategy, active power control was achieved, in addition to reactive power that was injected into the grid network based on the coordinated control of the ECS Pulse Width Modulation DC chopper presented in Figure 2. The grid frequency was controlled almost within the permissible limit set by the grid codes in order to avoid shutting down of the wind farm considering an LPF time constant of 120 seconds. In a bid to further improve the grid frequency performance of the network, the proposed control scheme with the two-trap shunt RC damper was used as shown in Figure 7. The two-trap RC shunt damper helped

boost the grid frequency during dynamics by damping the system and also filtering the attenuated harmonics based on the analysis presented earlier in this paper.

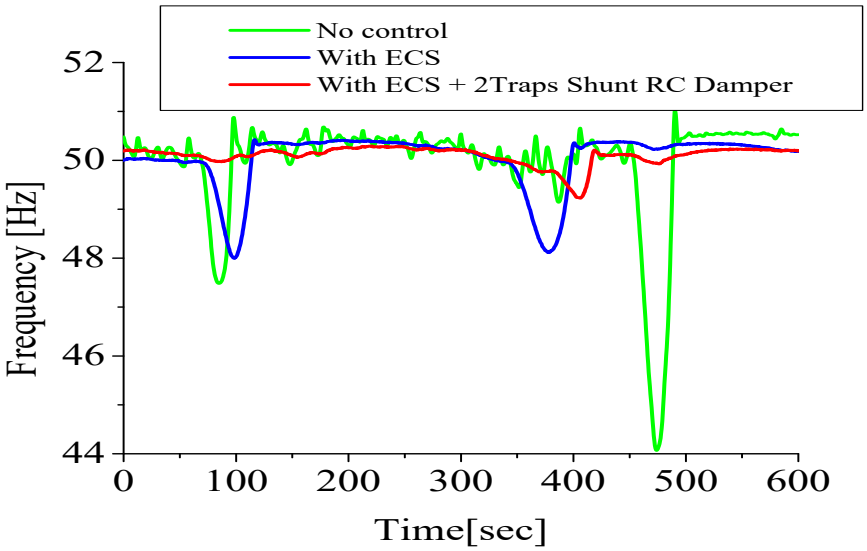

Figure 7. Frequency response of the grid network

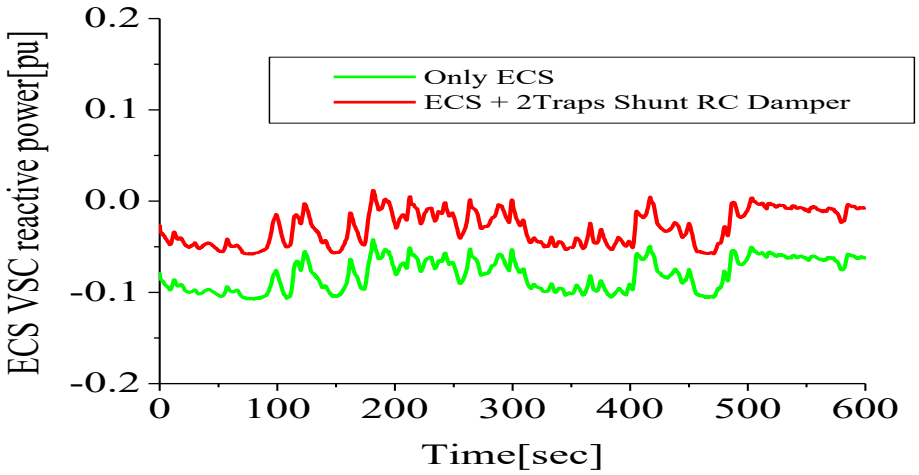

Figure 8. Reactive power of energy capacitor system

Figure 8 shows that the proposed coordinated control topology is able to boost the reactive power production of the ECS grid connected VSC to help in further stabilizing the grid system with faster recovery of the grid variables. This is because the proposed control will increase the mechanical power extracted from the drive train of the wind turbine, thus reducing its speed excursion during grid disturbances as shown in Figure 9 for the wind turbine speed. Moreover, based on the fact that mechanical torque is proportional to the square of the stator voltage of the wind generator, the effect would enhance the recovery of the wind turbine after the grid dynamics.

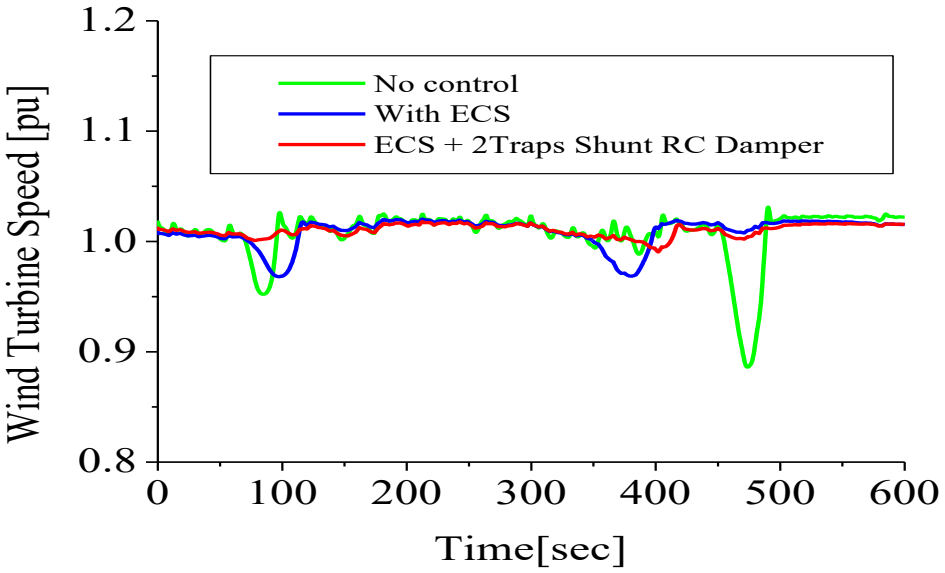

Figure 9. Wind turbine speed

CONCLUSIONS

In this paper, a more efficient coordination of voltage source converter energy capacitor based system and two-trap shunt RC damper is proposed to enhance the performance of the frequency of a grid network during dynamic conditions. The working principle of the pulse width modulation voltage source converter and the operation principle of the proposed two-trap shunt RC damper were presented. The simulation results show that the proposed control strategy was able to enhance not only the grid frequency, but other variables of the network by boosting the performance of the energy capacitor system during grid disturbances. Also, with this topology, wind farms would remain connected to the grid network during grid disturbances because the permissible limit of operation of the grid frequency would be met based on the stipulated grid requirements.

CONFLICTS OF INTEREST

The author declares that there is no conflict of interests regarding the publication of this paper.

REFERENCES

[1] Popović-Gerber, J., Oliver, J. A., Cordero, N., Harder, T., Cobos, J. A., Hayes, M., O'Mathuna, S. C., Prem, E. (2012). Power electronics enabling efficient energy

usage: energy savings potential and technological challenges. *IEEE Trans. Power Electronic.* 27(5), 2338 – 2353.

[2] Okedu, K. E. (2016). Enhancing DFIG wind turbine during three-phase fault using parallel interleaved converters and dynamic resistor. *IET Renewable Power Generation*. 10 (6), 1211-1219.

[3] Okedu, K. E., Muyeen, S. M., Takahashi R., and Tamura, J. (2011). Protection schemes for DFIG considering rotor current and DC-link voltage. *24th IEEE-ICEMS (International Conference on Electrical Machines and System)*, Beijing, China, 1-6. DOI: 10.1109/ICEMS.2011.6073453

[4] Ramesh S., and Krishnan, A. (2011). Stabilization of frequency deviation in an AC-DC interconnected power systems using supervisory fuzzy controller. *Tamkang Journal of Science and Engineering*. 14(4), 341-349.

[5] Gross, G., and Lee J. W. (2001). Analysis of load frequency control performance assessment criteria. *IEEE Transactions on Power Systems*. 16, 520-525.

[6] Venkata P. B., Jayaram K. S. V. (2008) Load frequency control for two area interconnected power system using robust genetic algorithm controller. *Journal of theoretical and applied information technology*. 4(12), 1204-1221. http://www.jatit.org/volumes/research-papers/Vol4No12/7Vol4No12.pdf (accessed on 6/1/2018)

[7] Hulst, D., Fernadez, M., *et al*. (2015). Voltage and frequency control for future power systems: the Electra IRP Proposal. *Proceedings International symposium in smart electric distribution systems and technologies*, 245-250. DOI: 10.1109/SEDST.2015.7315215

[8] Jagathessan K., and Dey N. (2015). Artificial intelligence in performance analysis of load frequency control in thermal wind hydropower system. *International Journal of Advanced Computer Science and Applications*. 6 (7), 203-212.

[9] Messikh, T., Mekhilef S., and Rahim, N. A. (2008). Adaptive notch filter for harmonic current mitigation. *World Academy of Science Engineering and Technology*. 22, 907-913.

[10] Saiteja K., and Krishnarayalu, M. S. (2015). Load frequency control of two area smart grid. *International Journal of Computer Applications*. 117(14), 1-9.

[11] Wilches-Bernal F., Chow, J. H., and Sanchez-Gasca, J. J. (2015). A fundamental study of applying wind turbines for power system frequency control. *IEEE Transactions on Power Systems.* 31(2), 1496-1505.

[12] Liserre, M., Blaabjerg, F., and Hansen, S. (2005). Design and control of an LCL-filter-based three-phase active rectifier, *IEEE Trans. on Ind. Applications.* 41(5), 1281–1291.

[13] Patel, Y., Pixler, D., and Nasiri, A. (2010). Analysis and design of trap and LCL filters for active switching converters. *IEEE Int. Symp. on Ind. Electron*. 638–643. DOI: 10.1109/ISIE.2010.5637475

[14] Dannehl, J., Liserre, M., and Fuchs, F. W. (2011). Filter-based active damping of voltage source converters with LCL filter. *IEEE Trans. Ind. on Electronic*. 58(8), 3623–3633.

[15] Teodorescu, R., Blaabjerg, F., Liserre, M., and Dell'Aquila, A. (2003). A stable three-phase LCL-filter based active rectifier without damping. *38th IAS Annual Meeting on Conference Record of the Industry Applications Conference*, 3, 1552–1557. DOI: 10.1109/IAS.2003.1257762

[16] Beres, R., Wang, X., Blaabjerg, F., Bak, C. L., and Liserre, M. (2014). A review of passive filters for grid-connected voltage source converters. *2014 IEEE Applied Power Electronics Conference and Exposition - APEC 2014*. 2208–2215. DOI: 10.1109/APEC.2014.6803611

[17] Friedrich L., and Gautschi, M. (2009). Grid stabilization control and frequency regulation for inverted connected distribution renewable source. *Master Thesis, Department of Electrical and Computer Engineering, Power System Research*, University of Wisconsin- Madison. https://pdfs.semanticscholar.org/b478/00585681f7880da0c2b7ae02222efca9cf78.pdf (accessed on 6/1/2018)

[18] Okedu, K. E. (2017). Effect of ECS low pass filter timing on grid frequency dynamics of a power network considering wind energy penetration. *IET Renewable Power Generation*. 11(9), 1194-1199.

[19] Okedu, K. E. (2017). Improving grid frequency dynamics of synchronous generators considering wind energy penetration. *IEEE International Electric Machines and Drives Conference (IEMDC)*, Paper ID 112, May 21-24, Miami, Florida, USA. DOI: 10.1109/IEMDC.2017.8001865

[20] Okedu, K. E., Muyeen, S. M., Takahashi, R., and Tamura, J. (2012). Wind farms fault ride through using DFIG with new protection scheme. *IEEE Transactions on Sustainable Energy*. 3(2), 242-254, April. DOI: 10.1109/TSTE.2011.2175756

[21] Manitoba HVDC research center, (2004). *PSCAD/EMTDC Manuals*. https://hvdc.ca/uploads/knowledge_base/pscad_users_guide_v4_6.pdf?t=1497534232, and https://hvdc.ca/uploads/knowledge_base/emtdc_users_guide_v4_6.pdf?t=1497534178 (accessed on 6/1/2018)

[22] Usluer, S. N. (2014). Switch mode converter based damping of PWM converter with LCL type filter for grid interface of renewable energy. *Thesis, Natural and Applied Science,* Middle East Technical University. http://etd.lib.metu.edu.tr/upload/12618359/index.pdf (accessed on 6/1/2018)

[23] Beres, R., Wang X., and Blaabjerg, F. (2015). Improved passive-damped LCL filter to enhance stability in grid-connected voltage source converters. *Proceedings of the 23rd International Conference and Exhibition on Electricity Distribution,* Lyon France, 15-18 June, Paper 1093.

[24] IEEE. (1993). *IEEE Recommended Practices and Requirements for Harmonic Control in Electrical Power Systems*. IEEE Std 519-1992, 1-112. https://ieeexplore.ieee.org/document/210894/ (accessed on 6/1/2018)

[25] Dugan, R. C. McGranaghan, M. F., Santoso, S., Beaty, H.W. (2012). *Electrical power systems quality*, Mc Graw Hill, New York, United States of America, 290.

[26] Wu, W., He, Y., and Blaabjerg, F. (2012). An LCL power filter for single-phase grid-tied inverter. IEEE Trans. on Power Electronic. 27(2), 782–789.

Trends in Renewable Energy
OPEN ACCESS ISSN: 2376-2144
Peer-Reviewed Article futureenergysp.com/index.php/tre

Reconfiguration Technique for Optimization of the Photovoltaic Array Output Power under Partial Shading Conditions

Ahmed M. Mahmoud[1*], Salah M. Saafan[2], Ahmed M. Attalla[3] and Hamdy Elgohary[3]

1: MS. Student, Department of Electrical Power and Machines, Faculty of Engineering- Ain Shams University, Cairo, Egypt
2: Dr., Electric and Computer Engineering Department, Higher Technological Institute (HTI), 10th of Ramadan City, Egypt
3: Professor Dr., Department of electrical power and machines, Faculty of Engineering- Ain Shams University, Cairo, Egypt

Received April 14, 2018; Accepted May 30, 2018; Published June 5, 2018

A partial shading condition is a case under which the PV array is exposed to many problems such as losses of the output power of the PV array, and the PV array has more than one maximum power point (MPP), which makes it so difficult to track the MPP. This paper presents the effect of different partial shading patterns on PV array characteristics and the effect on the output power of the PV array, and provides a comparative literature review on methods to mitigate these effects and the drawbacks of these methods. It also proposed a new reconfiguration strategy that increases the output power of the PV array by 13.8 % from the total power under shadow condition, and a new technique for enhancing the output power of the PV array by 20 % of the total power under fully illumining conditions by controlling the switch matrix between the photovoltaic array and adaptive batteries bank. This paper gives a solution for the problem of the difficulty of tracking the MPP, because the proposed strategy makes only one MPP. The simulation was carried out by using MATLAB Simulink under different shading patterns.

Keywords: Photovoltaic Array; Partial shading; Reconfiguration; MATLAB Simulink; Optimization

1. Introduction

The use of photovoltaic (PV) cells for producing electricity has been recently increased due to reduced costs and increased efficiency of the energy conversion. They are widely used in many applications to reduce the effect of CO_2 emission. However, two of the problems that still affect the performance and reliability of PV modules are shading and mismatch. Shading occurs, when PV system has been installed in some locations where exposure to shading is inevitable. For example, there is not enough land available to build a PV installation to prevent all types of shading. Shading of PV may also occur in the case of leaves, bird droppings or dirt falling on PV cells as well as surrounding structures (building and trees) and the shadows casting over PV cells. The effect of partial shading will reduce the output power of the PV array, and the mismatch may be occurring because cells with different characteristic performance are combined together in an array. The condition of a mismatch may cause power loss. When the characteristic of cells within the

*Corresponding author: engahmedyousf@yahoo.com

Tr Ren Energy, 2018, Vol.4, No.2, 111-124. doi: 10.17737/tre.2018.4.2.0068

PV array differs, individual cells may not operate at the optimal condition. As a result, some shaded cells consume power from the unshaded cells, and the output power of the PV array reduces and the shaded cells overheat. This phenomenon is called hot spot and it may cause damage of the PV cells. Bypass diodes are commonly used in PV arrays to protect against the effect of partial shading and hotspot power dissipation. A bypass diode is connected in parallel but in opposite polarity with the PV cell. Under normal operation, each solar cell will be forward biased and therefore the bypass diode will be reverse biased. Typically, one bypass diode is connected with a string [1]. Since the string has the same current because of the series connection, but the shaded cell is reverse biased to conduct the large current of unshaded cells [2-3]. The activation of bypass diodes causes presence of multiple maximum power peaks that make it difficult to track the maximum power point (MPP). This paper presents a solution for optimization of the maximum output power of the PV array and enhancement of the PV array performance. The remaining of the paper is organized as the following: Section 2 Literature review, Section 3 Modelling of the PV array, Section 4 Research method, Section 5 Simulation and results, and Section 6 Conclusions.

2. Literature Review

Some authors discussed a great number of methods to track the global MPP of the PV array under partial shading conditions. Ref [4] covered a comparison between some techniques for tracking of the global MPP.

Ref [5] studied the effect of the interconnection of the array according to the shading pattern. The author made simulation on three interconnections of PV: array series-parallel connection (SP), total cross tie connection (TCT) and bridge linked connection (BL) at different shading patterns. The author concluded that Series-Parallel (SP) interconnection produces the maximum power as compared to Total-Cross-Tied (TCT) interconnection when shadow is portended to be progress on the last row of horizontal modules, while TCT interconnection produces the maximum power as compared to SP interconnections when shadow is portended to be progress on the left column of vertical modules. The drawback of this technique is that the shading pattern must be known.

In Ref [6], a DC–DC converter controlled by a DC signal of adjustable amplitude was used to track the global MPP.

Ref [7] discussed the optimal layout of PV modules within a PV array giving the maximum output power. Author found that the scheme of parallel connection of all the panels of the system was the best possible configuration.

In Ref [8], a reconfiguration of the shaded modules was made within the fixed PV array by using adaptive bank PV modules and switching matrix. The drawbacks of this technique are the high cost of adaptive bank of PV modules and some of this adaptive bank PV modules may be shaded.

In Ref [9], reconfiguration of the PV array by using the rough set technique (RST) was done. This technique depends on a complex mathematical method for reconfiguration of the PV array.

Ref [10] developed a power optimizer software for executing a power conversion and distributing maximum power point tracking to capture maximum PV array tied to the

electric grid by taking input parameter data about panel, array, shading obstacles, weather data and using this information to perform plane of array irradiance mapping and using this data to develop annual simulation software for power recovery in array during complete or partial shading. But this system required annual update for data and it didn't work accurately if there are unpredictable reason for shading.

In Ref [11], a basic boost converter with several channels was used and the output of the two channel boosts was combined with an uncoupled reactor. This two-channel boost converter increased the output power and efficiency of the PV array, and reduced the harmonic in the output power. This system was controlled by pulse width modulation (PWM) based PI voltage mode controller. However, this converter has non-linearity and non-stability due to its parameter variation and is suitable for low power application only. If the power increased, the size of reactor and the cost increased.

These literature reviews can be summarized as follows: Some authors used different methods for reconfiguration of photovoltaic array during normal operation condition such as ref. [5, 7-9]. Ref. [5] required the user to predict the shading pattern and use the appropriate system configuration, but still there are power losses that didn't substitute. Ref. [4] didn't consider the reconfiguration due to unpredictable condition such as birds and clouds. Ref. [7] suggested a good method for reconfiguration under different shading conditions and ref. [8] substituted the loss occurring due to partial shading by using adaptive PV array, but didn't take in account that the partial shading occurs in the main and alternative PV arrays due to clouds. Ref. [9] suggested a complex method for reconfiguration of the PV array depending on data entry about the shading pattern. If this parameter changed, the system won't work correctly.

Some authors such as ref. [6] and [11] substituted the loss during partial shading by using a power electronics converter that causes the output power of the photovoltaic array to generate multiple power points and causes losses. Some authors suggested different methods for maximum power point such as ref. [4] and [10].

3. Modelling of the PV Array Circuit

3.1 Electrical Model of PV Module (five parameter model)

There are three models of the PV cell, *i.e.,* ideal model, single diode model and two diode model. In this paper, a single diode five parameter model is used as illustrated in Fig. 1. This electrical circuit of the PV cell represents the behavior of the real cell. This model is called a single diode five parameter model because it depends on five parameters that are the nominal PV current, diode current, series resistance, parallel resistance and output voltage of the PV array. These parameters can be estimated as shown in the literature [12].

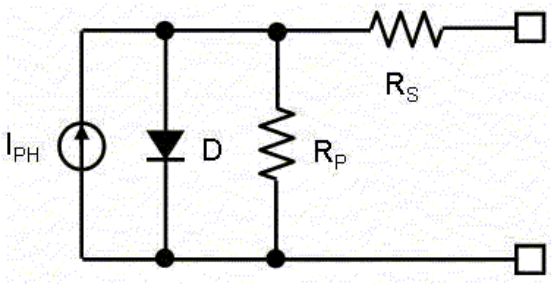

Figure 1. Equivalent circuit of PV cell single diode five parameter model

3.2 Mathematical Model of PV Module (five parameter model)

For the circuit shown in Fig. 1 it is possible to obtain Eq. 1:

$$I = IpH - ID\left(e^{\frac{V}{a\,vt}} - 1\right) - \frac{V+IRs}{Rp} \quad (1)$$

Where IPH is the photovoltaic current, ID is the diode current, V is the PV output voltage, Vt is the thermal voltage and Rs is the series resistance. Rp is the parallel resistance and I is the PV output current. The solution of Eq. 1 gives the I-V characteristic curve of the PV array.

- Thermal voltage

The thermal voltage of a module with Nc cells is given by the Eq. 2.

$$Vth = \frac{K\,T}{q} \quad (2)$$

Where the k is the Boltzmann's constant (1.38×10^{-23} J/K), q is the electron charge (1.6×10^{-19} C) and T is the temperature.

- Diode reverse saturation current (ID)

The diode reverse saturation current can be calculated by substituting the open circuit conditions (V=Voc, I=0) as shown in Eq. 3.

$$ID = \frac{Isc}{\exp\left(\frac{Voc}{aNcVth}\right)-1} \quad (3)$$

Where Voc is the open circuit voltage, Isc is the short circuit current, a is the ideality factor of the diode and Nc is the number of cells.

- Photovoltaic current (IPH)

The photovoltaic current IPH depends on the temperature and the solar irradiation as shown in Eq. 4.

$$IpH = (Iph,reference + Kt(T - Tref))\frac{G}{Gref} \quad (4)$$

Where Iph, ref is the photovoltaic current at reference irradiance and temperature (1000 w/m^2 and 25ºC), G is the incident irradiation (w/m^2), Tref is the reference temperature at normal condition (25ºC) and Gref is the reference irradiance or nominal irradiance (1000 w/m^2).

4. Methods and Results

4.1 Proposed Reconfiguration Strategy

The PV array under partial shading conditions has a preferable performance and output power when the shaded modules are located in the same column or in a limited number of columns. Therefore, to obtain optimal optimization of the output power of the

PV array during shading conditions, it is required to reconfigure the electrical connection of the PV array where the new reconfiguration of the electrical connection of the PV array must make the shaded modules in the same column or in a limited number of columns. The implementation of this task required using of some components (such as a current transformer to measure (Ib) the current passes through a bypass diode and a potential transformer to measure the voltage (v) across the module) and using of electronic switches to make automatic reconfiguration of the modules when the shading occurs. The controller takes order from the current transformer and potential transformer to control the switching of the modules to achieve the best reconfiguration.

The processes of reconfiguration of a PV matrix M × N where M is the number of rows and N is the number of columns are shown in the following flow chart (Fig. 2).

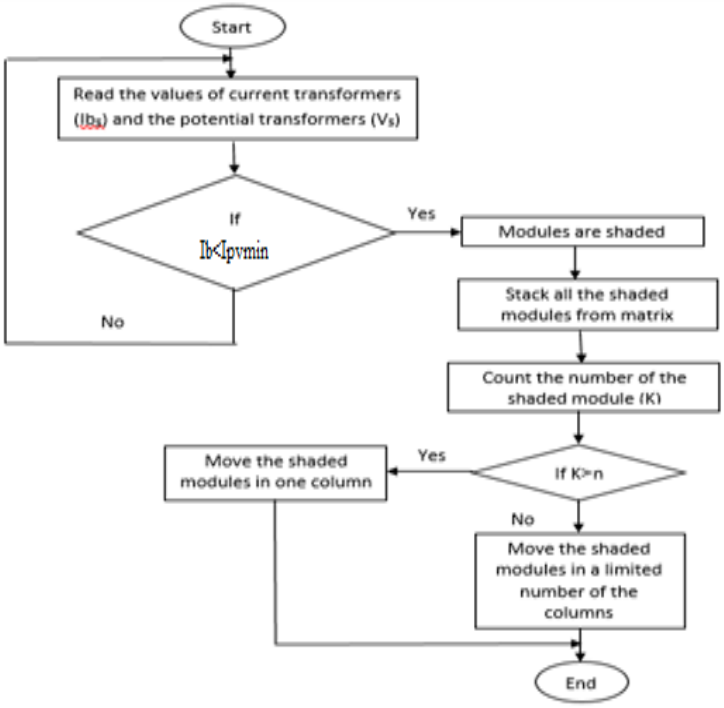

Figure 2. Flow chart of the proposed reconfiguration strategy

4.2 The Principle of Operation of the Proposed Unit

The reconfiguration strategy makes optimization of the output power of the PV array during partial shading condition, but the output power of the array is still lower than the output of the PV array under fully illumining condition. Therefore, a new technique as shown in Fig. 3 is used for substituting this loss of the output power of the PV array during partial shading conditions by using a lead acid battery connected in parallel with the PV array. The parameters of the lead acid battery are shown in Table 1. The voltage of battery is equal to the minimum voltage of series modules under uniform irradiation. When the partial shading occurs, the output current of the photovoltaic array reduced due to partial shading. The current transformer senses the current of the PV array (Ib) and sends the

signal to the controller. The controller compares the current value sent by the current transformer with the preset value of the current (Ipvm) equal to the minimum value of the PV array current under uniform irradiation. If the current measurement of the current transformers of some modules is lower than Ipvm, then the controller will send commands for electronic switches to stack all shaded modules from the matrix and count all shaded modules. If the number of the shaded modules is equal to the number of the columns, then the controller connects all shaded modules in one column for optimization of the output of the PV array and the battery substitutes these losses due to shadowing. If the number of shaded modules is more than / less than the number of columns, then the controller will connect the shaded modules in less number of columns as shown in m-file shown in Appendix.

Table 1. The parameters of lead acid battery

Parameter	Value
Nominal voltage	30 V
Rated capacity	0.4 AH
Fully charged voltage	38.87 V
Nominal discharge current	0.08 A
Internal resistance	0.03 Ω

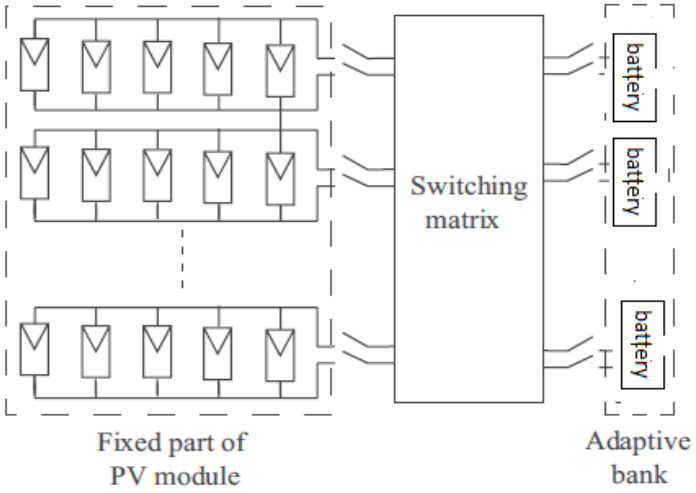

Figure 3. The new proposed unit

5. The Simulation

The simulated PV array system of 3×3 matrix as shown in Fig. 4. The PV module's parameters were taken from National Renewable Energy Laboratory (NREL)'s System advisor model (January 2014) and sorted in Table 2.

Table 2. The parameters of the PV module

Parameter	Value
I_{MPP}	8.07 A
V_{MPP}	10.32 V
P_{MPP}	83.28 W
$I_{s.c.n.}$	8.62 A
$V_{o.c.n.}$	13.30 V
$I_{0.n}$	1.4176e-10A
a	0.99132
Rs	0.098 ohms
Rp	82.11 ohms

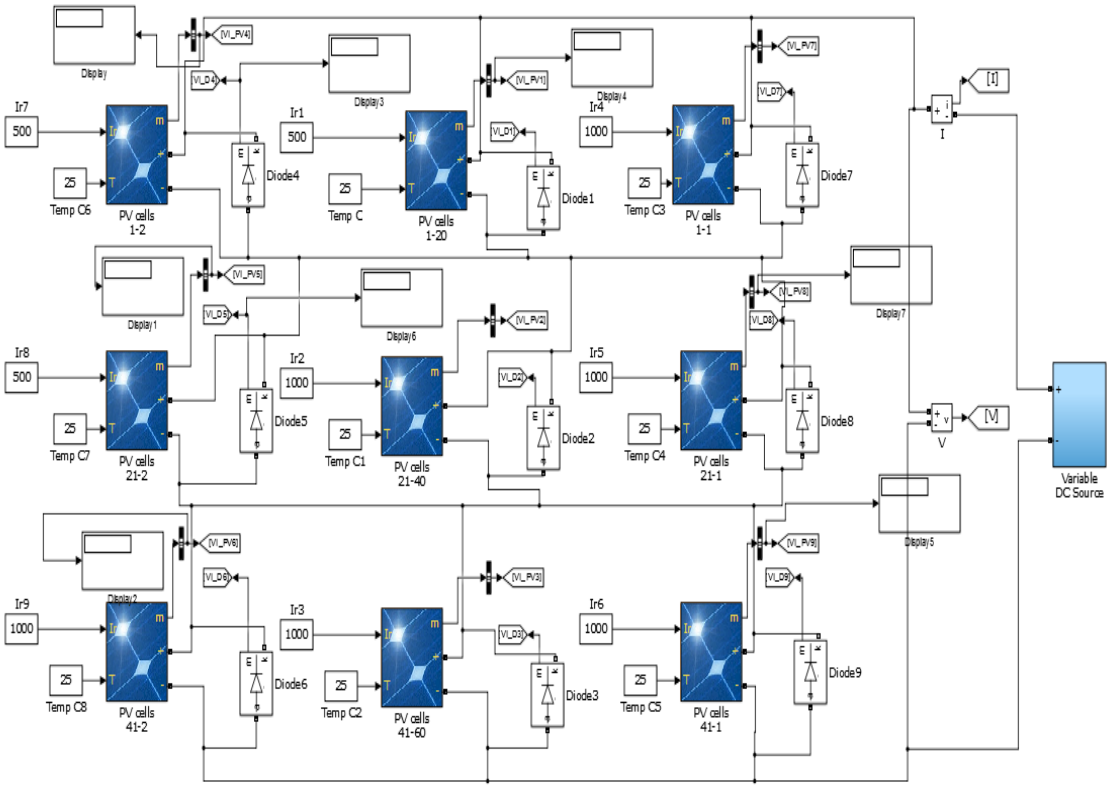

Figure 4. The simulated PV array matrix.

The simulated system was exposed to different irradiance conditions:

5.1 Uniform Illumination Condition

The simulated PV array system under uniform illumination condition where all modules are exposed to the same irradiance of 1000 w/m^2. Fig. 5(a) shows the I-V and P-V curve characteristics of the simulated system under uniform illumination condition.

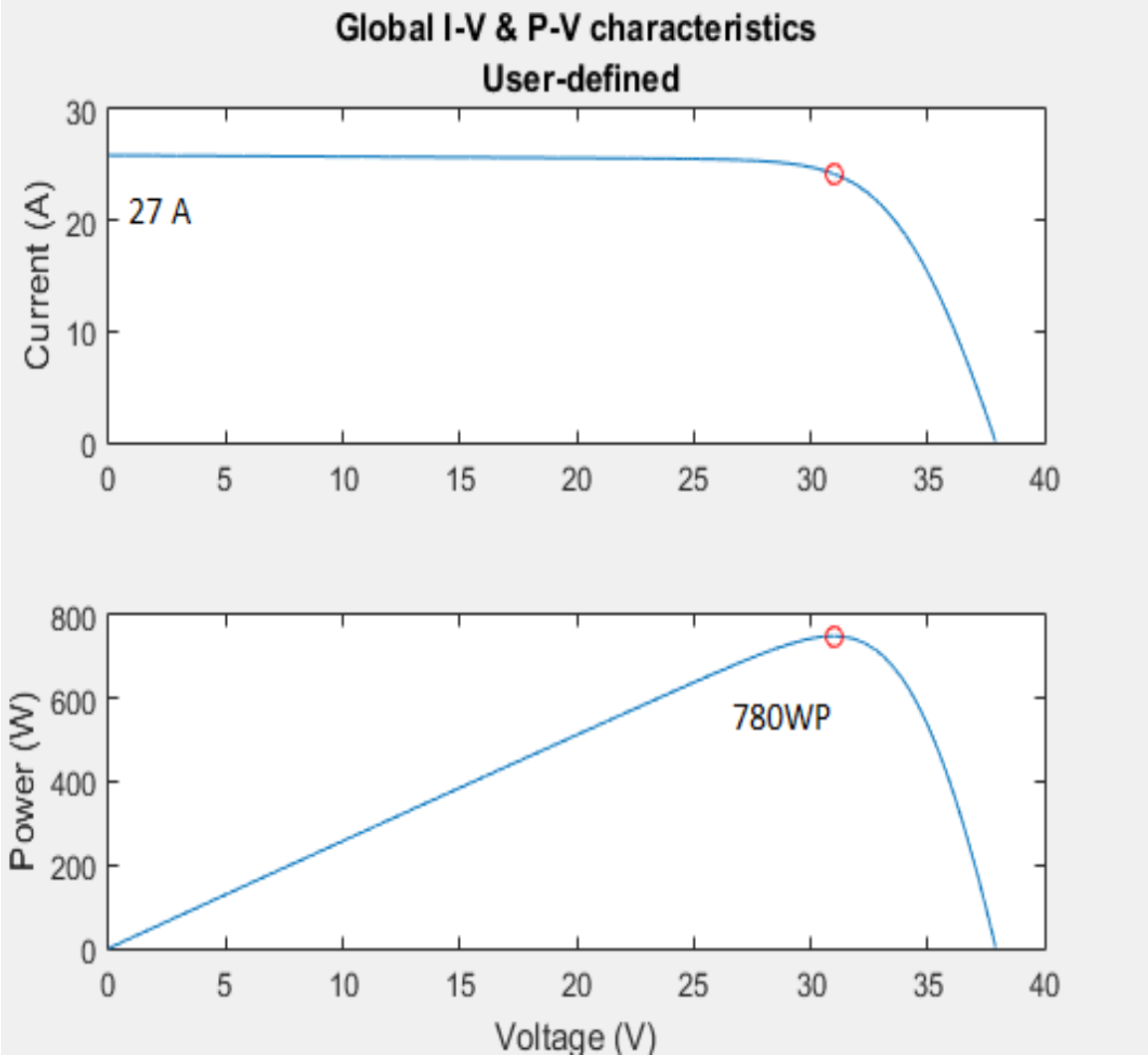

Figure 5 (a). The characteristics of PV matrix under uniform irradiance

5.2 Partial Shading Condition

The influence of the shading on the output power of the PV array is discussed with some simulations. The reference pattern is fully illuminated modules that is an array of 3×3 matrix at irradiance 1000 w/m^2 and temperature of 25ºC. This array of 9 modules with its progressive shading is analyzed. Several simulations are carried out considering that the modules from 0 to 9 are shaded. The percentage of the shaded modules to all modules are 33.33%, *i.e.,* three modules are shaded from the matrix. The shading pattern may occur in different manners in the same column or in different columns. The different cases of shading pattern are simulated, and the results are shown in Fig. 5 (b, c, d).

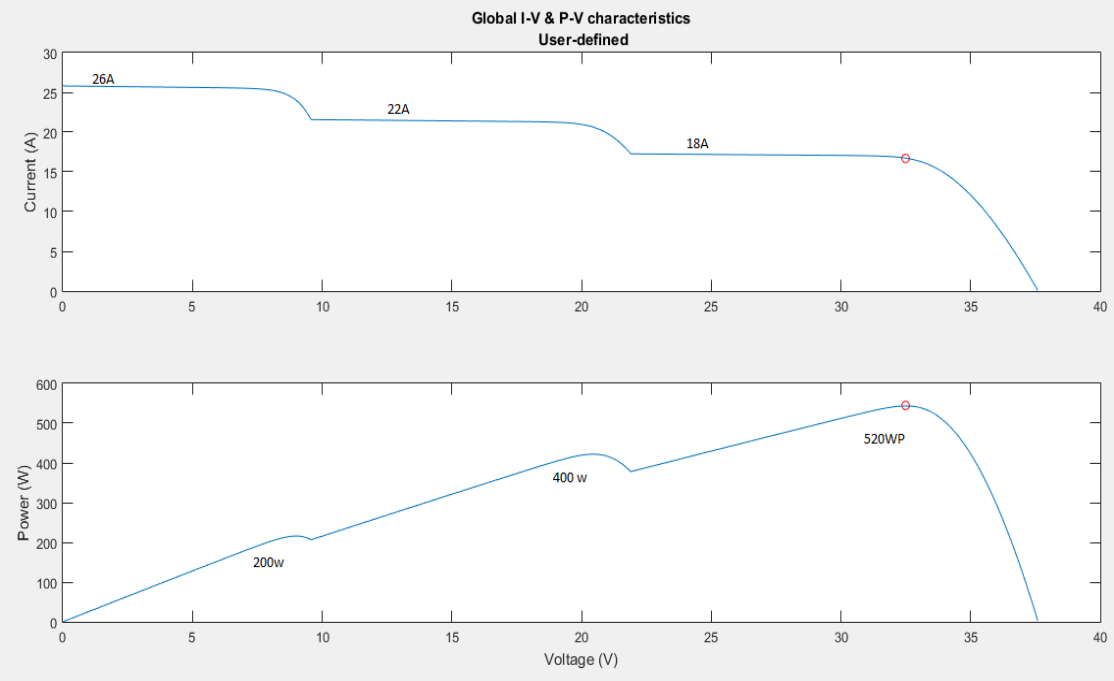

Figure 5 (b). The characteristics of PV matrix under shading pattern in different columns

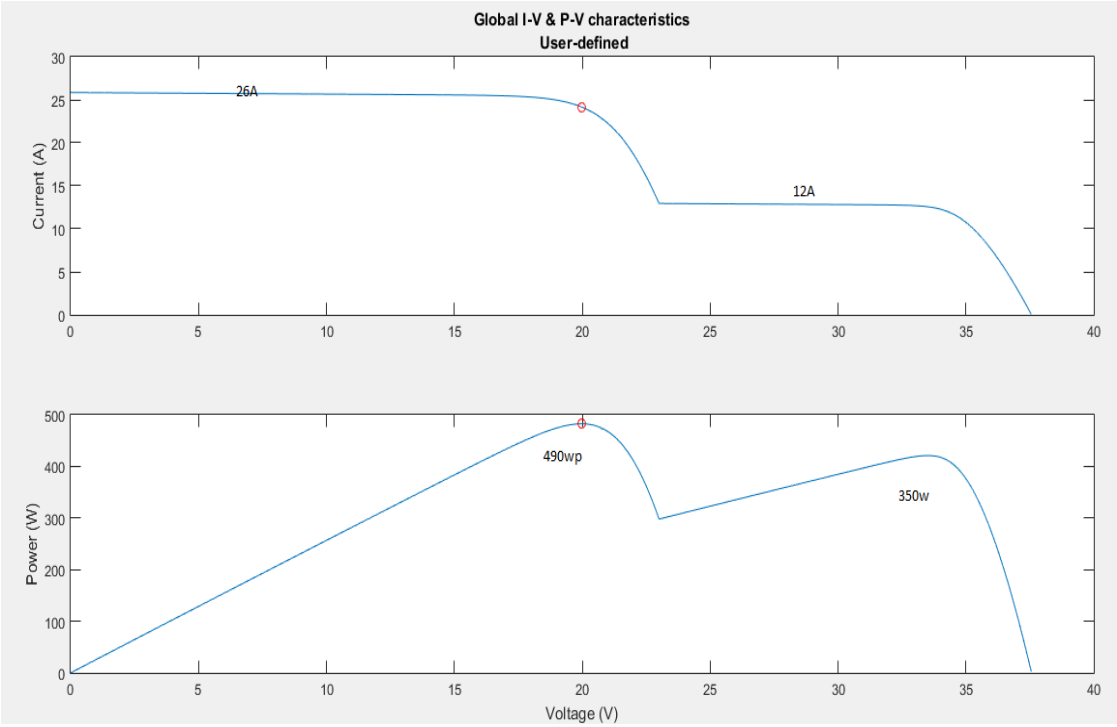

Figure 5 (c). The characteristics of PV matrix under shading pattern in the same row

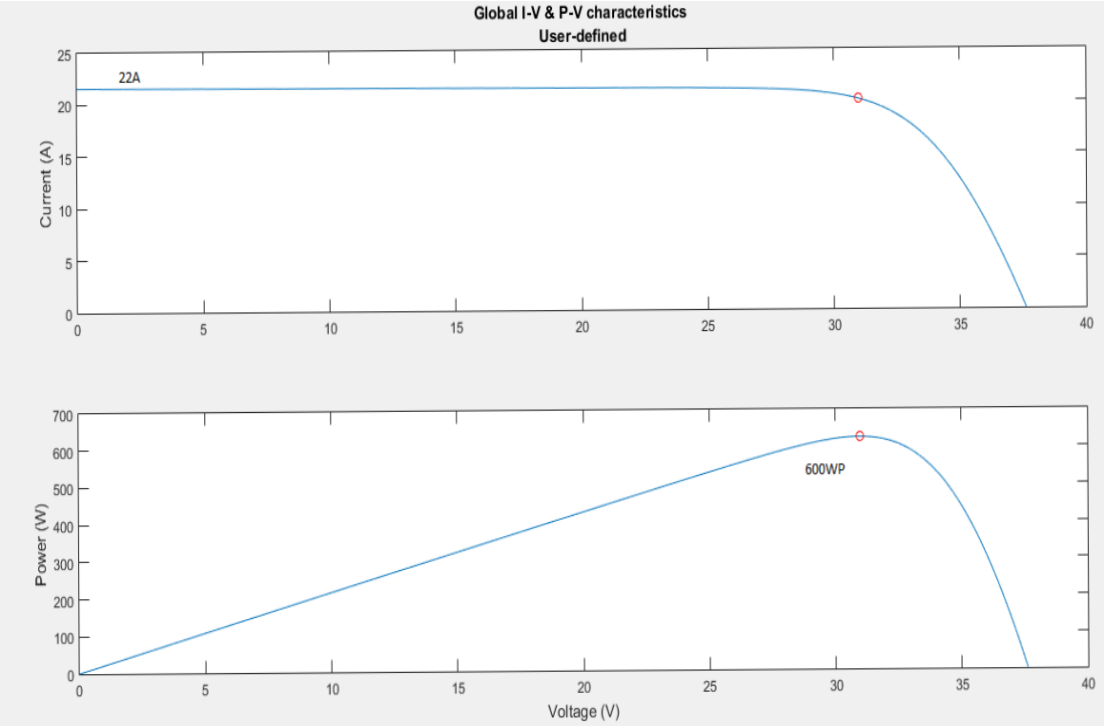

Figure 5 (d). The characteristics of PV matrix under shading pattern in the same column

It's shown from the simulation of the PV matrix under different shading pattern cases that the maximum output power occurred, when all shaded modules in the same columns or in minimum numbers of columns. The maximum power (600 Wp) of the shaded modules in the same column is about 13.8 % higher than the maximum power (490 Wp) of the shaded modules in the same row. Table 3 shows the output power for different reconfiguration at different percentages of shading.

Table 3. The output power for different reconfiguration at different percentage of shading

Percentage of shading	Number of the shaded modules	Pout (the shaded modules in the same row)	Pout (the shaded module in the same column)	Pout (the shaded module in different columns)
10%	1	700 Wp	700 Wp	700 Wp
20%	2	580 Wp	650 Wp	650 Wp
30%	3	490 Wp	600 Wp	520 Wp
40%	4	400 WP	500 Wp	500 Wp
50%	5	480 Wp	480 Wp	480 Wp

The simulated system of the proposed unit is shown in Fig. 6(a). The output power of the PV array will increase by 20% of the total output power during fully illumining by using the new technique as shown in Fig. 6 (b).

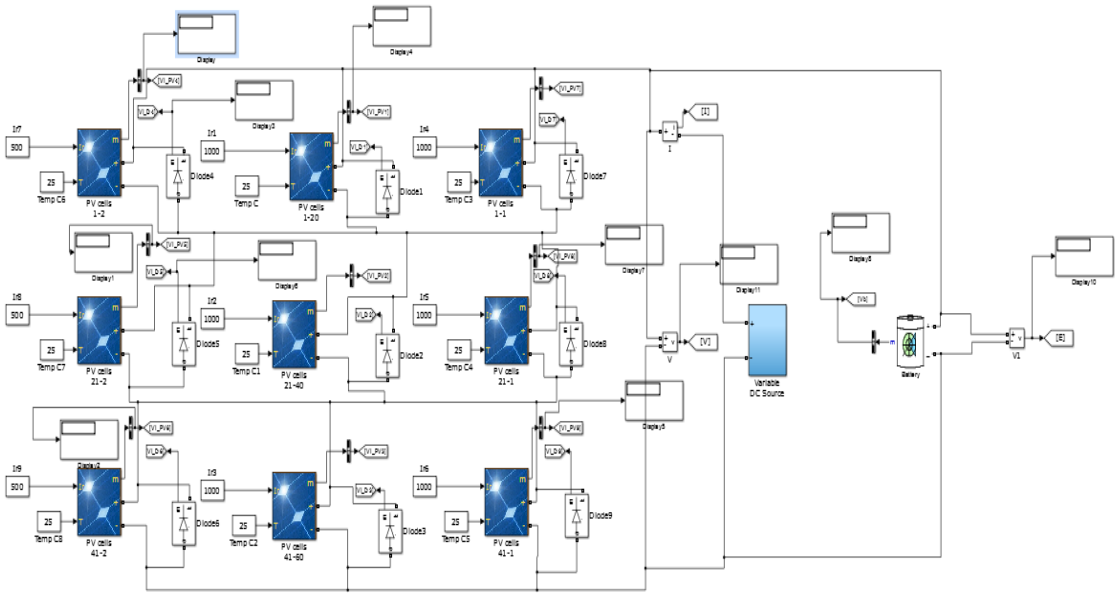

Figure 6 (a). The proposed unit of PV 3×3 matrix by using a new technique

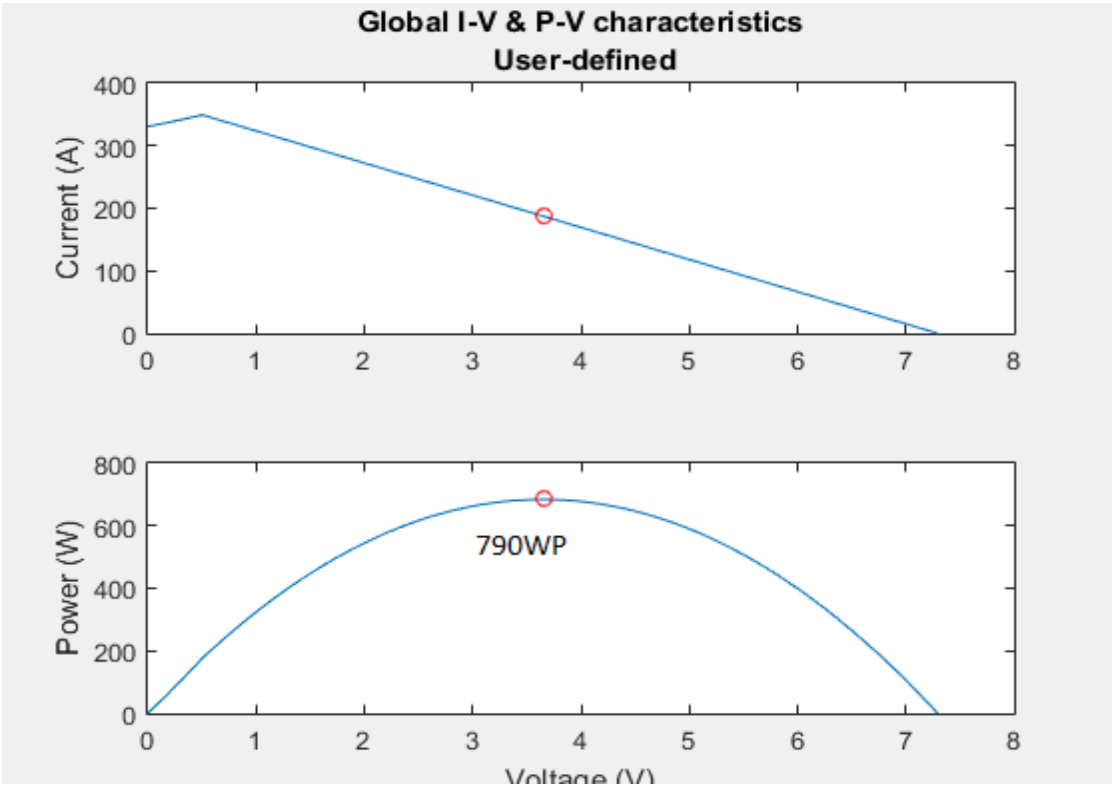

Figure 6 (b). The characteristic of PV 3×3 matrix by using a new technique

5.3 A Comparison of Power Enhancement of the Proposed Method with Different Existing Methods

There are three existing methods for reconfiguration of the PV array under partial shading conditions. In the literature [8], authors made reconfiguration during the partial shading and substituted the loss of power by using alternative PV modules. But this method isn't an effective approach when the partial shading is due to clouds covering the main and alternative PV modules. The proposed technique in this paper used a storage device (a battery) to substitute the loss that occurs during the partial shading condition and also minimize the loss during partial shading. In the literature [9], authors made reconfiguration by a complex method and didn't substitute the loss of the power. In the literature [13], authors maximized the output power of the PV array by using a battery, but the output of the PV array has multiple power peaks that cause problem for MPPT. In this paper, the output waveform has a unique MPP.

6. Conclusions

In this paper, a novel strategy for reconfiguration of the PV array under partial shading conditions is presented. This new strategy increases the output power during the partial shading by 13.8%, prevents producing multiple MPPs, and solves the problems of tracking the MPP during the partial shading. A new technique with using a lead acid battery is presented to increase the output power of the PV under shading condition by 20%, which is similar to the output power of the array under fully illumining condition. The paper simulated the PV array with different shading parameters to optimize the output power during partial shading.

CONFLICTS OF INTEREST

The authors declare that there is no conflict of interests regarding the publication of this paper.

REFERENCES

[1] Mäki, A., Valkealahti, S., & Leppäaho, J. (2012). Operation of series-connected silicon-based photovoltaic modules under partial shading conditions. *Progress in photovoltaics: research and applications*, *20*(3), 298-309.

[2] Spertino, F., & Akilimali, J. S. (2009). Are Manufacturing I –V Mismatch and Reverse Currents Key Factors in Large Photovoltaic Arrays? *IEEE Transactions on Industrial Electronics*, *56*(11), 4520-4531.

[3] Mastromauro, R. A., Liserre, M., & Dell'Aquila, A. (2012). Control issues in single-stage photovoltaic systems: MPPT, current and voltage control. *IEEE Transactions on Industrial Informatics*, *8*(2), 241-254.

[4] Subudhi, B., & Pradhan, R. (2013). A comparative study on maximum power point tracking techniques for photovoltaic power systems. *IEEE Transactions on sustainable energy*, *4*(1), 89-98.

[5] Pareek, S., & Dahiya, R. (2014). Output Power Maximization of Partially Shaded 4* 4 PV field by Altering its Topology. *Energy Procedia*, *54*, 116-126.

[6] Koutroulis, E., & Blaabjerg, F. (2012). A new technique for tracking the global maximum power point of PV arrays operating under partial-shading conditions. *IEEE Journal of Photovoltaics*, *2*(2), 184-190.

[7] Candela, R., Di Dio, V., Sanseverino, E. R., & Romano, P. (2007, May). Reconfiguration techniques of partial shaded PV systems for the maximization of electrical energy production. In *Clean Electrical Power, 2007. ICCEP'07. International Conference on* (pp. 716-719). IEEE. DOI: 10.1109/ICCEP.2007.384290

[8] Bidram, A., Davoudi, A., & Balog, R. S. (2012). Control and circuit techniques to mitigate partial shading effects in photovoltaic arrays. *IEEE Journal of Photovoltaics*, *2*(4), 532-546.

[9] dos Santos, P., Vicente, E. M., & Ribeiro, E. R. (2011, September). Reconfiguration methodology of shaded photovoltaic panels to maximize the produced energy. In *Power Electronics Conference (COBEP), 2011 Brazilian* (pp. 700-706). IEEE. DOI: 10.1109/COBEP.2011.6085266

[10] MacAlpine, S. M., Erickson, R. W., & Brandemuehl, M. J. (2013). Characterization of power optimizer potential to increase energy capture in photovoltaic systems operating under nonuniform conditions. *IEEE Transactions on Power Electronics*, *28*(6), 2936-2945.

[11] Emar, W., Huneiti, Z., & Hayajneh, S. (2015). Analysis, Synthesis and Simulation of Compact Two-channel Boost Converter for Portable Equipments Operating with a Battery or Solar Cell. *Procedia Computer Science*, *65*, 241-248.

[12] Belhaouas, N., Cheikh, M. A., Malek, A., & Larbes, C. (2013). Matlab-Simulink of photovoltaic system based on a two-diode model simulator with shaded solar cells. *Revue des Energies Renouvelables*, *16*(1), 65-73.

[13] Aldaoudeyeh, A. M. I. (2016). Photovoltaic-battery scheme to enhance PV array characteristics in partial shading conditions. *IET Renewable Power Generation*, *10*(1), 108-115.

Appendix

```
m=input('Enter the number of rows')
n=input('Enter the number of columns')
ipvmin=input('Enter the minimum PV array current under unform irradiation')
pvconfiguration=ones(m,n);
k1=m*n;
for i=1:m
    for j=1:n
        i;
        j;

        if (i==2)
            k0=3;
        else
            k0=0;
        end
        ipv_min(i,j)=ipvmin;
        i_b=input('Enter the measured value of the current transormer');
        ib(i,j)=i_b;
        if ib(i,j)<ipv_min(i,j);
            k=(k0+j);
         Pvnewconfiguration (i,j)=0;
        else
            pvnewconfiguration (i,j)=1;
            end
    end
end

   pvnewnconfiguration=find(pvnewconfiguration==0);
   if k==n
       pvnewconfiguration(pvnewnconfiguration)=1;
   end
```

Trends in Renewable Energy
OPEN ACCESS ISSN:2376-2144
Peer-Reviewed Article futureenergysp.com/index.php/tre

Smart Energy and Spectral Efficiency (SE) of Distribution Broadband over Power Lines (BPL) Networks – Part 1: The Impact of Measurement Differences on SE Metrics

Athanasios G. Lazaropoulos*

School of Electrical and Computer Engineering / National Technical University of Athens / 9 Iroon Polytechniou Street / Zografou, GR 15780

Received June 7, 2018; Accepted August 17, 2018; Published August 21, 2018

This paper assesses the impact of measurement differences on the spectral efficiency (SE) of distribution broadband over power lines (BPL) networks when CS2 module is applied. The broadband performance of distribution BPL networks is investigated in the 3-88 MHz frequency range when appropriate injected power spectral density limits (IPSD limits) and uniform additive white Gaussian noise (AWGN) PSD levels from the BPL literature are assumed. The impact of measurement differences on SE of the distribution BPL networks is here assessed through appropriate SE metrics. These SE metrics assessing this impact are detailed in order to act as the benchmark metrics of the countermeasures techniques against measurement differences of the companion paper.

Keywords: Smart Grid; Broadband over Power Lines (BPL); Power Line Communications (PLC); Distribution Power Grid; Spectral Efficiency.

1. Introduction

Smart grid allows the transformation of today's power grid to an advanced IP-based power network with a plethora of relevant broadband applications. Depending on the number and the requirements of the supported smart grid applications, high spectral efficiency (SE) potential of this power network should be assured [1]-[9].

Apart from the smart grid applications, which act as SE consumers, the various communications technologies, which interoperate in order to assure the fine operation of the smart grid, act as the SE producers. Among the available communications technologies that can interoperate under the aegis of the smart grid, a significant role can be played by the broadband over power lines (BPL) technology that exploits the already installed power grid infrastructure [10]-[12].

Since distribution BPL networks –*i.e.*, overhead (OV) and underground (UN) medium-voltage (MV) and low-voltage (LV) BPL networks– are benchmarked in this paper, the spectral behavior of distribution BPL networks is described through the hybrid model [1]-[8], [13]-[22]. Hybrid model has extensively been employed to examine the behavior of various multiconductor transmission line (MTL) configurations in BPL

*Corresponding author: AGLazaropoulos@gmail.com

Tr Ren Energy, 2018, Vol.4, No.2, 125-184. doi: 10.17737/tre.2018.4.2.0076

networks and, of course, in distribution BPL networks such those that are examined in this paper. The hybrid model is modular and consists of: (i) a bottom-up approach that is based on an appropriate combination of MTL theory and similarity transformations; and (ii) a top-down approach that is based on the concatenation of multidimensional transmission matrices of the cascaded network BPL connections. Recently, a refinement of a top-down approach that is denoted as CS2 module, which affects the way that BPL signals are injected onto and extracted from the power lines of distribution BPL connections, has been proposed in [23]. CS2 module is the improved offspring of the initial CS1 module. On the basis of broadband performance metrics supported by the hybrid method such as coupling channel attenuation, capacity and SE, the impact of CS2 module on the performance of the distribution BPL networks has been assessed in [24].

Nevertheless, as already been mentioned in [25]-[32], measurement differences between the experimental and theoretical results occur during the transfer function determination of distribution BPL networks that further affect the computation of all the derivative spectral efficiency metrics, such as capacity and SE. These measurement differences are due to a number of practical reasons and "real-life" conditions. In accordance with [25], [26], [28], [31], these measurement differences can comfortably be handled as error distributions such as continuous uniform distributions (CUDs). Since measurement differences affect the measurement process of coupling channel attenuation of CS2 module, further theoretical computations of capacity and, thus, SE are also influenced. In this paper, the correlation between measurement differences and SE performance of CS2 module is first presented when appropriate injected power spectral density limits (IPSD limits) and uniform additive white Gaussian noise (AWGN) PSD levels from the BPL literature are assumed. A set of statistical metrics is applied in order to assess the impact of measurement differences on the SE of distribution BPL networks. Among these, two sets of SE metrics are going to be used as the benchmark metrics either for assessing the impact of measurement differences on SE in this paper or for the assessment of the mitigation of measurement differences in the companion paper are reported while their behavior is investigated.

The rest of this paper is organized as follows: In Section 2, a brief synopsis of MTL configurations of distribution power grids, indicative distribution BPL topologies, signal transmission in distribution BPL networks and CS2 module is given. Section 3 deals with the measurement differences, applied IPSD limits, AWGN PSD levels and SE. In Section 4, numerical results and discussion are provided, aiming at numerically correlating the measurement differences and SE when CS2 module is applied. Two sets of statistical metrics are applied while those that are going to be used as the benchmark during the countermeasure techniques against the measurement differences of the companion paper are reported and highlighted. Section 5 concludes this paper.

2. Distribution BPL Network Synopsis

2.1 Distribution Power Grid MTL Configuration

A typical case of an OV MV and LV distribution line is depicted in Figs. 1(a) and 1(b), respectively. Overhead distribution lines hang above the ground and they consist of the three parallel non-insulated phase conductors and the neutral

conductor. In this paper, the neutral conductor is considered only in the case of the

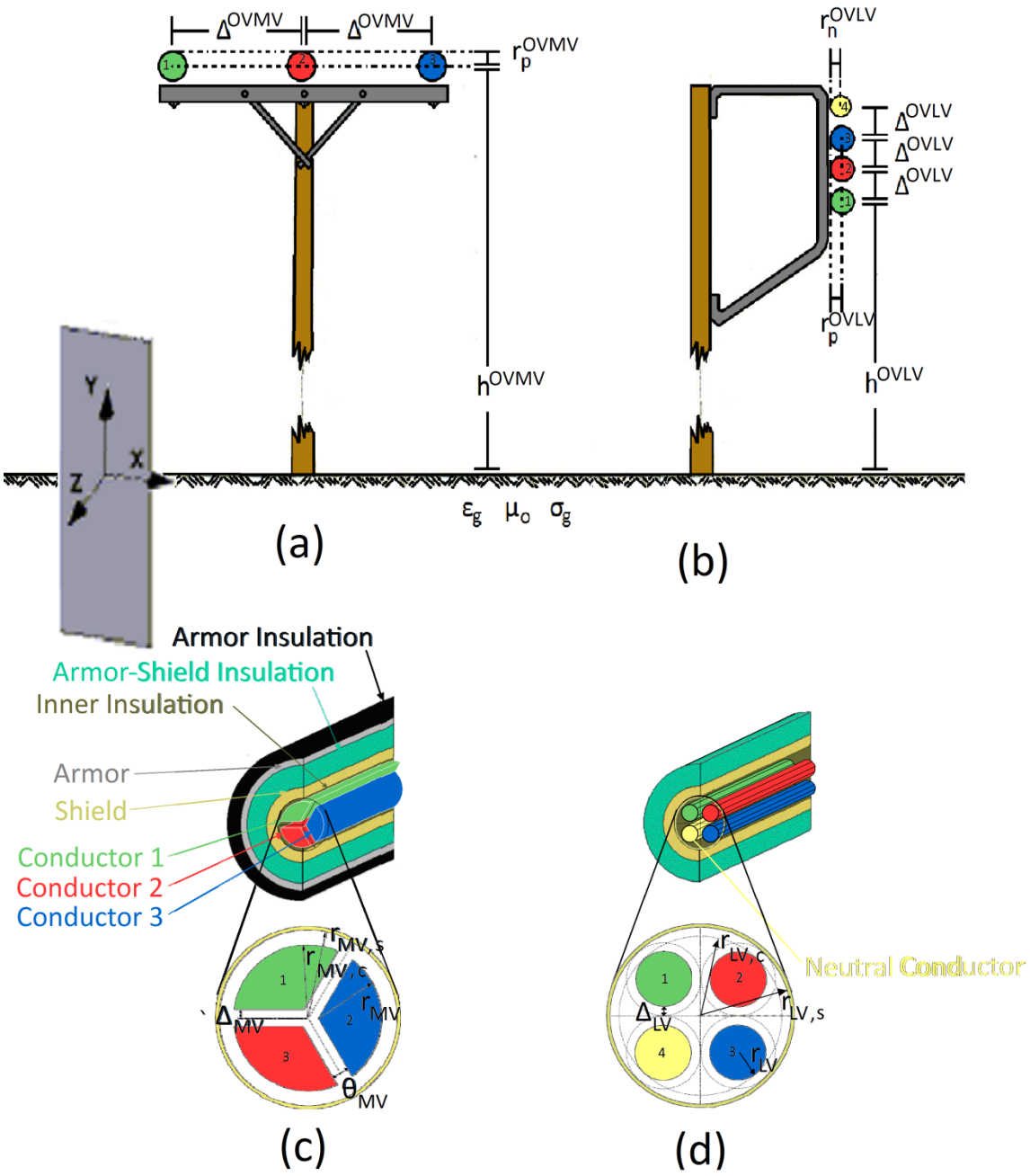

Fig. 1. Typical MTL configurations. (a) Overhead MV [1]. (b) Overhead LV [1]. (c) Underground MV [1]. (d) Underground LV [2].

OV LV distribution line while the conductors are assumed to be steel reinforced aluminum conductors (ACSR conductors). More details regarding the dimensions of the overhead distribution MTL configurations are given in [1], [3], [4], [15], [33], [34].

In Figs. 1(c) and 1(d), the UN MV and UN LV distribution lines are depicted, respectively. As the UN MV distribution line is concerned, the three-phase sector-type Paper Insulated Lead Covered (PILC) cable is assumed while in the case of the UN LV distribution line, three-phase four-conductor core-type Cross-linked polyethylene (XLPE) cable is assumed. Both cables of this paper are buried inside the ground and they consist of one shield conductor that is grounded at both ends. More details regarding the dimensions of the OV distribution MTL configurations are given in [1], [2], [5], [16], [17], [34]-[39].

In all the MTL configurations of the distribution power grid, which are examined in this paper, the conductivity of the ground is assumed σ_g =5mS/m and its relative permittivity is equal to ε_{rg} =13, which define a realistic scenario [1], [3], [4], [7], [13]-[15]. In OV distribution power grids, the ground is considered as the reference conductor whereas the grounded shield is considered as the reference conductor in the UN distribution power grids. The impact of imperfect ground on high frequency signal propagation via distribution power grids is detailed in [2]-[7], [13]-[15], [33], [38], [40]-[43].

2.2 Indicative Distribution BPL Topologies

In accordance with [23], BPL networks are divided into cascaded BPL connections, which can be treated separately. Each BPL connection is bounded by the transmitting end and receiving end repeaters that allow the amplification and regeneration of the attenuated BPL signals. Between the transmitting and receiving end of a BPL connection, the number of branches as well as the topological characteristics may vary depending on the type of the supported power grid. On the basis of its topological characteristics, each BPL connection can be treated as a different distribution BPL topology. This BPL connection consideration remains common either OV or UN distribution BPL networks are studied. In Fig. 2(a), a typical BPL connection with *N* branches is shown.

With respect to Figs. 2(b) and 2(c), the hybrid model is interested in the topology of the BPL connections. Since the distribution BPL topology is known, the hybrid model separates the BPL topology into network modules. Through the two supported approaches of the hybrid model, each network module is treated separately and then their results are synthesized in order to produce the required metrics of the examined distribution BPL topology. In Table 1, the topological characteristics of indicative OV distribution BPL topologies are reported, which are common for both MV and LV power grids. Similarly to Table 1, indicative BPL topologies are presented in Table 2 but in the case of UN distribution BPL topologies.

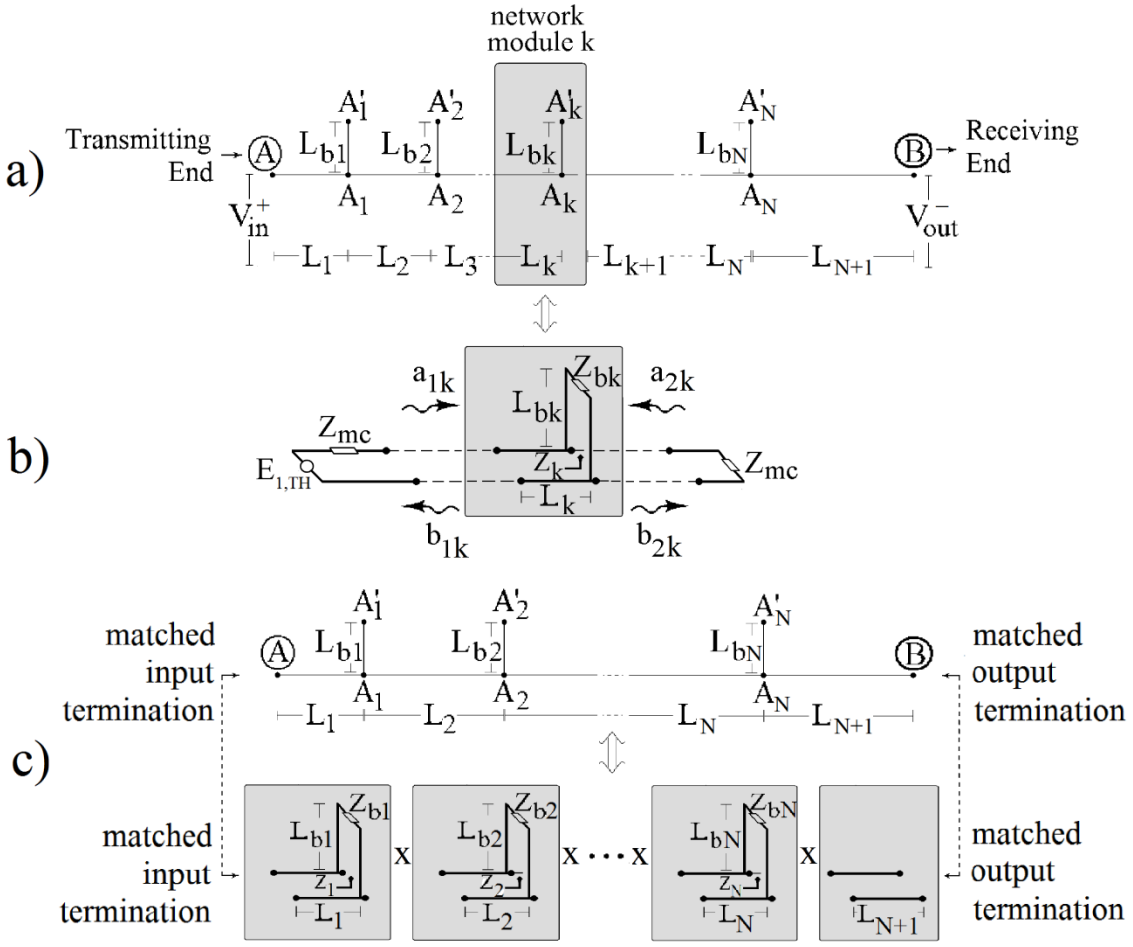

Fig. 2. (a) End-to-end BPL connection with *N* branches. (b) Network module. (c) An indicative BPL topology considered as a cascade of *N*+1 modules corresponding to *N* branches [1], [23].

Table 1. OV Distribution BPL Topologies

Topology Name	Topology Description	Number of Branches	Length of Distribution Lines	Length of Branching Lines
Urban case A	Typical OV urban topology	3	L_1=500m, L_2=200m, L_3=100m, L_4=200m	L_{b1}=8m, L_{b2}=13m, L_{b3}=10m
Urban case B	Aggravated OV urban topology	5	L_1=200m, L_2=50m, L_3=100m, L_4=200m, L_5=300m, L_6=150m	L_{b1}=12m, L_{b2}=5m, L_{b3}=28m, L_{b4}=41m, L_{b5}=17m
Suburban case	OV suburban topology	2	L_1=500m, L_2=400m, L_3=100m	L_{b1}=50m, L_{b2}=10m
Rural case	OV rural topology	1	L_1=600m, L_2=400m	L_{b1}=300m
"LOS" case	OV Line-of-Sight transmission	0	L_1=1000m	-

Table 2. UN Distribution BPL Topologies

Topology Name	Topology Description	Number of Branches	Length of Distribution Lines	Length of Branching Lines
Urban case A	Typical UN urban topology	3	L_1=70m, L_2=55m, L_3=45m, L_4=30m	L_{b1}=12m, L_{b2}=7m, L_{b3}=21m
Urban case B	Aggravated UN urban topology	5	L1=40m, L_2=10m, L_3=20m, L_4=40m, L_5=60m, L_6=30m	L_{b1}=22m, L_{b2}=12m, L_{b3}=8m, L_{b4}=2m, L_{b5}=17m
Suburban case	UN suburban topology	2	L_1=50m, L_2=100m, L_3=50m	L_{b1}=60m, L_{b2}=30m
Rural case	UN rural topology	1	L_1=50m, L_2=150m	L_{b1}=100m
"LOS" case	UN Line-of-Sight transmission	0	L_1=200m	-

Apart from the topological characteristics of Tables 1 and 2, the hybrid model receives as input the circuital parameters of the distribution BPL topologies as well as several assumption affecting the transmission and propagation of the BPL signal across the distribution BPL topologies. As the circuital parameters are concerned, those are detailed in [1]-[8], [13], [15], [17], [34], [35], [44]-[46]. As the transmission and propagation assumptions are concerned, those can be synopsized as follows: (i) the cables of the branching lines are assumed identical to the distribution ones; (ii) the interconnections between the distribution and branch lines are assumed to be fully activated; (iii) the transmitting and the receiving ends are assumed matched to the characteristic impedance of the distribution lines; and (iv) the branch terminations are assumed open circuit.

2.3 BPL Signal Transmission

Hybrid model that deals with the BPL signal propagation and transmission across MTL configurations of distribution BPL networks is based on: (i) a matrix approach of the bottom-up approach that extends the standard transmission line (TL) analysis to the MTL one, which involves more than two conductors; and (ii) the concatenation of multidimensional transmission matrices of the cascaded network modules of the top-down approach. One of the main outputs of the hybrid model is the $n^{\mathrm{G}} \times n^{\mathrm{G}}$ channel transfer function matrix $\mathbf{H}\{\cdot\}$ that relates line voltages $\mathbf{V}(z) = [V_1(z) \quad \cdots \quad V_{n^{\mathrm{G}}}(z)]^{\mathrm{T}}$ at the transmitting (z=0) and the receiving (z=L) ends where n^{G} is the number of the conductors of the examined MTL configuration and $[\cdot]^{\mathrm{T}}$ denotes the transpose of a matrix. The channel transfer function matrix depends on the frequency, the power grid type, the physical properties of the cables and the geometry of the MTL configuration [1], [3], [44], [47].

2.4 BPL Signal Coupling and CS2 Module

According to how signals are injected onto and extracted from the lines of distribution BPL networks, different coupling schemes occur [1], [4], [7], [13]-[15]. With reference to Figs. 3(a) and 3(b), the components of a coupling scheme module at the transmitting and the receiving end are highlighted, respectively.

In [23], [24], CS2 module has been introduced and compared against its predecessor CS1 module. The performance differences among different coupling scheme

modules come from the adjustment of the elements $C_i^{\text{in}}, i = 1, \cdots, n^{\text{G}}$ at the transmitting end and of the elements C_i^{out}, $i = 1, \cdots, n^{\text{G}}$ at the receiving end. The elements $C_i^{\text{in}}, i = 1, \cdots, n^{\text{G}}$ of the input coupling vector $\mathbf{C}^{\text{in}}$ are the input coupling coefficients as well as the participation percentages of the conductors of the MTL configuration during the BPL signal injection while the elements $C_i^{\text{out}}, i = 1, \cdots, n^{\text{G}}$ of the output coupling vector $\mathbf{C}^{\text{out}}$ are the output coupling coefficients. On the basis of a number of restrictions detailed in [23], [24], the coupling scheme channel transfer function of a coupling scheme module that relates output BPL signal $V^{\text{out}-}$ and input BPL signal $V^{\text{in}+}$ is given by

$$H^{\text{C}}\{\cdot\} = \frac{\left[V^{\text{out}-}\right]^{\text{C}}}{\left[V^{\text{in}+}\right]^{\text{C}}} = \left[\mathbf{C}^{out}\right]^{\text{C}} \cdot \mathbf{H}\{\cdot\} \cdot \left[\mathbf{C}^{in}\right]^{\text{C}} \quad (1)$$

where $[\cdot]^{\text{C}}$ denotes the applied coupling scheme.

In accordance with [23], [24] and eq. (1), CS2 module can support three types of coupling schemes, namely:

- *Coupling Scheme Type 1: Wire-to-Ground (WtG) or Shield-to-Phase (StP)* coupling schemes. The signal is injected into only one conductor at the transmitting end and returns via the ground or the shield for overhead or underground BPL connections, respectively. The signal is extracted from the same conductor at the receiving end. Hereafter, WtG or StP coupling between conductor s, $s = 1, \cdots, n^{\text{G}}$ and ground or shield will be detoned as WtG^{s} or StP^{s}, respectively.
- *Coupling Scheme Type 2: Wire-to-Wire (WtW) or Phase-to-Phase (PtP)* coupling schemes. The signal is injected in equal parts between two conductors. The signal is extracted from the same conductors. WtW or PtP coupling between conductors p and q, $p, q = 1, \cdots, n^{\text{G}}$ will be detoned as $\text{WtW}^{p\text{-}q}$ or $\text{PtP}^{p\text{-}q}$, respectively.
- *Coupling Scheme Type 3*: MultiWire-to-MultiWire(MtM) or MultiPhase-to-MultiPhase (MtM) coupling schemes. The signal is injected among multiple conductors with different participation percentages for OV or UN BPL connections, respectively. Similarly to the previous coupling scheme types, the signal is extracted from the same conductor set at the receiving end. As it concerns MTM coupling scheme notation, for example, MtM coupling among the three conductors p, q and r, $p, q, r = 1, \cdots, n^{\text{G}}$ with participation percentages equal to C_p^{in}, C_q^{in} and C_r^{in}, respectively, will be detoned as $\text{MtM}_{C_{\text{p}}^{\text{in}}\_C_{\text{q}}^{\text{in}}\_C_{\text{r}}^{\text{in}}}^{p-q-r}$.

3. Factors Affecting SE Performance

3.1 Measurement Differences

Although the theoretical computation of the coupling scheme channel transfer function, as described in eq. (1), is well-defined and verified, a set of practical reasons

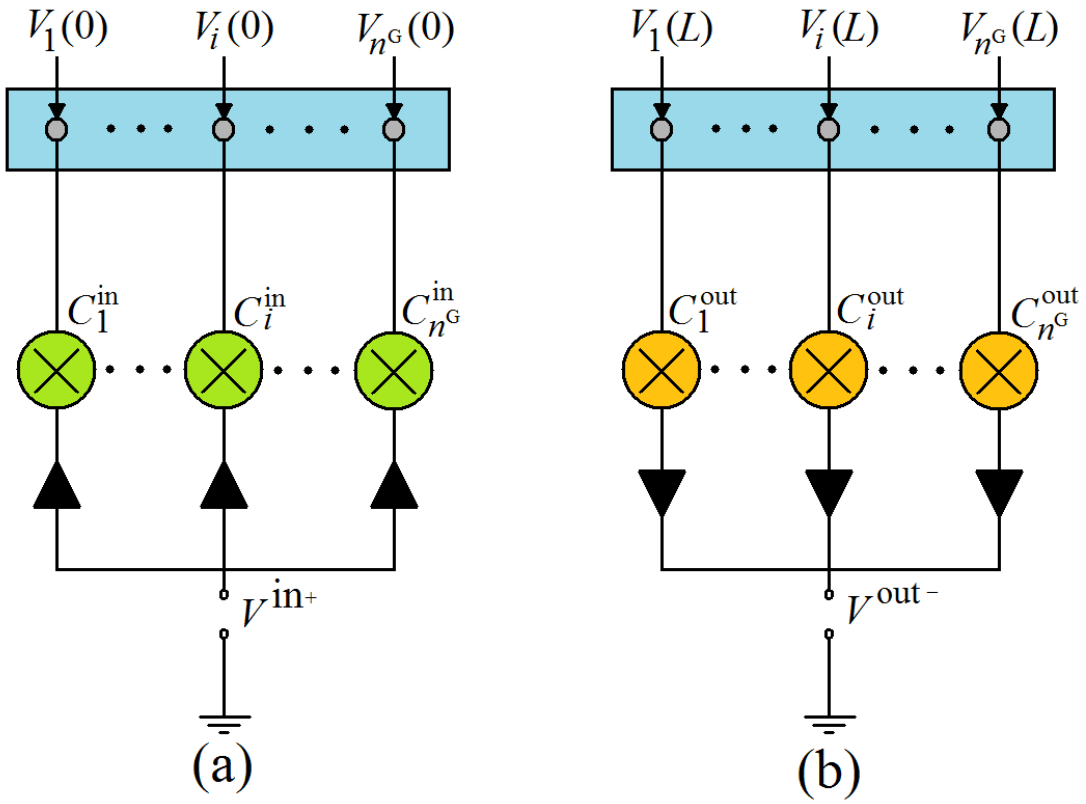

Fig. 3. Coupling scheme module [23], [24]. (a) BPL signal injection interface at the transmitting end. (b) BPL signal extraction interface at the receiving end.

and "real-life" conditions create significant differences between experimental measurements and theoretical results during the determination of the measured coupling scheme channel transfer function of distribution BPL topologies. In accordance with [25], [27], [30], the causes of these measurement differences can be grouped into six categories while the measured coupling scheme transfer function $\overline{H^C}\{\cdot\}$ for given coupling scheme can be determined in mathematical terms by

$$\overline{H^C}(f_i) = H^C(f_i) + e(f_i),\ i=1,\ldots,u \quad (2)$$

where f_i, i=1,…,u denotes the measurement frequency, $e(f_i)$ synopsizes the total measurement difference in dB due to the six categories and u is the number of subchannels in the examined frequency range. According to [27], [30]-[32], the total measurement difference can be assumed to follow either continuous uniform distribution (CUD) with minimum value $-a_{\mathrm{CUD}}$ and maximum value a_{CUD} or normal distribution (ND) with mean μ_{ND} and standard deviation σ_{ND}. In this pair of papers, only the CUD case is examined.

3.2 EMI Policies and Power Constraints

A variety of EMI policies that implies corresponding IPSD limits concerning the BPL operation occurs. The goal of these IPSD limits is to regulate the EMI emissions of the BPL technology in order not to interfere with other wireless and wireline services that operate at the same frequency band. The IPSD limits proposed by Ofcom are adopted in this paper [1]-[8], [13], [48]-[54]. Synoptically, in the 3-30 MHz frequency range,

maximum levels of -60 dBm/Hz and –40 dBm/Hz constitute appropriate IPSD limits $p(f)$ for OV and UN distribution BPL networks, respectively, whereas in the 30-88MHz frequency range, maximum IPSD limits $p(f)$ equal to -77 dBm/Hz and –57 dBm/Hz for the respective OV and UN distribution BPL networks are assumed.

3.3 Noise Characteristics

As the noise properties of distribution BPL networks are concerned in the 3-88 MHz frequency range [1]-[8], a uniform AWGN PSD levels $N(f)$ will be assumed equal to -105 dBm/Hz and -135 dBm/Hz in the case of OV and UN distribution BPL networks, respectively.

3.4 SE

In accordance with [24], SE refers to the information in bps/Hz that can be reliably transmitted over the used BPL bandwidth for the examined distribution BPL topology. In general terms, SE describes the maximum achievable transmission rate per Hz that can be reliably transmitted over the examined BPL network. SE depends on the applied MTL configuration, the examined BPL topology, the coupling scheme applied, the EMI policies adopted and the noise environment [1]-[8]. SE for given coupling scheme channel is determined from

$$SE(f_i) = \log_2\left\{1 + \left[\frac{\langle p(f_i)\rangle_L}{\langle N(f_i)\rangle_L} \cdot |H^C(f_i)|^2\right]\right\}, i = 1, \dots, u \quad (3)$$

where $\langle\cdot\rangle_L$ is an operator that converts dBm/Hz into a linear power ratio (W/Hz). On the basis of eq. (3), the min, max and average SE are going to be examined in this paper in order to highlight the impact of the measurement differences and the different coupling schemes.

4. Numerical Results and Discussion

The numerical results of the supported coupling schemes by the CS2 module for various power grid types and distribution BPL topologies as well as the different intensity levels of measurement differences aim at assessing the impact of the measurement differences on the SE performance.

4.1 SE without Measurement Differences

The broadband performance, in terms of SE in the 3-88 MHz frequency band, is assessed by applying CS2 module when the indicative OV and UN distribution BPL topologies of Sec.2.2 are considered. The IPSD limits of Sec.3.2 and the AWGN levels of Sec.3.3 are applied. Also, three representative coupling schemes, each one representing a coupling scheme type, are considered in OV distribution BPL networks; say, WtG^{1}, $\mathrm{WtW}^{1\text{-}2}$ and $\mathrm{MtM}^{1\text{-}2\text{-}3}_{0.8\_-0.1\_-0.1}$ coupling schemes for the coupling scheme type 1, 2 and 3, respectively. Similarly to OV distribution BPL networks, StP^{1}, $\mathrm{PtP}^{1\text{-}2}$ and $\mathrm{MtM}^{1\text{-}2\text{-}3}_{0.8\_-0.1\_-0.1}$ coupling schemes for the coupling scheme type 1, 2 and 3, respectively, are considered for the UN distribution BPL networks.

In Figs. 4(a)-(c), SE of the indicative OV MV BPL topologies is plotted versus the frequency when WtG^{1}, $\mathrm{WtW}^{1\text{-}2}$ and $\mathrm{MtM}^{1\text{-}2\text{-}3}_{0.8\_-0.1\_-0.1}$ coupling scheme is applied,

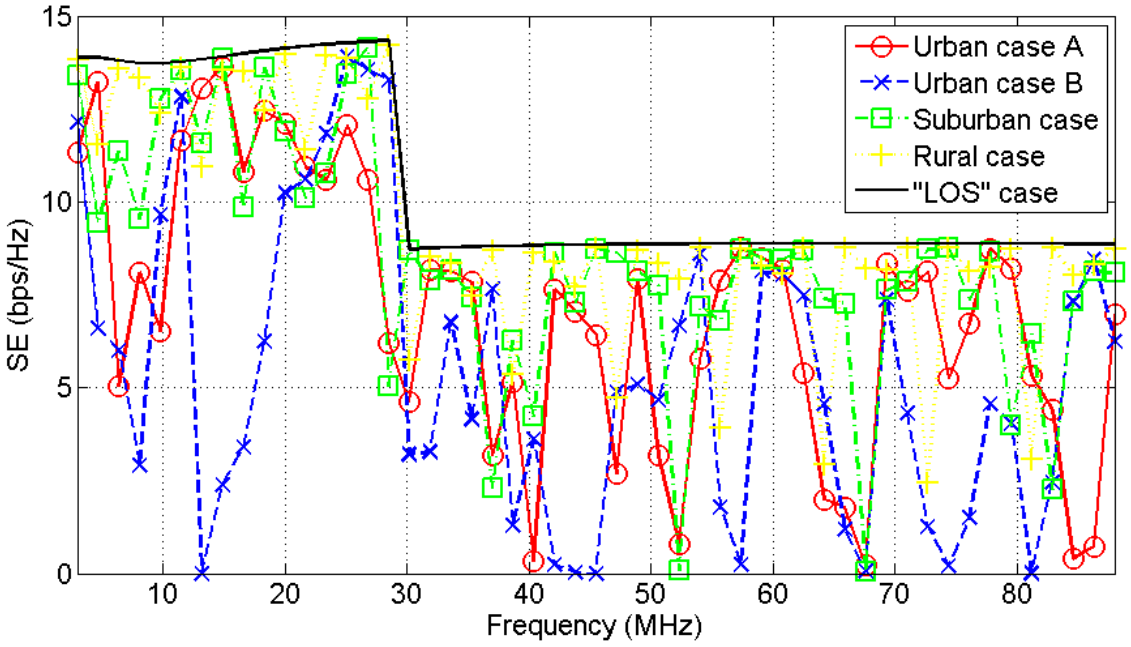
Urban case A
Urban case B
Suburban case
Rural case
"LOS" case
SE (bps/Hz)
Frequency (MHz)
0
5
10
15
10
20
30
40
50
60
70
80

(a)

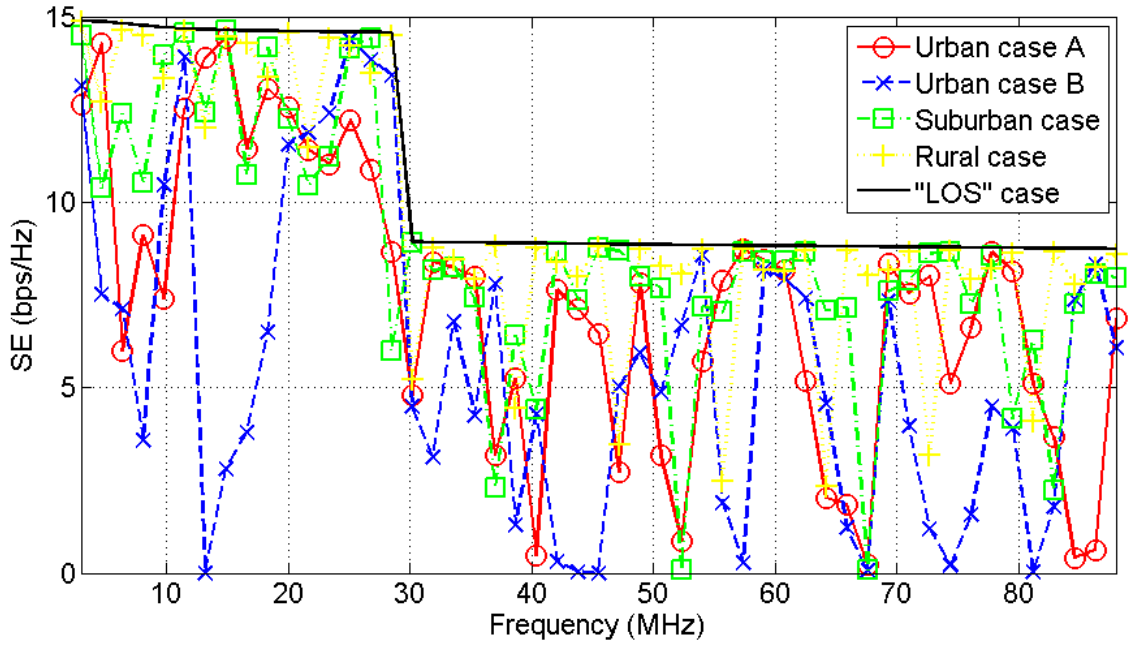
Urban case A
Urban case B
Suburban case
Rural case
"LOS" case
SE (bps/Hz)
Frequency (MHz)
0
5
10
15
10
20
30
40
50
60
70
80

(b)

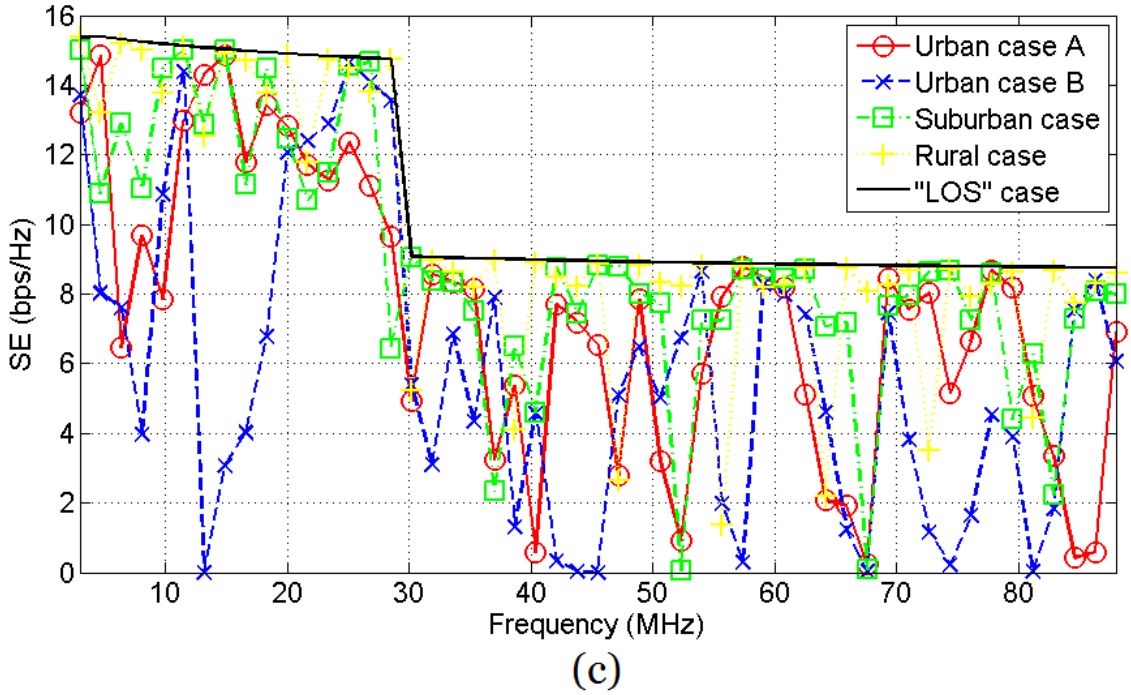

Fig. 4. SE of the indicative OV MV BPL topologies in the 3-88 MHz frequency band when different coupling schemes are applied. (a) WtG^{1} coupling scheme. (b) $WtW^{1\text{-}2}$ coupling scheme. (c) $MtM^{1\text{-}2\text{-}3}_{0.8\_-0.1\_-0.1}$ coupling scheme.

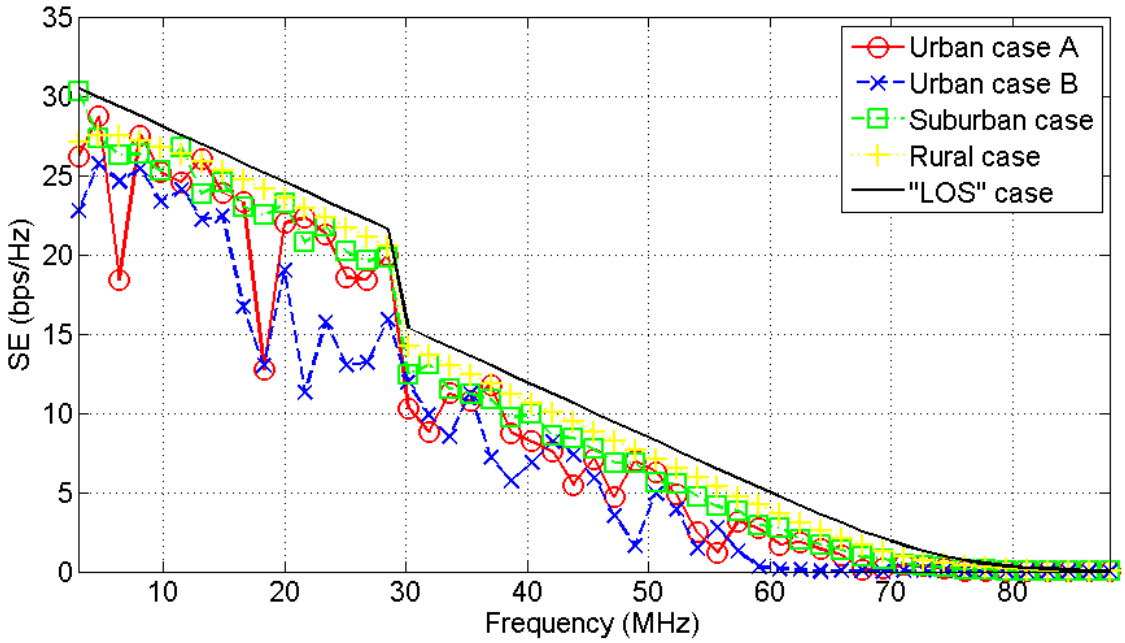
Urban case A
Urban case B
Suburban case
Rural case
"LOS" case
SE (bps/Hz)
Frequency (MHz)
0
5
10
15
20
25
30
35
10
20
30
40
50
60
70
80

(a)

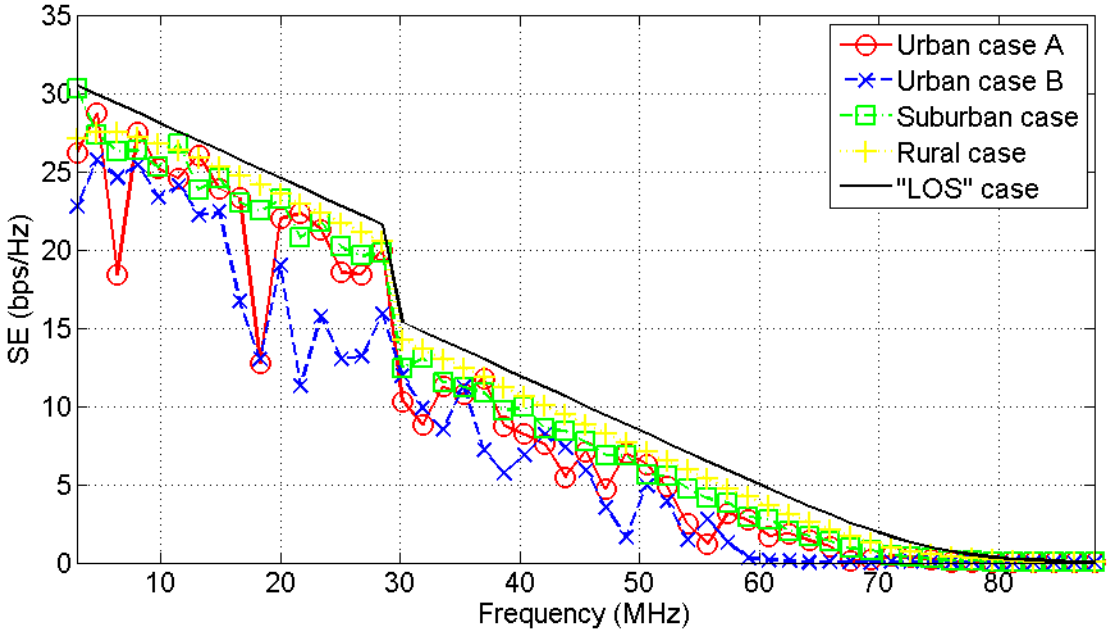
Urban case A
Urban case B
Suburban case
Rural case
"LOS" case
SE (bps/Hz)
Frequency (MHz)
0
5
10
15
20
25
30
35
10
20
30
40
50
60
70
80

(b)

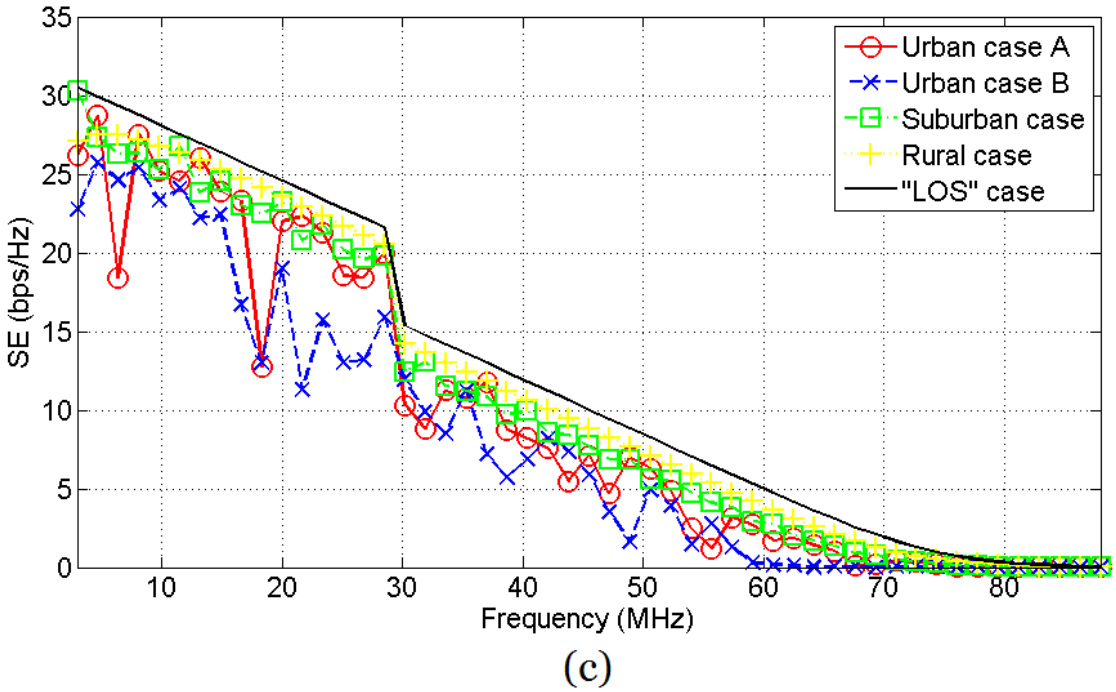

(c)

Fig. 5. SE of the indicative UN MV BPL topologies in the 3-88 MHz frequency band when different coupling schemes are applied. (a) StP^{1} coupling scheme. (b) $PtP^{1\text{-}2}$ coupling scheme. (c) $MtM^{1\text{-}2\text{-}3}_{0.8\_-0.1\_-0.1}$ coupling scheme.

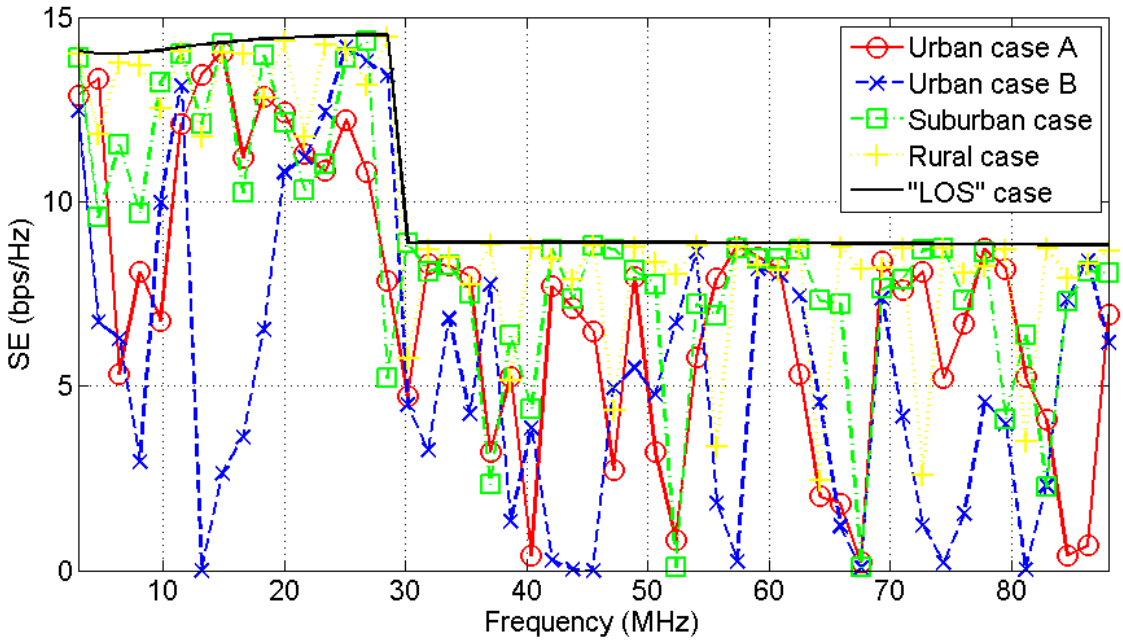
Urban case A
Urban case B
Suburban case
Rural case
"LOS" case
SE (bps/Hz)
Frequency (MHz)
0
5
10
15
10
20
30
40
50
60
70
80

(a)

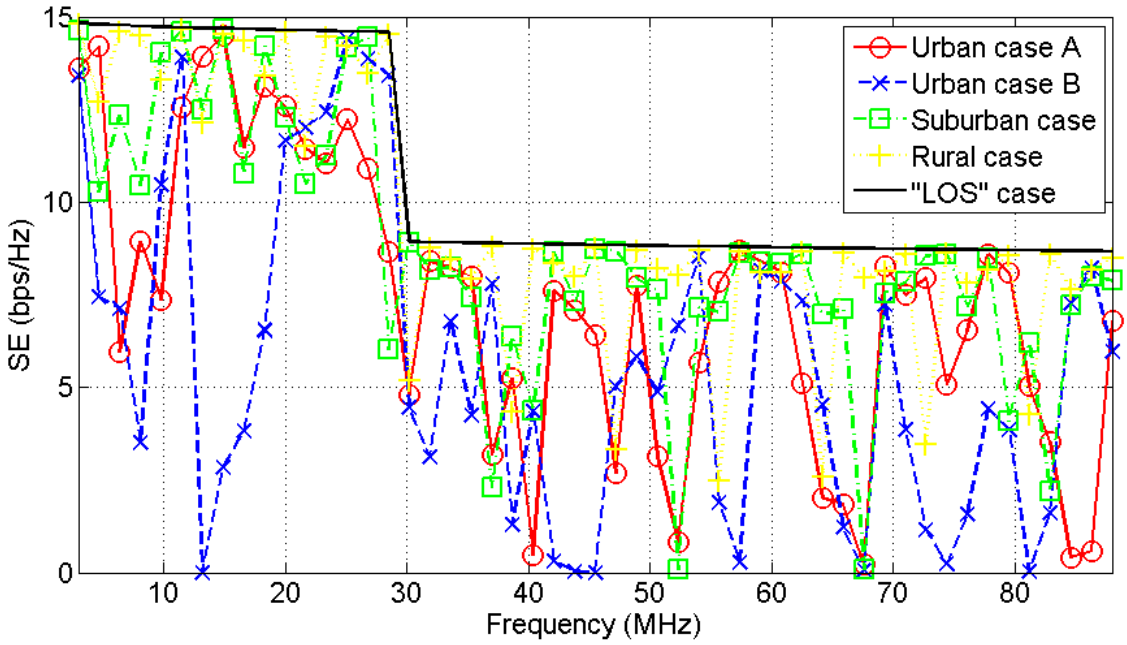
Urban case A
Urban case B
Suburban case
Rural case
"LOS" case
SE (bps/Hz)
Frequency (MHz)
0
5
10
15
10
20
30
40
50
60
70
80

(b)

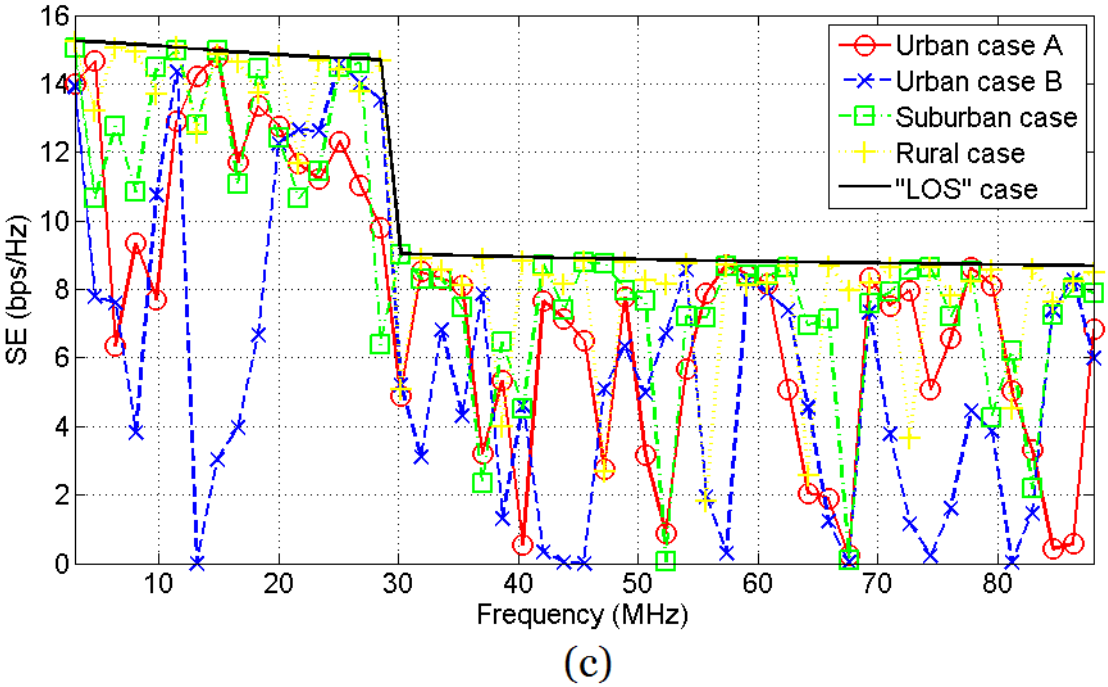

(c)

Fig. 6. Same with Fig. 4 but for the case of the indicative OV LV BPL topologies.

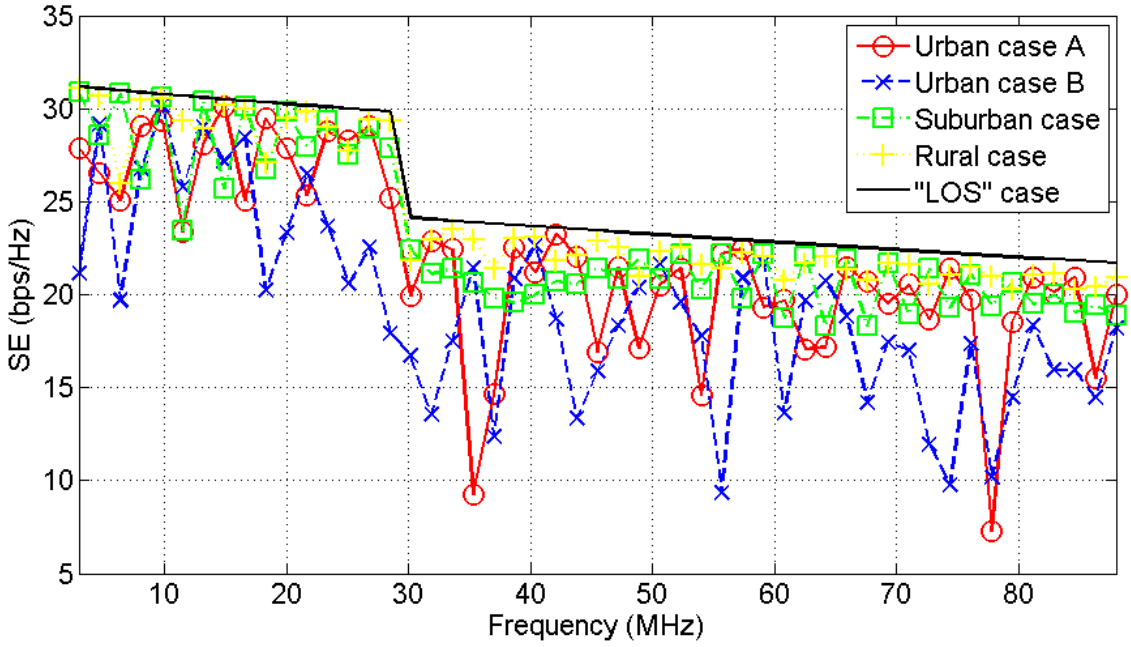
Urban case A
Urban case B
Suburban case
Rural case
"LOS" case
SE (bps/Hz)
Frequency (MHz)
35
30
25
20
15
10
5
10
20
30
40
50
60
70
80

(a)

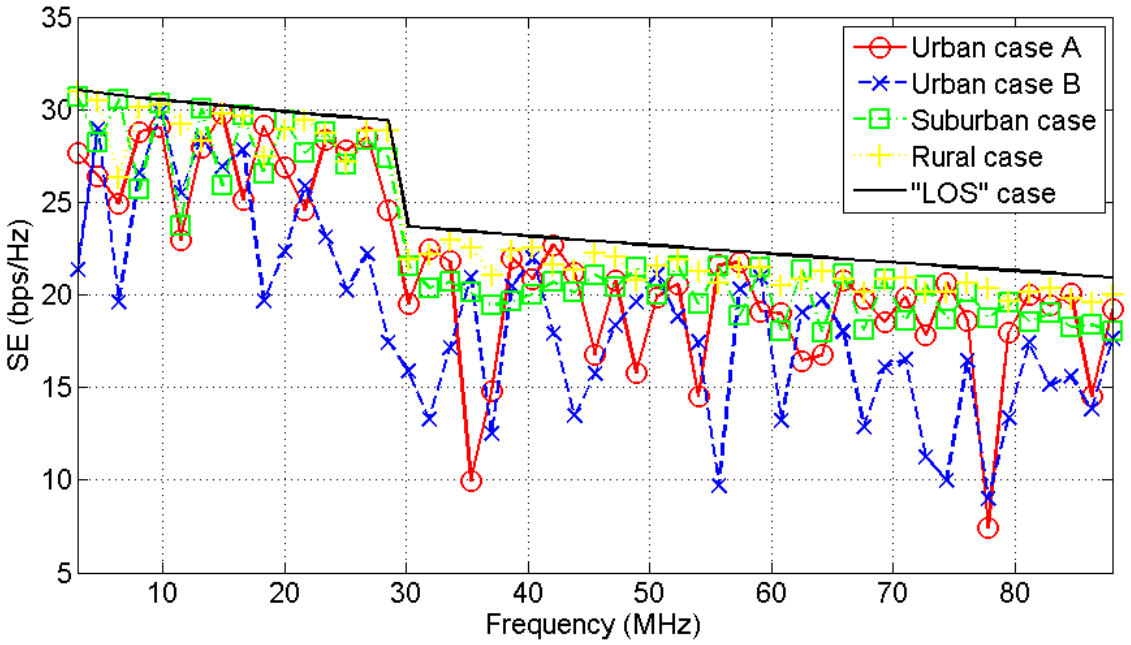
Urban case A
Urban case B
Suburban case
Rural case
"LOS" case
SE (bps/Hz)
Frequency (MHz)
35
30
25
20
15
10
5
10
20
30
40
50
60
70
80

(b)

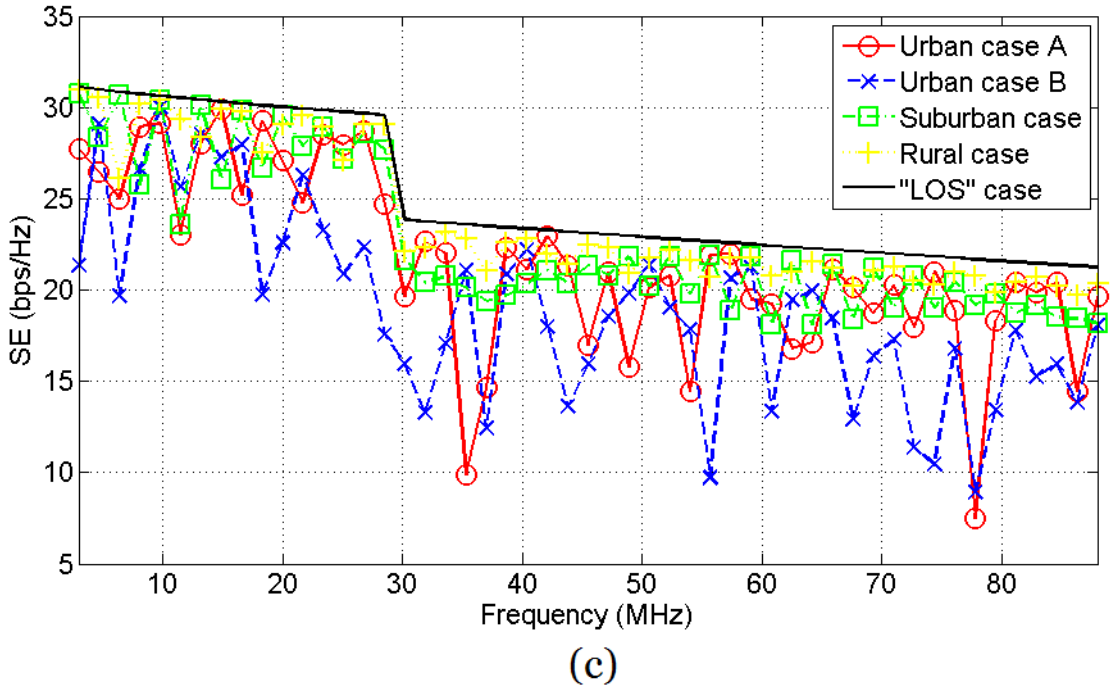

Fig. 7. Same with Fig. 5 but for the case of the indicative UN LV BPL topologies.

respectively. In Figs. 5(a)-(c), SE of the indicative UN MV BPL topologies is plotted versus the frequency when StP^{1}, $PtP^{1\text{-}2}$ and $MtM^{1\text{-}2\text{-}3}_{0.8\_-0.1\_-0.1}$ coupling scheme is applied, respectively. In Figs. 6(a)-(c), same plots with Figs. 4(a)-(c) are given but for the case of the indicative OV LV BPL topologies while in Figs. 7(a)-(c), same curves with Figs. 5(a)-(c) are presented but for the case of the indicative UN LV BPL topologies.

Observing Figs. 4(a)-(c), 5(a)-(c), 6(a)-(c) and 7(a)-(c), it is evident that the SE of the "LOS" case acts as a SE mask for the other indicative distribution BPL topologies of the same distribution power grid type and coupling scheme. Since "LOS" topologies present the most favorable transmission behavior in comparison with the other branched BPL topologies, this profile of low channel attenuation of "LOS" topologies is also reflected on a favorable SE performance that is the best of the other respective ones of the other distribution BPL topologies.

Also, in all the indicative BPL topologies examined, there are two distinctive frequency bands of SE performance that are bounded by a SE step of the "LOS" case. This SE step is approximately equal to 5 bps/Hz and is located at 30 MHz in all the indicative distribution BPL topologies regardless of their distribution power grid type and the coupling scheme. This SE step is explained by the fact that a significant change of the applied IPSD limits occurs at 30 MHz, while IPSD limits remain higher at the frequency band of 3-30 MHz in comparison with the ones at the frequency band of 30-88 MHz despite the examined power grid type. In general, the higher IPSD limits of UN distribution BPL networks with the lower noise AWGN levels explain the higher SE values of distribution BPL topologies.

In addition, the recent research effort regarding the capacity enhancement of distribution BPL networks through the wise use of coupling scheme modules has significantly improved the SE of WtW/PtP coupling schemes while proposes new

SE efficient with low electromagnetic interference (EMI) such as MtM coupling schemes [23], [24]. Indeed, for the same power grid type and coupling scheme, the SE differences among the different applied coupling schemes remain now relatively low. In contrast with CS1 module [1], [8], [47], CS2 module allows the WtW and PtP coupling schemes to present approximately the same SE results with the WtG and StP coupling schemes, respectively. Here it should be reminded the better EMC performance of WtW and PtP coupling schemes [15], [33]. Also, the careful selection of the used conductors of the examined MTL configurations as well as the respective participation percentages can offer higher SE results than the SE of the traditional WtG and WtW coupling schemes with even better electromagnetic compatibility (EMC) behavior through the use of MtM coupling schemes in OV and UN distribution BPL topologies.

In order to easily distinguish the SE performance differences among different power grid types, indicative BPL topologies and coupling schemes, a set of statistical metrics, which is denoted hereafter as set A and consists of the minimum, the maximum and the average value, of SE for each of the examined cases in Figs. 4(a)-(c), 5(a)-(c), 6(a)-(c) and 7(a)-(c), is reported in Table 3.

From Table 3, it is evident that MtM coupling schemes achieve the best SE performance statistical metrics in comparison with the coupling schemes of coupling scheme type 1 and 2. This favorable SE performance can be combined with appropriate adjustment of the participation percentages so that better EMC can be assured and IPSD limits can be further relaxed. However, the complexity of the BPL unit installation is a critical issue since more than two conductors of the MTL configurations are required. As the coupling schemes of the coupling scheme type 1 and 2 are examined, WtW and PtP coupling schemes are indeed almost SE equivalent to WtG and StP coupling schemes, respectively, when CS2 module is adopted. In addition, by observing SE minimum values of all the cases examined, it is evident that the rich multipath environment of the urban and suburban distribution BPL topologies creates spectral notches that further affect the SE performance regardless of the examined power grid type. This last observation explains the almost zero values of the SE minimum values of the Table 3. In contrast, in accordance with the Figs. 4(a)-(c), 5(a)-(c), 6(a)-(c) and 7(a)-(c), the SE maximum values of the examined distribution BPL topologies follow the "LOS" mask for given power grid type and coupling scheme type. In fact, the maximum value for the "LOS" cases is observed at 3 MHz whereas in all the other cases their SE maximum value is observed in the 3-30 MHz frequency band in relation with the "LOS" mask. Hence, the average SE for each examined distribution BPL topology offers a very descriptive statistical metric for the performance since describes the impact of the channel attenuation, IPSDM limits and AWGN levels across the entire 3-88 MHz frequency band. In order to examine the impact of the measurement differences on the SE performance, only the average SE performance for each distribution BPL topology is examined, hereafter.

Table 3. SE Statistical Metrics of Set A for the Different Indicative Distribution BPL Topologies (the frequency spacing is equal to 0.1 MHz)

		SE (bps/Hz)								
		(WtG^{1} / StP^{1})			(WtW^{1-2} / PtP^{1-2})			$MtM^{1-2-3}_{0.8\_-0.1\_-0.1}$		
Distribution power grid type	**Topology Name**	Min	Max	Average	Min	Max	Average	Min	Max	Average
OVMV	Urban case A	0	13.96	7.00	0	14.57	7.19	0	15.00	7.35
	Urban case B	0	14.19	5.39	0	14.51	5.59	0	14.77	5.74
	Suburban case	0	14.35	8.29	0	14.63	8.49	0	15.05	8.64
	Rural case	2.45	14.25	9.25	2.25	14.87	9.43	1.34	15.41	9.58
	"LOS" case	8.73	14.37	10.48	8.75	14.89	10.68	8.76	15.41	10.83
OVLV	Urban case A	0	14.34	7.12	0	14.62	7.19	0	15.04	7.30
	Urban case B	0	14.43	5.51	0	14.53	5.58	0	14.75	5.70
	Suburban case	0	14.51	8.40	0	14.76	8.47	0	15.18	8.59
	Rural case	2.33	14.45	9.37	2.38	14.81	9.43	1.83	15.24	9.55
	"LOS" case	8.82	14.53	10.60	8.67	14.83	10.67	8.69	15.23	10.78
UNMV	Urban case A	0	28.69	9.57	0	28.69	9.57	0	28.69	9.57
	Urban case B	0	28.52	8.05	0	28.52	8.05	0	28.52	8.05
	Suburban case	0	30.26	10.46	0	30.26	10.46	0	30.26	10.46
	Rural case	0.02	30.07	11.37	0.02	30.07	11.37	0.02	30.07	11.37
	"LOS" case	0.05	30.51	12.33	0.05	30.51	12.33	0.05	30.51	12.33
UNLV	Urban case A	6.89	30.50	21.73	7.12	30.19	21.21	7.19	30.31	21.41
	Urban case B	5.67	30.36	19.20	5.80	30.07	18.68	5.75	30.20	18.89
	Suburban case	17.62	31.10	22.95	17.16	30.92	22.43	17.26	30.98	22.64
	Rural case	20.00	31.10	24.12	19.38	30.93	23.60	19.59	30.99	23.81
	"LOS" case	21.69	31.20	25.29	20.93	31.06	24.77	21.25	31.11	24.97

4.2 SE with Biased Measurement Differences

With reference to eq. (2), the SE impact of measurement differences is examined in this subsection. As measurement differences can be expressed in dB, the average SE and the range of the average SE for given positive value a in dB is presented in the following figures when the indicative distribution BPL topologies are assumed. In detail, the lower and the upper limit of the average SE range are calculated for given a value when the minimum value $-a$ and the maximum value a are applied across the entire set of the measured coupling scheme transfer function, respectively. In this subsection, it should be noted that the assumed value of a is added to the measured coupling scheme transfer function of each measurement frequency thus acting as a bias.

More specifically, in Figs. 8(a)-(c), the upper and the lower limits of the average SE range of the indicative OV MV BPL topologies are plotted versus the value a when WtG^{1}, $\mathrm{WtW}^{1\text{-}2}$ and $\mathrm{MtM}^{1\text{-}2\text{-}3}_{0.8\_-0.1\_-0.1}$ coupling scheme is applied, respectively. In Figs. 9(a)-(c), the upper and the lower limit of the average SE range of the indicative UN MV BPL topologies is plotted versus the value a when StP^{1}, $\mathrm{PtP}^{1\text{-}2}$ and $\mathrm{MtM}^{1\text{-}2\text{-}3}_{0.8\_-0.1\_-0.1}$ coupling scheme is applied, respectively. In Figs. 10(a)-(c), same plots with Figs. 8(a)-(c) are given but for the case of the indicative OV LV BPL topologies while in Figs. 11(a)-(c), same curves with Figs. 9(a)-(c) are presented but for the case of the indicative UN LV BPL topologies. In Table 3, the results concerning the average SE range of Figs. 8-11 with respect to the different a values of the measurement differences are reported.

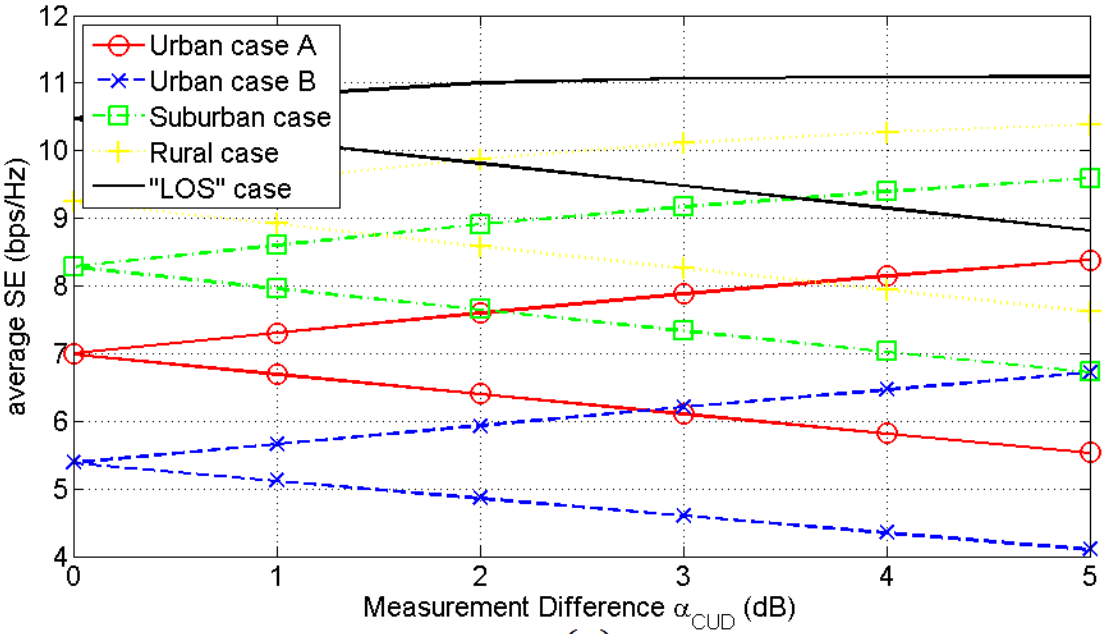
Urban case A
Urban case B
Suburban case
Rural case
"LOS" case
average SE (bps/Hz)
Measurement Difference α_{CUD} (dB)

(a)

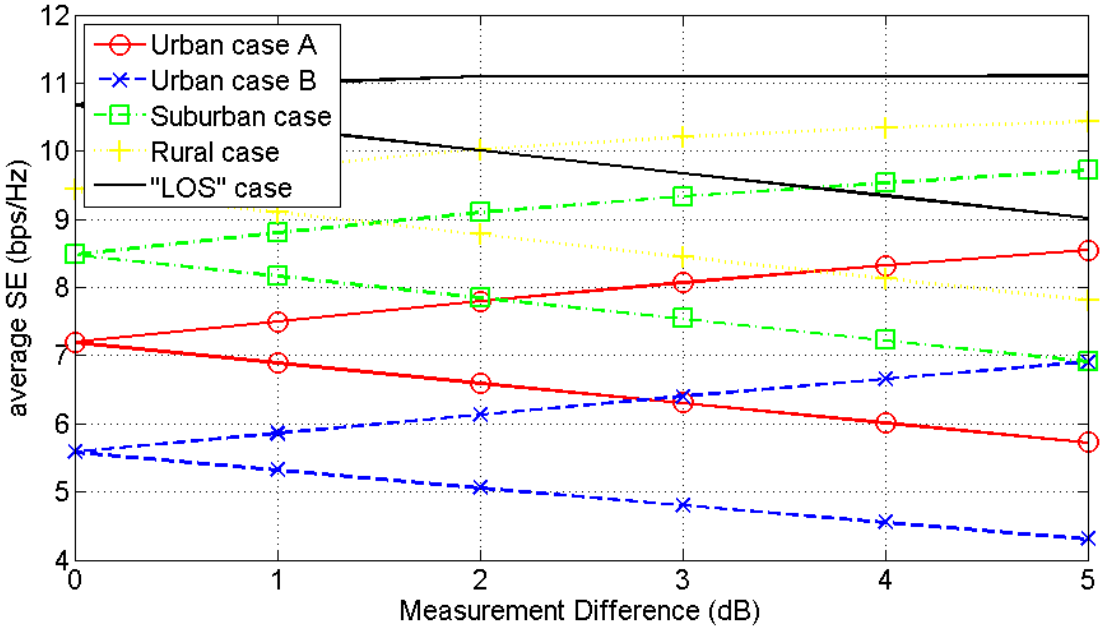
Urban case A
Urban case B
Suburban case
Rural case
"LOS" case
average SE (bps/Hz)
Measurement Difference (dB)

(b)

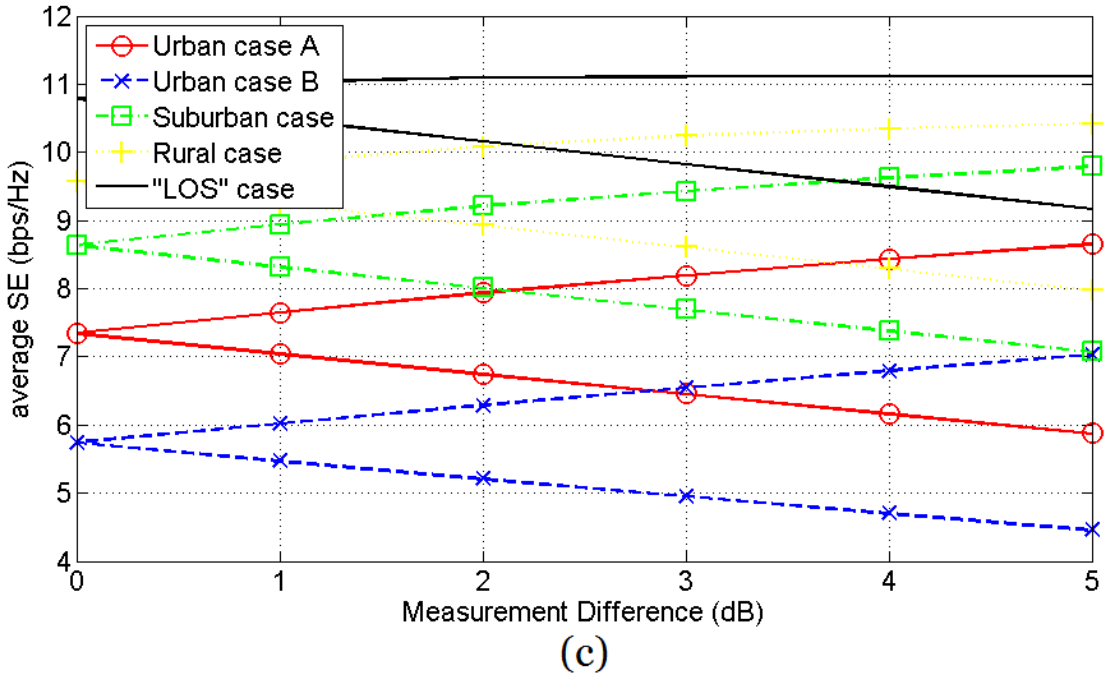

Fig. 8. Limits of the average SE range of the indicative OV MV BPL topologies in the 3-88 MHz frequency band when FCC limits are assumed and different coupling schemes are applied. (a) WtG^{1} coupling scheme. (b) $WtW^{1\text{-}2}$ coupling scheme. (c) $MtM^{1\text{-}2\text{-}3}_{0.8\_-0.1\_-0.1}$ coupling scheme.

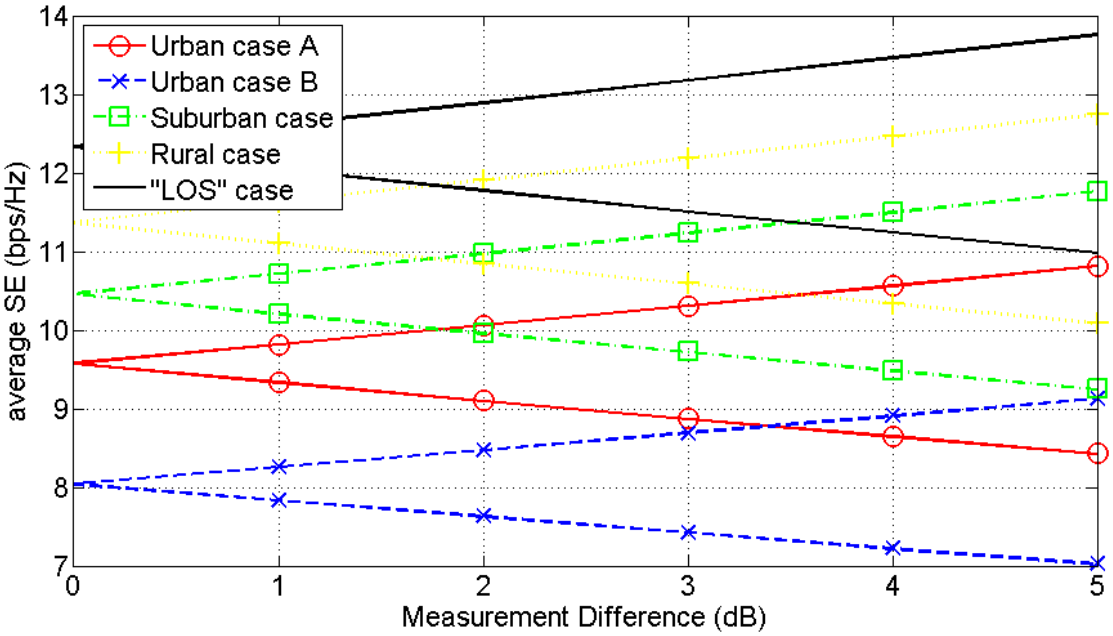
Urban case A
Urban case B
Suburban case
Rural case
"LOS" case
average SE (bps/Hz)
Measurement Difference (dB)
14
13
12
11
10
9
8
7
0
1
2
3
4
5

(a)

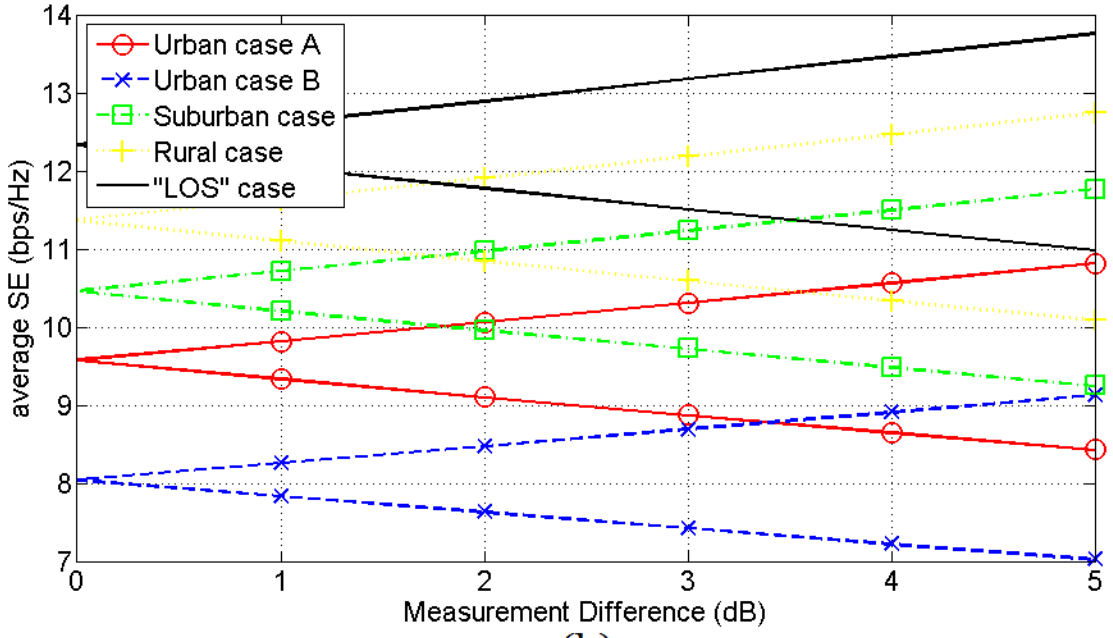
Urban case A
Urban case B
Suburban case
Rural case
"LOS" case
average SE (bps/Hz)
Measurement Difference (dB)
14
13
12
11
10
9
8
7
0
1
2
3
4
5

(b)

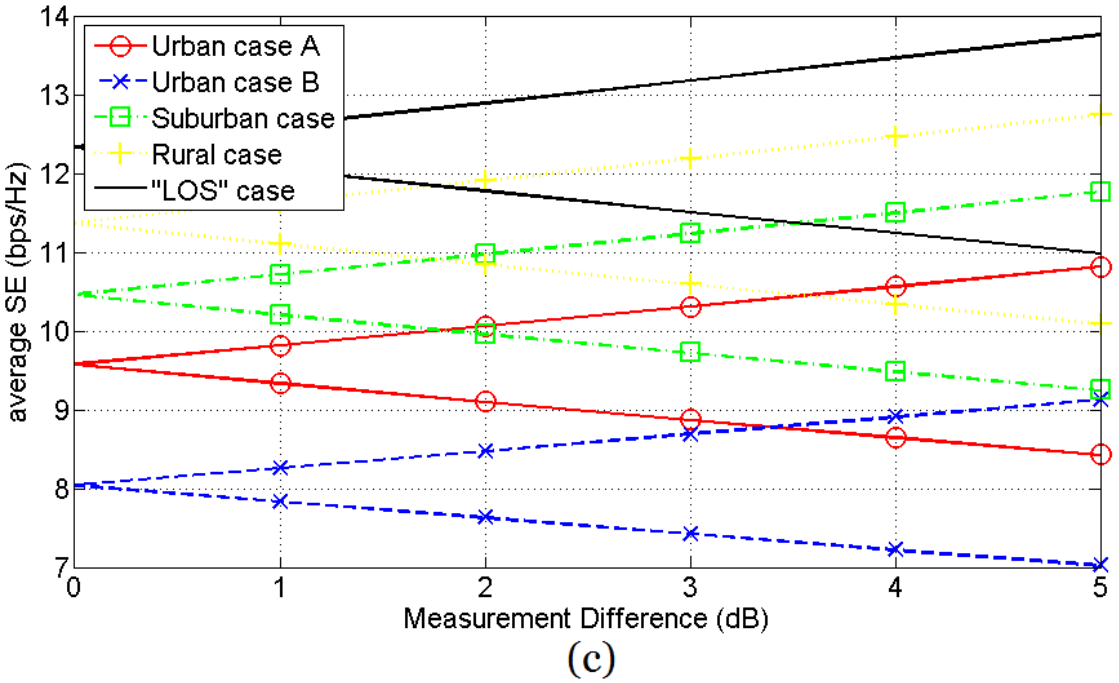

Fig. 9. Limits of the average SE range of the indicative UN MV BPL topologies in the 3-88 MHz frequency band when FCC limits are assumed and different coupling schemes are applied. (a) StP^{1} coupling scheme. (b) $PtP^{1\text{-}2}$ coupling scheme. (c) $MtM^{1\text{-}2\text{-}3}_{0.8\_-0.1\_-0.1}$ coupling scheme.

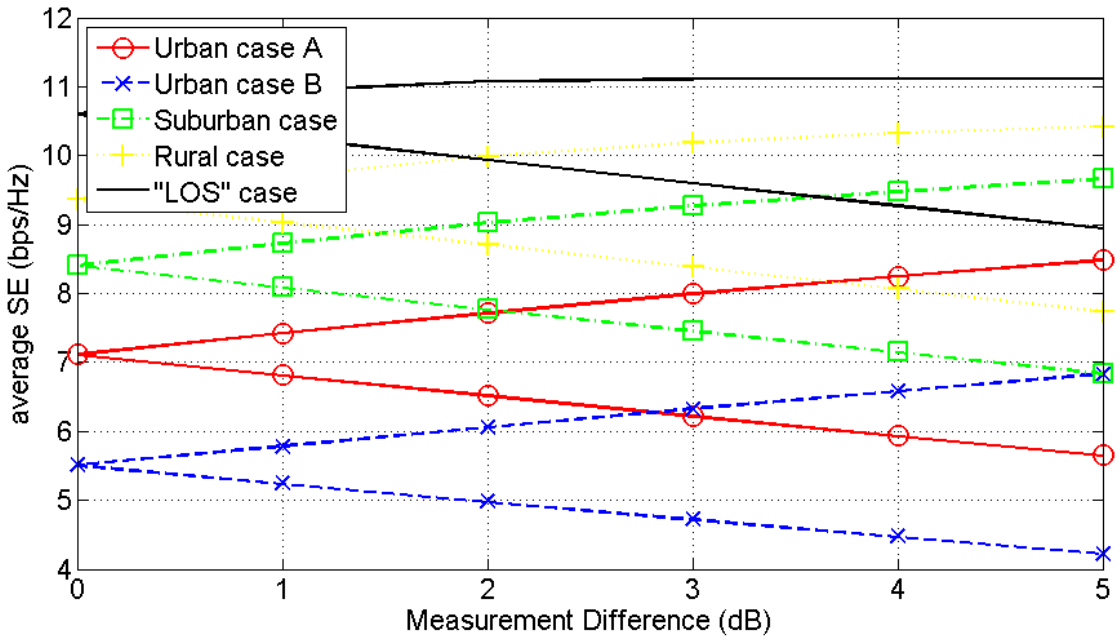
Urban case A
Urban case B
Suburban case
Rural case
"LOS" case
average SE (bps/Hz)
Measurement Difference (dB)
12
11
10
9
8
7
6
5
4
0
1
2
3
4
5

(a)

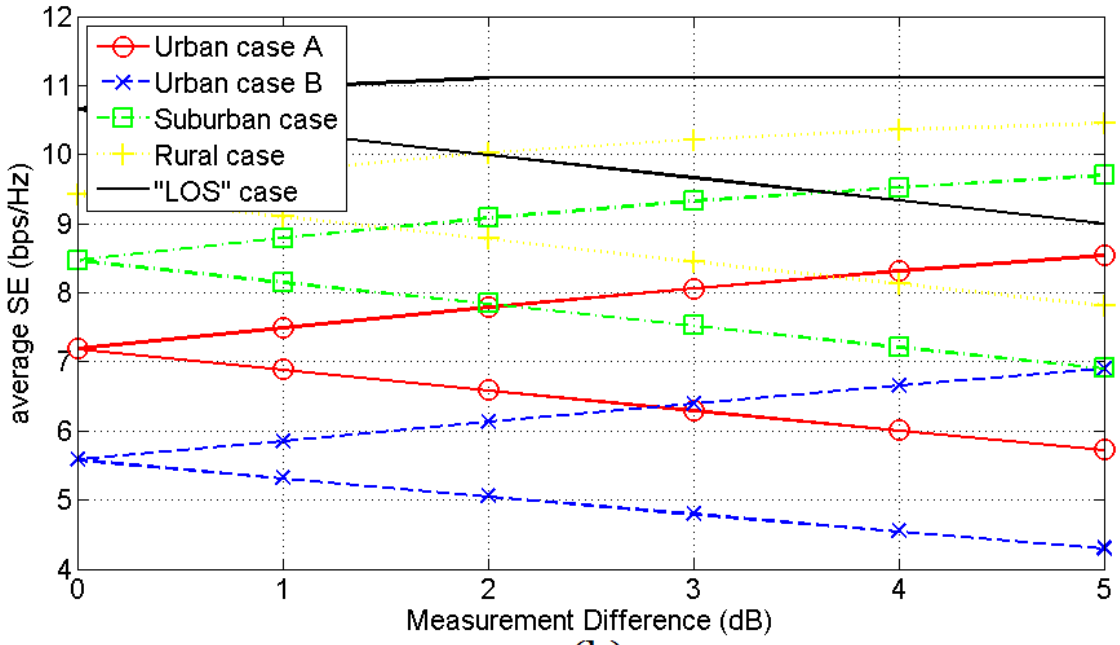
Urban case A
Urban case B
Suburban case
Rural case
"LOS" case
average SE (bps/Hz)
Measurement Difference (dB)
12
11
10
9
8
7
6
5
4
0
1
2
3
4
5

(b)

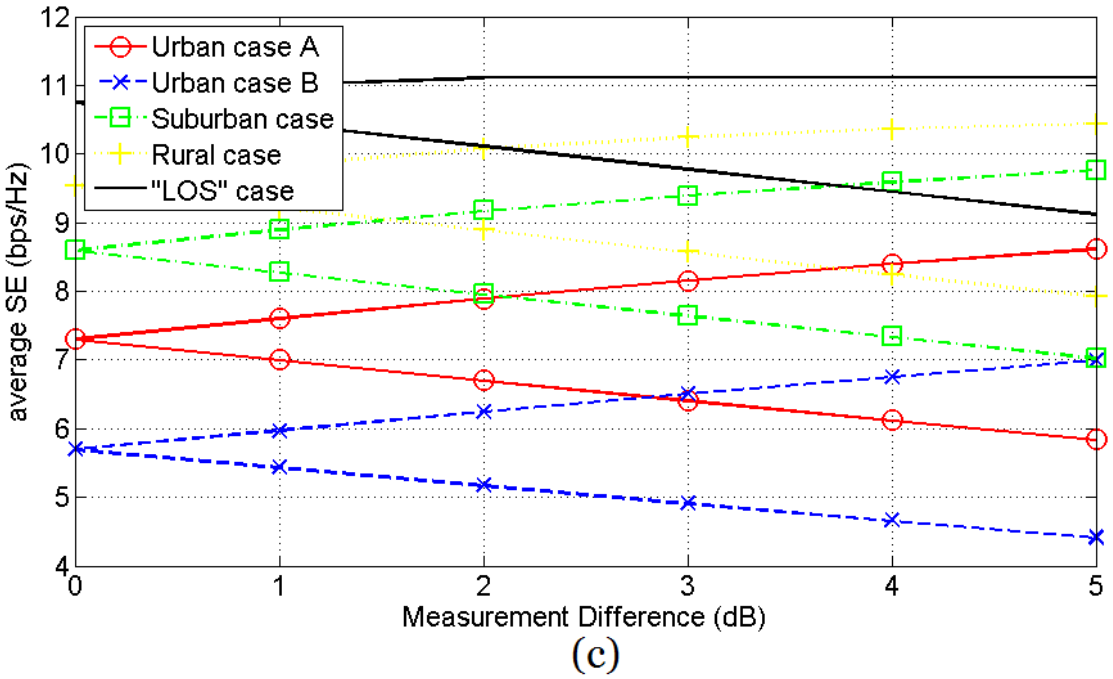

Fig. 10. Same with Fig. 8 but for the case of the indicative OV LV BPL topologies.

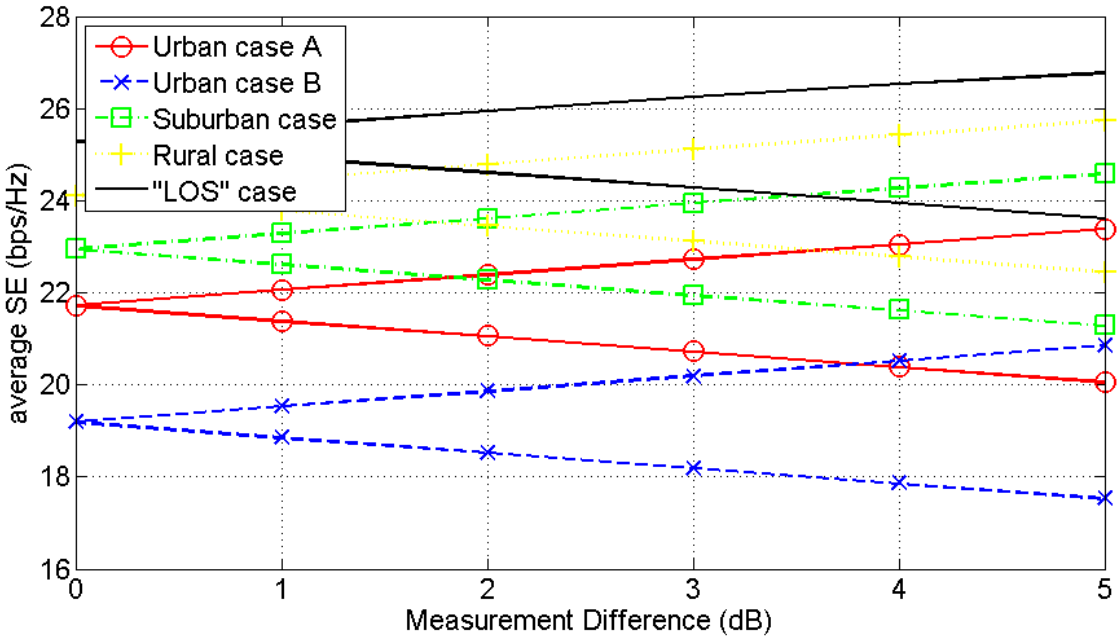
Urban case A
Urban case B
Suburban case
Rural case
"LOS" case
average SE (bps/Hz)
Measurement Difference (dB)
28
26
24
22
20
18
16
0
1
2
3
4
5

(a)

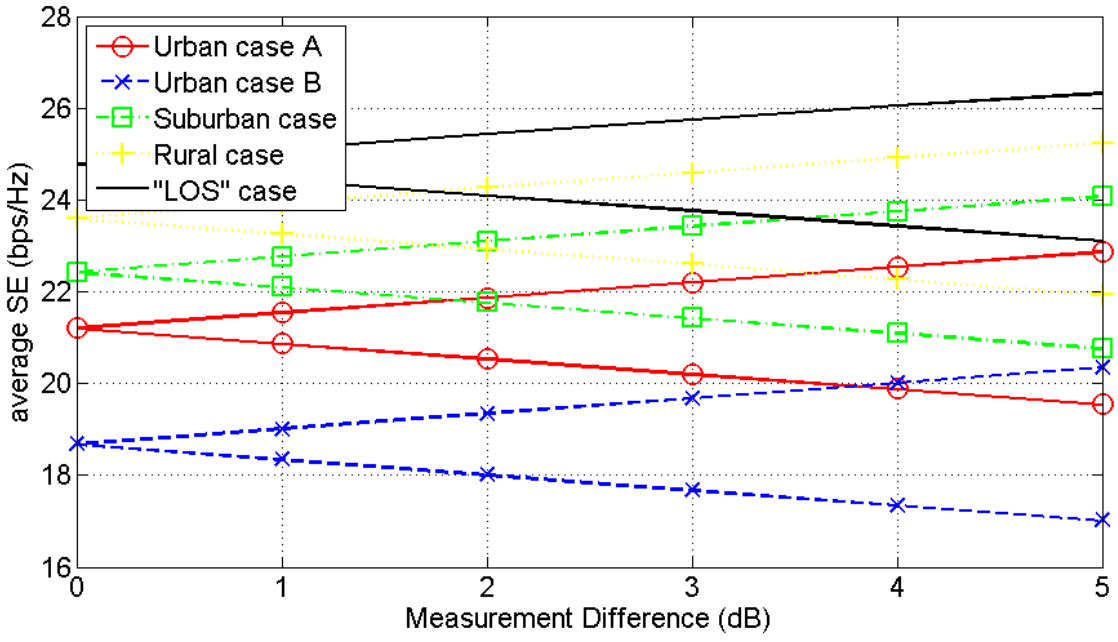
Urban case A
Urban case B
Suburban case
Rural case
"LOS" case
average SE (bps/Hz)
Measurement Difference (dB)
28
26
24
22
20
18
16
0
1
2
3
4
5

(b)

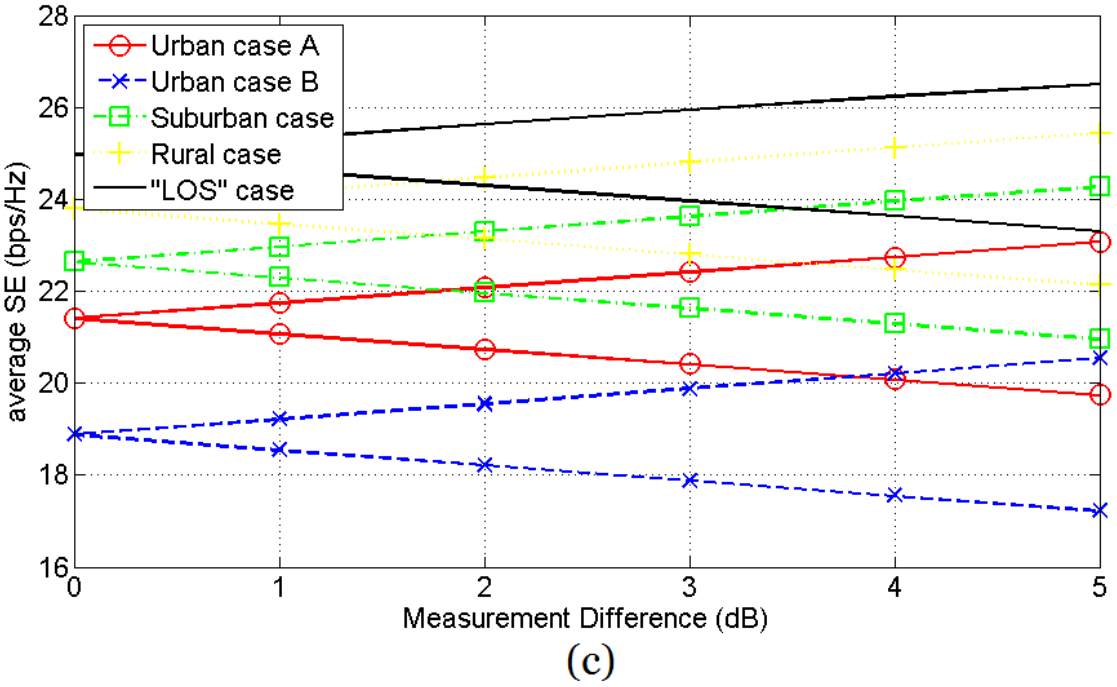

Fig. 11. Same with Fig. 9 but for the case of the indicative UN LV BPL topologies.

Table 4. Average SE Range for Different a Values
(the frequency spacing is equal to 0.1 MHz)

		Average SE Range (bps/Hz)											
		(WtG[1] / StP[1])				(WtW[1-2] / PtP[1-2])				$MtM^{1\text{-}2\text{-}3}_{0.8\_-0.1\_-0.1}$			
Distribution power grid type	**Topology Name**	a_{CUD} = 0dB	a_{CUD} = 1dB	a_{CUD} = 2dB	a_{CUD} = 5dB	a_{CUD} = 0dB	a_{CUD} = 1dB	a_{CUD} = 2dB	a_{CUD} = 5dB	a_{CUD} = 0dB	a_{CUD} = 1dB	a_{CUD} = 2dB	a_{CUD} = 5dB
OVMV	Urban case A	0.00	0.60	1.20	2.85	0.00	0.60	1.20	2.81	0.00	0.60	1.19	2.77
	Urban case B	0.00	0.54	1.07	2.61	0.00	0.54	1.07	2.60	0.00	0.54	1.07	2.57
	Suburban case	0.00	0.63	1.26	2.87	0.00	0.63	1.24	2.79	0.00	0.62	1.20	2.72
	Rural case	0.00	0.66	1.29	2.77	0.00	0.65	1.25	2.61	0.00	0.60	1.15	2.44
	"LOS" case	0.00	0.66	1.18	2.27	0.00	0.65	1.08	2.08	0.00	0.54	0.94	1.93
OVLV	Urban case A	0.00	0.60	1.20	2.83	0.00	0.60	1.20	2.81	0.00	0.60	1.19	2.77
	Urban case B	0.00	0.54	1.07	2.60	0.00	0.54	1.07	2.59	0.00	0.54	1.07	2.58
	Suburban case	0.00	0.63	1.25	2.82	0.00	0.63	1.24	2.79	0.00	0.62	1.21	2.74
	Rural case	0.00	0.65	1.27	2.68	0.00	0.65	1.25	2.63	0.00	0.61	1.18	2.50
	"LOS" case	0.00	0.66	1.14	2.16	0.00	0.64	1.10	2.09	0.00	0.56	0.98	1.98
UNMV	Urban case A	0.00	0.48	0.96	2.39	0.00	0.48	0.96	2.39	0.00	0.48	0.96	2.39
	Urban case B	0.00	0.42	0.84	2.10	0.00	0.42	0.84	2.10	0.00	0.42	0.84	2.10
	Suburban case	0.00	0.50	1.01	2.52	0.00	0.50	1.01	2.52	0.00	0.50	1.01	2.52
	Rural case	0.00	0.53	1.06	2.65	0.00	0.53	1.06	2.65	0.00	0.53	1.06	2.65
	"LOS" case	0.00	0.56	1.11	2.77	0.00	0.56	1.11	2.77	0.00	0.56	1.11	2.77
UNLV	Urban case A	0.00	0.66	1.33	3.32	0.00	0.66	1.33	3.32	0.00	0.66	1.33	3.32
	Urban case B	0.00	0.66	1.33	3.32	0.00	0.66	1.33	3.32	0.00	0.66	1.33	3.32
	Suburban case	0.00	0.66	1.33	3.29	0.00	0.66	1.33	3.31	0.00	0.66	1.33	3.30
	Rural case	0.00	0.66	1.33	3.27	0.00	0.66	1.33	3.29	0.00	0.66	1.33	3.29
	"LOS" case	0.00	0.66	1.32	3.15	0.00	0.66	1.33	3.22	0.00	0.66	1.33	3.19

From Figs. 8-11, it is clear that the measurement differences significantly influence the computation accuracy of the average SE of the examined indicative distribution BPL topologies. As the measurement uncertainty increases so does the limits

as well as the average SE range for given BPL topology and coupling scheme type. In accordance with the figures and the Table 4, each dB increase of the measurement difference uncertainty creates an average uncertainty of 0.60 bps/Hz in the computed average SE. Also, the average SE range cumulatively increases with the measurement uncertainty. Graphically, this almost stable cumulative relation between the average SE range and a values of the measurement differences explains the linear representation of the upper and lower limits of the average SE range in Figs. 8-11 for given distribution BPL topology and coupling scheme type. Here, it should be noted that some deviations from the linear consideration, such as the "LOS" cases of Figs. 8(a)-(c) and 10(a)-(c), are due to the minimum channel attenuation restriction of 0dB. In addition, it should be pointed out that the SE impact of measurement differences remains almost the same regardless of the considered coupling scheme of the CS2 module.

4.3 SE with CUD Measurement Differences

As already been mentioned in [25], [26], [28], [31], measurement differences can comfortably be handled as error distributions such as CUDs. However, the handling of measurement differences through CUDs rather than the biased values of the previous subsection becomes a challenging issue due to the behavior of the traditional statistical metrics of maximum, minimum and average SE.

In order to examine the impact of real measurement differences CUDs on the SE as well as the measurement differences countermeasures of [55], five representative CUD measurement differences, which are denoted as CUD1-5, with respective a_{CUD} ranging from 1dB to 5dB are assumed. In Figs. 12(a)-(c), the metrics of set A, say, maximum, minimum and average SE of the indicative OV MV BPL topologies are plotted versus the value a_{CUD} when WtG^{1}, $\mathrm{WtW}^{1\text{-}2}$ and $\mathrm{MtM}^{1\text{-}2\text{-}3}_{0.8\_-0.1\_-0.1}$ coupling scheme is applied, respectively. Note that each a_{CUD} corresponds to the respective CUD measurement difference whereas at zero the results refer to the SE case without measurement differences. In Figs. 13(a)-(c), maximum, minimum and average SE of the indicative UN MV BPL topologies are plotted versus the value a_{CUD} when StP^{1}, $\mathrm{PtP}^{1\text{-}2}$ and $\mathrm{MtM}^{1\text{-}2\text{-}3}_{0.8\_-0.1\_-0.1}$ coupling scheme is applied, respectively. In Figs. 14(a)-(c), same plots with Figs. 12(a)-(c) are given but for the case of the indicative OV LV BPL topologies while in Figs. 15(a)-(c), same curves with Figs. 13(a)-(c) are presented but for the case of the indicative UN LV BPL topologies.

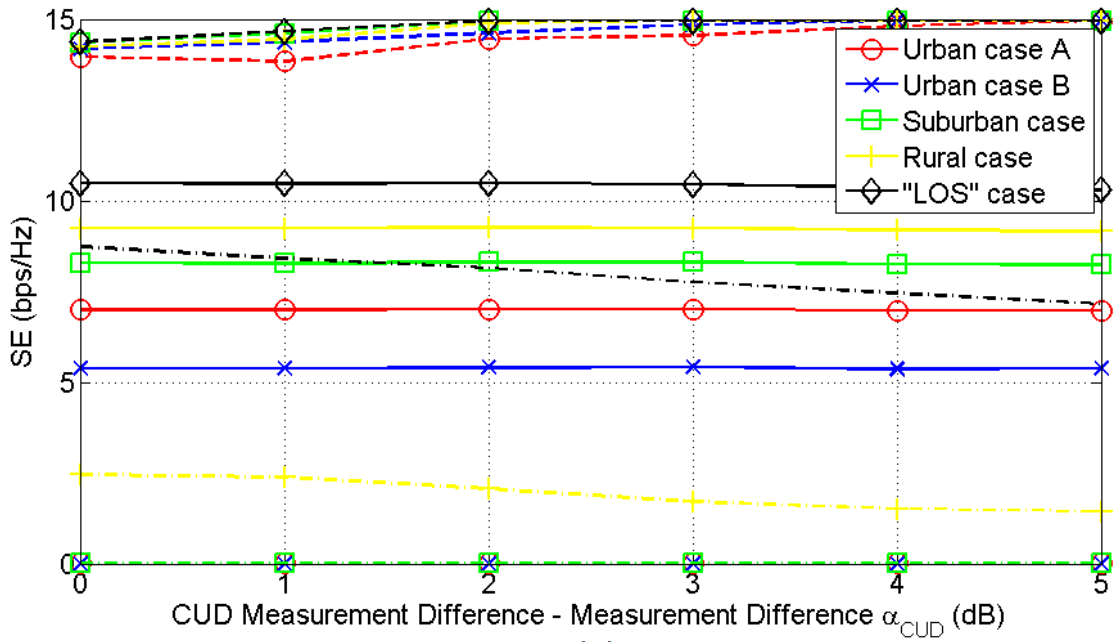
Urban case A
Urban case B
Suburban case
Rural case
"LOS" case
SE (bps/Hz)
CUD Measurement Difference - Measurement Difference α_{CUD} (dB)

(a)

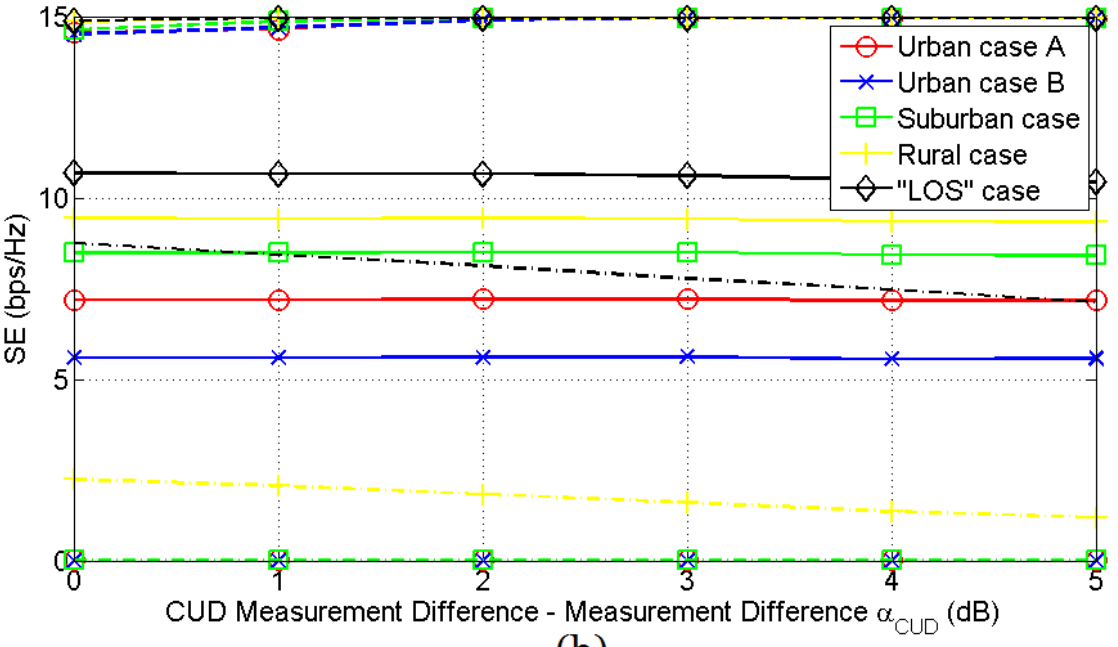
Urban case A
Urban case B
Suburban case
Rural case
"LOS" case
SE (bps/Hz)
CUD Measurement Difference - Measurement Difference α_{CUD} (dB)

(b)

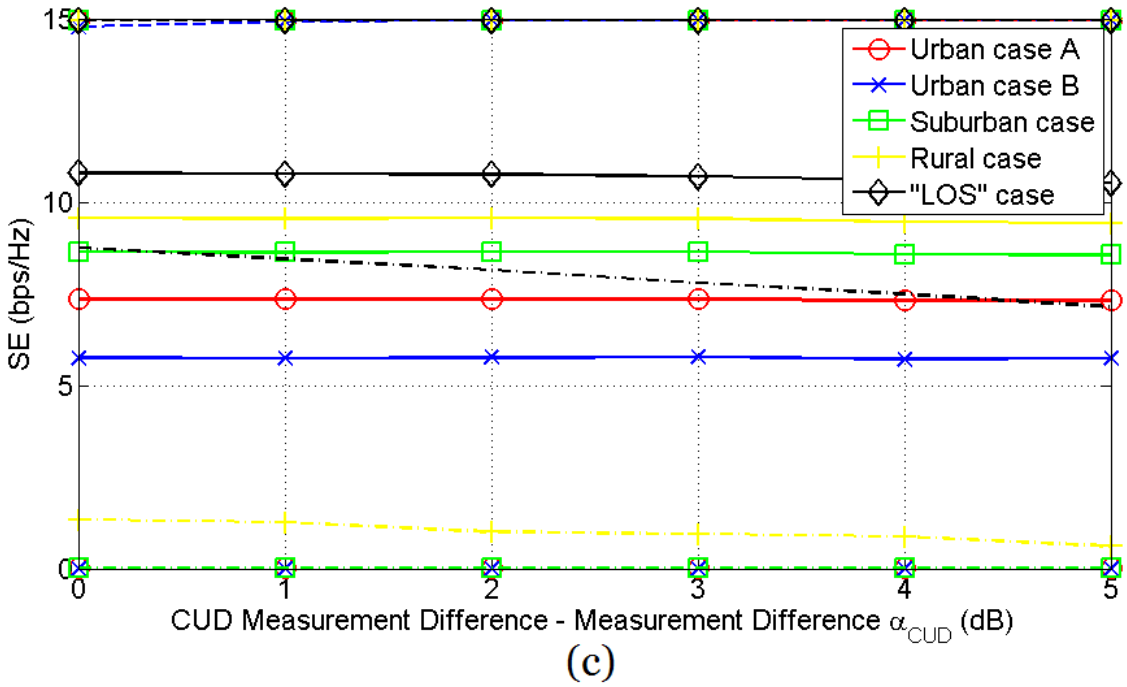

Fig. 12. Maximum, minimum and average SE of the indicative OV MV BPL topologies in the 3-88 MHz frequency band when FCC limits are assumed and different coupling schemes are applied for different CUD measurement differences. (a) WtG^{1} coupling scheme. (b) $WtW^{1\text{-}2}$ coupling scheme. (c) $MtM^{1\text{-}2\text{-}3}_{0.8\_-0.1\_-0.1}$ coupling scheme.

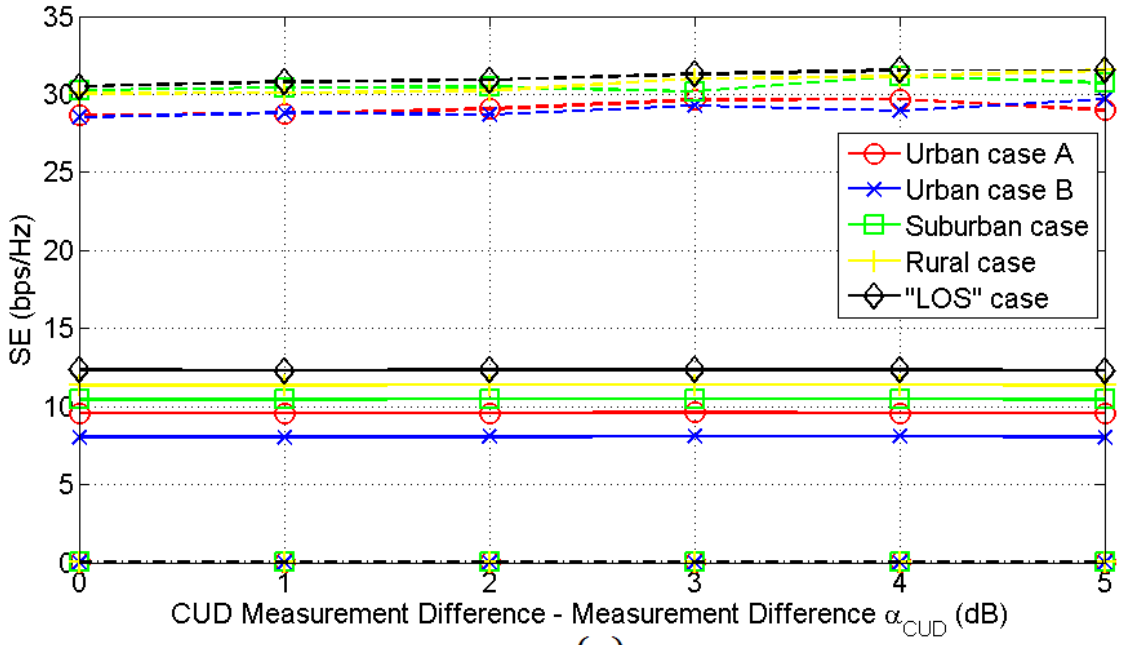
SE (bps/Hz)
CUD Measurement Difference - Measurement Difference α_{CUD} (dB)
Urban case A
Urban case B
Suburban case
Rural case
"LOS" case

(a)

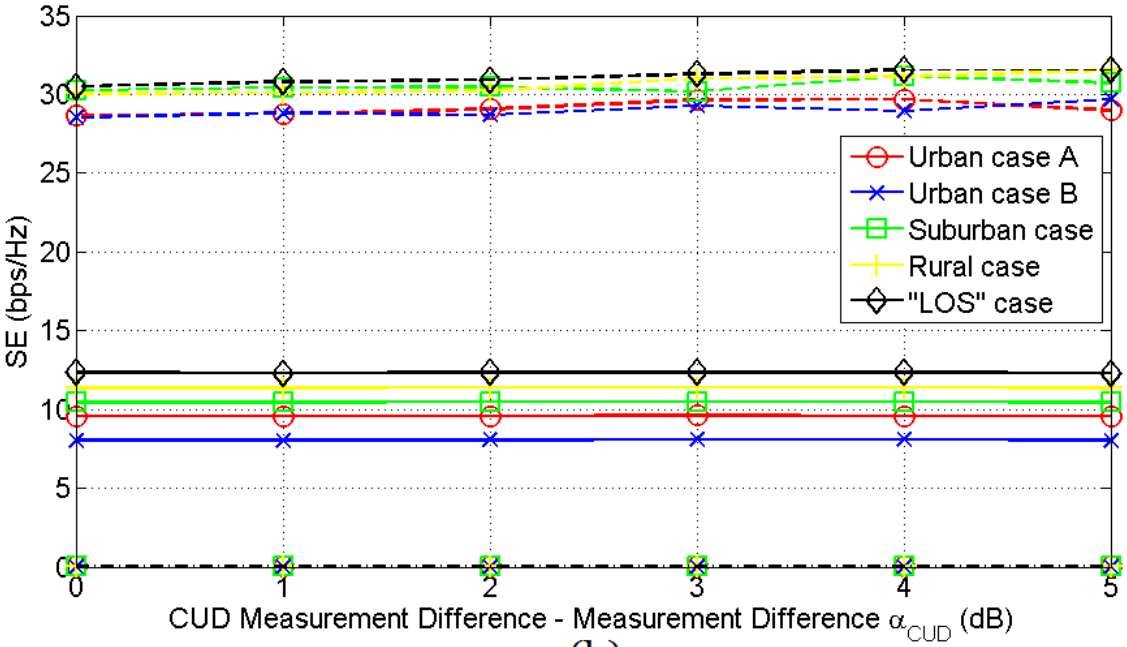
SE (bps/Hz)
CUD Measurement Difference - Measurement Difference α_{CUD} (dB)
Urban case A
Urban case B
Suburban case
Rural case
"LOS" case

(b)

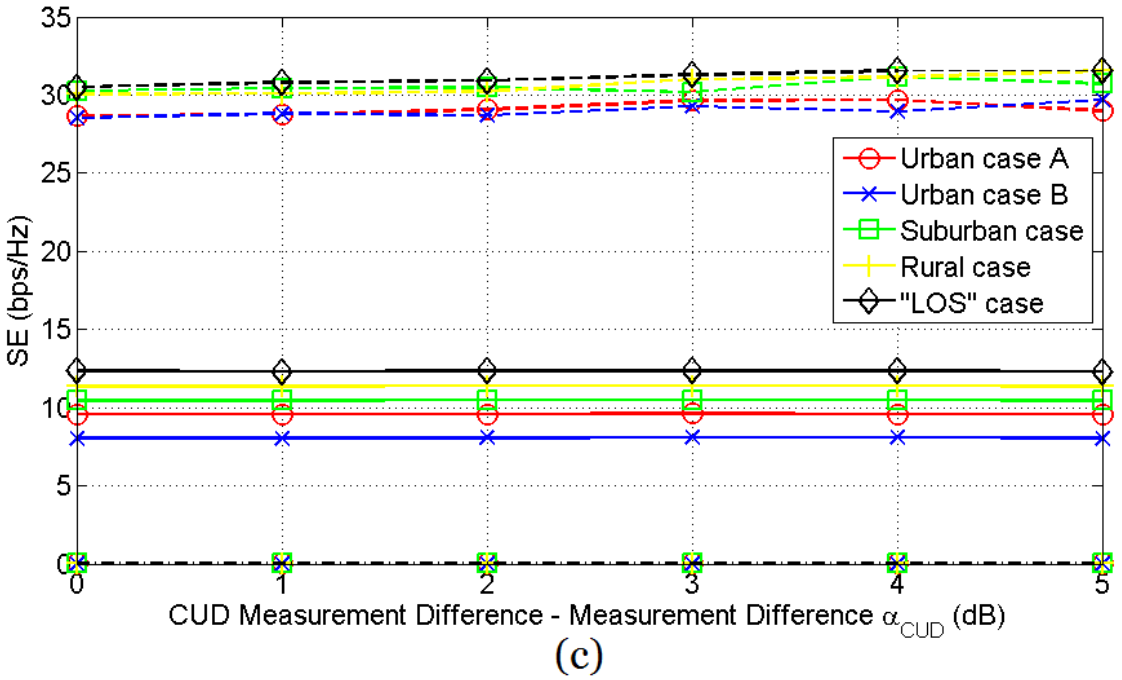

Fig. 13. Maximum, minimum and average SE of the indicative UN MV BPL topologies in the 3-88 MHz frequency band when FCC limits are assumed and different coupling schemes are applied for different CUD measurement differences. (a) StP^{1} coupling scheme. (b) $PtP^{1\text{-}2}$ coupling scheme. (c) $MtM^{1\text{-}2\text{-}3}_{0.8\_-0.1\_-0.1}$ coupling scheme.

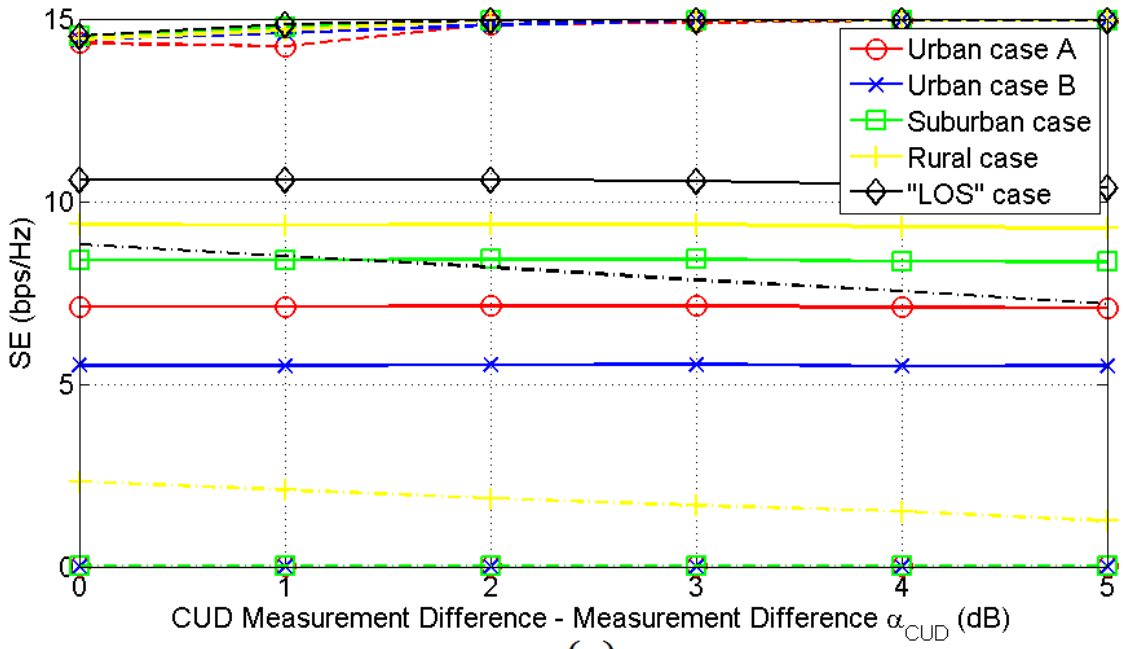
Urban case A
Urban case B
Suburban case
Rural case
"LOS" case
SE (bps/Hz)
CUD Measurement Difference - Measurement Difference α_{CUD} (dB)

(a)

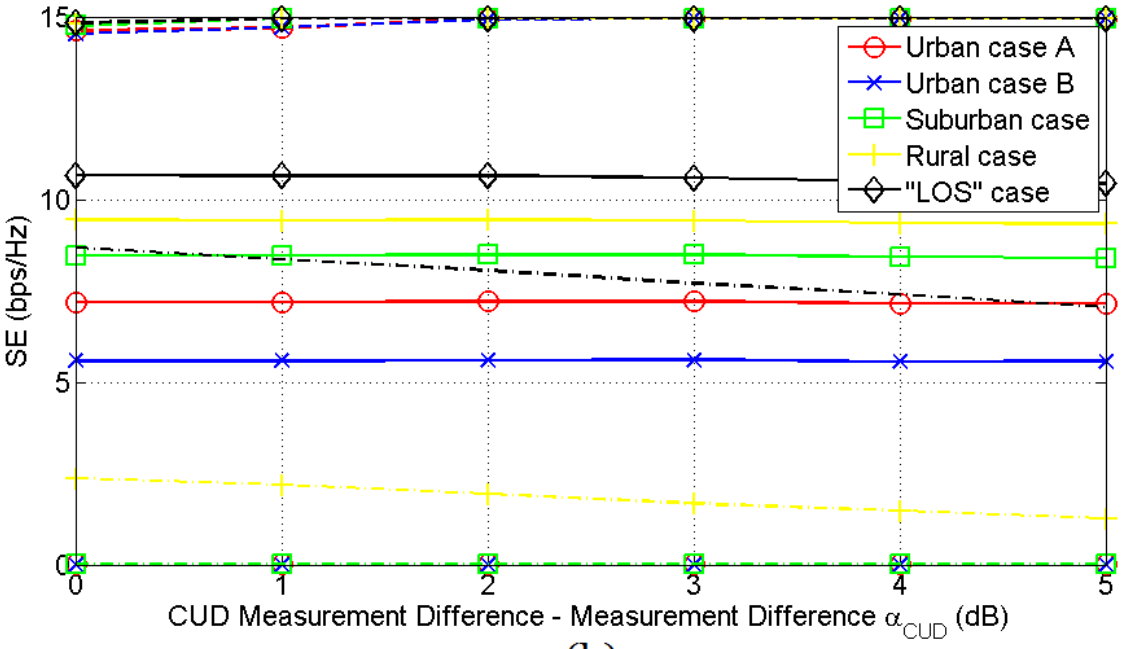
Urban case A
Urban case B
Suburban case
Rural case
"LOS" case
SE (bps/Hz)
CUD Measurement Difference - Measurement Difference α_{CUD} (dB)

(b)

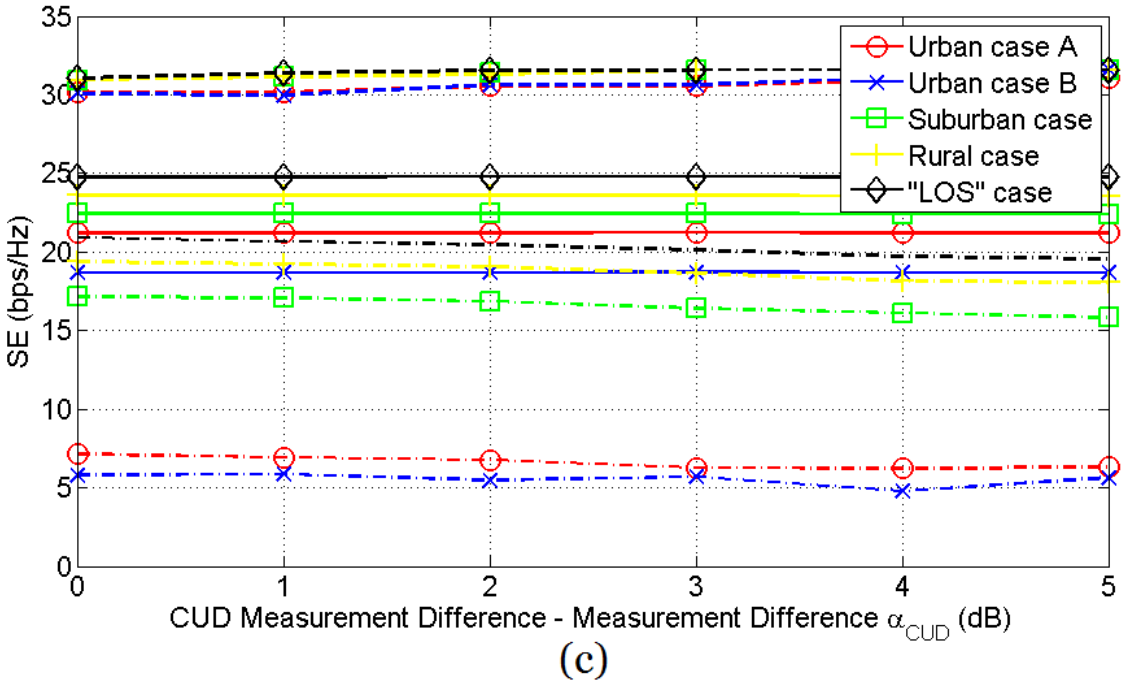

Fig. 14. Same with Fig. 12 but for the case of the indicative OV LV BPL topologies.

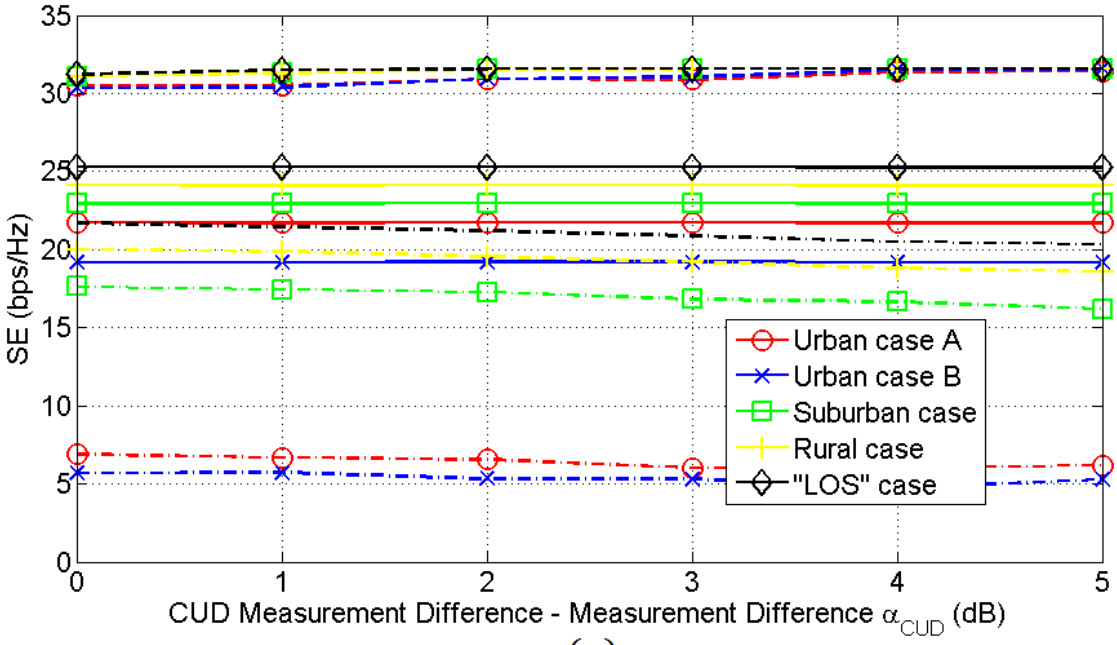
SE (bps/Hz)
CUD Measurement Difference - Measurement Difference α_{CUD} (dB)
Urban case A
Urban case B
Suburban case
Rural case
"LOS" case

(a)

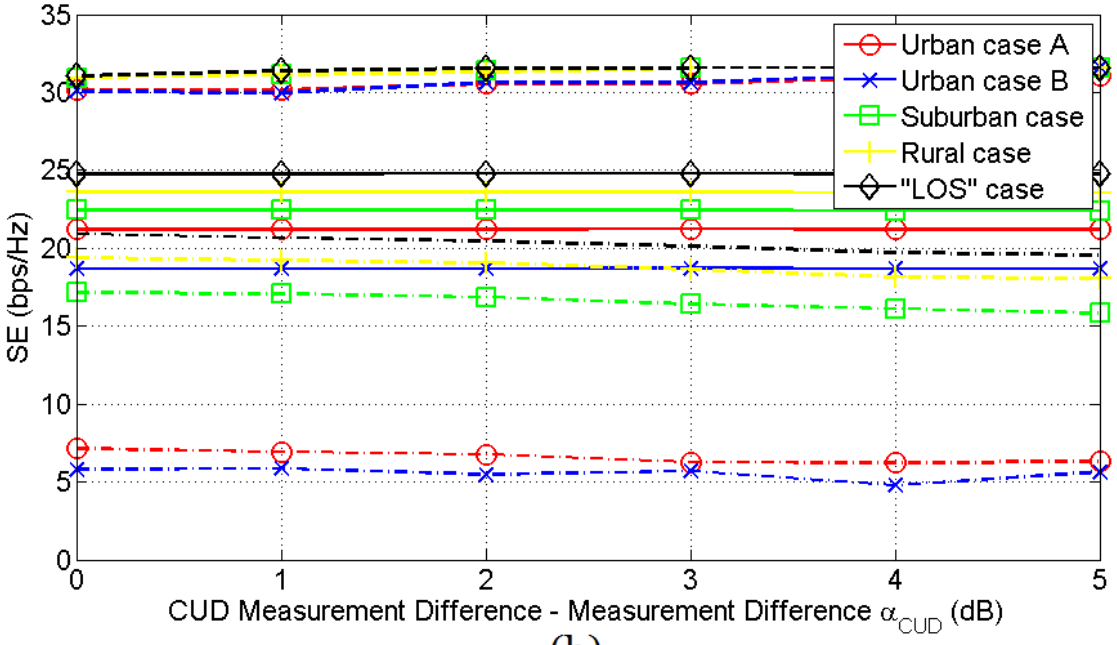
SE (bps/Hz)
CUD Measurement Difference - Measurement Difference α_{CUD} (dB)
Urban case A
Urban case B
Suburban case
Rural case
"LOS" case

(b)

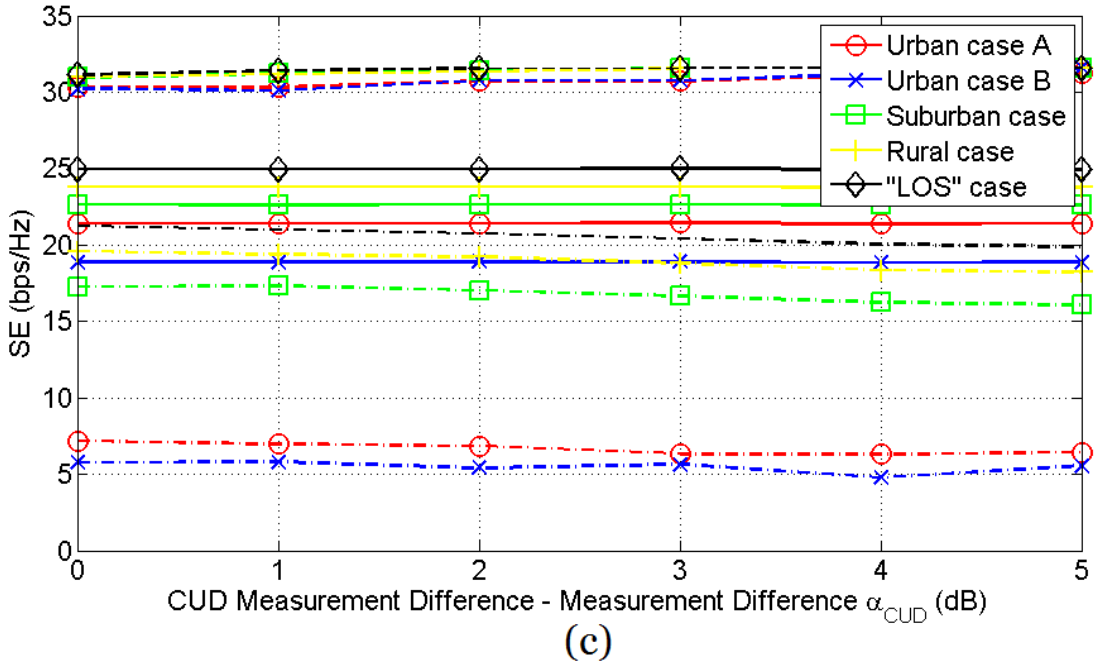

Fig. 15. Same with Fig. 13 but for the case of the indicative UN LV BPL topologies.

By observing Figs. 12-15, measurement differences slightly affect the maximum, minimum and average SE for given distribution BPL topology and coupling scheme type regardless of their maximum value a_{CUD}. This is a rational result since CUDs are adopted in order to describe the distribution of measurement differences. Although small differences of the average SE can be observed, these differences are not efficient to give an accurate estimation of the intensity of the occurred measurement differences in comparison with the respective results of biased measurement differences. Anyway, small average SE differences can be observed for the same maximum value a_{CUD} if the different CUD is considered. However, after the application of countermeasures against the measurement differences, it is expected that the set A metrics after the measurement difference mitigation techniques should present values closer to the theoretical ones than set A metrics of the measured SE now do. This hypothesis is examined in [55].

The need for assessing the intensity of the measurement differences urges the application of statistical metrics that depend on the value a_{CUD} of the CUD measurement differences. In accordance with [25]-[29], two statistical metrics, *i.e.*, mean absolute error (MAE) and root mean square deviation (RMSD), can easily assess the impact of measurement differences while their behavior depends on the value a_{CUD} of the CUD measurement differences. Set B consists of these two metrics.

In Figs. 16(a)-(c), the MAE of the average SE of the indicative OV MV BPL topologies are plotted versus the value a_{CUD} when WtG^{1}, $\mathrm{WtW}^{1\text{-}2}$ and $\mathrm{MtM}^{1\text{-}2\text{-}3}_{0.8\_-0.1\_-0.1}$ coupling scheme is applied, respectively. Note again that each a_{CUD} corresponds to the respective CUD measurement difference whereas at zero the results refer to the SE case without measurement differences. In Figs. 17(a)-(c), the MAE of the average SE of the indicative UN MV BPL topologies are plotted versus the value a_{CUD} when StP^{1}, $\mathrm{PtP}^{1\text{-}2}$ and $\mathrm{MtM}^{1\text{-}2\text{-}3}_{0.8\_-0.1\_-0.1}$ coupling scheme is applied, respectively.

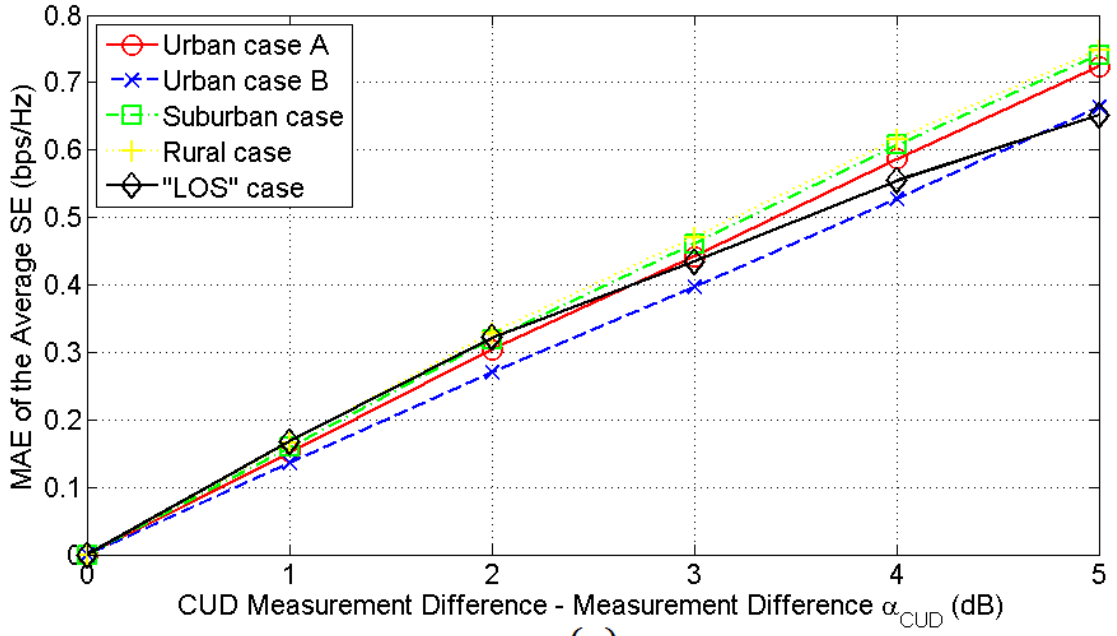
Urban case A
Urban case B
Suburban case
Rural case
"LOS" case
MAE of the Average SE (bps/Hz)
CUD Measurement Difference - Measurement Difference α_{CUD} (dB)
0
0.1
0.2
0.3
0.4
0.5
0.6
0.7
0.8
1
2
3
4
5

(a)

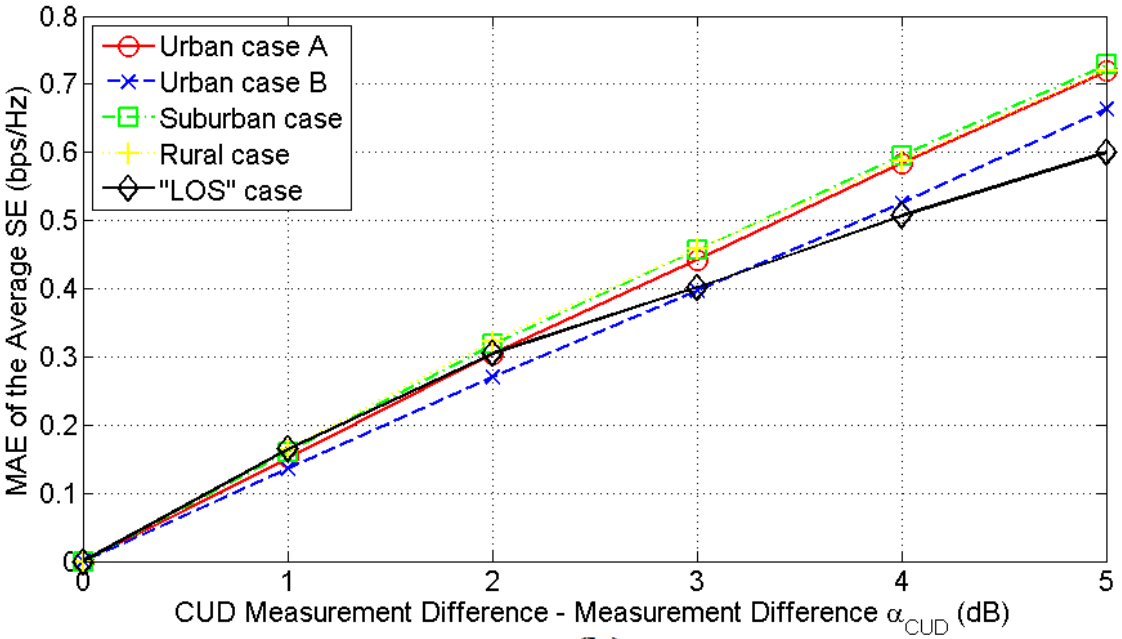
Urban case A
Urban case B
Suburban case
Rural case
"LOS" case
MAE of the Average SE (bps/Hz)
CUD Measurement Difference - Measurement Difference α_{CUD} (dB)
0
0.1
0.2
0.3
0.4
0.5
0.6
0.7
0.8
1
2
3
4
5

(b)

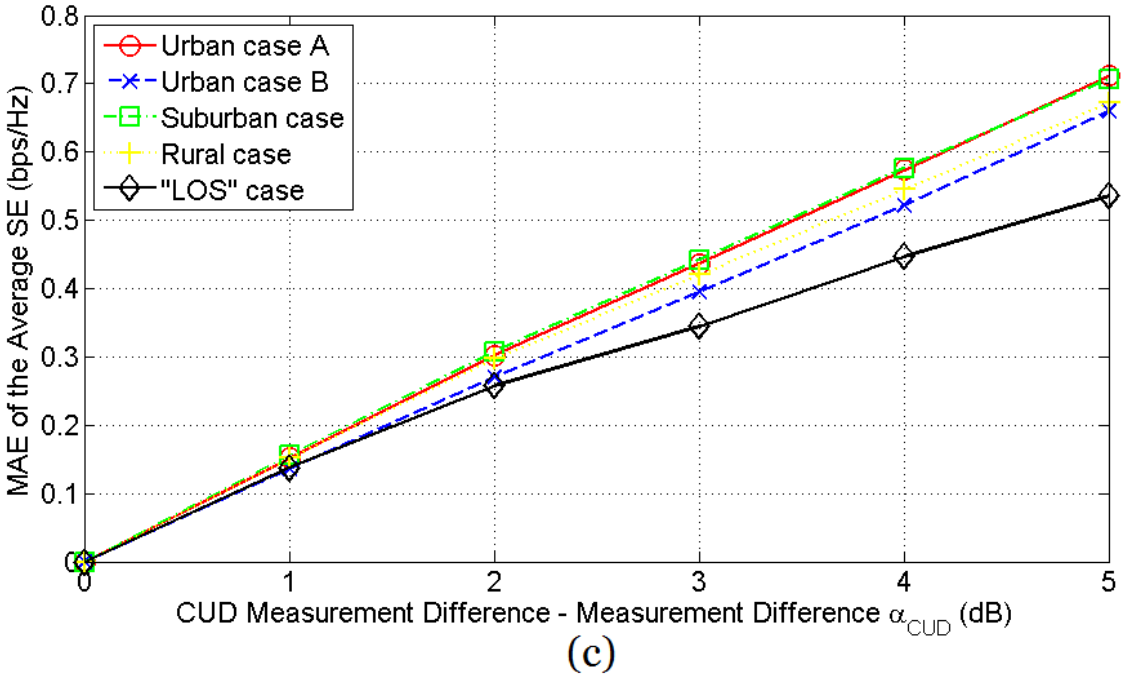

Fig. 16. MAE of SE of the indicative OV MV BPL topologies in the 3-88 MHz frequency band when FCC limits are assumed and different coupling schemes are applied for different CUD measurement differences. (a) WtG^{1} coupling scheme. (b) $WtW^{1\text{-}2}$ coupling scheme. (c) $MtM^{1\text{-}2\text{-}3}_{0.8\_-0.1\_-0.1}$ coupling scheme.

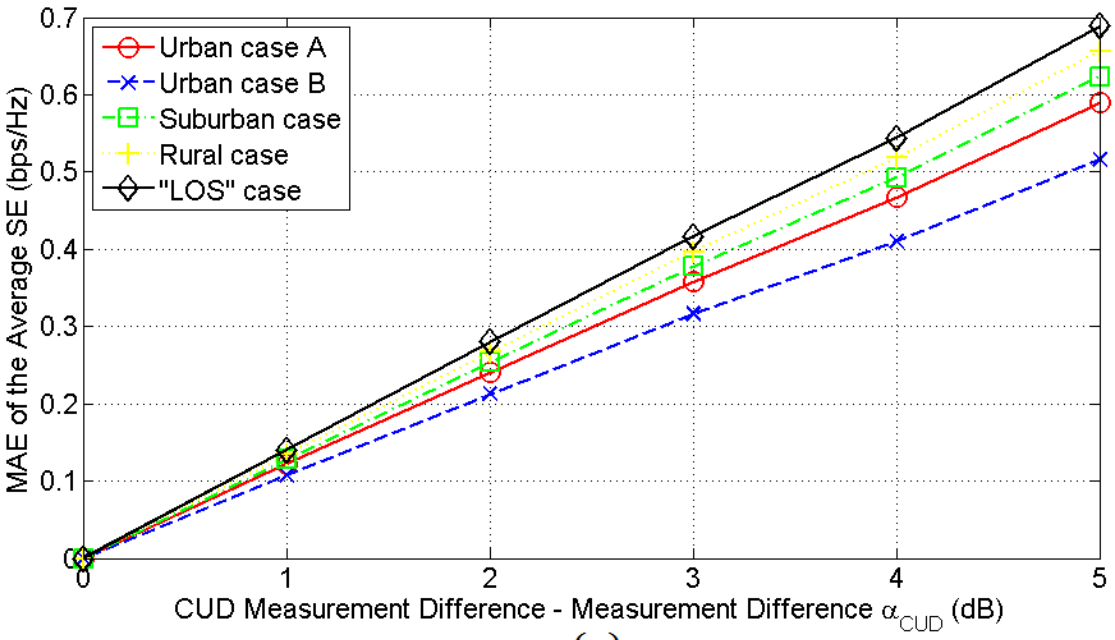
Urban case A
Urban case B
Suburban case
Rural case
"LOS" case
MAE of the Average SE (bps/Hz)
CUD Measurement Difference - Measurement Difference α_{CUD} (dB)
0
0.1
0.2
0.3
0.4
0.5
0.6
0.7
1
2
3
4
5

(a)

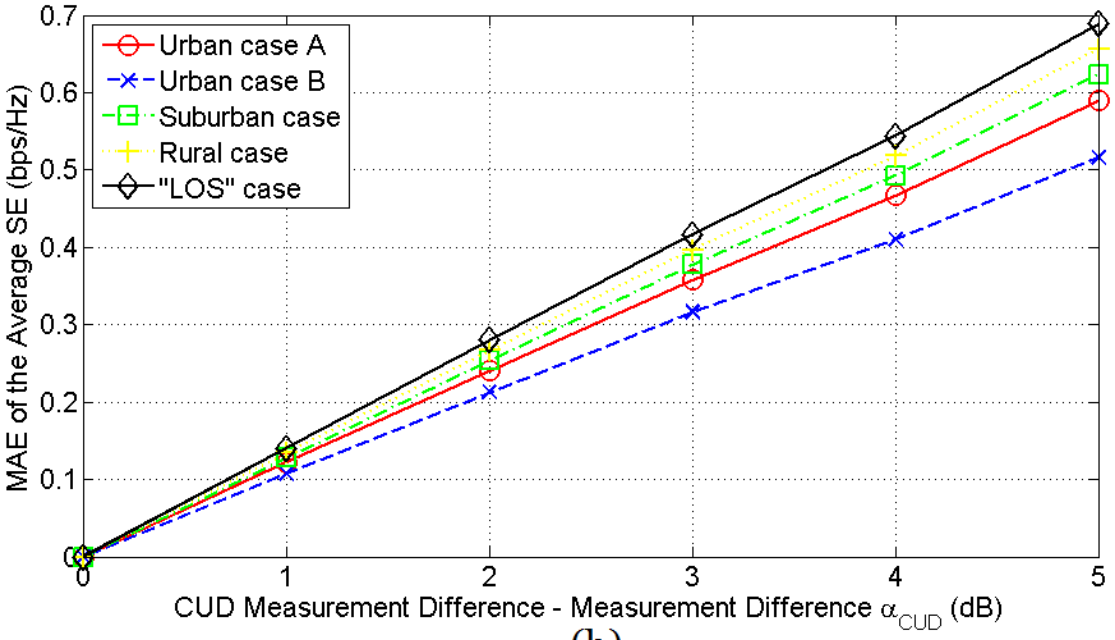
Urban case A
Urban case B
Suburban case
Rural case
"LOS" case
MAE of the Average SE (bps/Hz)
CUD Measurement Difference - Measurement Difference α_{CUD} (dB)
0
0.1
0.2
0.3
0.4
0.5
0.6
0.7
1
2
3
4
5

(b)

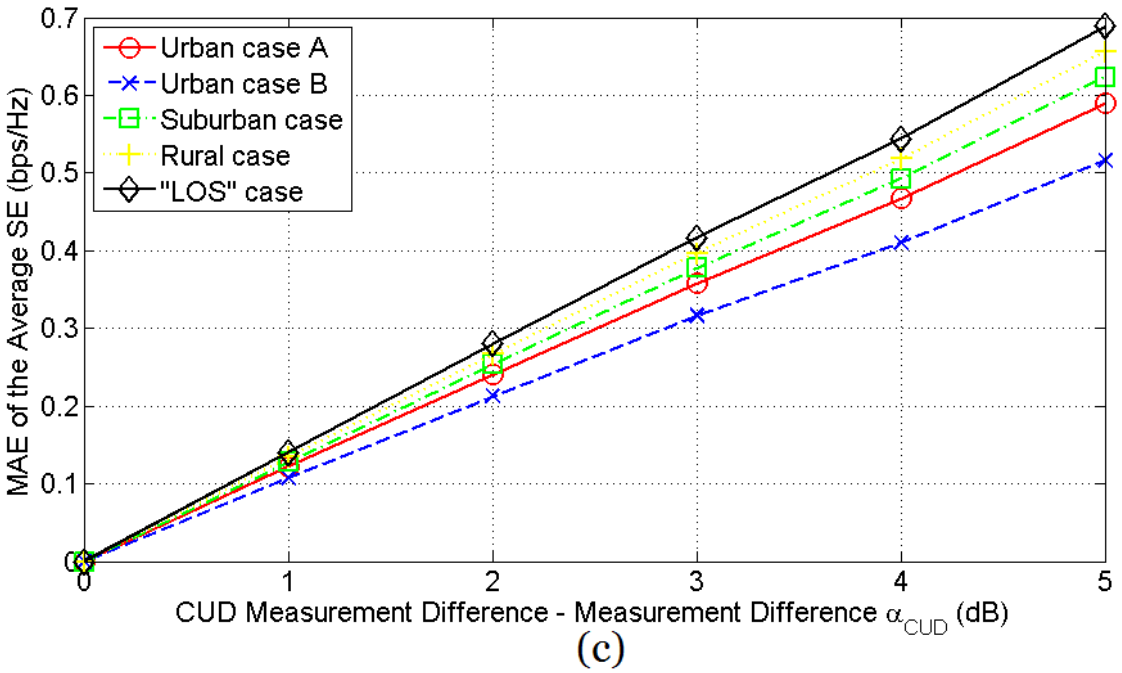

Fig. 17. MAE of SE of the indicative UN MV BPL topologies in the 3-88 MHz frequency band when FCC limits are assumed and different coupling schemes are applied for different CUD measurement differences. (a) StP^{1} coupling scheme. (b) $PtP^{1\text{-}2}$ coupling scheme. (c) $MtM^{1\text{-}2\text{-}3}_{0.8\_-0.1\_-0.1}$ coupling scheme.

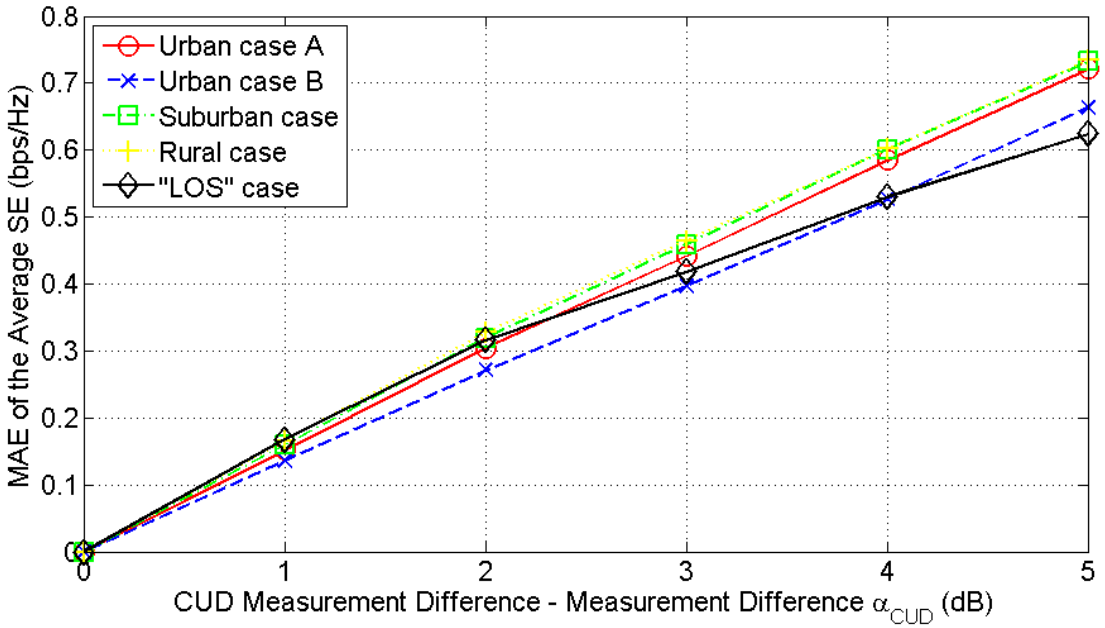
Urban case A
Urban case B
Suburban case
Rural case
"LOS" case
MAE of the Average SE (bps/Hz)
CUD Measurement Difference - Measurement Difference α_{CUD} (dB)
0
0.1
0.2
0.3
0.4
0.5
0.6
0.7
0.8
1
2
3
4
5

(a)

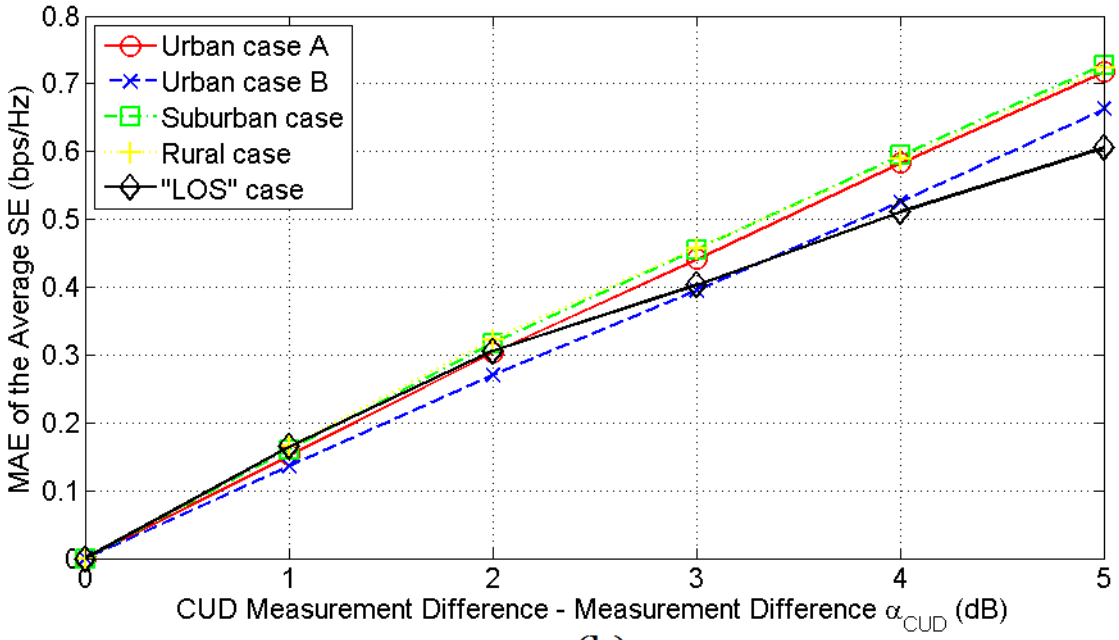
Urban case A
Urban case B
Suburban case
Rural case
"LOS" case
MAE of the Average SE (bps/Hz)
CUD Measurement Difference - Measurement Difference α_{CUD} (dB)
0
0.1
0.2
0.3
0.4
0.5
0.6
0.7
0.8
1
2
3
4
5

(b)

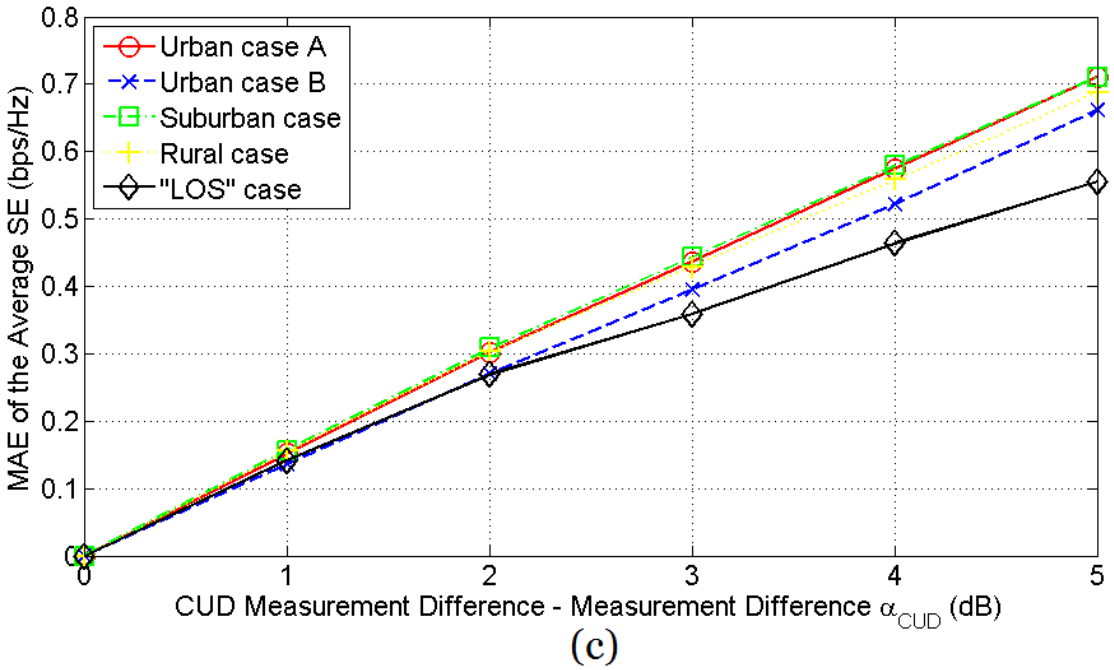

Fig. 18. Same with Fig. 16 but for the case of the indicative OV LV BPL topologies.

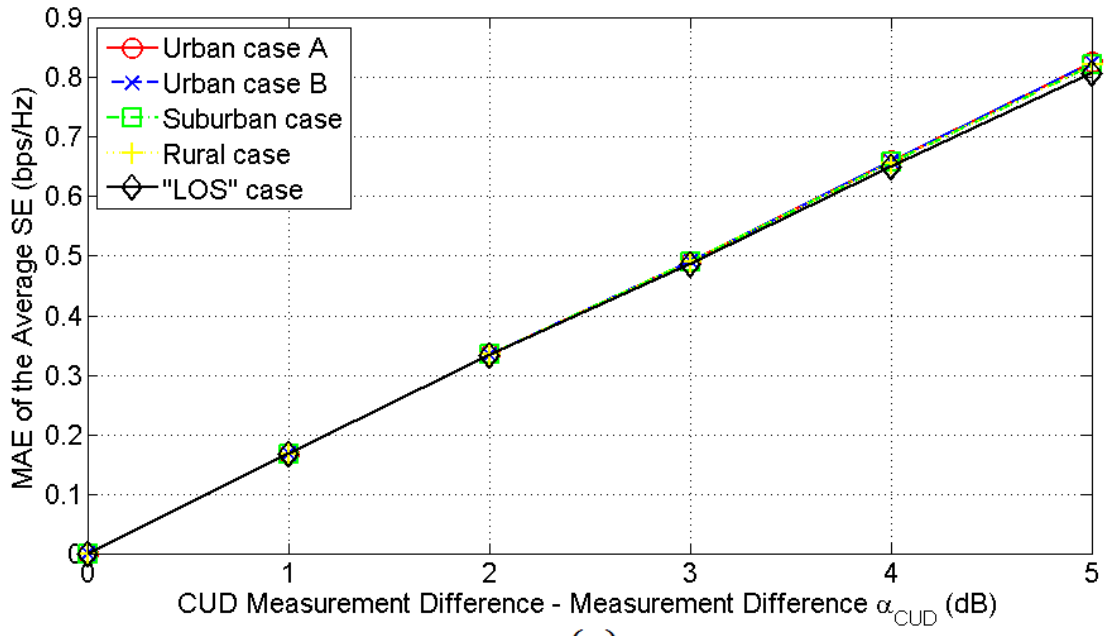
Urban case A
Urban case B
Suburban case
Rural case
"LOS" case
MAE of the Average SE (bps/Hz)
CUD Measurement Difference - Measurement Difference α_{CUD} (dB)
0
0.1
0.2
0.3
0.4
0.5
0.6
0.7
0.8
0.9
1
2
3
4
5

(a)

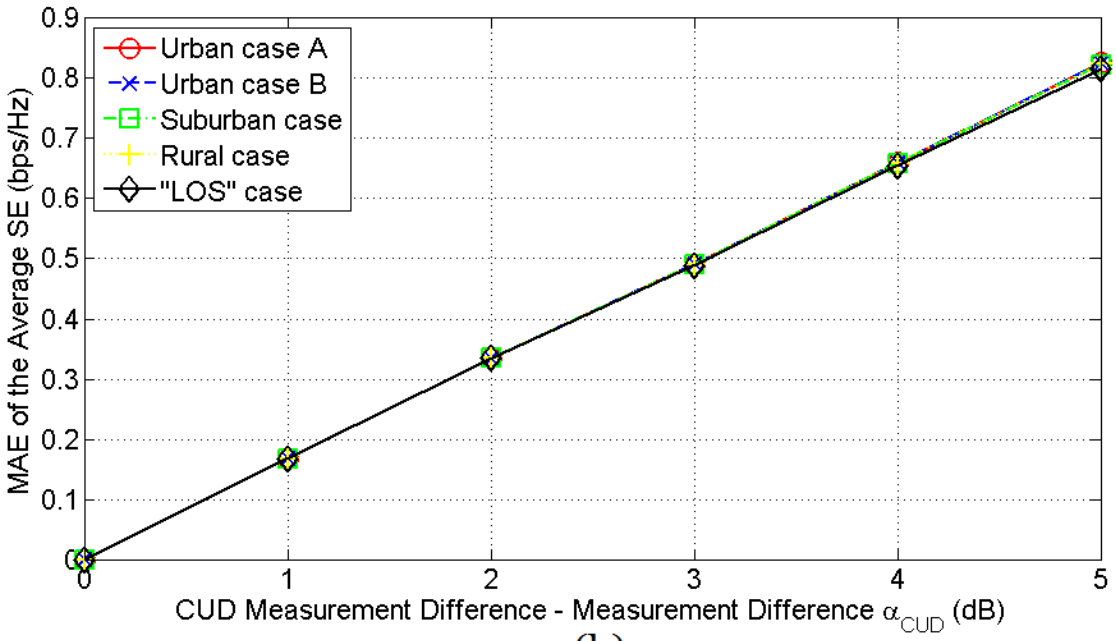
Urban case A
Urban case B
Suburban case
Rural case
"LOS" case
MAE of the Average SE (bps/Hz)
CUD Measurement Difference - Measurement Difference α_{CUD} (dB)
0
0.1
0.2
0.3
0.4
0.5
0.6
0.7
0.8
0.9
1
2
3
4
5

(b)

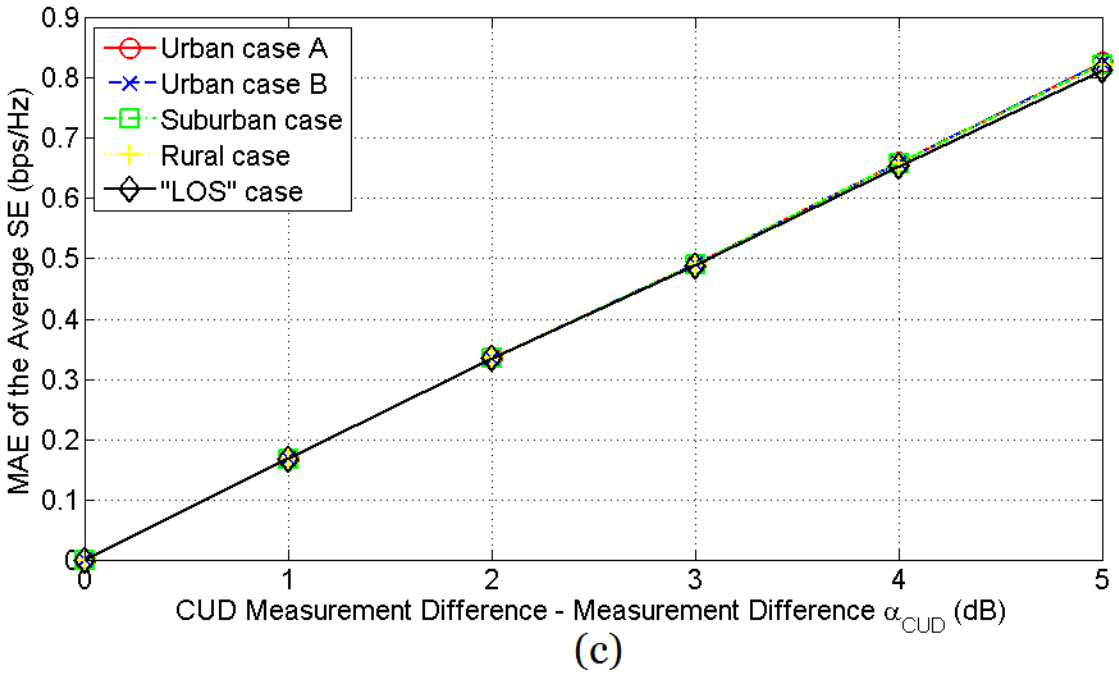

Fig. 19. Same with Fig. 17 but for the case of the indicative UN LV BPL topologies.

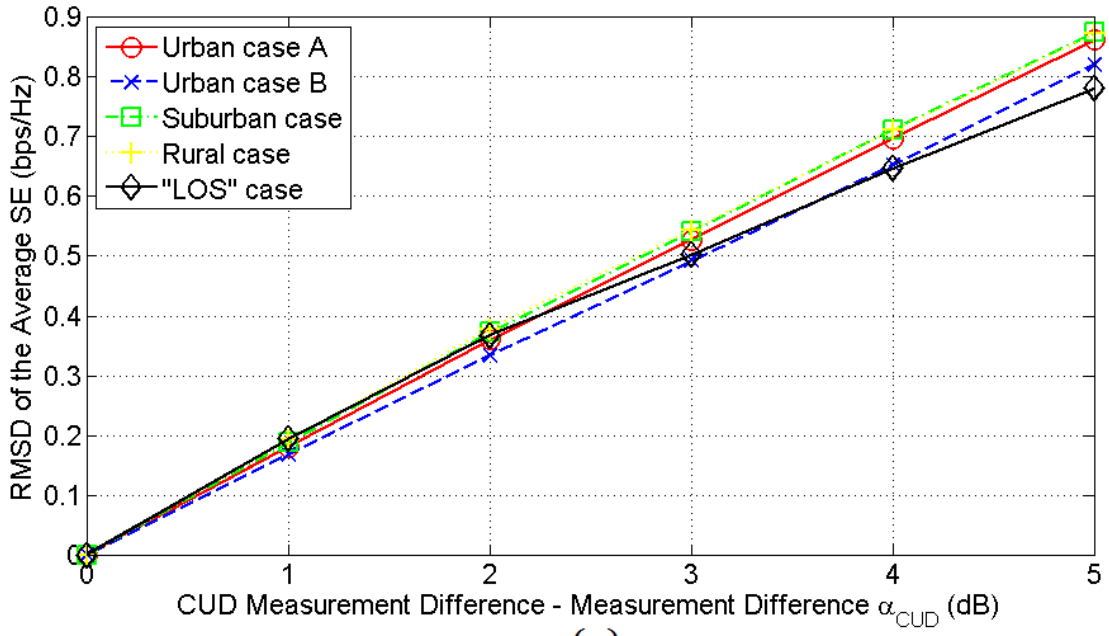
Urban case A
Urban case B
Suburban case
Rural case
"LOS" case
RMSD of the Average SE (bps/Hz)
CUD Measurement Difference - Measurement Difference α_{CUD} (dB)
0
0.1
0.2
0.3
0.4
0.5
0.6
0.7
0.8
0.9
1
2
3
4
5

(a)

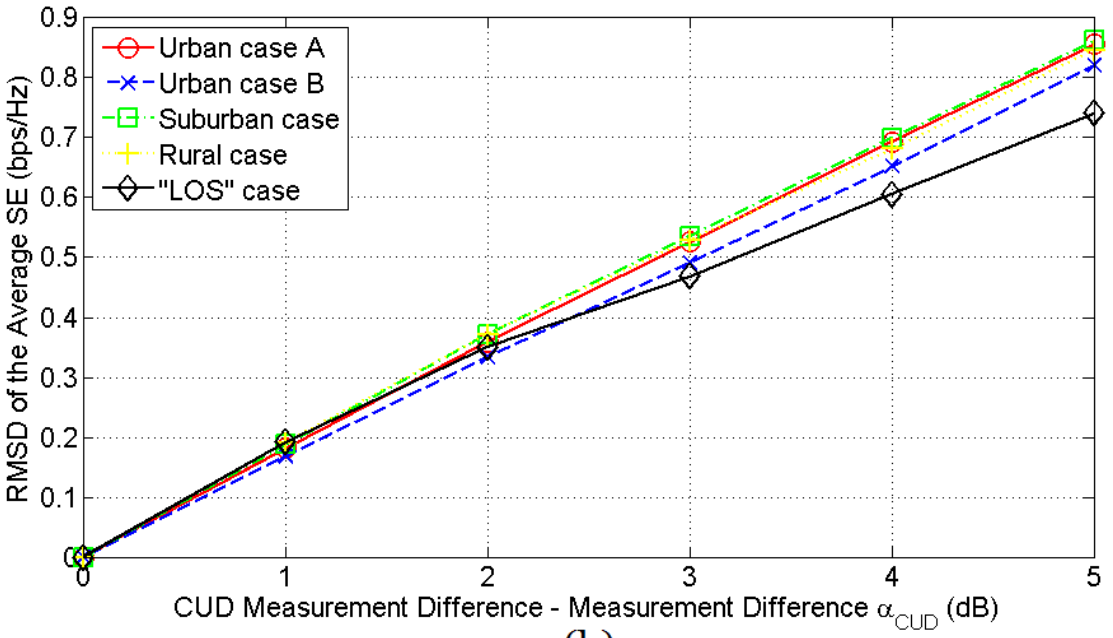
Urban case A
Urban case B
Suburban case
Rural case
"LOS" case
RMSD of the Average SE (bps/Hz)
CUD Measurement Difference - Measurement Difference α_{CUD} (dB)
0
0.1
0.2
0.3
0.4
0.5
0.6
0.7
0.8
0.9
1
2
3
4
5

(b)

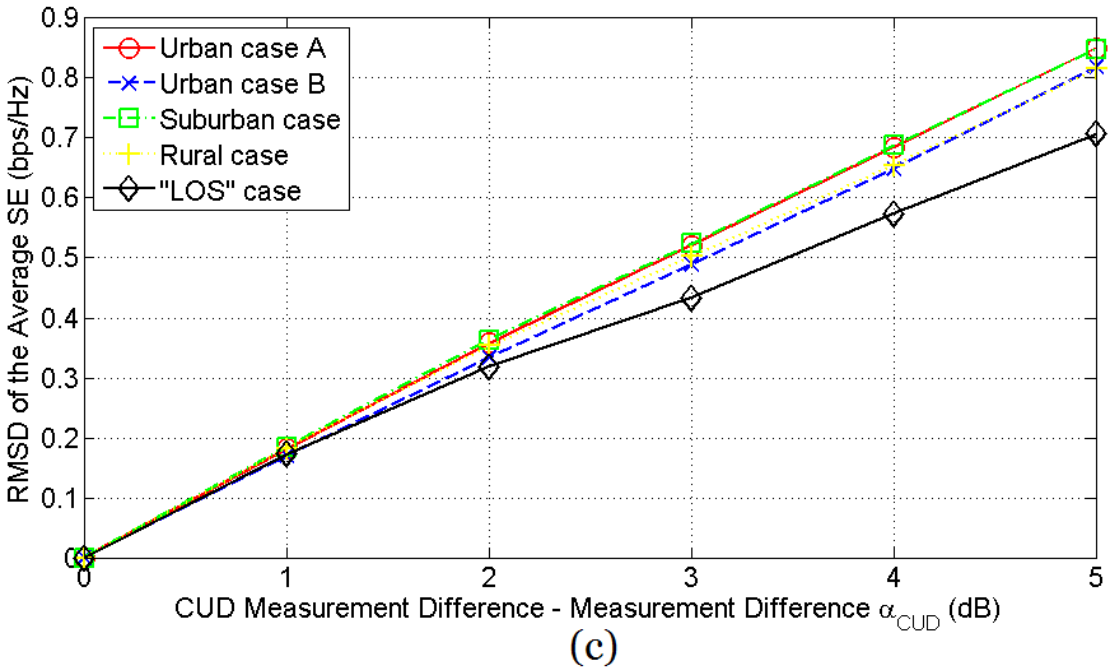

Fig. 20. RMSD of SE of the indicative OV MV BPL topologies in the 3-88 MHz frequency band when FCC limits are assumed and different coupling schemes are applied for different CUD measurement differences. (a) WtG^{1} coupling scheme. (b) $WtW^{1\text{-}2}$ coupling scheme. (c) $MtM^{1\text{-}2\text{-}3}_{0.8\_-0.1\_-0.1}$ coupling scheme.

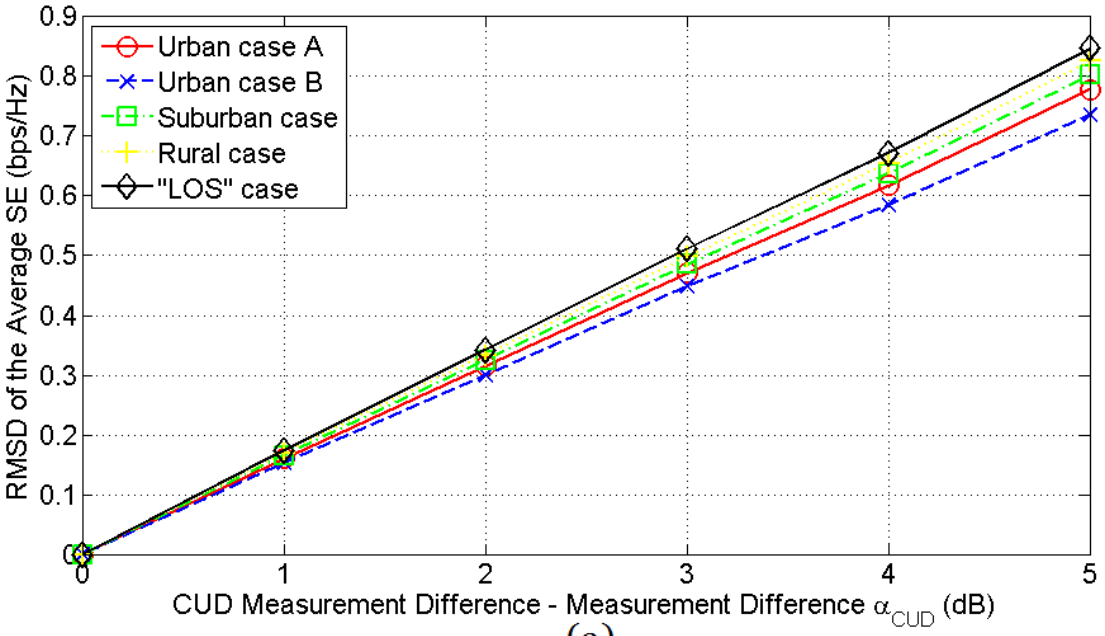
Urban case A
Urban case B
Suburban case
Rural case
"LOS" case
RMSD of the Average SE (bps/Hz)
CUD Measurement Difference - Measurement Difference α_{CUD} (dB)
0
0.1
0.2
0.3
0.4
0.5
0.6
0.7
0.8
0.9
1
2
3
4
5

(a)

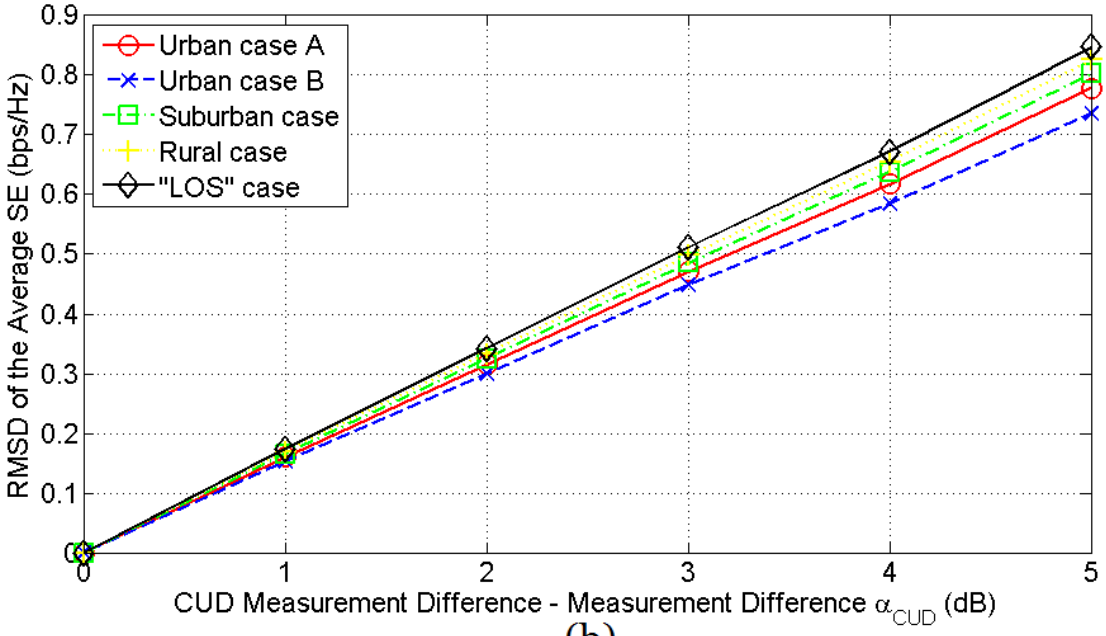
Urban case A
Urban case B
Suburban case
Rural case
"LOS" case
RMSD of the Average SE (bps/Hz)
CUD Measurement Difference - Measurement Difference α_{CUD} (dB)
0
0.1
0.2
0.3
0.4
0.5
0.6
0.7
0.8
0.9
1
2
3
4
5

(b)

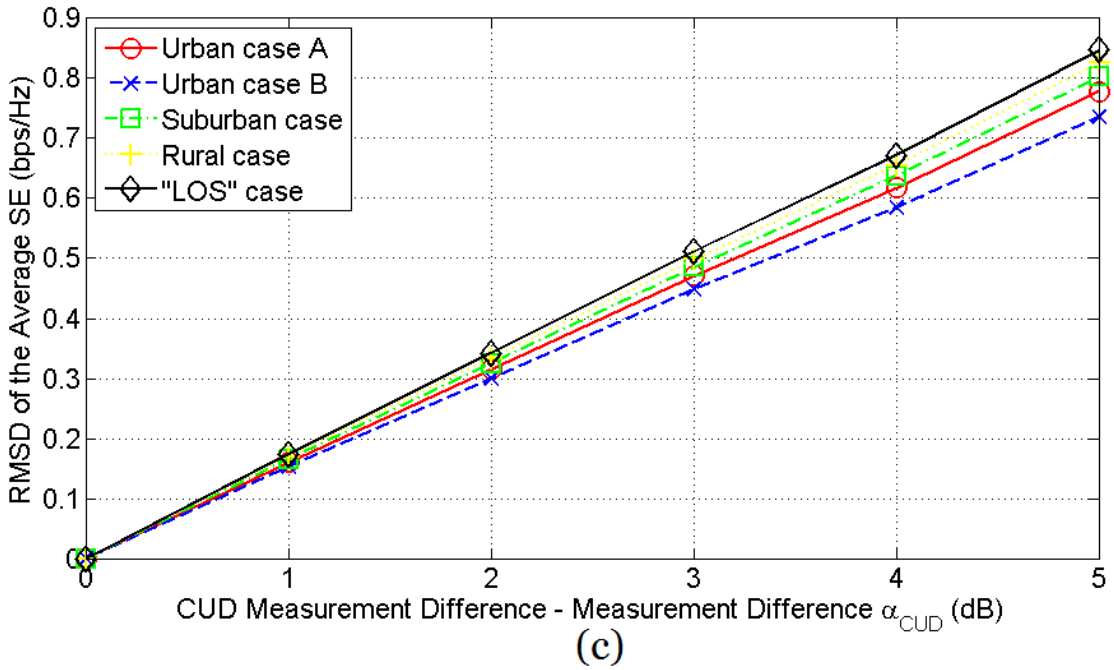

Fig. 21. RMSD of SE of the indicative UN MV BPL topologies in the 3-88 MHz frequency band when FCC limits are assumed and different coupling schemes are applied for different CUD measurement differences. (a) StP^{1} coupling scheme. (b) $PtP^{1\text{-}2}$ coupling scheme. (c) $MtM^{1\text{-}2\text{-}3}_{0.8\_-0.1\_-0.1}$ coupling scheme.

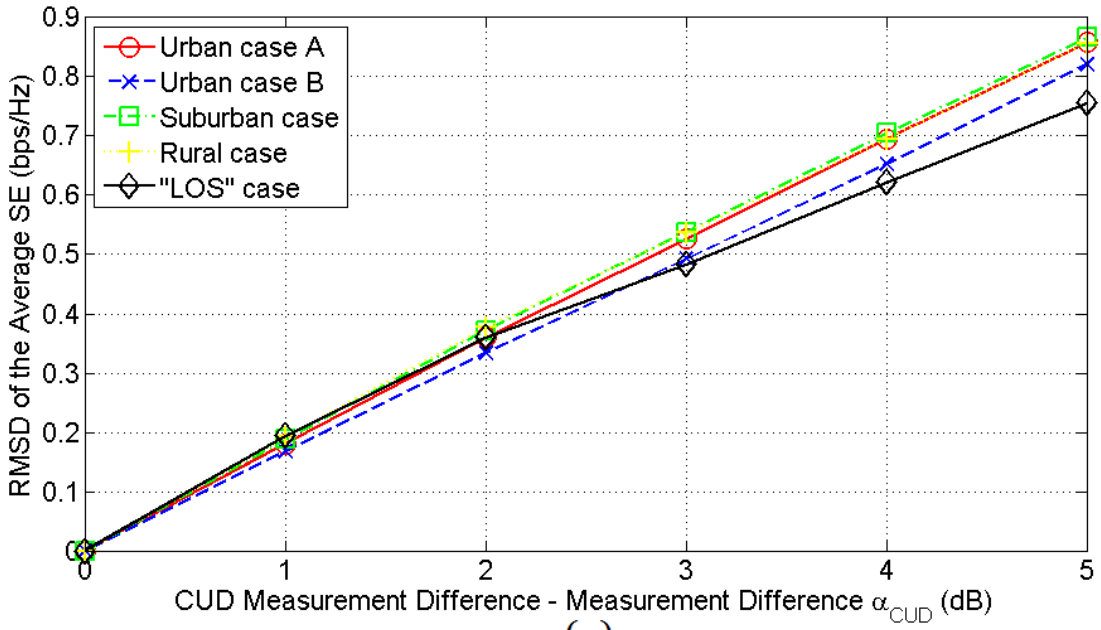
Urban case A
Urban case B
Suburban case
Rural case
"LOS" case
RMSD of the Average SE (bps/Hz)
CUD Measurement Difference - Measurement Difference α_{CUD} (dB)

(a)

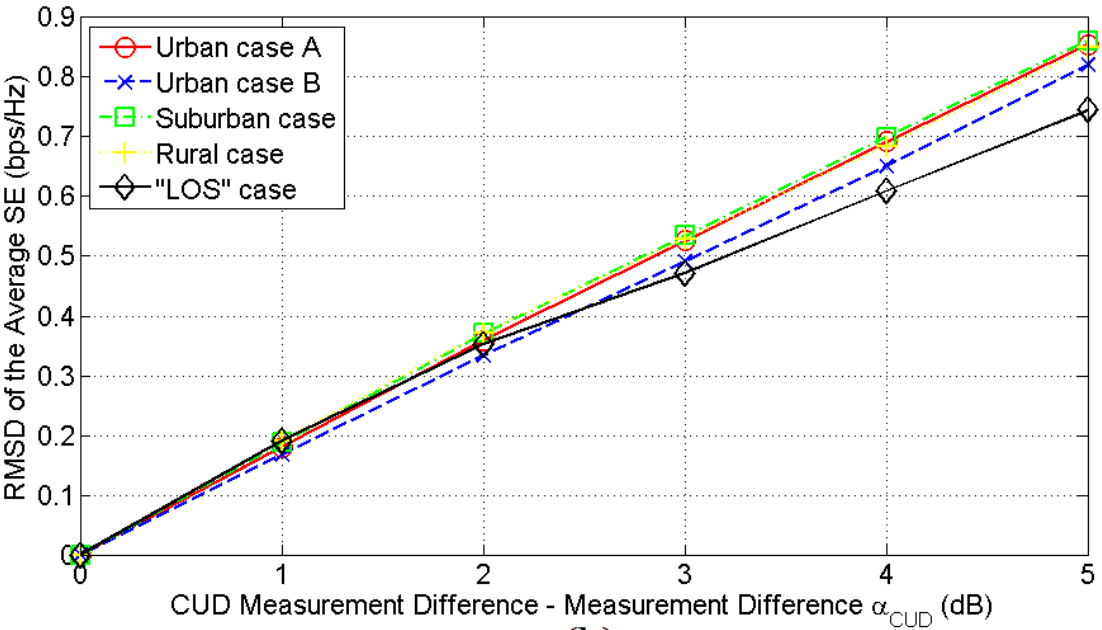
Urban case A
Urban case B
Suburban case
Rural case
"LOS" case
RMSD of the Average SE (bps/Hz)
CUD Measurement Difference - Measurement Difference α_{CUD} (dB)

(b)

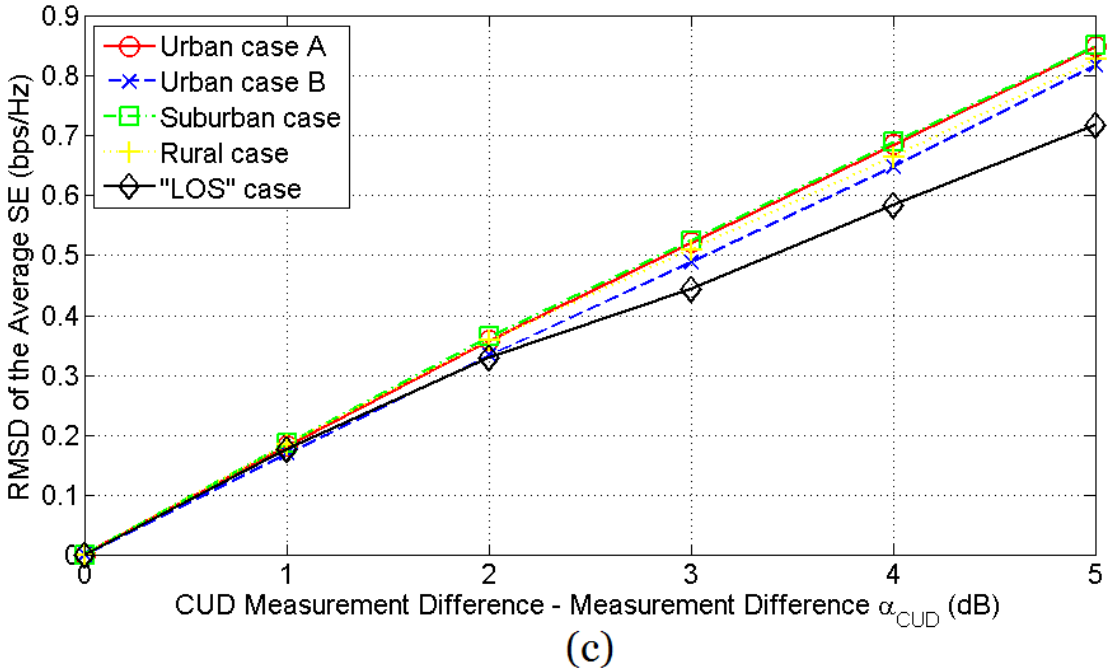

Fig. 22. Same with Fig. 20 but for the case of the indicative OV LV BPL topologies.

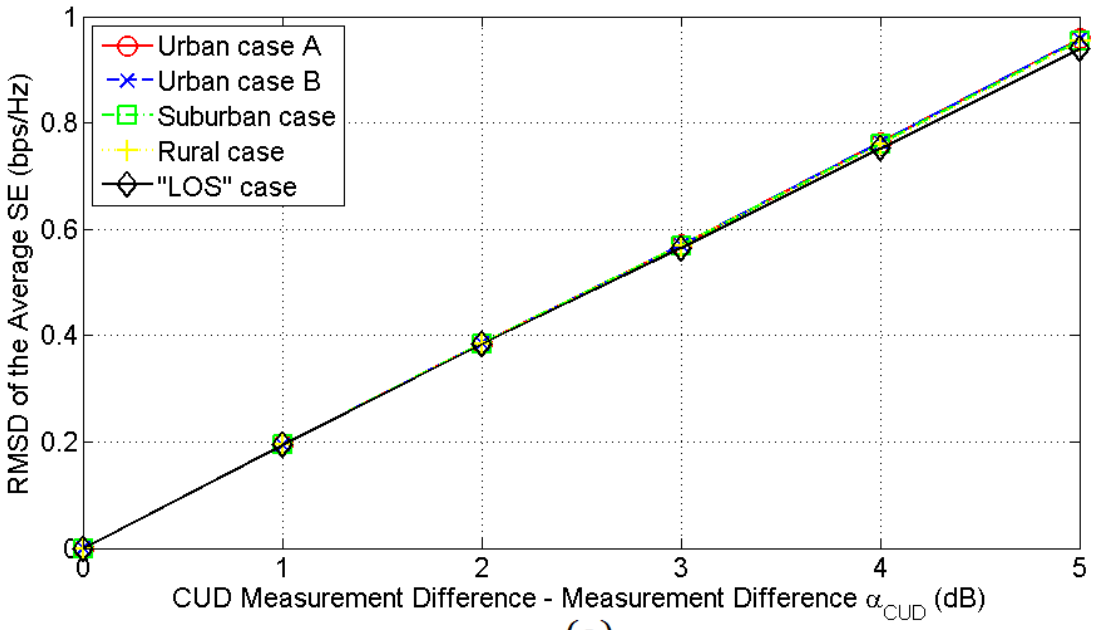
Urban case A
Urban case B
Suburban case
Rural case
"LOS" case
RMSD of the Average SE (bps/Hz)
CUD Measurement Difference - Measurement Difference α_{CUD} (dB)
0
0.2
0.4
0.6
0.8
1
0
1
2
3
4
5

(a)

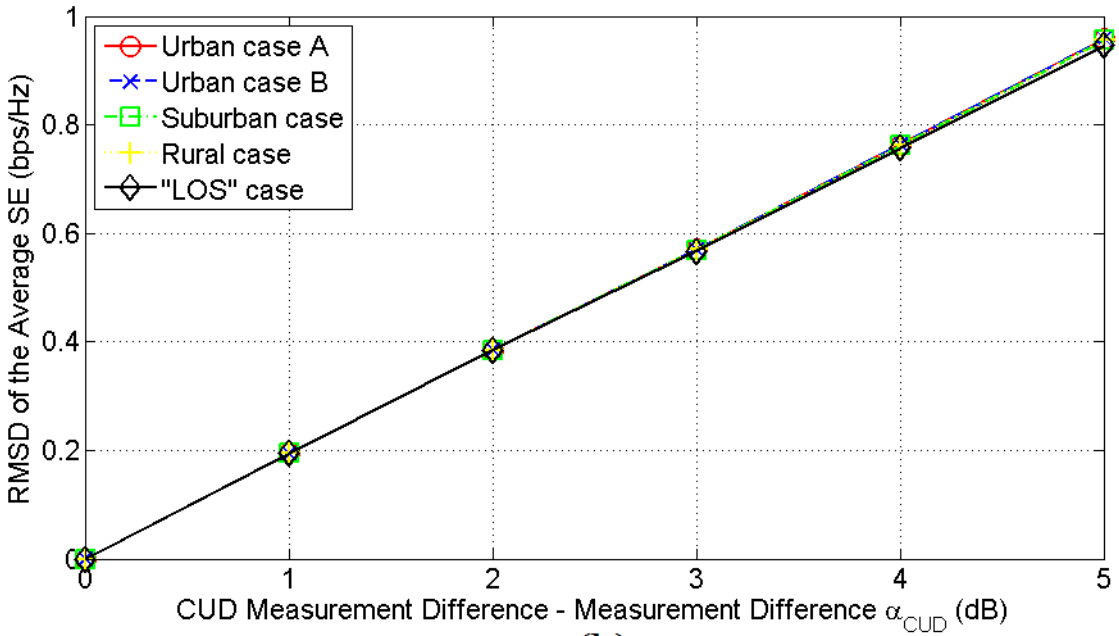
Urban case A
Urban case B
Suburban case
Rural case
"LOS" case
RMSD of the Average SE (bps/Hz)
CUD Measurement Difference - Measurement Difference α_{CUD} (dB)
0
0.2
0.4
0.6
0.8
1
0
1
2
3
4
5

(b)

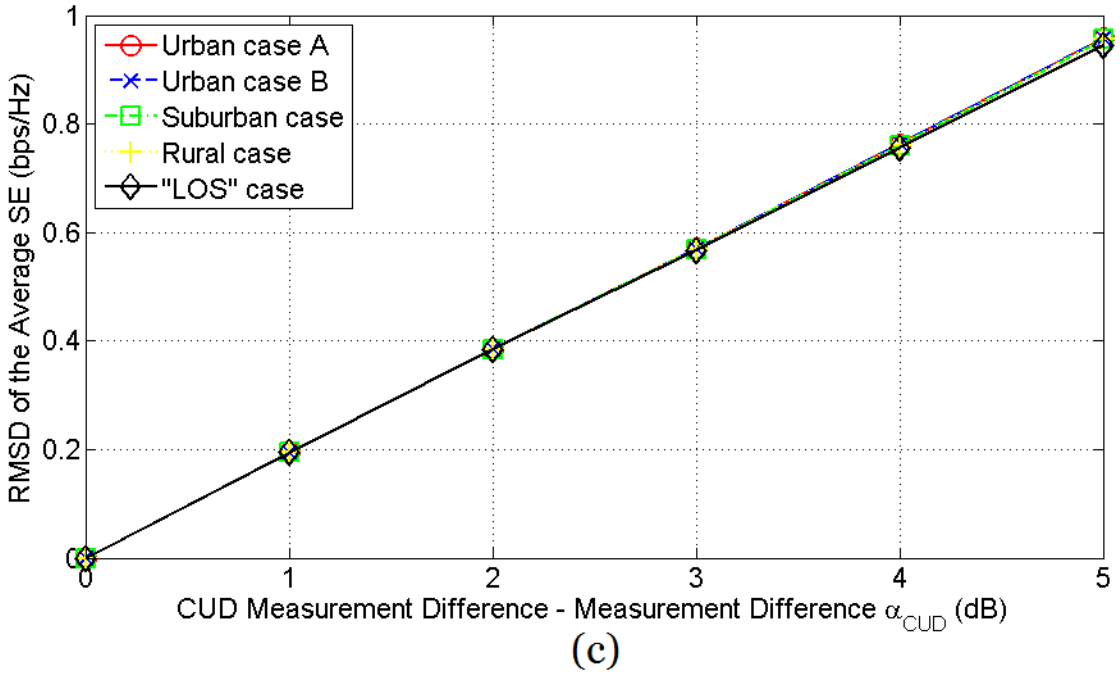

Fig. 23. Same with Fig. 21 but for the case of the indicative UN LV BPL topologies.

In Figs. 18(a)-(c), same plots with Figs. 12(a)-(c) are given but for the case of the indicative OV LV BPL topologies while in Figs. 19(a)-(c), same curves with Figs. 13(a)-(c) are presented but for the case of the indicative UN LV BPL topologies. In Figs. 20-23, same curves for the root mean square deviation (RMSD) of SE are given for the Figs. 16-19, respectively.

By observing Figs. 16-23, several interesting conclusions can be deduced. More specifically:

- In contrast with the traditional metrics of the maximum, minimum and average SE (*i.e.*, metrics of Set A), the metrics of Set B (*i.e.*, MAE and RMSD) can detect the existence of measurement differences while their values increase with the increase of the measurement difference a_{CUD}.
- Measurement differences influence in a different way the MAE and RMSD of the average SE depending on the distribution power grid type and distribution BPL topology. However, small order differences among the indicative distribution BPL topologies can be pointed out. Anyway, approximately 0.2 bps/Hz of RMSD is added for each 1dB increase of maximum value a_{CUD} regardless of the distribution power grid type and distribution BPL topology. Note that when measurement differences of a_{CUD} that is equal to 5 dB are assumed RMSD of 1 bps/Hz can be observed.
- When the SE is computed for given distribution BPL network and coupling scheme, it is unknown if measurement differences occur and if do which is their intensity. The countermeasures techniques of [55] aim at restoring the actual SE without a priori knowledge of the intensity of the measurement differences. In fact, the proposed SE countermeasure techniques can act as a necessary filter after the SE computation in order to identify and restore the actual SE that is free from measurement differences.

- Although maximum, minimum and average SE cannot provide evidence about the intensity of measurement differences and their impact, they can act as integrity metric for the countermeasures techniques of [55] that aim at retrieving the real SE of distribution BPL topologies.

5. Conclusions

This paper has focused on the SE performance of distribution BPL networks when different coupling schemes of the CS2 module, different BPL topologies and different types and intensities of measurement differences are assumed. It has been revealed that the SE performance depends on the type of the distribution power grid type, IPSD limits, noise levels and the examined distribution BPL topology. Also, the maximum, minimum and average SE (*i.e.*, metrics of Set A) significantly depend on the level of the biased measurement differences. In contrast with the biased measurement differences, CUD measurement differences have little effect to the maximum, minimum and average SE of the distribution BPL topologies. In order to identify the existence and the intensity of the measurement differences, MAE and RMSD (*i.e.*, metrics of Set B) are employed during the SE computation in distribution BPL topologies. The behavior of MAE and RMSD strongly depends on the value a_{CUD} of the CUD measurement differences rather than the distribution power grid type, distribution BPL topology and the applied coupling scheme. The role of MAE and RMSD is important since they can assess the mitigation efficiency of the measurement difference countermeasure techniques of [55].

CONFLICTS OF INTEREST

The author declares that there is no conflict of interests regarding the publication of this paper.

References

[1] A. G. Lazaropoulos, "Towards Modal Integration of Overhead and Underground Low-Voltage and Medium-Voltage Power Line Communication Channels in the Smart Grid Landscape: Model Expansion, Broadband Signal Transmission Characteristics, and Statistical Performance Metrics (Invited Paper)," *ISRN Signal Processing*, vol. 2012, Article ID 121628, pp. 1-17, 2012. [Online]. Available: http://www.hindawi.com/isrn/sp/2012/121628/

[2] A. G. Lazaropoulos, "Towards broadband over power lines systems integration: Transmission characteristics of underground low-voltage distribution power lines," *Progress in Electromagnetics Research B*, 39, pp. 89-114, 2012. [Online]. Available: http://www.jpier.org/PIERB/pierb39/05.12012409.pdf

[3] A. G. Lazaropoulos and P. G. Cottis, "Transmission characteristics of overhead medium voltage power line communication channels," *IEEE Trans. Power Del.*, vol. 24, no. 3, pp. 1164-1173, Jul. 2009.

[4] A. G. Lazaropoulos and P. G. Cottis, "Capacity of overhead medium voltage power line communication channels," *IEEE Trans. Power Del.*, vol. 25, no. 2, pp. 723-733, Apr. 2010.

[5] A. G. Lazaropoulos and P. G. Cottis, "Broadband transmission via underground medium-voltage power lines-Part I: transmission characteristics," *IEEE Trans. Power Del.*, vol. 25, no. 4, pp. 2414-2424, Oct. 2010.

[6] A. G. Lazaropoulos and P. G. Cottis, "Broadband transmission via underground medium-voltage power lines-Part II: capacity," *IEEE Trans. Power Del.*, vol. 25, no. 4, pp. 2425-2434, Oct. 2010.

[7] A. G. Lazaropoulos, "Broadband transmission characteristics of overhead high-voltage power line communication channels,"*Progress in Electromagnetics Research B*, vol. 36, pp. 373-398, 2012. [Online]. Available: http://www.jpier.org/PIERB/pierb36/19.11091408.pdf

[8] A. G. Lazaropoulos, "Green Overhead and Underground Multiple-Input Multiple-Output Medium Voltage Broadband over Power Lines Networks: Energy-Efficient Power Control,"*Springer Journal of Global Optimization*, vol. 2012 / Print ISSN 0925-5001, pp. 1-28, Oct. 2012.

[9] H. Ferreira, L. Lampe, J. Newbury, and T. G. Swart, *Power Line Communications, Theory and Applications for Narrowband and Broadband Communications over Power Lines*. New York: Wiley, 2010.

[10] K. Sharma and L. M. Saini, "Power-line communications for smart grid: Progress, challenges, opportunities and status," *Elsevier Renewable and Sustainable Energy Reviews,* vol. 67, pp. 704-751, 2017.

[11] T. A. Papadopoulos, A. I. Chrysochos, A. ElSamadouny, N. Al-Dhahir, and G. K. Papagiannis, "MIMO-OFDM narrowband-PLC in distribution systems: Impact of power transformers on achievable data rates,". *Elsevier Electric Power Systems Research*, vol. 151, pp. 251-265, 2017.

[12] E. O. Kontis, T. A. Papadopoulos, A. I. Chrysochos, and G. K. Papagiannis, "Measurement-Based Dynamic Load Modeling Using the Vector Fitting Technique," *IEEE Transactions on Power Systems*, vol. 33, no. 1, pp. 338-351, 2018.

[13] A. G. Lazaropoulos, "Deployment Concepts for Overhead High Voltage Broadband over Power Lines Connections with Two-Hop Repeater System: Capacity Countermeasures against Aggravated Topologies and High Noise Environments," *Progress in Electromagnetics Research B*, vol. 44, pp. 283-307, 2012. [Online]. Available: http://www.jpier.org/PIERB/pierb44/13.12081104.pdf

[14] A. G. Lazaropoulos, "Broadband transmission and statistical performance properties of overhead high-voltage transmission networks,"*HindawiJournal of Computer Networks and Commun.*, 2012, article ID 875632, 2012. [Online]. Available: http://www.hindawi.com/journals/jcnc/aip/875632/

[15] P. Amirshahi and M. Kavehrad, "High-frequency characteristics of overhead multiconductor power lines for broadband communications," *IEEE J. Sel. Areas Commun.*, vol. 24, no. 7, pp. 1292-1303, Jul. 2006.

[16] T. Calliacoudas and F. Issa, ""Multiconductor transmission lines and cables solver," An efficient simulation tool for plc channel networks development," presented at the *IEEE Int. Conf. Power Line Communications and Its Applications*, Athens, Greece, Mar. 2002.

[17] T. Sartenaer and P. Delogne, "Deterministic modelling of the (Shielded) outdoor powerline channel based on the multiconductor transmission line equations," *IEEE J. Sel. Areas Commun.*, vol. 24, no. 7, pp. 1277-1291, Jul. 2006.

[18] C. R. Paul, *Analysis of Multiconductor Transmission Lines*. New York: Wiley, 1994.

[19] H. Meng, S. Chen, Y. L. Guan, C. L. Law, P. L. So, E. Gunawan, and T. T. Lie, "Modeling of transfer characteristics for the broadband power line communication channel," *IEEE Trans. Power Del.*, vol. 19, no. 3, pp. 1057-1064, Jul. 2004.

[20] B. Li, D. Mansson, and G. Yang, "An efficient method for solving frequency responses of power-line networks," Progress In Electromagnetics Research B, Vol. 62, 303-317, 2015. doi:10.2528/PIERB15013008 http://www.jpier.org/pierb/pier.php?paper=15013008

[21] M. Chaaban, K. El KhamlichiDrissi, and D. Poljak, "Analytical model for electromagnetic radiation by bare-wire structures," Progress In Electromagnetics Research B, Vol. 45, 395-413, 2012. doi:10.2528/PIERB12091102 http://www.jpier.org/pierb/pier.php?paper=12091102

[22] Y. H. Kim, S. Choi, S. C. Kim, and J. H. Lee, "Capacity of OFDM two-hop relaying systems for medium-voltage power-line access networks," *IEEE Trans. Power Del.*, vol. 27, no. 2, pp. 886-894, Apr. 2012.

[23] A. G. Lazaropoulos, "New Coupling Schemes for Distribution Broadband over Power Lines (BPL) Networks," *Progress in Electromagnetics Research B*, vol. 71, pp. 39-54, 2016. [Online]. Available: http://www.jpier.org/PIERB/pierb71/02.16081503.pdf

[24] A. G. Lazaropoulos, "Broadband Performance Metrics and Regression Approximations of the New Coupling Schemes for Distribution Broadband over Power Lines (BPL) Networks," *Trends in Renewable Energy*, vol. 4, no. 1, pp. 43 – 73, 2018. [Online]. Available: http://www.futureenergysp.com/index.php/tre/article/view/59/pdf

[25] A. G. Lazaropoulos, "Measurement Differences, Faults and Instabilities in Intelligent Energy Systems – Part 1: Identification of Overhead High-Voltage Broadband over Power Lines Network Topologies by Applying Topology Identification Methodology (TIM)," *Trends in Renewable Energy*, vol. 2, no. 3, pp. 85 – 112, Oct. 2016. [Online]. Available: http://futureenergysp.com/index.php/tre/article/download/26/32

[26] A. G. Lazaropoulos, "Measurement Differences, Faults and Instabilities in Intelligent Energy Systems – Part 2: Fault and Instability Prediction in Overhead High-Voltage Broadband over Power Lines Networks by Applying Fault and Instability Identification Methodology (FIIM)," *Trends in Renewable Energy*, vol. 2, no. 3, pp. 113 – 142, Oct. 2016. [Online]. Available: http://futureenergysp.com/index.php/tre/article/view/27/33

[27] A. G. Lazaropoulos, "Best L1 Piecewise Monotonic Data Approximation in Overhead and Underground Medium-Voltage and Low-Voltage Broadband over Power Lines Networks: Theoretical and Practical Transfer Function Determination," *Hindawi Journal of Computational Engineering*, vol. 2016, Article ID 6762390, 24 pages, 2016. doi:10.1155/2016/6762390. [Online]. Available: https://www.hindawi.com/journals/jcengi/2016/6762390/cta/

[28] A. G. Lazaropoulos, "Power Systems Stability through Piecewise Monotonic Data Approximations – Part 2: Adaptive Number of Monotonic Sections and Performance of L1PMA, L2WPMA and L2CXCV in Overhead Medium-Voltage Broadband over Power Lines Networks," Trends in Renewable Energy, vol. 3, no.

1, pp. 33 – 60, Jan. 2017. [Online]. Available: http://futureenergysp.com/index.php/tre/article/view/30/35

[29] A. G. Lazaropoulos, "Power Systems Stability through Piecewise Monotonic Data Approximations – Part 1: Comparative Benchmarking of L1PMA, L2WPMA and L2CXCV in Overhead Medium-Voltage Broadband over Power Lines Networks," *Trends in Renewable Energy*, vol. 3, no. 1, pp. 2 – 32, Jan. 2017. [Online]. Available: http://futureenergysp.com/index.php/tre/article/view/29/34

[30] A. G. Lazaropoulos, "Main Line Fault Localization Methodology in Smart Grid – Part 1: Extended TM2 Method for the Overhead Medium-Voltage Broadband over Power Lines Networks Case," *Trends in Renewable Energy*, vol. 3, no. 3, pp. 2-25, Dec. 2017. [Online]. Available: http://futureenergysp.com/index.php/tre/article/view/36

[31] A. G. Lazaropoulos, "Main Line Fault Localization Methodology in Smart Grid – Part 2: Extended TM2 Method, Measurement Differences and L1 Piecewise Monotonic Data Approximation for the Overhead Medium-Voltage Broadband over Power Lines Networks Case," *Trends in Renewable Energy*, vol. 3, no. 3, pp. 26-61, Dec. 2017. [Online]. Available: http://futureenergysp.com/index.php/tre/article/view/37

[32] A. G. Lazaropoulos, "Main Line Fault Localization Methodology in Smart Grid – Part 3: Main Line Fault Localization Methodology (MLFLM)," *Trends in Renewable Energy*, vol. 3, no. 3, pp. 62-81, Dec. 2017. [Online]. Available: http://futureenergysp.com/index.php/tre/article/view/38

[33] P. Amirshahi and M. Kavehrad, "Medium voltage overhead powerline broadband communications; Transmission capacity and electromagnetic interference," in *Proc. IEEE Int. Symp. Power Line Commun. Appl.*, Vancouver, BC, Canada, Apr. 2005, pp. 2-6.

[34] OPERA1, D44: Report presenting the architecture of plc system, the electricity network topologies, the operating modes and the equipment over which PLC access system will be installed, IST Integr. Project No 507667, Dec. 2005.

[35] OPERA1, D5: Pathloss as a function of frequency, distance and network topology for various LV and MV European powerline networks. IST Integrated Project No 507667, Apr. 2005.

[36] P. C. J. M. van der Wielen, "On-line detection and location of partial discharges in medium-voltage power cables" Ph.D. dissertation, Tech. Univ. Eindhoven, Eindhoven, the Netherlands, Apr. 2005. [Online]. Available: http://alexandria.tue.nl/extra2/200511097.pdf

[37] P. C. J. M. van der Wielen, E. F. Steennis, and P. A. A. F. Wouters, "Fundamental aspects of excitation and propagation of on-line partial discharge signals in three-phase medium voltage cable systems," *IEEE Trans. Dielectr. Electr. Insul.*, vol. 10, no. 4, pp. 678-688, Aug. 2003.

[38] M. Tang, and M. Zhai, "Research of transmission parameters of four-conductor cables for power line communication," in *Proc. Int. Conf. on Computer Science and Software Engineering*, Wuhan, China, Dec. 2008, vol. 5, pp. 1306–1309.

[39] F. Issa, D. Chaffanjon, E. P. de la Bâthie, and A. Pacaud, "An efficient tool for modal analysis transmission lines for PLC networks development," presented at the *IEEE Int. Conf. Power Line Communications and Its Applications*, Athens, Greece, Mar. 2002.

[40] M. D'Amore and M. S. Sarto, "A new formulation of lossy ground return parameters for transient analysis of multiconductor dissipative lines," *IEEE Trans. Power Del.*, vol. 12, no. 1, pp. 303-314, Jan. 1997.
[41] M. D'Amore and M. S. Sarto, "Simulation models of a dissipative transmission line above a lossy ground for a wide-frequency range-Part I: Single conductor configuration," *IEEE Trans. Electromagn. Compat.*, vol. 38, no. 2, pp. 127-138, May 1996.
[42] M. D'Amore and M. S. Sarto, "Simulation models of a dissipative transmission line above a lossy ground for a wide-frequency range-Part II: Multi-conductor configuration," *IEEE Trans. Electromagn. Compat.*, vol. 38, no. 2, pp. 139-149, May 1996.
[43] N. Theethayi, "Electromagnetic interference in distributed outdoor electrical systems, with an emphasis on lightning interaction with electrified railway network," Ph.D. dissertation, Uppsala Univ., Uppsala, Sweden, Sep. 2005, [Online]. Available: http://uu.diva-portal.org/smash/get/diva2:166746/FULLTEXT01
[44] A. G. Lazaropoulos, "Factors Influencing Broadband Transmission Characteristics of Underground Low-Voltage Distribution Networks,"*IET Commun.*, vol. 6, no. 17, pp. 2886-2893, Nov. 2012.
[45] J. Anatory, N. Theethayi, and R. Thottappillil, "Power-line communication channel model for interconnected networks-Part II: Multiconductor system," *IEEE Trans. Power Del.*, vol. 24, no. 1, pp. 124-128, Jan. 2009.
[46] J. Anatory, N. Theethayi, R. Thottappillil, M. M. Kissaka, and N. H. Mvungi, "The effects of load impedance, line length, and branches in typical low-voltage channels of the BPLC systems of developing countries: transmission-line analyses," *IEEE Trans. Power Del.*, vol. 24, no. 2, pp. 621-629, Apr. 2009.
[47] A. G. Lazaropoulos, "A Panacea to Inherent BPL Technology Deficiencies by Deploying Broadband over Power Lines (BPL) Connections with Multi-Hop Repeater Systems," *Bentham Recent Advances in Electrical & Electronic Engineering*, vol. 10, no. 1, pp. 30-46, 2017.
[48] M. Gebhardt, F. Weinmann, and K. Dostert, "Physical and regulatory constraints for communication over the power supply grid," *IEEE Commun. Mag.*, vol. 41, no. 5, pp. 84-90, May 2003.
[49] P. S. Henry, "Interference characteristics of broadband power line communication systems using aerial medium voltage wires," *IEEE Commun. Mag.*, vol. 43, no. 4, pp. 92-98, Apr. 2005.
[50] Ofcom, "Amperion PLT Measurements in Crieff," Ofcom, Tech. Rep., Sept. 2005.
[51] NATO, "HF Interference, Procedures and Tools (Interférences HF, procédures et outils) Final Report of NATO RTO Information Systems Technology," RTO-TR-ISTR-050, Jun. 2007, [Online]. Available: http://ftp.rta.nato.int/public/PubFullText/RTO/TR/RTO-TR-IST-050/$$TR-IST-050-ALL.pdf
[52] FCC, "In the Matter of Amendment of Part 15 regarding new requirements and measurement guidelines for Access Broadband over Power Line Systems," FCC 04-245 Report and Order, Jul. 2008.
[53] Ofcom, "DS2 PLT Measurements in Crieff," Ofcom, Tech. Rep. 793 (Part 2), May 2005.

[54] Ofcom, "Ascom PLT Measurements in Winchester," Ofcom, Tech. Rep. 793 (Part 1), May 2005.
[55] A. G. Lazaropoulos, "Smart Energy and Spectral Efficiency (SE) of Distribution Broadband over Power Lines (BPL) Networks – Part 2: L1PMA, L2WPMA and L2CXCV for SE against Measurement Differences in Overhead Medium-Voltage BPL Networks," *Trends in Renewable Energy*, DOI: 10.17737/tre.2018.4.2.0077.

Trends in Renewable Energy
OPEN ACCESS ISSN:2376-2144
Peer-Reviewed Article futureenergysp.com/index.php/tre

Smart Energy and Spectral Efficiency (SE) of Distribution Broadband over Power Lines (BPL) Networks – Part 2: L1PMA, L2WPMA and L2CXCV for SE against Measurement Differences in Overhead Medium-Voltage BPL Networks

Athanasios G. Lazaropoulos*

School of Electrical and Computer Engineering / National Technical University of Athens / 9 Iroon Polytechniou Street / Zografou, GR 15780

Received June 7, 2018; Accepted August 17, 2018; Published August 21, 2018

This second paper assesses the performance of piecewise monotonic data approximations, such as L1PMA, L2WPMA and L2CXCV, against the measurement differences during the spectral efficiency (SE) calculations in overhead medium-voltage broadband over power lines (OV MV BPL) networks. In this case study paper, the performance of the aforementioned three already known piecewise monotonic data approximations, which are considered as countermeasure techniques against measurement differences, is here extended during the SE computations. The indicative BPL topologies of the first paper are again considered while the 3-30MHz frequency band of the BPL operation is assumed.

Keywords: Smart Grid; Broadband over Power Lines (BPL); Power Line Communications (PLC); Distribution Power Grid; Spectral Efficiency.

1. Introduction

Smart energy is a sustainable and worthwhile energy system where energy production, transmission and delivery are integrated and coordinated with the energy consumption, smart grid applications, energy services, active producers / consumers, renewable / storage solutions and enabling communications technologies. However, the emerging advanced IP-based power network requires high spectral efficiency (SE) potential so that the supported plethora of relevant broadband applications can be easily supported [1]-[3].

Among the enabling communications technology solutions of the smart grid, Broadband over Power Lines (BPL) technology attracts the interest of many decision makers due to the low installation cost of the BPL devices on the existing power grid infrastructure. Already presented in [4], the spectral behavior of distribution BPL networks –*i.e.*, overhead (OV) and underground (UN) medium-voltage (MV) and low-voltage (LV) BPL networks– is assessed through the hybrid model [5]-[22]. In this paper, CS2 module, which constitutes a refinement of the hybrid model concerning its containing top-down approach, is adopted. On the basis of the SE,

**Corresponding author:* AGLazaropoulos@gmail.com

Tr Ren Energy, 2018, Vol.4, No.2, 185-212. doi: 10.17737/tre.2018.4.2.0077

the impact of CS2 module and of the measurement differences between the experimental and theoretical results on the broadband performance of the distribution BPL networks has been assessed in [4]. Here, it should be noted that measurement differences have been handled as error distributions and especially by following continuous uniform distributions (CUDs) of maximum and minimum value a_{CUD} and -a_{CUD}, respectively. The assessment has been accomplished through the lens of appropriate statistical performance metrics of SE that are classified into two metric sets. Set A consists of the maximum, minimum and average SE while Set B comprises the mean absolute error (MAE) and the root mean square deviation (RMSD) of SE.

To mitigate the aforementioned measurement differences that further affect the statistical performance metrics, three well-known piecewise monotonic data approximations (*i.e.*, L1PMA, L2WPMA and L2CXCV) are going to be applied [23]-[32]. Until now, L1PMA, L2WPMA and L2CXCV have been applied and examined in transmission and distribution BPL networks in order to counteract the occurred measurement differences during the channel attenuation computations [31]-[37]. Useful results, which are going to be adopted in this paper, concerning the application properties of piecewise monotonic data approximations against the measurement differences during the channel attenuation computations have been deduced in [36], [37]. On the basis of these application properties, the application of the piecewise monotonic data approximations is extended to the SE results in order to reveal the theoretical SE values by ignoring the fluctuations of channel attenuation computations due to the measurement differences and without knowing the CUD measurement difference properties (*i.e.*, maximum and minimum values of the CUD measurement distributions). The countermeasure efficiency of the L1PMA, L2WPMA and L2CXCV against the measurement differences during the SE computation is assessed for comparison reasons on the basis of: (i) the main performance metric of the piecewise monotonic data approximation method [33], [36], that is the percent error sum (PES); and (ii) the statistical performance metrics of set A and B that already been applied in [4].

The rest of this paper is organized as follows: In Sec.2, a brief presentation of the L1PMA, L2WPMA and L2CXCV is given. Sec.3 synopsizes the applied performance metrics, already been presented in [4]. The strong and the weak points of the performance metrics are demonstrated. Sec.4 discusses the simulation results of various distribution BPL topologies intending to mark out the efficiency of L1PMA, L2WPMA and L2CXCV against the restoration of the theoretical SE when measurement differences of various CUD properties are considered. Sec.5 concludes this paper.

2. Measurement Differences and Piecewise Monotonic Data Approximation Methods

2.1 Measured and Theoretical SE

As already been mentioned in [4], [36], [37], a number of practical reasons and "real-life" conditions create significant differences between experimental measurements and theoretical results during the determination of transfer functions. However, these transfer function computation fluctuations affect SE.

In fact, the measurement differences that occur during the transfer function determination of BPL networks indirectly affect the determination of SE. Numerically,

when measurement differences are taken into consideration, the measured distribution BPL coupling transfer function $\overline{H^C}\{\cdot\}$ for given coupling scheme *C* is determined by

$$\overline{H^C}(f_i) = H^C(f_i) + e(f_i) \quad (1)$$

where f_i, i=1,…,u denotes the measurement frequency, $H^C(f_i)$ is the theoretical coupling transfer function that is given by the application of the hybrid model presented in [4], $e(f_i)$ synopsizes the total measurement difference that follows continuous uniform distributions (CUDs) in dB with minimum value $-a_{\mathrm{CUD}}$ and maximum value a_{CUD} and u is the number of subchannels in the examined frequency range. On the basis of eq. (3) of [4], the measured and theoretical SE for given coupling scheme channel *C* can be respectively determined by

$$\overline{SE^C}(f_i) = \log_2\left\{1 + \left[\frac{\langle p(f_i)\rangle_L}{\langle N(f_i)\rangle_L} \cdot \left|\overline{H^C}(f_i)\right|^2\right]\right\}, i = 1, \dots, u \quad (2)$$

$$SE^C(f_i) = \log_2\left\{1 + \left[\frac{\langle p(f_i)\rangle_L}{\langle N(f_i)\rangle_L} \cdot |H^C(f_i)|^2\right]\right\}, i = 1, \dots, u \quad (3)$$

where $p\{\cdot\}$ are appropriate IPSD limits expressed in dBm/Hz that ensure the low electromagnetic interference (EMI) of BPL system operation to the other telecommunication systems that operate at the same frequency band, $N\{\cdot\}$ are uniform additive white Gaussian noise (AWGN) PSD levels expressed in dBm/Hz and $\langle\cdot\rangle_L$ is an operator that converts dBm/Hz into a linear power ratio (W/Hz). By comparing eqs. (2) and (3), it is evident that SE depends on the assumed coupling transfer function while significant differences between measured and theoretical coupling transfer functions entail differences between measured and theoretical SE.

In order to cope with the measurement differences, various monotonic data approximation methods, which treated as countermeasure techniques against measurement differences, have been proposed by Demetriou, such as L1PMA, L2WPMA and L2CXCV [23]-[32]. Their countermeasure efficiency against measurement differences during the determination of the coupling transfer functions of distribution BPL networks has been extensively validated in [34]-[41] while a number of useful smart grid applications concerning the power grid monitoring and control have been proposed on the basis of these piecewise monotonic data approximations. Here, the aforementioned three piecewise monotonic data approximations are applied in order to reveal the theoretical SE when measured SE, the distribution BPL topology and the applied coupling scheme are already known. Actually, piecewise monotonic data approximations aim at mitigating the deviations between the measured and the theoretical SE which are the result of the existence of measurement differences. With reference to eq. (2) and (3), piecewise monotonic data approximations give as output the approximated SE for given coupling scheme channel *C*, say:

$$\overline{\overline{SE^C}}(f_i) = q\left\{\overline{SE^C}(f_i)\right\},\ i = 1, \dots, u \quad (4)$$

where $q\{\cdot\}$ is the general function of the applied piecewise monotonic data approximations. It should be noted that during the determination of the approximated SE of eq. (4), CUD properties of measurement differences are not known.

To apply the aforementioned three piecewise monotonic data approximations (*i.e.*, L1PMA, L2WPMA and L2CXCV) and to determine the piecewise monotonic data approximation of eq. (4), the special application characteristics of each one are mentioned in the following subsections.

2.2 L1PMA

L1PMA decomposes the input data (*i.e.*, SE data in this paper) into separate monotonous sections between its adjacent turning points (primary extrema) by exploiting the piecewise monotonicity property of transmission and distribution BPL transfer functions [25], [26]. On the basis of the minimization of the moduli sum between the output data (L1PMA approximation data of SE) and input data into the separate monotonous sections, L1PMA achieves to mitigate the uncorrelated SE differences, which come from the assumed measurement differences, by neglecting the existence of few large ones [33], [36], [37]. The L1PMA application is based on the Fortran software package that is freely available online in [42] receives as inputs the measured SE, the measurement frequencies and the number of monotonic sections (*i.e.*, either user- or computer-defined) and primarily gives as output the best fit of the measured SE. As already been presented in [36], [37], critical role during the computation of the best of the measured SE plays the selection of the number of the monotonic sections.

2.3 L2WPMA

Similarly to L1PMA, L2WPMA decomposes the examined input data (*i.e.*, either transfer function data or SE data of this paper), which are contaminated by measurement differences, into separate monotonous sections between its primary extrema [31], [36], [37]. L2WPMA is implemented by a Fortran software package that is freely available online in [31]. As in L1PMA case, L2WPMA software receives as input the measured SE, the measurement frequencies and the number of monotonic sections and primarily gives as output a spline representation of the measured SE. Conversely to L1PMA, L2WPMA focuses on the first divided of input data and demands the minimization of the weighted sum of the square of the measurement differences by requiring specific number of sign changes. The number of sign changes is equal to the number of monotonic sections minus one. Again, the number of monotonic sections is either user- or computer-defined.

2.4 L2CXCV

In accordance with [32], [36], [37], L2CXCV smooths the input data with measurement differences in the least square error sense. In contrast with L1PMA and L2WPMA, L2CXCV does not focus on the number of monotonic sections but on the second divided differences of the smoothed values by solving a strictly convex quadratic programming problem for each set [32]. Similarly to L1PMA and L2CXCV, the Fortran software package that is applied to implement L2CXCV is freely available online in [43]. In general, L2CXCV receives as input the measured SE and gives as output the fit of the measured SE.

3. Performance Metrics

3.1 PES

In accordance with [33], [36], PES is the main performance metric that is employed to assess the approximation accuracy when piecewise monotonic data approximation methods are applied in BPL networks. More specifically, in this paper, PES expresses as a percentage the total sum of the relative differences between the examined SE and the theoretical SE for all the used frequencies. There are two submetrics of PES that should be compared in order to benchmark the mitigation efficiency of the applied piecewise monotonic data approximation method, say:

- PES_{meas}: This PES submetric examines the relative difference between the SE, which is affected by the measurement differences, and the theoretical SE. With reference to eqs. (2) and (3), PES_{meas} is given by:

$$PES_{\text{meas}} = 100\% \cdot \frac{\sum_{i=1}^{u} |\overline{SE^C}(f_i) - SE^C(f_i)|}{\sum_{i=1}^{u} |SE^C(f_i)|} \tag{5}$$

- PES_{approx}: This PES submetric examines the relative difference between the approximated and the theoretical SE. With reference to eqs. (3) and (4), PES_{approx} is given by:

$$PES_{\text{approx}} = 100\% \cdot \frac{\sum_{i=1}^{u} \left|\overline{\overline{SE^C}}(f_i) - SE^C(f_i)\right|}{\sum_{i=1}^{u} |SE^C(f_i)|} \tag{6}$$

From eqs. (5) and (6), the PES difference that is given by

$$\Delta PES = PES_{\text{meas}} - PES_{\text{approx}} \tag{7}$$

determines the quality of the approximation. If ΔPES is positive, the examined approximation method successfully mitigates the measurement differences. ΔPES helps towards the determination of the optimal number of monotonic sections of L1PMA and L2WPMA [36], [37].

3.2 Metrics of Set A and B

In accordance with [4], two sets of performance metrics (*i.e.*, Set A and B) can be applied in order to assess either the SE impact of measurement differences or the SE mitigation efficacy of piecewise monotonic data approximations against measurement differences. Both performance metrics sets can give benchmark results to the aforementioned two issues. In [4], both sets have been applied and have assessed the SE impact of measurement differences. On the basis of the results of [4], these sets are here adopted in order to assess the mitigation efficiency of measurement differences by three piecewise monotonic data approximations. The first set of performance metrics, which is denoted as Set A, concerns the influence of the measurement differences on the general properties of the SE results while the second set, which is denoted as Set B, assesses the SE impact intensity of measurement differences. More specifically:

- *Set A*: With reference to eqs. (2) and (3), it is assumed that the measured and theoretical SE for given coupling scheme channel *C* are already known. Set A consists of the metrics of: (i) average value of SE; (ii) maximum value of SE; and (iii) minimum value of SE. Since measured SE is infected by unbiased measurement differences, it is expected that average, maximum and minimum values remain almost the same with the respective metrics of the theoretical SE. This has already been verified in [4]. Hence, the metrics of set A are unable to identify the existence and the intensity of measurement differences although even small divergences of the three metrics indicate the existence of measurement differences. If measurement differences occur and piecewise monotonic data approximations are applied in order to mitigate these measurement differences, the set A metrics of the approximated SE of eq. (4) should remain almost the same with the respective metrics of the theoretical SE. Therefore, the set A metrics act as an integrity metric for the countermeasures techniques of [4].
- *Set B*: Set B consists of two metrics, say: (i) MAE; and (ii) RMSD. With reference to [4] and in contrast with the metrics of Set A, the metrics of Set B can not only detect the existence but also to assess the intensity of the

measurement differences. In fact, the values of the Set B metrics increase with the increase of the measurement difference a_{CUD}. Anyway, the set B metrics constitute comparison metrics between measured and theoretical SE. If measurement differences occur and piecewise monotonic data approximations are applied in order to mitigate these measurement differences, the set B metrics of the approximated SE of eq. (4) should give closer values to the theoretical ones in comparison with the respective metrics of the measured SE.

4. Numerical Results and Discussion

Various topologies of OV MV BPL networks, which have been presented in Sec.2.2 of [4] and are also common in [36], [37], are here simulated with the purpose of comparatively benchmarking the SE mitigation efficiency of L1PMA, L2WPMA and L2CXCV against measurement differences added during the transfer function determination.

As the propagation and transmission specifications are regarded, those are the same with [33]-[37]. Arbitrarily, the WtG[1] coupling scheme is applied during the following simulations. As it is usually done [5], [11], [13], [44], the selection of representative coupling schemes is a typical procedure for the sake of reducing manuscript size.

As the spectral exploitation properties are concerned, injected power spectral density limits (IPSD limits) of Ofcom are adopted [4]-[13], [45]-[51], while a uniform AWGN PSD levels $N(f)$ will be assumed equal to -105 dBm/Hz in the case of OV MV BPL networks. In order to compute SE of OV MV BPL topologies, the BPL frequency range and flat-fading subchannel frequency spacing are first assumed equal to 3-30MHz and 0.1MHz, respectively, so that the required SE accuracy can be preserved. However, in order to apply the piecewise monotonic data approximations, the flat-fading subchannel frequency spacing is assumed equal to 0.1MHz. The latter specification has been made so that: (i) the results of SE can clearly be presented in the following figure; and (ii) the results concerning the selection of monotonic sections can be comparable with the respective results of [36], [37] that deal with the application behavior of piecewise monotonic data approximations in channel attenuation results. For the latter case, note that the BPL frequency range and flat-fading subchannel frequency spacing are assumed equal to 1-30MHz and 1MHz, respectively, in [36], [37].

Finally, as the nature of measurement differences and the mitigation of measurement differences are concerned, unbiased measurement differences are assumed, which affect the measurements of channel attenuation –see eqs. (1) and (2)– and [4]. Measurement differences follow continuous uniform distributions (CUDs) with minimum value $-a_{\mathrm{CUD}}$ and maximum value a_{CUD}. The piecewise monotonic data approximations are applied when the measured SE of eq. (1) are known for given maximum value a_{CUD} and the approximation results of piecewise monotonic data approximations are directly compared against the theoretical SE of eq. (2). Afterwards, the aforementioned difference is compared against the difference between the measured and the theoretical SE. The mitigation efficiency of piecewise monotonic data approximations depends on the relation between the aforementioned two differences.

4.1 SE ΔPES of L1PMA, L2WPMA and L2CXCV against Measurement Differences

By simply maintaining the monotonicity pattern, piecewise monotonic data approximations achieve to mitigate the additive measurement differences so that approximations that resemble the theoretical data can be made [36]. To examine the impact of measurement differences on the SE of OV MV BPL topologies and the potential of counterbalancing the measurement differences, in Figs. 1(a)-(d), the theoretical and the measured SE are plotted versus frequency for the four indicative OV MV BPL topologies, respectively. Note that the measured SE corresponds to measurement difference CUD of α_{CUD}=5dB. Also, in each figure, apart from the theoretical and measured SE curves, three L1PMA SE approximation curves are also presented when the number of monotonic sections is assumed to be equal to 2, 5 and 20. In Figs. 2(a)-(d) and 3(a)-(d), same plots are given with Figs. 1(a)-(d) but for the application of L2WPMA and L2CXCV, respectively.

Comparing Figs. 1-3 and Figs. 2-4 of [36], certain similarities and differences between SE and channel attenuation approximations can be pointed out:

- In [36], piecewise monotonic data approximations have mitigated the measurement differences that had been added to the measured channel attenuation while, in this paper, piecewise monotonic data approximations try to mitigate the measured SE whose calculations are based on the measured channel attenuation. Hence, piecewise monotonic data approximations have directly mitigated the measurement differences in [36] while they indirectly mitigate measurement differences in this paper.
- Although piecewise monotonic data approximations indirectly mitigate the measurement differences in this paper, L1PMA, L2WPMA and L2CXCV can satisfactorily retrieve the theoretical SE properties of the indicative OV MV BPL topologies.
- The performance of piecewise monotonic data approximations strongly depends on the examined OV MV BPL topology, the maximum value α_{CUD} of the applied measurement difference CUD and the number of monotonic sections.
- As the mitigation performance of piecewise monotonic data approximations is examined with relation to the OV MV BPL topology, the presence of many short branches along the end-to-end transmission path entails a rich multipath environment. As already been mentioned in [33], [36], the spectral notches (extrema) that appear in the rich multipath environments (*i.e.*, urban case) require additional monotonic sections so that the SE approximation may be accurate. Thanks to their adjustable number of monotonic sections, L1PMA and L2WMPA can be adaptive in order to improve their approximation efficiency by focusing on the improvement of SE ΔPES. Conversely, when OV MV BPL topologies of low number and long branches are examined (*i.e.*, "LOS", rural and suburban case), L1PMA and L2WPMA need low number of monotonic sections so that high SE ΔPES can be achieved. Also, L2CXCV, which does not take as input monotonic sections, can provide very good approximations of SE curves for specific OV MV BPL topologies.

To more elaborately examine the SE approximation by applying piecewise monotonic approximations, the relation among SE approximation accuracy, the maximum value α_{CUD}, the applied piecewise monotonic data approximation and the number of monotonic

sections should be investigated. As already been mentioned in Sec.3.1, SE ΔPES acts as the main metric that assesses the mitigation efficiency of the piecewise monotonic data

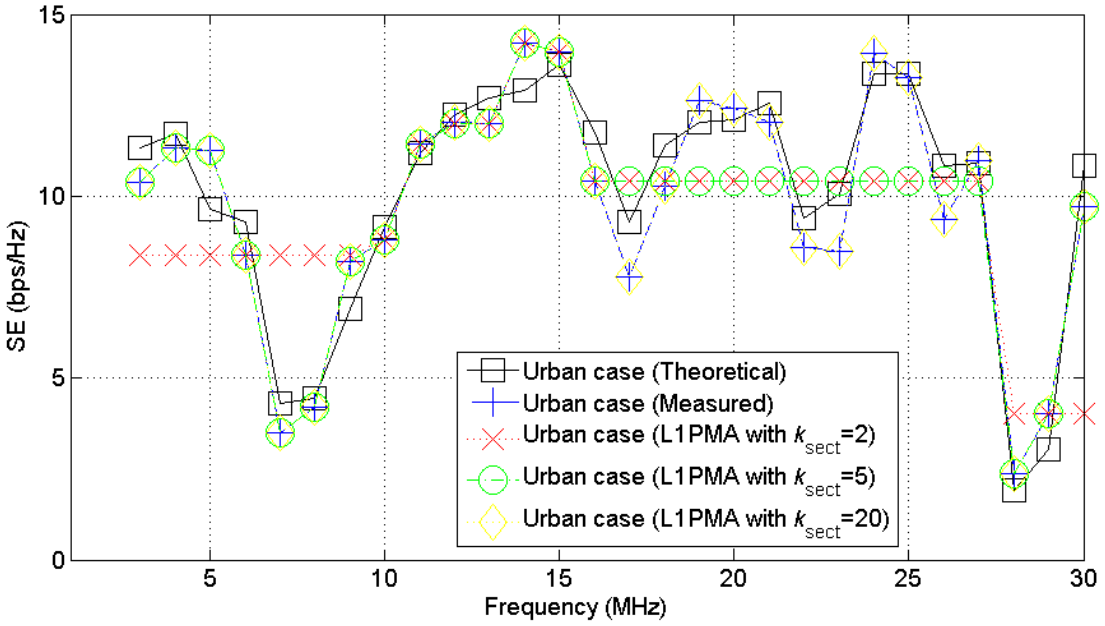

(a)

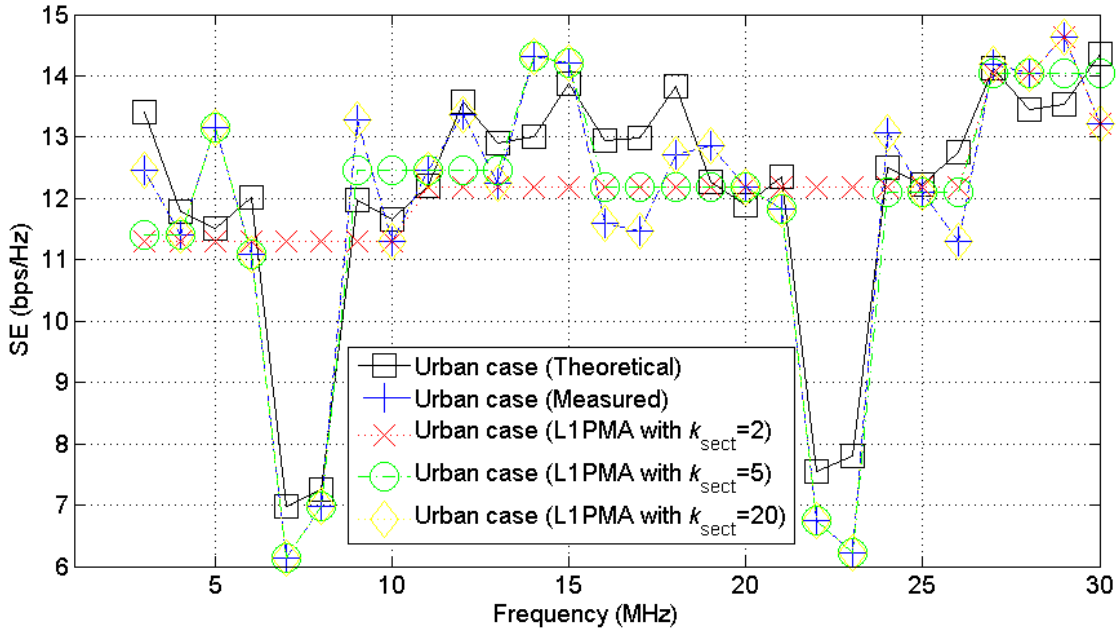

(b)

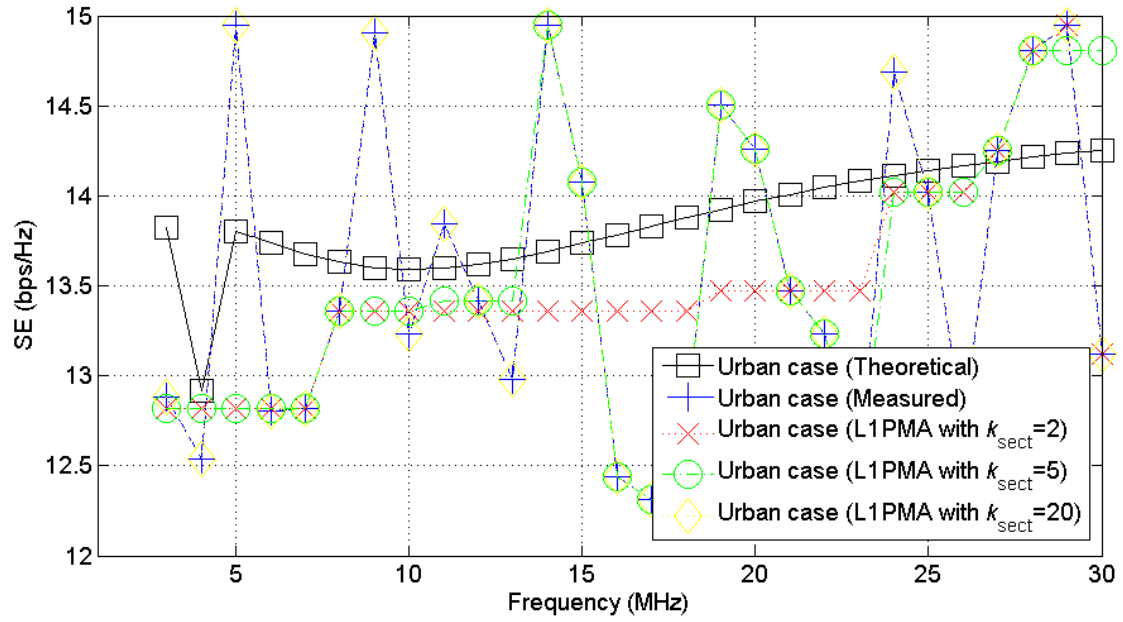

(c)

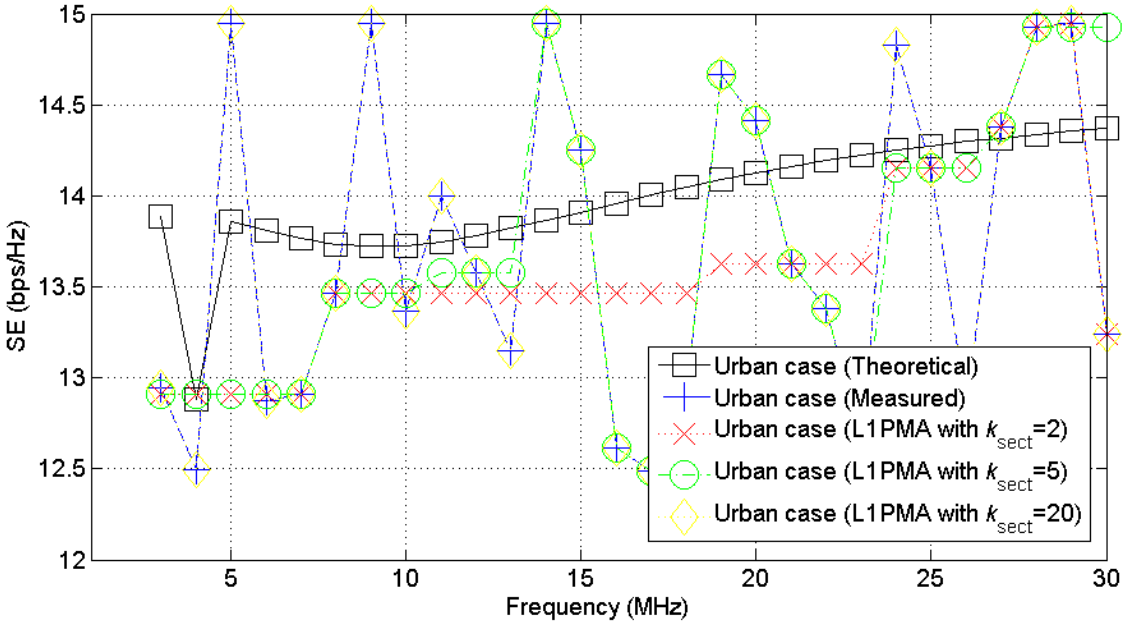

(d)

Fig. 1. Theoretical, measured and approximated SE of indicative OV MV BPL topologies when L1PMA is applied, measurement difference CUD of α_{CUD}=5dB is assumed. Three representative cases of monotonic sections (i.e, k=1, 2 and 20) are assumed for the SE approximation. (a) Urban case. (b) Suburban case. (c) Rural case. (d) "LOS" case.

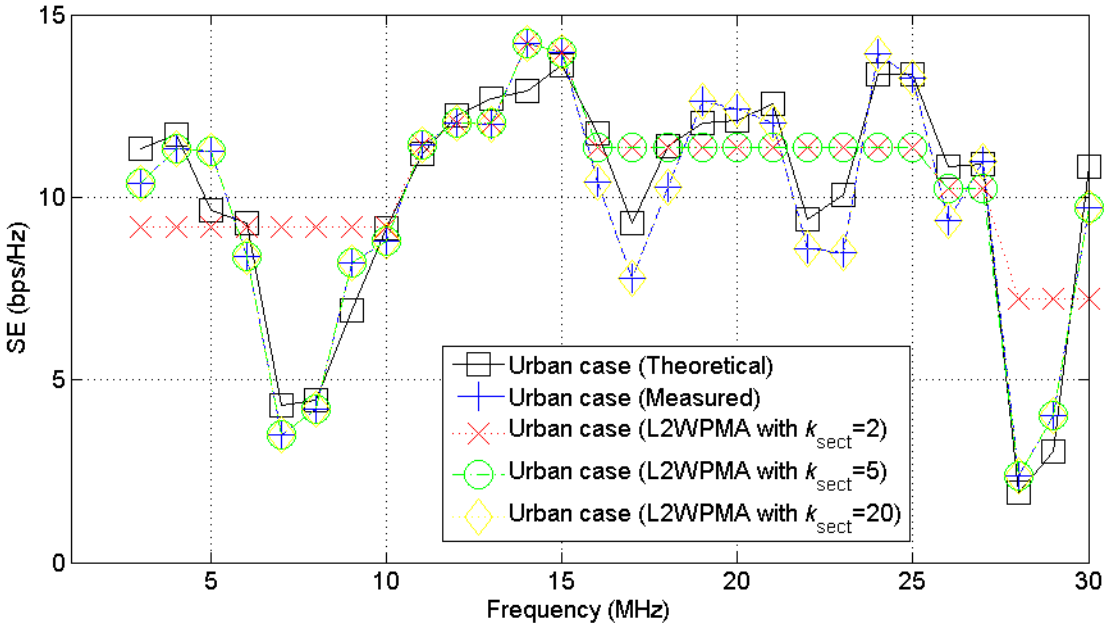
SE (bps/Hz)
Frequency (MHz)
Urban case (Theoretical)
Urban case (Measured)
Urban case (L2WPMA with k_{sect}=2)
Urban case (L2WPMA with k_{sect}=5)
Urban case (L2WPMA with k_{sect}=20)

(a)

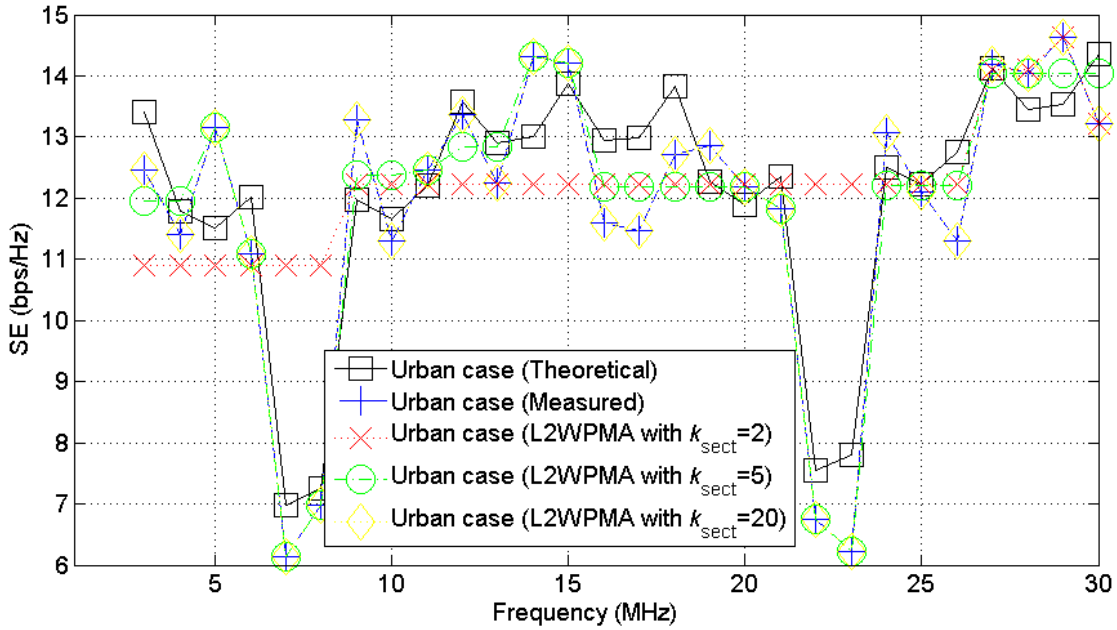
SE (bps/Hz)
Frequency (MHz)
Urban case (Theoretical)
Urban case (Measured)
Urban case (L2WPMA with k_{sect}=2)
Urban case (L2WPMA with k_{sect}=5)
Urban case (L2WPMA with k_{sect}=20)

(b)

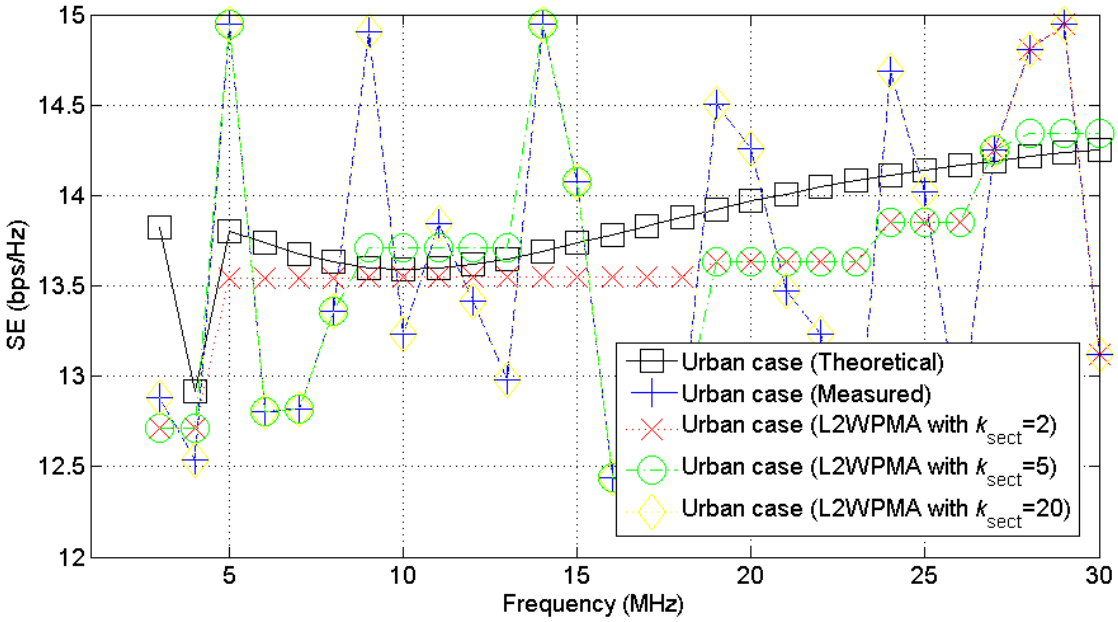

(c)

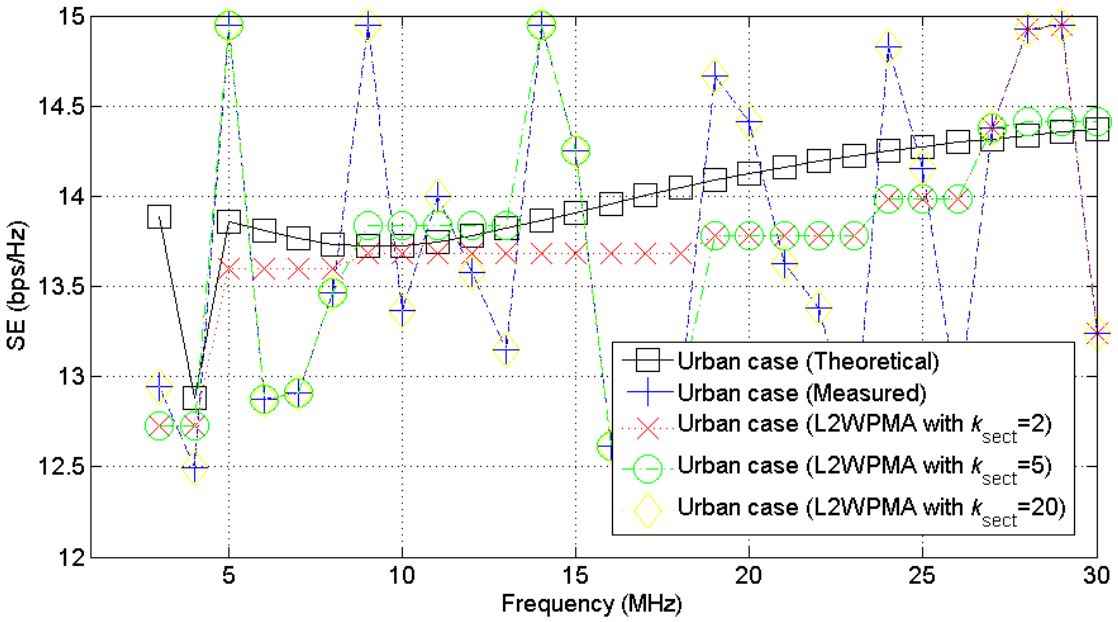

(d)

Fig. 2. Same curves with Fig.1 but for L2WPMA.

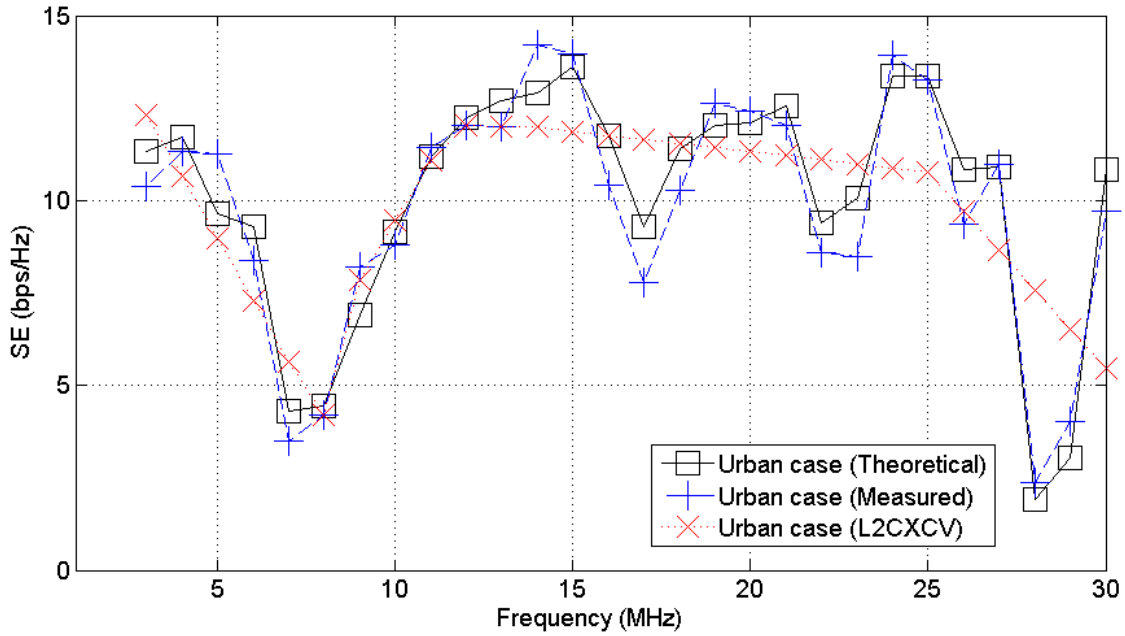
SE (bps/Hz)
Frequency (MHz)
Urban case (Theoretical)
Urban case (Measured)
Urban case (L2CXCV)

(a)

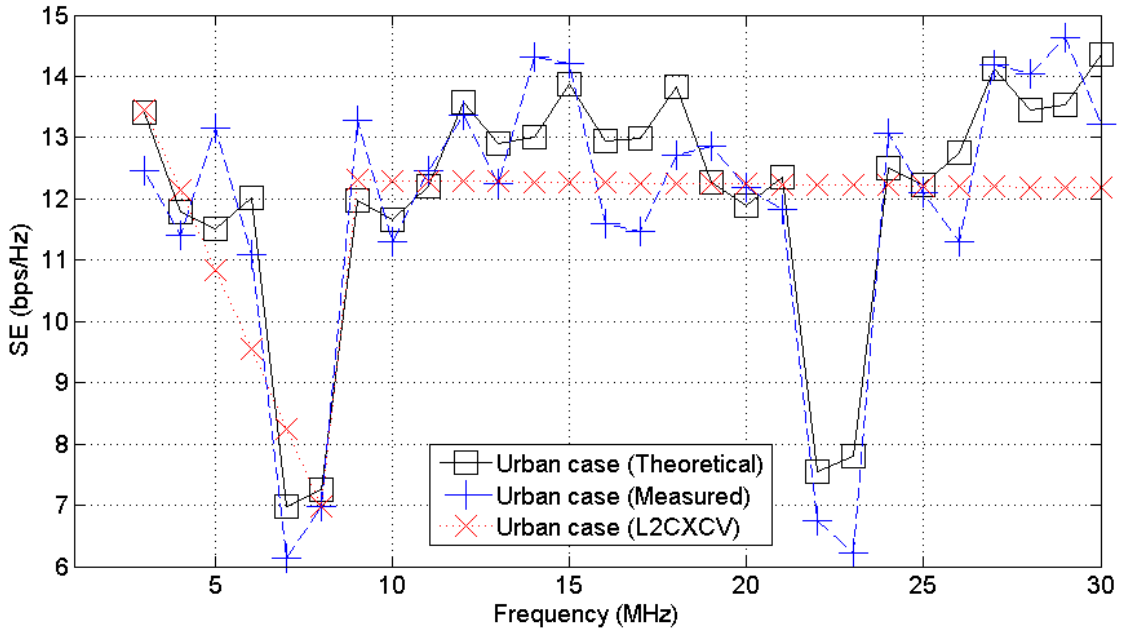
SE (bps/Hz)
Frequency (MHz)
Urban case (Theoretical)
Urban case (Measured)
Urban case (L2CXCV)

(b)

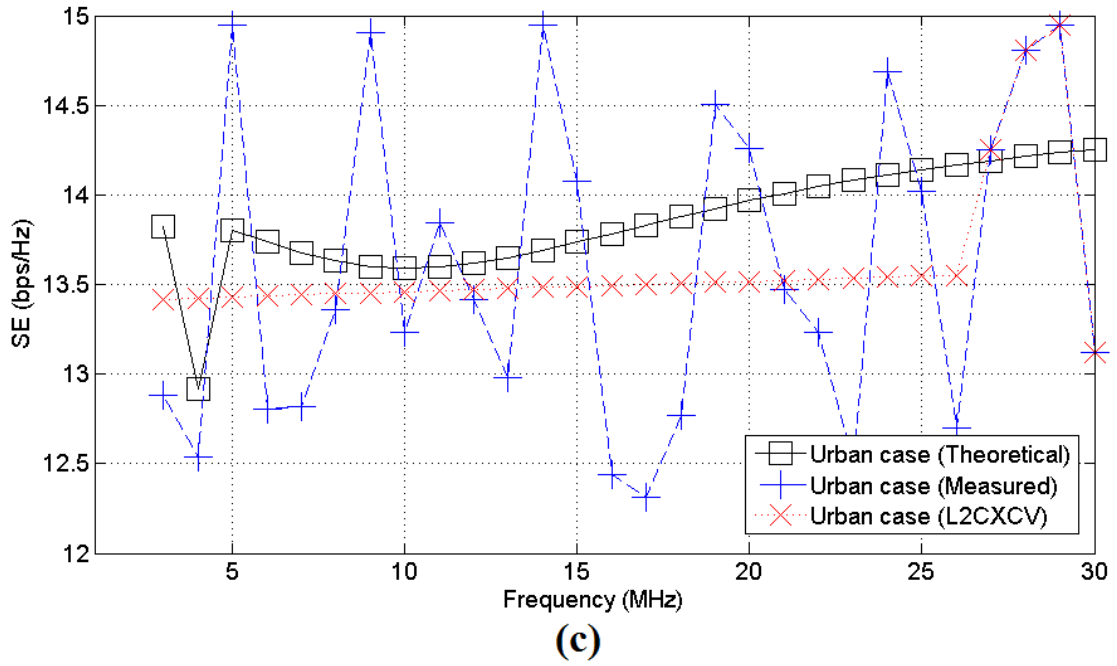

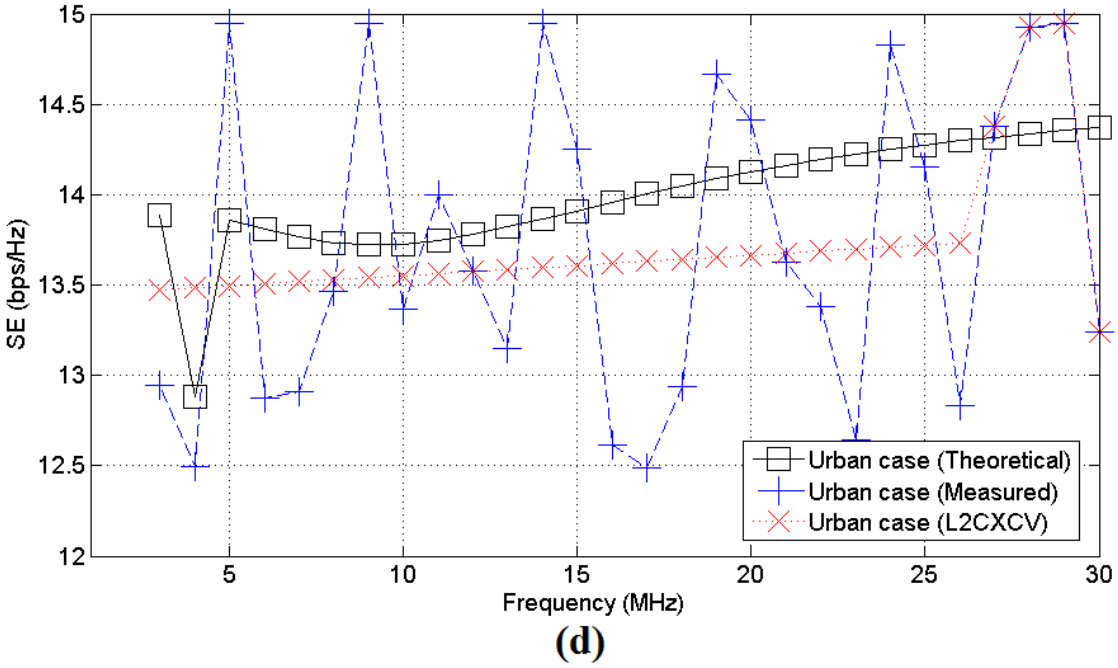

Fig. 3. Same curves with Fig.1 but for L2CXCV.

approximations. For the Figs. 1-3, the SE ΔPES curves of the applied piecewise monotonic data approximations are given in Figs. 4-6, respectively, when various measurement difference CUDs and number of monotonic sections are considered. In fact, maximum value α_{CUD} that ranges from 0 to 5dB is assumed. On the basis of Figs. 4-6, the maximum SE ΔPES and the corresponding number of monotonic sections are reported in Tables 1-3 when L1PMA, L2WPMA and L2CXCV are applied, respectively.

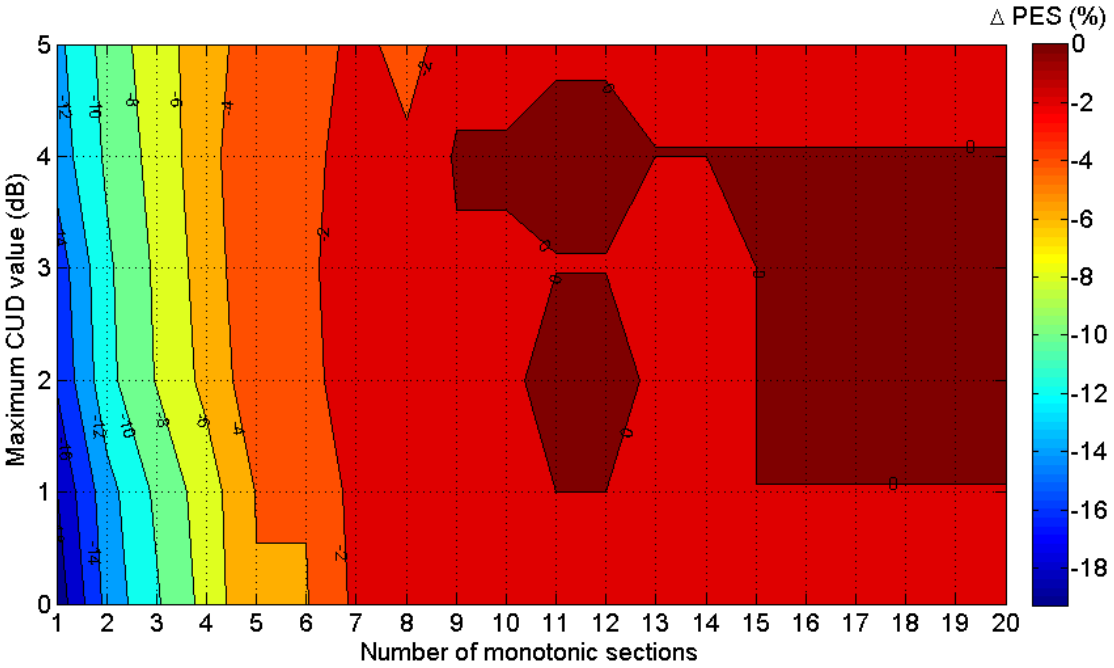
△ PES (%)
Maximum CUD value (dB)
Number of monotonic sections

(a)

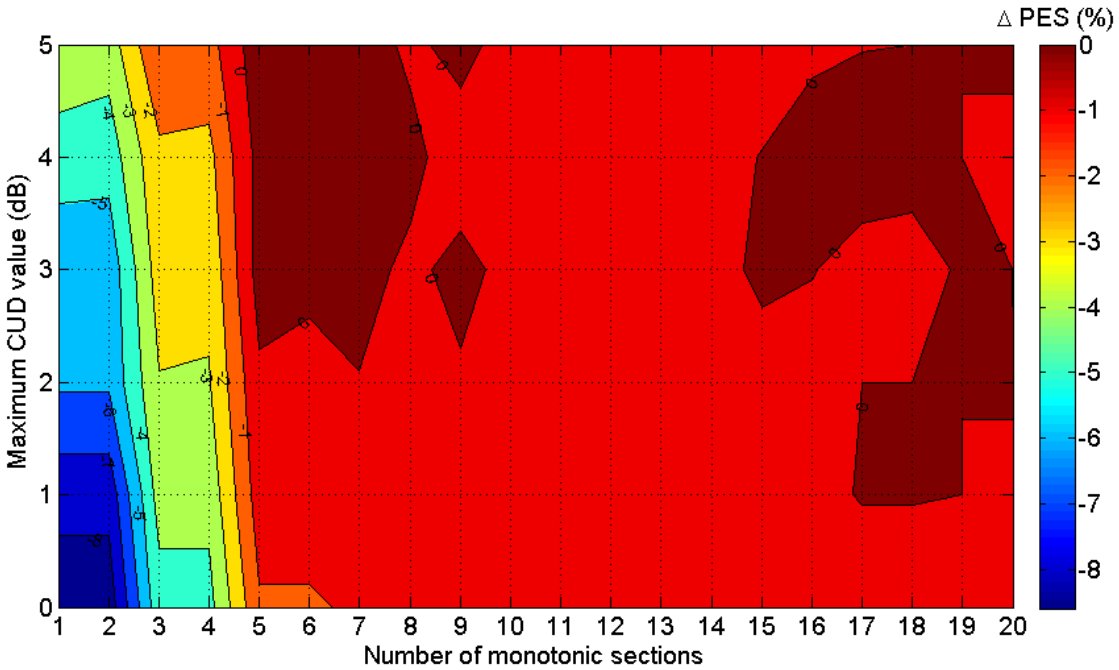
△ PES (%)
Maximum CUD value (dB)
Number of monotonic sections

(b)

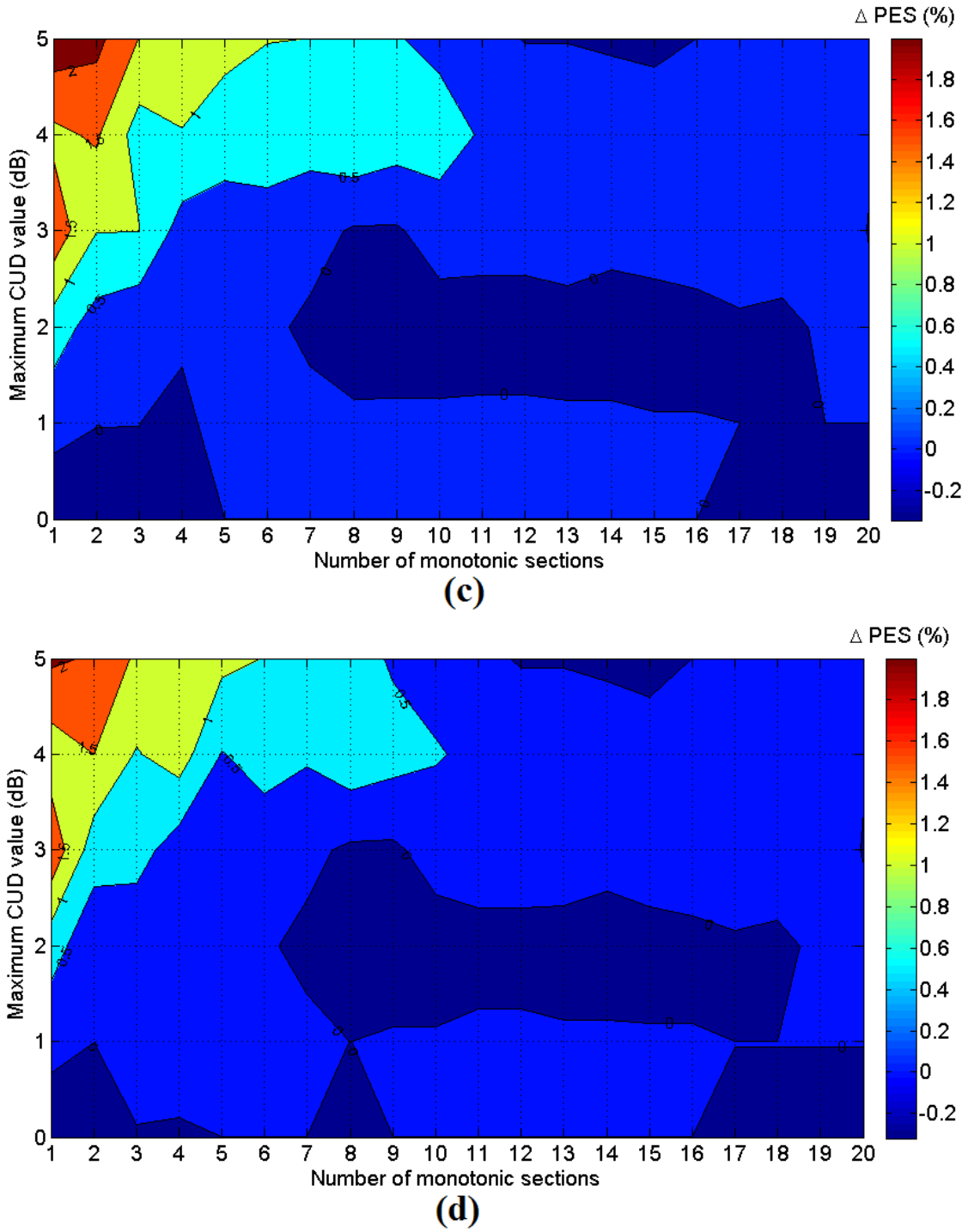

Fig. 4. SE ΔPES of indicative OV MV BPL topologies when L1PMA is applied and measurement difference CUD of αCUD=5dB is assumed. Three representative cases of monotonic sections (i.e, k=1, 2 and 20) are assumed for the SE approximation –see also Figs. 1(a)-(d)–. (a) Urban case. (b) Suburban case. (c) Rural case. (d) "LOS" case.

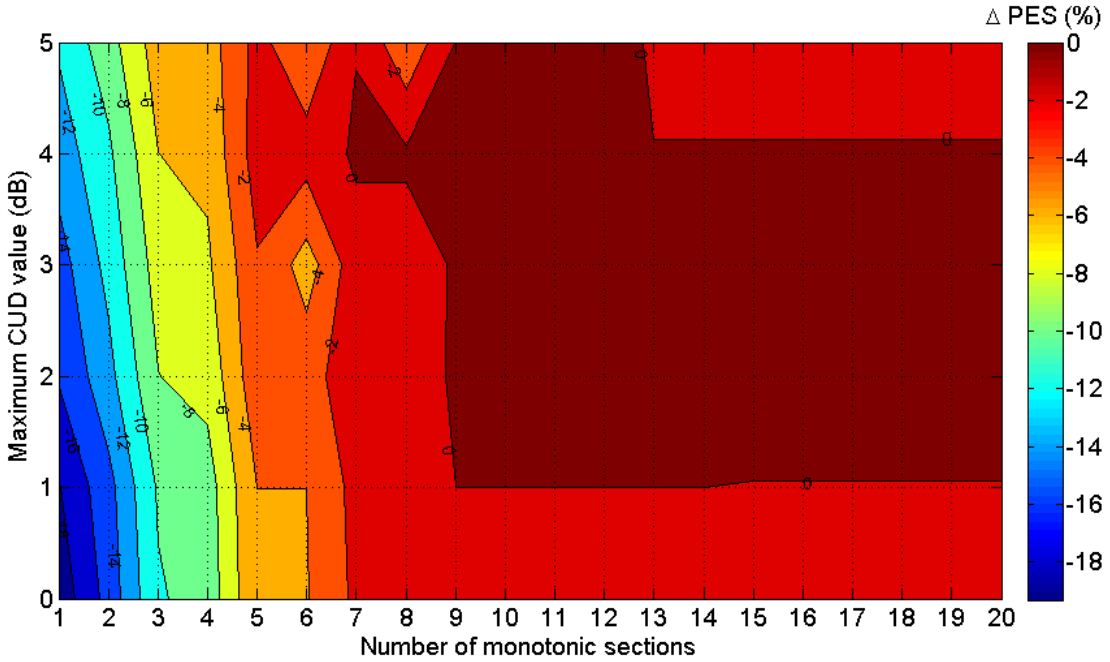
△ PES (%)
Maximum CUD value (dB)
Number of monotonic sections

(a)

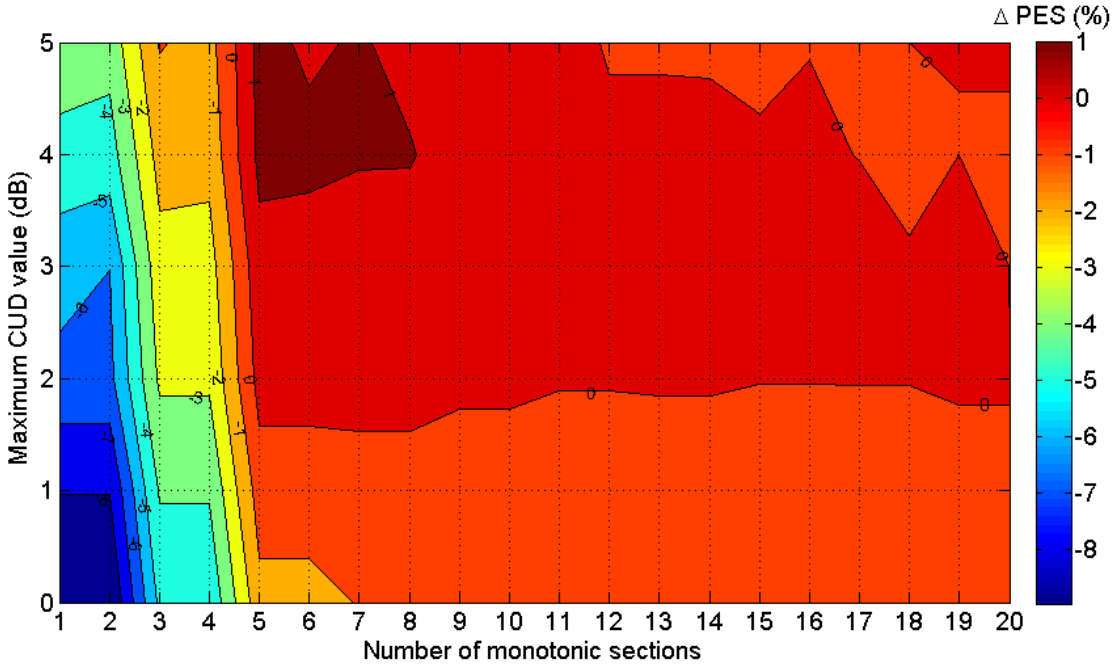
△ PES (%)
Maximum CUD value (dB)
Number of monotonic sections

(b)

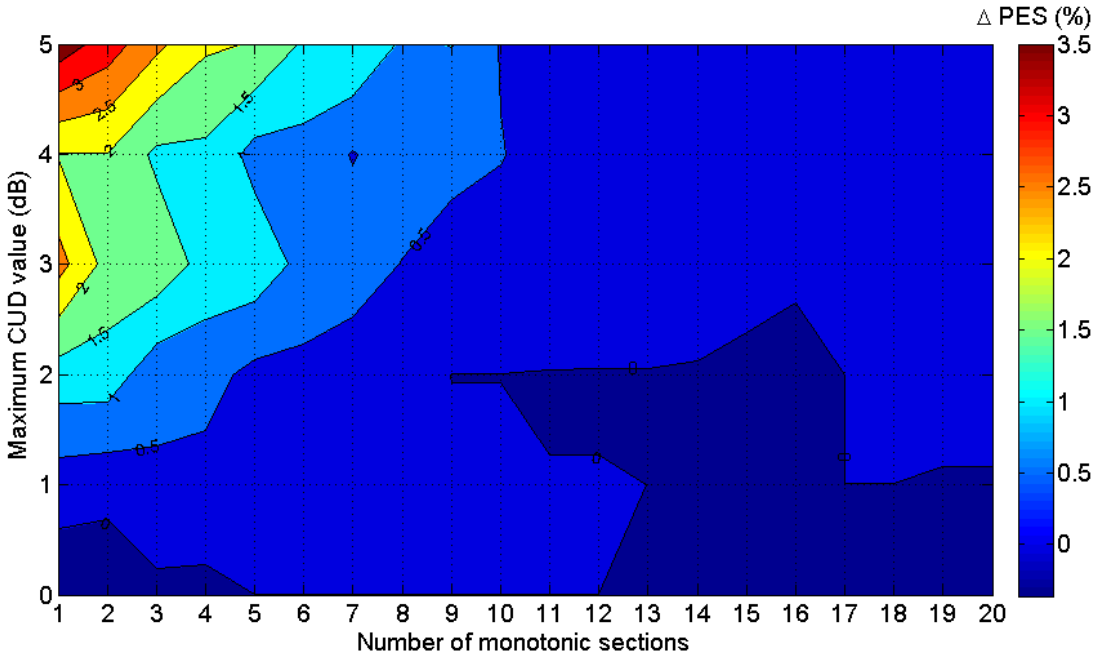

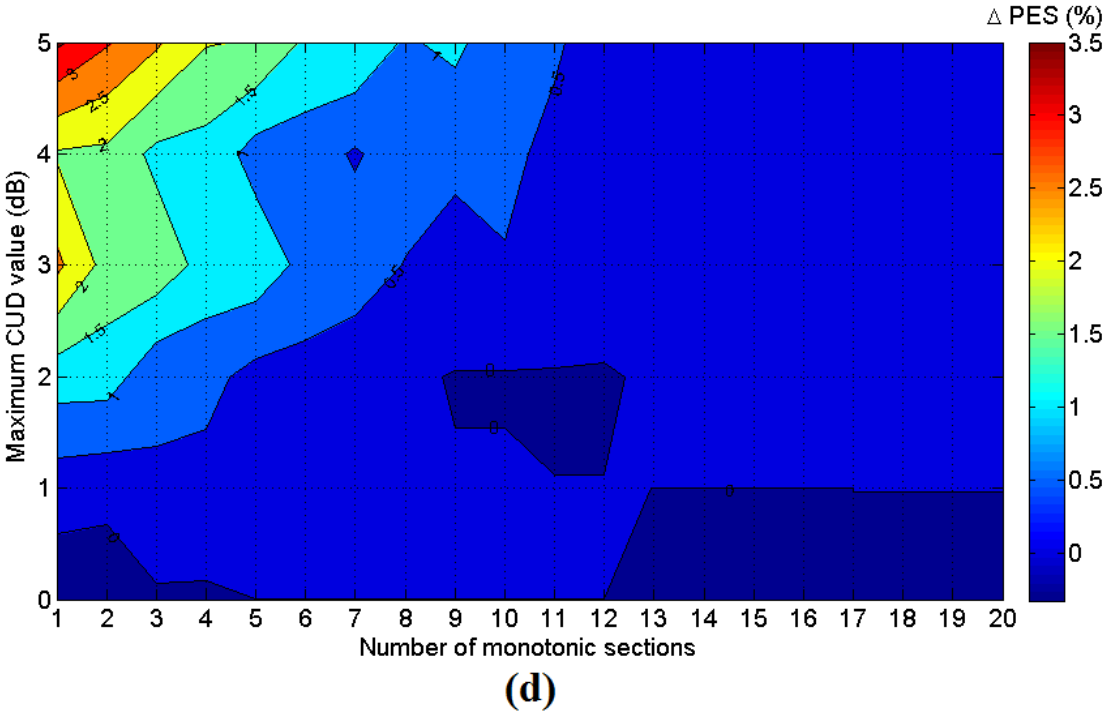

Fig. 5. Same curves with Fig.4 but for L2WPMA –see also Figs. 2(a)-(d)–.

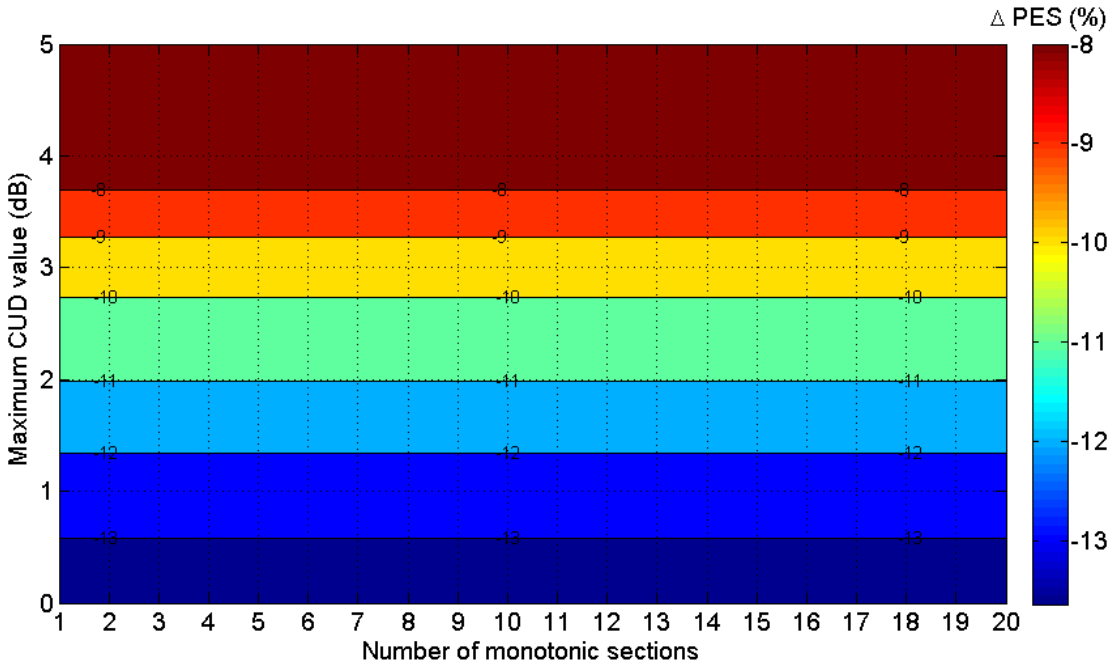
△ PES (%)
Maximum CUD value (dB)
Number of monotonic sections
-8
-9
-10
-11
-12
-13

(a)

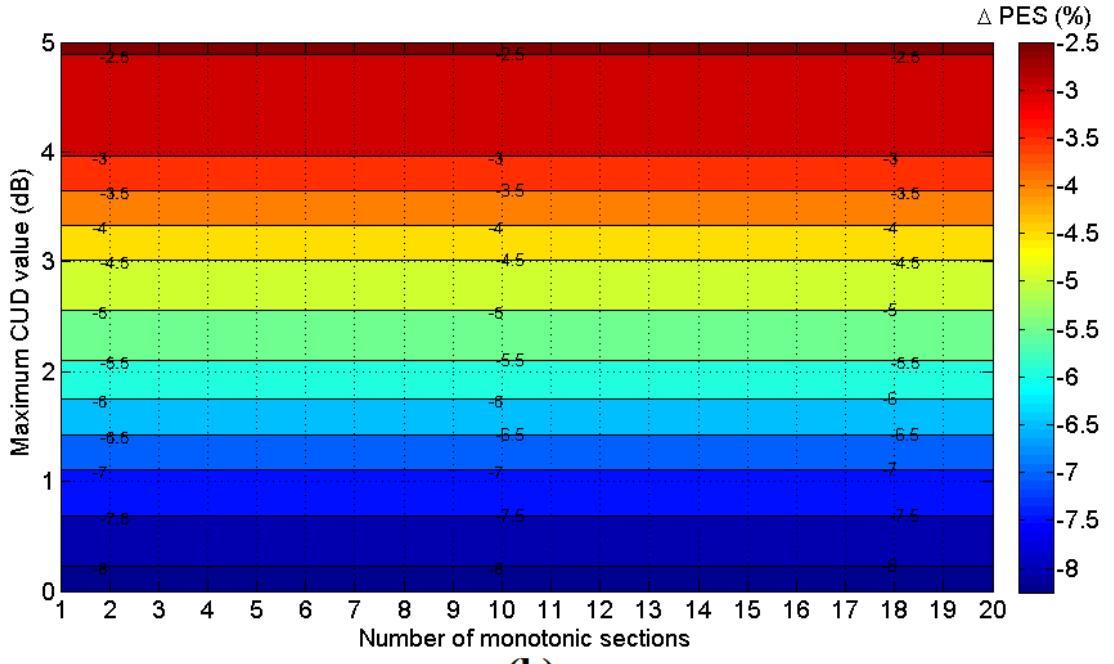
△ PES (%)
Maximum CUD value (dB)
Number of monotonic sections
-2.5
-3
-3.5
-4
-4.5
-5
-5.5
-6
-6.5
-7
-7.5
-8

(b)

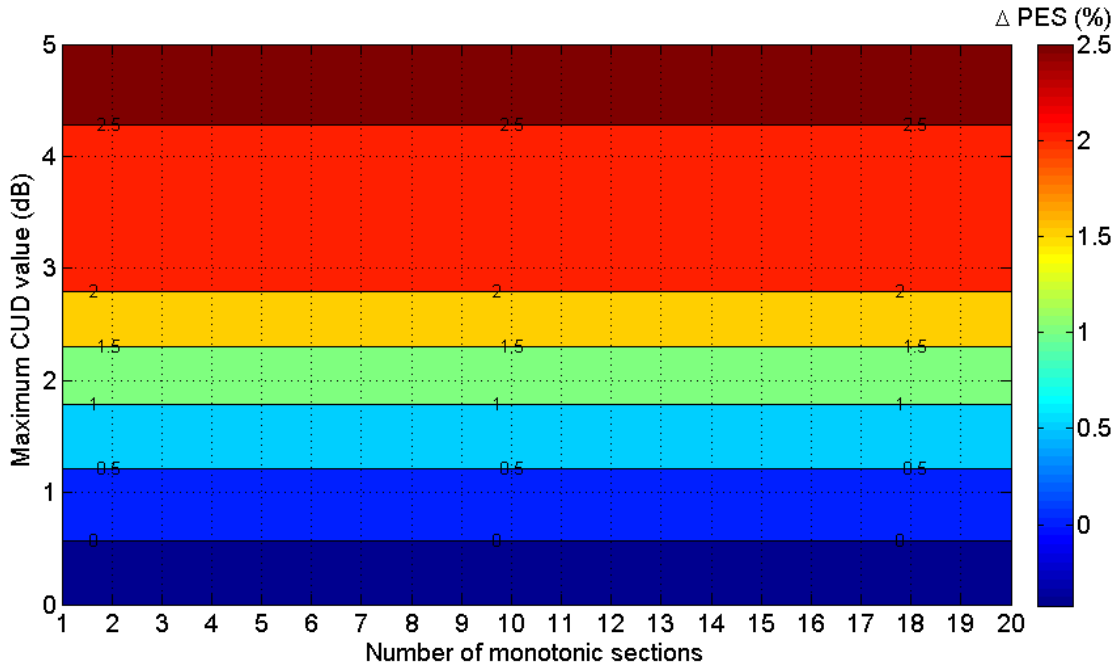

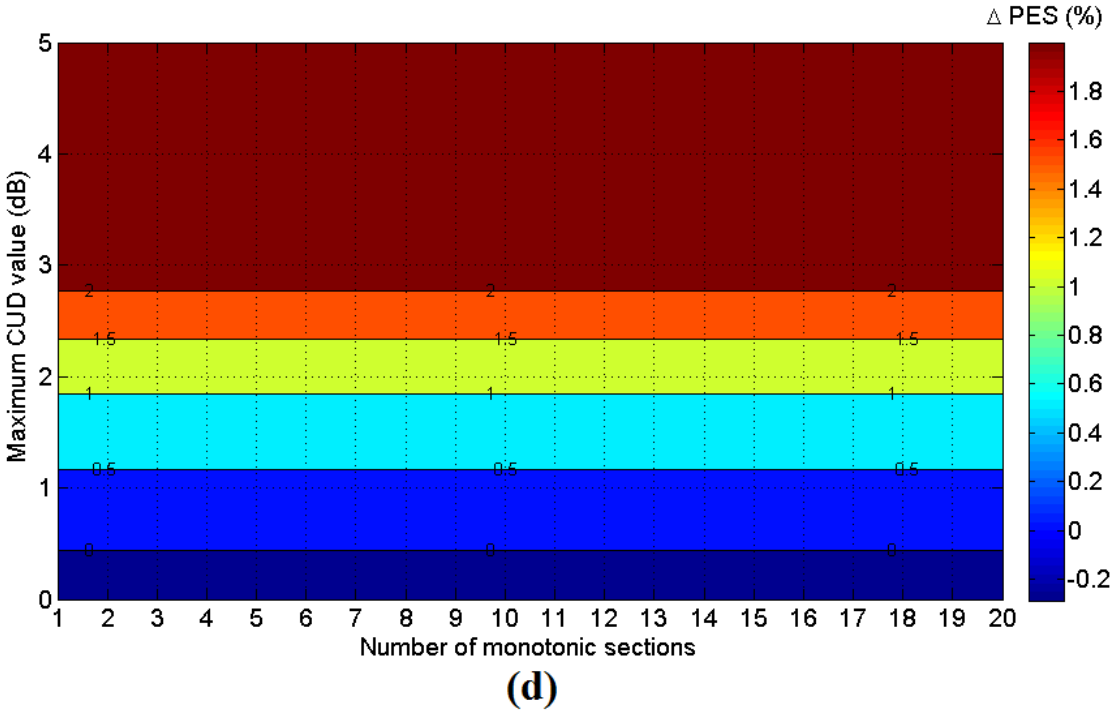

Fig. 6. Same curves with Fig.4 but for L2CXCV –see also Figs. 3(a)-(d)–.

Table 1. Maximum ΔPES and Corresponding Number of Monotonic Sections when L1PMA is Applied

Maximum Value α_{CUD} (dB)	Indicative OV MV BPL Topologies							
	Urban Case A		Suburban Case		Rural Case		"LOS" Case	
	SE ΔPES (%)	Number of Monotonic Sections	SE ΔPES (%)	Number of Monotonic Sections	SE ΔPES (%)	Number of Monotonic Sections	SE ΔPES (%)	Number of Monotonic Sections
0	-1.92×10^{-5}	11	-2.09×10^{-5}	19	-1.71×10^{-5}	5	-1.72×10^{-5}	5
1	-5.27×10^{-7}	9	7.7×10^{-3}	17	0.23	5	0.41	3
2	0.09	11	1.47×10^{-6}	17	0.76	1	0.71	1
3	3.18×10^{-6}	15	0.45	5	1.85	1	1.89	1
4	0.17	9	0.34	5	1.58	2	1.50	2
5	-4.97×10^{-6}	13	0.68	5	2.33	1	2.09	1

Table 2. Maximum ΔPES and Corresponding Number of Monotonic Sections when L2WPMA is Applied

Maximum Value α_{CUD} (dB)	Indicative OV MV BPL Topologies							
	Urban Case A		Suburban Case		Rural Case		"LOS" Case	
	SE ΔPES (%)	Number of Monotonic Sections	SE ΔPES (%)	Number of Monotonic Sections	SE ΔPES (%)	Number of Monotonic Sections	SE ΔPES (%)	Number of Monotonic Sections
0	-1.86×10^{-5}	11	-2.15×10^{-5}	19	-1.72×10^{-5}	5	-1.71×10^{-5}	5
1	-4.30×10^{-7}	9	-3.07×10^{-6}	19	0.41	3	0.42	3
2	0.23	9	0.41	7	1.28	1	1.24	1
3	0.14	9	0.67	5	2.69	1	2.62	1
4	0.71	9	1.23	5	1.98	2	1.95	1
5	0.09	9	1.27	5	3.81	1	3.59	1

Table 3. Maximum ΔPES and Corresponding Number of Monotonic Sections when L2CXCV is Applied

Maximum Value α_{CUD} (dB)	Indicative OV MV BPL Topologies							
	Urban Case A		Suburban Case		Rural Case		"LOS" Case	
	SE ΔPES (%)	Number of Monotonic Sections	SE ΔPES (%)	Number of Monotonic Sections	SE ΔPES (%)	Number of Monotonic Sections	SE ΔPES (%)	Number of Monotonic Sections
0	-13.64	-	-8.25	-	-0.42	-	-0.29	-
1	-15.53	-	-7.16	-	0.3185	-	0.38	-
2	-10.98	-	-5.61	-	1.18	-	1.11	-
3	-9.65	-	-4.52	-	2.22	-	2.27	-
4	-7.26	-	-2.93	-	2.42	-	2.19	-
5	-7.15	-	-2.44	-	2.70	-	2.47	-

From Figs. 4-6 and Tables 1-3, certain remarks can be reported that characterize the application behavior of piecewise monotonic data approximations for the various OV MV BPL topologies. More specifically:

- When urban OV MV BPL topologies are examined, piecewise monotonic data approximations cannot satisfactorily mitigate the added measurement differences. Actually, when the assumed maximum value α_{CUD} remains low (*i.e.*, below 2dB), all the applied piecewise monotonic data approximations of this paper cannot provide a clearly better SE approximation than the measured SE since SE ΔPES remains marginally lower than zero in these cases. In contrast, when the assumed maximum value α_{CUD} becomes high (*i.e.*, above 2dB), L2WPMA provides SE approximations that are better than measured SE (*i.e.*, SE ΔPES higher than

zero). These L2WPMA SE approximations are marginally better than the measured SE while these SE approximations of urban OV MV BPL topologies are achieved by using higher numbers of monotonic sections.

- Suburban OV MV BPL topologies present a similar SE ΔPES behavior with urban ones. L1PMA and L2WPMA offer a marginally improved SE ΔPES behavior when high maximum values α_{CUD} are observed. Although the SE approximation improvement still remains marginal in the majority of the examined cases (*i.e.*, below 1%), a relatively high number of monotonic sections, but smaller than the number of monotonic sections used in urban OV MV BPL topologies, is required. Either urban or suburban OV MV BPL topologies are examined, L2CXCV fail in all the cases to mitigate the measurement differences. Anyway, this behavior of L2CXCV in urban and suburban OV MV BPL topologies has also been verified when L2CXCV achieves to directly mitigate the measurement differences in channel attenuations curves (see Tables 2 and 3 of [36]).
- On the basis of the achieved SE ΔPES, all the applied piecewise monotonic data approximations provide significant improvement concerning the mitigation of measurement differences when SE is examined. The SE ΔPES improvement can reach up to 3.59% when severe measurement differences (*i.e.*, maximum values α_{CUD} of 5dB) are observed. Since rural and "LOS" OV MV BPL topologies present low and rare spectral notches, simple approximations, which ignore the frequent notches imposed by the measurement differences, can achieve high SE ΔPES. Therefore, due to this poor multipath environment of rural and "LOS" OV MV BPL topologies, L1PMA and L2WPMA require low number of monotonic sections to achieve these rather simple approximations. Since the simple approximations are the more suitable for the rural and "LOS" OV MV BPL topologies, L2CXCV also achieves high ΔPES in these cases.
- Although different CUDs are assumed between this paper and [36] and the nature of the measurement difference mitigation differs (*i.e.*, direct or indirect measurement difference mitigation), the results concerning the assessment of piecewise monotonic data approximations remain approximately the same:
    - The main contribution of piecewise monotonic data approximations against measurement differences is focused on rural and "LOS" OV MV BPL topologies when high maximum values α_{CUD} are considered. In these cases, L2WPMA and L2CXCV can offer SE ΔPES that reaches up to 3.81%.
    - Comparing Tables 1-3 of this paper with the Tables 2-5 of [36], small differences between the relative ranking of L2WPMA and L2CXCV are due to: (i) the different CUDs that are applied in these two papers; and (ii) the nature of the measurement difference mitigation.
    - With reference to the SE ΔPES, the best SE approximation for given OV MV BPL topology and maximum value α_{CUD}=5dB is highlighted with blue color in Table 2 (*i.e.*, blue L2WPMA SE approximations).

Apart from SE ΔPES, to evaluate the quality of the approximations, the metrics of the set A and B of the SE approximations should tend to the respective metrics of the theoretical SE. In the following subsection, the blue L2WPMA SE approximations will

be benchmarked against the respective theoretical SE and measured SE with reference to the metrics of set A and B.

4.2 Case Study – Piecewise Monotonic Data Approximations and Metrics of Set A and B

Apart from the improvement of SE ΔPES, which remains the basic metric of approximation evaluation, the metrics of set A and B of SE piecewise monotonic data approximations should comply with the respective metrics of the theoretical SE so that the approximation can be considered as successful for various computations. In the case study of this subsection, the metrics of the blue L2WPMA SE approximations of Sec.4.1 will be compared against the respective ones of the theoretical and measured SE. More specifically:

- *Set A*: The metrics of Set A are: (i) the average value of SE; (ii) the maximum value of SE; and (iii) the minimum value of SE. In Table 4, the metrics of Set A are reported for the theoretical SE, measured SE and the blue L2WPMA SE approximations for the indicative OV MV BPL topologies of this paper when the maximum value α_{CUD} is assumed equal to 5dB.
- *Set B*: The metrics of Set B are: (i) MAE; and (ii) RMSD. In Table 5, the metrics of Set B are reported for the theoretical SE, measured SE and the blue L2WPMA SE approximations for the indicative OV MV BPL topologies of this paper when the maximum value α_{CUD} is assumed equal to 5dB.

From Tables 4 and 5, piecewise monotonic data approximations not only improve the SE subchannel estimation but also improve the macroscopic SE estimation that is described by the metrics of Set A and Set B. More specifically:

- As blue L2WPMA SE approximation is assumed, its average values of SE remains greater or equal to the respective values of measured SE in all the indicative OV MV BPL topologies that are examined. In fact, the average values of SE of the blue L2WPMA SE approximation are closer to the respective values of the theoretical SE in comparison with the respective values of SE. This is valid even if high intensity of measurement differences is considered (*i.e.*, the maximum value α_{CUD} is assumed equal to 5dB). Same observations can also be made in the cases of the maximum and minimum value of SE.
- MAE and RMSD describe the deviation among the approximated, measured and theoretical SE data. Hence, the metrics of set B again validate the mitigation success of the blue L2WPMA SE approximation against measurement differences. In all the cases examined, blue L2WPMA SE approximation achieved MAE and RMSD with values lower or equal than the respective values of the measured SE. Also, the values of MAE and RMSD of the blue L2WPMA SE approximation tend to the zero values of the theoretical SE.
- Already been mentioned in [4], the metrics of set A cannot identify the intensity of measurement differences since the differences remain marginal. In contrast, the metrics of set B, which behave similar to PES, depend on the existence and the intensity of the measurement differences.

Table 4. Metrics of Set A for the Theoretical SE, Measured SE and blue L2WPMA SE approximations.

Indicative OV MV BPL Topology	Metrics of Set A								
	Average Value of SE (bps/Hz)			Maximum Value of SE (bps/Hz)			Minimum Value of SE (bps/Hz)		
	Theoretical SE	Measured SE (α_{CUD}=5)	Blue L2WPMA SE Approximation	Theoretical SE	Measured SE (α_{CUD}=5)	Blue L2WPMA SE Approximation	Theoretical SE	Measured SE (α_{CUD}=5)	Blue L2WPMA SE Approximation
Urban Case A	10.08	9.86	9.86	13.60	14.22	14.22	1.91	2.36	2.36
Suburban Case	12.03	11.81	11.83	14.35	14.63	14.31	6.98	6.13	6.13
Rural Case	13.85	13.60	13.65	14.25	14.95	14.34	12.92	12.32	12.71
"LOS" Case	13.98	13.71	13.76	14.37	14.95	14.42	12.88	12.49	12.72

Table 5. Metrics of Set B for the Theoretical SE, Measured SE and blue L2WPMA SE approximations.

Indicative OV MV BPL Topology	Metrics of Set B					
	MAE (bps/Hz)			RMSD (bps/Hz)		
	Theoretical SE	Measured SE (α_{CUD}=5)	Blue L2WPMA SE Approximation	Theoretical SE	Measured SE (α_{CUD}=5)	Blue L2WPMA SE Approximation
Urban Case A	0	0.78	0.78	0	0.92	0.89
Suburban Case	0	0.79	0.64	0	0.93	0.80
Rural Case	0	0.76	0.23	0	0.89	0.31
"LOS" Case	0	0.75	0.24	0	0.87	0.32

- Piecewise monotonic data approximations can act as a prerequisite subsystem when measurement differences exist. In fact, their presence becomes more critical when measurement differences of high intensities are present. If the suitable piecewise monotonic data approximation is selected, the measurement difference mitigation results can be achieved regardless of the maximum value α_{CUD}.
- The most crucial role for achieving high performances against measurement differences regardless of their maximum value α_{CUD} plays the selection of the suitable piecewise monotonic data approximation as well as its optimal number of monotonic sections. On the basis of the results of this Section and in accordance with [36], [37], the optimal number of monotonic sections can determine: (i) the accuracy of L1PMA and L2WPMA as expressed by PES; (ii) the accuracy of L1PMA and L2WPMA as expressed by the metrics of Set A and B; and (iii) the performance accuracy of the piecewise monotonic data approximations that use monotonic sections against the approximations that do not use (*i.e.*, L2CXCV).
- The indirect mitigation of measurement differences by using piecewise monotonic data approximations has revealed that even if same OV MV BPL topologies are examined the metric results are differentiated because of the different applied coupling schemes and the optimal number of monotonic sections. As concerns the direct mitigation of measurement differences by using piecewise monotonic data approximations, exhaustive investigation has been made in [33], [36], [37] for the impact of specific factors, such as the applied coupling scheme, the examined OV MV BPL topology, the maximum CUD value and the optimal number of

monotonic sections [33], [36], [37]. The observations made there are also valid during the indirect mitigation of measurement differences.

5. Conclusions

This paper constitutes a case study on the indirect measurement difference mitigation during SE computations in OV MV BPL networks by applying L1PMA, L2WPMA and L2CXCV. This paper has exploited the direct measurement difference mitigation observations during channel attenuation computations in distribution BPL networks. The impact of the different piecewise monotonic data approximations, the different OV MV BPL topologies, the number of monotonic sections (when they are required) and different types and intensities of measurement differences have been assessed. With reference to PES, it has been proven that the piecewise monotonic data approximations can provide significant mitigation of measurement differences during SE computations. The SE performance characteristics of piecewise monotonic data approximations is related with the respective channel attenuation performance characteristics. Since suitable piecewise monotonic data approximations have been selected, the maximum SE, minimum SE, average SE, SE MAE and SE RMSD of the approximation present values that are closer to the theoretical ones in comparison with the respective values of the measurements. Higher measurement difference mitigation performances are achieved when higher maximum values α_{CUD} of the CUD measurement differences are assumed.

CONFLICTS OF INTEREST

The author declares that there is no conflict of interests regarding the publication of this paper.

References

[1] M. Emmanuel and R. Ramesh, "Evolution of Dispatchable Photovoltaic System Integration with the Electric Power Network for Smart Grid Applications: A Review," *Elsevier Renewable and Sustainable Energy Reviews*, vol. 67, pp. 207-224, Jan. 2017.

[2] C. Zhao, J. He; P. Cheng and J. Chen, "Consensus-based Energy Management in Smart Grid with Transmission Losses and Directed Communication," *IEEE Trans. on Smart Grid*, vol. 8, no. 5, pp. 2049-2061, Sep. 2017.

[3] Y. Yoldaş, A. Önen, S. M. Muyeen, A. V., Vasilakos, and İ. Alan, "Enhancing Smart Grid with Microgrids: Challenges and Opportunities," *Elsevier Renewable and Sustainable Energy Reviews*, vol. 72, pp. 205-214, May 2017.

[4] A. G. Lazaropoulos, "Smart Energy and Spectral Efficiency (SE) of Distribution Broadband over Power Lines (BPL) Networks – Part 1: The Impact of Measurement Differences on SE Metrics," *Trends in Renewable Energy*, vol. 4, no. 2, pp. 125-184.

[5] A. G. Lazaropoulos, "Towards Modal Integration of Overhead and Underground Low-Voltage and Medium-Voltage Power Line Communication Channels in the Smart Grid Landscape: Model Expansion, Broadband Signal Transmission Characteristics, and Statistical Performance Metrics (Invited Paper)," *ISRN Signal*

Processing, vol. 2012, Article ID 121628, pp. 1-17, 2012. [Online]. Available: http://www.hindawi.com/isrn/sp/2012/121628/

[6] A. G. Lazaropoulos, "Towards broadband over power lines systems integration: Transmission characteristics of underground low-voltage distribution power lines," *Progress in Electromagnetics Research B*, 39, pp. 89-114, 2012. [Online]. Available: http://www.jpier.org/PIERB/pierb39/05.12012409.pdf

[7] A. G. Lazaropoulos and P. G. Cottis, "Transmission characteristics of overhead medium voltage power line communication channels," *IEEE Trans. Power Del.*, vol. 24, no. 3, pp. 1164-1173, Jul. 2009.

[8] A. G. Lazaropoulos and P. G. Cottis, "Capacity of overhead medium voltage power line communication channels," *IEEE Trans. Power Del.*, vol. 25, no. 2, pp. 723-733, Apr. 2010.

[9] A. G. Lazaropoulos and P. G. Cottis, "Broadband transmission via underground medium-voltage power lines-Part I: transmission characteristics," *IEEE Trans. Power Del.*, vol. 25, no. 4, pp. 2414-2424, Oct. 2010.

[10] A. G. Lazaropoulos and P. G. Cottis, "Broadband transmission via underground medium-voltage power lines-Part II: capacity," *IEEE Trans. Power Del.*, vol. 25, no. 4, pp. 2425-2434, Oct. 2010.

[11] A. G. Lazaropoulos, "Broadband transmission characteristics of overhead high-voltage power line communication channels," *Progress in Electromagnetics Research B*, vol. 36, pp. 373-398, 2012. [Online]. Available: http://www.jpier.org/PIERB/pierb36/19.11091408.pdf

[12] A. G. Lazaropoulos, "Green Overhead and Underground Multiple-Input Multiple-Output Medium Voltage Broadband over Power Lines Networks: Energy-Efficient Power Control," *Springer Journal of Global Optimization*, vol. 2012 / Print ISSN 0925-5001, pp. 1-28, Oct. 2012.

[13] A. G. Lazaropoulos, "Deployment Concepts for Overhead High Voltage Broadband over Power Lines Connections with Two-Hop Repeater System: Capacity Countermeasures against Aggravated Topologies and High Noise Environments," *Progress in Electromagnetics Research B*, vol. 44, pp. 283-307, 2012. [Online]. Available: http://www.jpier.org/PIERB/pierb44/13.12081104.pdf

[14] A. G. Lazaropoulos, "Broadband transmission and statistical performance properties of overhead high-voltage transmission networks," *Hindawi Journal of Computer Networks and Commun.*, 2012, article ID 875632, 2012. [Online]. Available: http://www.hindawi.com/journals/jcnc/aip/875632/

[15] P. Amirshahi and M. Kavehrad, "High-frequency characteristics of overhead multiconductor power lines for broadband communications," *IEEE J. Sel. Areas Commun.*, vol. 24, no. 7, pp. 1292-1303, Jul. 2006.

[16] T. Calliacoudas and F. Issa, ""Multiconductor transmission lines and cables solver," An efficient simulation tool for plc channel networks development," presented at the *IEEE Int. Conf. Power Line Communications and Its Applications*, Athens, Greece, Mar. 2002.

[17] T. Sartenaer and P. Delogne, "Deterministic modelling of the (Shielded) outdoor powerline channel based on the multiconductor transmission line equations," *IEEE J. Sel. Areas Commun.*, vol. 24, no. 7, pp. 1277-1291, Jul. 2006.

[18] C. R. Paul, *Analysis of Multiconductor Transmission Lines*. New York: Wiley, 1994.

[19] H. Meng, S. Chen, Y. L. Guan, C. L. Law, P. L. So, E. Gunawan, and T. T. Lie, "Modeling of transfer characteristics for the broadband power line communication channel," *IEEE Trans. Power Del.*, vol. 19, no. 3, pp. 1057-1064, Jul. 2004.

[20] B. Li, D. Mansson, and G. Yang, "An efficient method for solving frequency responses of power-line networks," *Progress In Electromagnetics Research B*, Vol. 62, 303-317, 2015. doi:10.2528/PIERB15013008 http://www.jpier.org/pierb/pier.php?paper=15013008

[21] M. Chaaban, K. El KhamlichiDrissi, and D. Poljak, "Analytical model for electromagnetic radiation by bare-wire structures," *Progress In Electromagnetics Research B*, Vol. 45, 395-413, 2012. doi:10.2528/PIERB12091102 http://www.jpier.org/pierb/pier.php?paper=12091102

[22] Y. H. Kim, S. Choi, S. C. Kim, and J. H. Lee, "Capacity of OFDM two-hop relaying systems for medium-voltage power-line access networks," *IEEE Trans. Power Del.*, vol. 27, no. 2, pp. 886-894, Apr. 2012.

[23] I. C. Demetriou and M. J. D. Powell, "Least squares smoothing of univariate data to achieve piecewise monotonicity,"*IMA J. of Numerical Analysis*, vol. 11, pp. 411-432, 1991.

[24] I. C. Demetriou and V. Koutoulidis, "On Signal Restoration by Piecewise Monotonic Approximation", in Lecture Notes in Engineering and Computer Science: *Proceedings of The World Congress on Engineering 2013*,London, U.K., Jul. 2013, pp. 268-273.

[25] I. C. Demetriou, "An application of best *L*1 piecewise monotonic data approximation to signal restoration," *IAENG International Journal of Applied Mathematics*, vol. 53, no. 4, pp. 226-232, 2013.

[26] I. C. Demetriou, "L1PMA: A Fortran 77 Package for Best L1 Piecewise Monotonic Data Smoothing," *Computer Physics Communications*, vol. 151, no. 1, pp. 315-338, 2003.

[27] I. C. Demetriou, "Data Smoothing by Piecewise Monotonic Divided Differences,"*Ph.D. Dissertation*, Department of Applied Mathematics and Theoretical Physics, University of Cambridge, Cambridge, 1985.

[28] I. C. Demetriou, "Best L1 Piecewise Monotonic Data Modelling,"*Int. Trans. Opl Res.*, vol. 1, no. 1, pp. 85-94,1994.

[29] C. de Boor, *A Practical Guide to Splines*. Revised Edition, NY: Springer-Verlag, Applied Mathematical Sciences, vol. 27, 2001.

[30] M. Holschneider, *Wavelets. An Analysis Tool*, Oxford: Clarendon Press, 1997.

[31] I. C. Demetriou, "Algorithm 863: L2WPMA, a Fortran 77 package for weighted least-squares piecewise monotonic data approximation," *ACM Transactions on Mathematical Software (TOMS)*, vol. 33, no.1, pp. 6, 2007.

[32] I. C. Demetriou, "L2CXCV: A Fortran 77 package for least squares convex/concave data smoothing," *Computer physics communications*, vol. 174, no.8,pp. 643-668, 2006.

[33] A. G. Lazaropoulos, "Best L1 Piecewise Monotonic Data Approximation in Overhead and Underground Medium-Voltage and Low-Voltage Broadband over Power Lines Networks: Theoretical and Practical Transfer Function Determination," *Hindawi Journal of Computational Engineering*, vol. 2016, Article ID 6762390, 24 pages, 2016. doi:10.1155/2016/6762390. [Online]. Available: https://www.hindawi.com/journals/jcengi/2016/6762390/cta/

[34] A. G. Lazaropoulos, "Measurement Differences, Faults and Instabilities in Intelligent Energy Systems – Part 1: Identification of Overhead High-Voltage Broadband over Power Lines Network Topologies by Applying Topology Identification Methodology (TIM)," *Trends in Renewable Energy*, vol. 2, no. 3, pp. 85 – 112, Oct. 2016.

[35] A. G. Lazaropoulos, "Measurement Differences, Faults and Instabilities in Intelligent Energy Systems – Part 2: Fault and Instability Prediction in Overhead High-Voltage Broadband over Power Lines Networks by Applying Fault and Instability Identification Methodology (FIIM)," *Trends in Renewable Energy*, vol. 2, no. 3, pp. 113 – 142, Oct. 2016. [Online]. Available: http://futureenergysp.com/index.php/tre/article/view/27/33

[36] A. G. Lazaropoulos, "Power Systems Stability through Piecewise Monotonic Data Approximations – Part 1: Comparative Benchmarking of L1PMA, L2WPMA and L2CXCV in Overhead Medium-Voltage Broadband over Power Lines Networks," Trends in Renewable Energy, vol. 3, no. 1, pp. 2 – 32, Jan. 2017. [Online]. Available: http://futureenergysp.com/index.php/tre/article/view/29/34

[37] A. G. Lazaropoulos, "Power Systems Stability through Piecewise Monotonic Data Approximations – Part 2: Adaptive Number of Monotonic Sections and Performance of L1PMA, L2WPMA and L2CXCV in Overhead Medium-Voltage Broadband over Power Lines Networks," Trends in Renewable Energy, vol. 3, no. 1, pp. 33 – 60, Jan. 2017. [Online]. Available: http://futureenergysp.com/index.php/tre/article/view/30/35

[38] A. G. Lazaropoulos, "Main Line Fault Localization Methodology in Smart Grid – Part 1: Extended TM2 Method for the Overhead Medium-Voltage Broadband over Power Lines Networks Case," *Trends in Renewable Energy*, vol. 3, no. 3, pp. 2-25, Dec. 2017. [Online]. Available: http://futureenergysp.com/index.php/tre/article/view/36

[39] A. G. Lazaropoulos, "Main Line Fault Localization Methodology in Smart Grid – Part 2: Extended TM2 Method, Measurement Differences and L1 Piecewise Monotonic Data Approximation for the Overhead Medium-Voltage Broadband over Power Lines Networks Case," *Trends in Renewable Energy*, vol. 3, no. 3, pp. 26-61, Dec. 2017. [Online]. Available: http://futureenergysp.com/index.php/tre/article/view/37

[40] A. G. Lazaropoulos, "Main Line Fault Localization Methodology in Smart Grid – Part 3: Main Line Fault Localization Methodology (MLFLM)," *Trends in Renewable Energy*, vol. 3, no. 3, pp. 62-81, Dec. 2017. [Online]. Available: http://futureenergysp.com/index.php/tre/article/view/38

[41] A. G. Lazaropoulos, "Improvement of Power Systems Stability by Applying Topology Identification Methodology (TIM) and Fault and Instability Identification Methodology (FIIM) – Study of the Overhead Medium-Voltage Broadband over Power Lines (OV MV BPL) Networks Case," *Trends in Renewable Energy*, vol. 3, no. 2, pp. 102-128, Apr. 2017. [Online]. Available: http://futureenergysp.com/index.php/tre/article/view/34

[42] http://cpc.cs.qub.ac.uk/summaries/ADRF

[43] http://www.cpc.cs.qub.ac.uk/summaries/ADXM_v1_0.html

[44] A. G. Lazaropoulos, "Factors Influencing Broadband Transmission Characteristics of Underground Low-Voltage Distribution Networks," *IET Commun.*, vol. 6, no. 17, pp. 2886-2893, Nov. 2012.

[45] M. Gebhardt, F. Weinmann, and K. Dostert, "Physical and regulatory constraints for communication over the power supply grid," *IEEE Commun. Mag.*, vol. 41, no. 5, pp. 84-90, May 2003.
[46] P. S. Henry, "Interference characteristics of broadband power line communication systems using aerial medium voltage wires," *IEEE Commun. Mag.*, vol. 43, no. 4, pp. 92-98, Apr. 2005.
[47] Ofcom, "Amperion PLT Measurements in Crieff," Ofcom, Tech. Rep., Sept. 2005.
[48] NATO, "HF Interference, Procedures and Tools (Interférences HF, procédures et outils) Final Report of NATO RTO Information Systems Technology," RTO-TR-ISTR-050, Jun. 2007, [Online]. Available: http://ftp.rta.nato.int/public/PubFullText/RTO/TR/RTO-TR-IST-050/$$TR-IST-050-ALL.pdf
[49] FCC, "In the Matter of Amendment of Part 15 regarding new requirements and measurement guidelines for Access Broadband over Power Line Systems," FCC 04-245 Report and Order, Jul. 2008.
[50] Ofcom, "DS2 PLT Measurements in Crieff," Ofcom, Tech. Rep. 793 (Part 2), May 2005.
[51] Ofcom, "Ascom PLT Measurements in Winchester," Ofcom, Tech. Rep. 793 (Part 1), May 2005.

Trends in Renewable Energy
OPEN ACCESS ISSN: 2376-2144
Peer-Reviewed Article futureenergysp.com/index.php/tre

Development of Feed-Forward Back-Propagation Neural Model to Predict the Energy and Exergy Analysis of Solar Air Heater

Harish K. Ghritlahre*

Department of Mechanical Engineering, National Institute of Technology, Jamshedpur, Jharkhand, 831014, India

Received June 27, 2018; Accepted August 23, 2018; Published August 27, 2018

In the present work, Artificial Neural Network (ANN) model has been developed to predict the energy and exergy efficiency of a roughened solar air heater (SAH). Total fifty data sets of samples, obtained by conducting experiments on SAHs with three different specification of wire-rib roughness on the absorber plates, have been used in this work. These experimental data and calculated values of thermal efficiency and exergy efficiency have been used to develop an ANN model. Levenberg-Marquardt (LM) and Scaled Conjugate Gradient (SCG) learning algorithm were used to train the proposed ANN model. Six numbers of neurons were found with LM learning algorithm in the hidden layer as the optimal value on the basis of statistical error analysis. In the input layer, the time of experiments, mass flow rate, ambient temperature, mean temperature of air, absorber plate temperature and solar radiation intensity have been taken as input parameters; and energy efficiency and exergy efficiency have been taken as output parameters in the output layer. The 6-6-2 neural model has been obtained as the optimal model for prediction. Performance predictions using ANN were compared with the experimental data and a close agreement was observed. Statistical error analysis was used to evaluate the results.

Keywords: Solar air heater; Energy analysis; Exergy analysis; Artificial Neural Network; Multi-layer perceptron

Introduction

In view of limited reserves of fossil fuels on the earth, it is necessary to develop efficient systems to use alternative sources of energy. Many types of renewable energy are available on the earth, in which solar energy is one of the most abundant and clean sources of energy. Solar energy can be utilized in two ways: active and passive. In passive solar energy utilization, sun rays are directly used without the aid of any equipment. In the active way of utilization of solar energy, sun rays are not directly used, and some kind of mechanical equipment is needed for conversion of the solar energy into other forms of energy. Solar air heater (SAH) comes in the category of active solar energy utilization.

In solar air heating systems, the solar collector or absorber plate is the main component which collects the solar energy in form of thermal energy and transfers the same to flowing air through the SAH duct. Due to the low heat capacity of flowing air,

*Corresponding author: harish.ghritlahre@gmail.com

Tr Ren Energy, 2018, Vol.4, No.2, 213-235. doi: 10.17737/tre.2018.4.2.0078

the convective heat transfer coefficient between the absorber plate and air is low. Hence, the main aim is to increase the heat transfer coefficient and thereby the heat flow rate. This objective can be achieved by using extended surfaces [1] or artificial roughness [2-5] on the absorber plate on the air flow side, or porous heat absorbing materials in the air flow duct of SAH [6,7].

In the present work, concepts of energy and exergy analyses have been used for evaluating the performances of roughened absorber plate SAH by ANN modeling. The quantitative energy analysis of any system is based on first law of thermodynamics, whereas the qualitative analysis is based on second law of thermodynamics. In recent years many researchers have carried out energy and exergy analyses of thermal systems. A mathematical model was developed by Ajam *et al.* [8] to study the exergetic performance of SAHs and optimize the system by using MATLAB. Esen [9] conducted experiments on double flow SAH with different obstacles on the absorber plate and did the energy and exergy analysis. Akpinar *et al.* [10] also used the concept of energy and exergy analysis for solar air heating unit with four different types of absorber plate with obstacles and without obstacles. Alta *et al.* [11] conducted experiments to investigate the energy and exergy analysis of 3 different types of SAHs. Bayrak *et al.* [12] performed energy and exergy analysis for porous bed SAH. Panwar *et al.* [13] reviewed energy and exergy analysis for solar drying systems. Saidur *et al.* [14] used the concept of energy and exergy analysis for various solar energy utilized equipment and concluded that exergy analysis is necessary to examine the system performance. Kumar *et al.* [15] conducted experiments on packed bed SAH for various mass flow rates of air and for different porosities of packing material and evaluated exergy of the system. Park *et al.* [16] studied the energy and exergy analysis of different types of renewable energy systems.

The performance analysis of solar air heaters using experimental and analytical study takes more time to solve problems and requires programming for solving in conventional software in analytical approach. Now a day, soft computing technique is attracting researchers for solving various complicated problems of nonlinear nature. The traditional approaches for such analysis cannot be solved without using fundamental equations, conventional correlations, or developing unique designs from experimental data through trial and error. To avoid these problems, artificial neural network (ANN) technique has been implemented in various types of complicated problems which are not solved by conventional method and in various fields. This technique computes data with very less time and more accurately predicted. Therefore, this technique has been becoming increasingly popular in Science and Engineering, especially in Thermal Engineering applications in recent years. Many researchers have used ANN in the past.

Kalogirou [17] used neural network in renewable energy systems to predict solar radiation and wind speed, and also for load forecasting of PV and building service systems. Yang *et al.* [18] have applied ANN technique for the heating system in building. They constructed optimal ANN model and predicted the room temperature by using experimental data. Facao *et al.* [19] used ANN for plate and tube type heat pipe hybrid solar collector. They constructed two different types of ANN model by use of multilayer perceptron (MLP) and radial basis function (RBF), and predicted the collector efficiency and useful heat gained. They found that the MLP model performed slightly better than

the RBF model. Ertunc and Hosoz [20] used ANN for performance analysis of refrigeration unit. They constructed a 5-4-5 neuron model using experimental data and successfully predicted performance parameters such as power absorbed by refrigerant, compressor input power, mass flow rate of refrigerants, heat rejection rate of condenser and coefficient of performance (COP) of refrigeration unit. Kalogirou [21] applied ANN for predicting performance parameters of flat plate collector. To predict these parameters, he constructed six different types of ANN model on the basis of measured experimental data and got satisfactory results. Yilmaz and Atik [22] used ANN in a mechanical cooling system. They conducted experiments with different flow rates of cooling water and determined the power consumption, thermal performance, COP of heating and cooling. By using experimental data and calculated values they constructed an ANN model with 1-6-4 neurons to predict the power consumption, thermal efficiency, COP of heating and cooling. Sozen *et al.* [23] conducted experiments on flat plate SAH and calculated the thermal efficiency. By the use of experimental and calculated data optimal ANN was constructed using 7-20-20-1 and predicted the thermal efficiency with satisfactory results. Kurt *et al.* [24] conducted an experiment on solar cooker with various working conditions and collected the data. By the use of this data sample they constructed an ANN model to predict the enclosure air, pot water and absorber plate temperature of hot box type solar cooker with very less errors. Caner *et al.* [25] used ANN for estimating the thermal efficiency of solar air collector. Experiments were performed with two types of zigzagged absorber plat in SAH and collected the data for five days for constructing ANN model designed on the LM learning algorithm in *nftool* tool module in MATLAB. They found on the basis of statistical error analysis that the predicted thermal efficiency obtained by ANN model was reliable and accurate. Nazghelichi *et al.* [26] conducted experiments with different air temperatures, bed width and square cubed: carrot, collected total 518 data and determined energy and exergy of carrot cubes in fluidized bed dryer. By the use of this data they constructed an ANN model, and successfully predicted energy and exergy with minimum errors. Aghbashlo *et al.* [27] applied ANN for estimating the exergetic behavior of spray drying. The data was obtained from the experiments. They used optimum ANN model on the basis of minimum error and maximum R^2 value, and successfully predicted the exergetic performance of the unit by the use of this model. Benli [28] also applied ANN technique for determining the thermal efficiency of SAH with trapeze and corrugated absorber plate. For estimating the collector efficiency, experiments were performed, and data was collected for developing of ANN model with LM learning algorithms. The ANN predicted results on thermal performance of solar air collector, which were found accurate with LM-3 neurons in hidden layer. Kalogirou *et al.* [29] applied ANN for predicting the performance of large solar systems. For predicting the performance, ANN model was constructed on measured experimental data of over one year and successfully predicted results with higher coefficient of determinations. Hamdan *et al.* [30] developed a 5-20-5 multiple output parameter NARX neural model to predict the heat transfer analysis of flat plate solar air collector. Jani *et al.* [31, 32] used ANN technique to predict the performance of a solid desiccant – vapor compression hybrid air-conditioning system. Ghritlahre and Prasad [33-40] implemented MLP neural model to predict the performances of various types of solar air heaters.

From the literature, it has been found that the ANN technique is used for performance analysis of various types of thermal systems, but very few work in the field of solar systems, especially in the topic of solar air heater performance analysis. In the view of above the energy and exergy analysis of solar air heater, using MLP neural model is new research work and has been taken in the present work.

The aim of this work is to predict the energy efficiency and the exergy efficiency of solar air heaters using the ANN model on the basis of actual experimental data and the calculated values. Total fifty sets of data have been obtained by conducting experiments on three types of transverse wire rib roughened solar air heaters. The ANN model consists of six variables in the input layer and two variables in the output layer. Two different types of training functions with 4-7 neurons have been used to obtain the best network for prediction of output parameters. Six neurons in the hidden layer with LM learning function is obtained as an optimal topology. Statistical error analysis has been performed for predicted values of energy and exergy efficiency.

Materials and Methods

Experimental System and Data Collection

The line diagram of the experimental system is shown in Fig. 1. The system consists of an artificial roughened SAH having entrance section, test section, exit section, absorber plate and glass cover and equipped with galvanized iron (GI) pipe, flange coupling, orifice plate, U-tube manometer, thermometers, a suction blower, a valve and a Variac transformer. In the present work, the SAH duct length is 168 cm, width is 28 cm and height is 4 cm. The test section is a rectangular duct having wire- roughened absorber plate and a back plate. It consists of a 4 mm thick glass cover at its top. Fig. 2 shows the structure of the test section. The absorber plate is made of 1 mm thick GI sheet provided with transvers wire of three different specifications as given in Table 1. A configuration of wire-roughness used on the absorber plate has been shown in Fig. 3a, where as a photographic view of the same has been given in Fig. 3b. The test section is connected with 3 inch diameter GI pipe provided with an Orifice meter to measure the mass flow rate of air through the SAH. The pressure drop was measured with the help of a U-tube Manometer fitted across the orifice plate. The mass flow rate was varied from 0.0235 to 0.0270 kg/sec. A 2 HP/3-phase suction blower was used to carry air through the SAH duct. The intensity of solar radiation was measured with a digital pyranometer. For measuring the temperature at various sections of absorber plate and air temperatures at inlet and outlet, digital thermometers were used. The experiments were conducted in clear sky in the month of April 2014 and data were taken from 10:30 am to 1:00 pm. Total 50 sets of experimental data were collected from experiments with three different types of roughened absorber plate, categorised on the basis of roughness height (e), relative roughness pitch (P/e) and relative roughness height (e/D) [5].

The experiments were conducted in Jamshedpur (India), where latitude and longitude are 22.77^{o} N & 86.14^{o} E, respectively. The variation of wind speed and solar intensity of radiation with different months of the year, obtained at Jamshedpur from RETScreen database, have been shown in Fig. 4 and Fig. 5, respectively. Fig.5 shows that

the maximum solar energy of 6.21 kwh/m^2/day is obtained in the month of April, and the lowest solar energy of 3.95 kwh/m^2/day is obtained in the month of August. Air temperature is recorded maximum in the month of May, which is 32^{o}C and minimum in January, which is 18^{o}C. The gross incident solar radiation has been estimated as 1744.7 kwh/m^2/year.

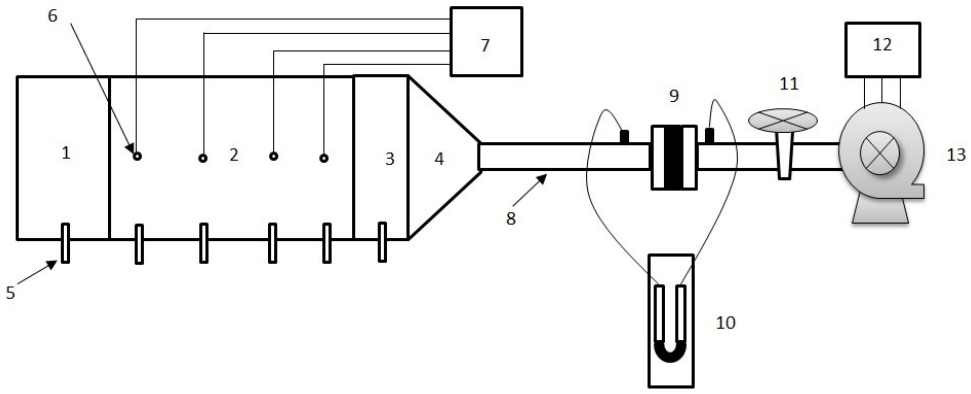

Figure 1. Experimental system

1. Entrance section
2. Test section
3. Exit section
4. Diverging section
5. Digital thermometer
6. Thermocouples
7. Temperature display unit
8. GI pipe
9. Orifice plate
10. U-tube manometer
11. Valve
12. Variac transformer
13. Suction blower

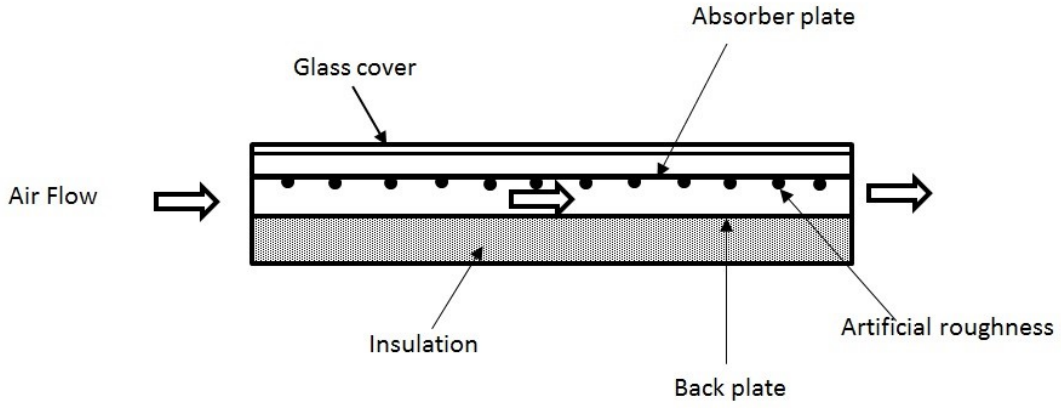

Figure 2. Test section

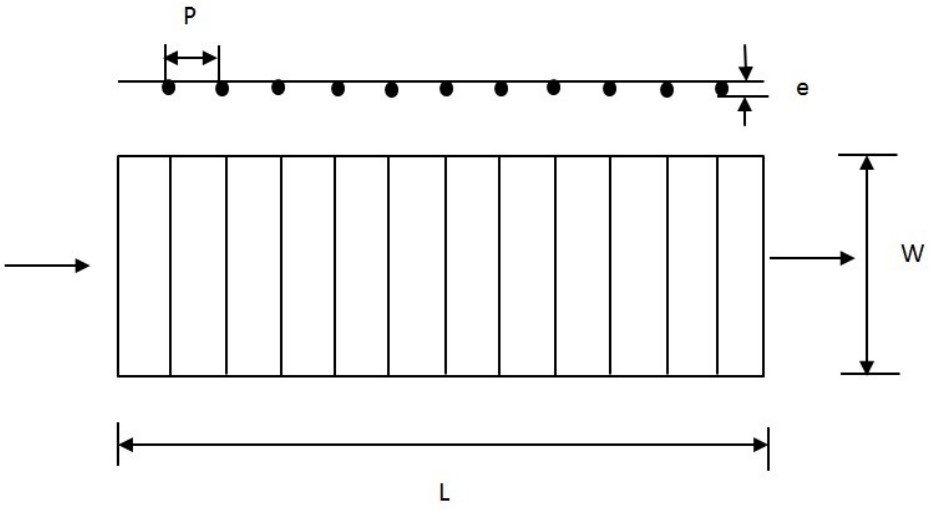

Figure 3a. Wire roughened Absorber plate

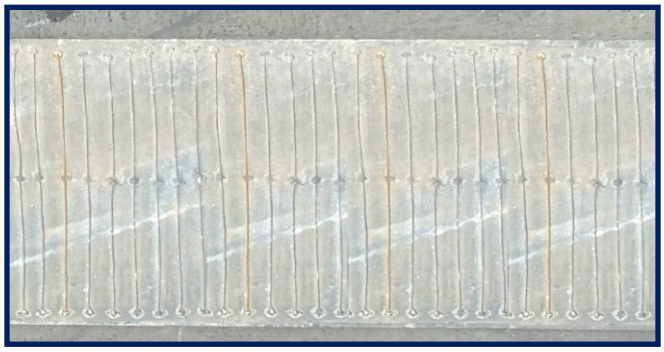

Figure 3b. Photographic view of absorber plate

Table 1. Specification of wire roughness.

Roughness parameter	Absorber roughness type		
	Type A	Type B	Type C
Relative roughness pitch (P/e)	10	10	10
Relative roughness height (e/D)	0.014	0.01740	0.009571
Roughness height (e), mm	0.98	1.2	0.67

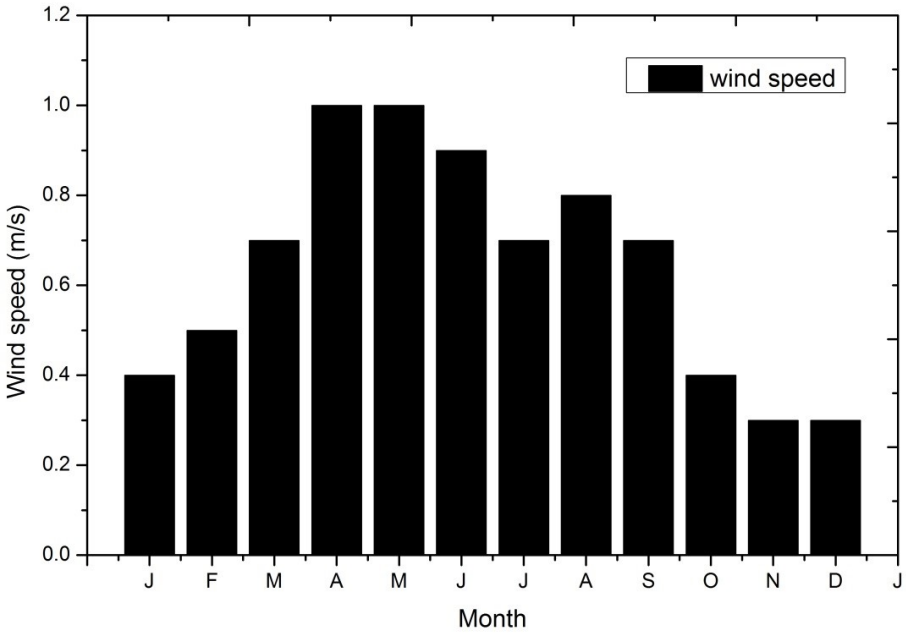

Figure 4. Local weather graph showing wind speed in different months of a year.

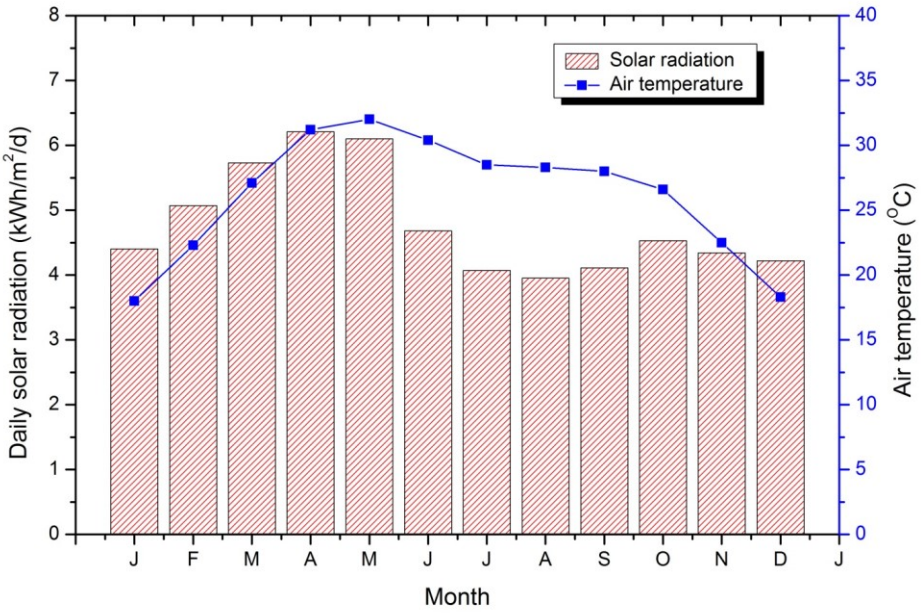

Figure 5. Local weather graph showing intensity of solar radiation and air temperature in different months of a year.

Energy and Exergy Analysis

Analysis of Energy

Energy analysis of a SAH is represented by its thermal efficiency, which is defined as the ratio of energy gained to incident solar radiation [1] and is given as

$$\eta_{th} = \frac{\dot{Q}_u}{\dot{Q}_c} \tag{1}$$

where Q_u is the useful heat gain and the incident radiation of solar energy Q_c is given by

$$\dot{Q}_c = IA_c \tag{2}$$

In Eq. (2), I is solar radiation intensity and A_c is collector area.

The useful energy gained by air is written as

$$\dot{Q}_u = \dot{m} C_p . \Delta T_f = \dot{m} C_p (T_{fo} - T_{fi}) \tag{3}$$

where m is the mass flow rate of air, T_{fo} and T_{fi} are outlet and inlet temperature of air respectively.

Thus, the thermal efficiency of collector is [1]:

$$\eta_{th} = \frac{\dot{Q}_u}{IA_c} \tag{4}$$

Analysis of Exergy

The analysis of exergy is the most useful concept for optimal utilization of energy. This analysis is used to make strategies for designing and operation of industrial processes. The exergetic efficiency is defined as the ratio of exergy gained from the system to exergy input to the system [40].

Following assumptions have been undertaken in the present analysis:

(i) The system works under the steady state condition.
(ii) Kinetic Energy and Potential Energy are negligible.
(iii) Chemical and nuclear reactions are not possible to occur in operation of the system.
(iv) The air specific heat is constant and it is considered as an ideal fluid.
(v) The heat transfer to the system and work transfer from the system are positive

In general, energy and exergy balance equations in rate form with negligible kinetic and potential energies can be written as [11,12, 16, 42]:

$$\sum \dot{E}_i = \sum \dot{E}_o \tag{5}$$

$$\sum \dot{Ex}_i - \sum \dot{Ex}_o = \sum \dot{Ex}_d \tag{6}$$

or

$$\sum \dot{E}x_{heat} - \sum \dot{E}x_{work} + \sum \dot{E}x_{mass,in} - \sum \dot{E}x_{mass,out} = \sum \dot{E}x_{dest} \tag{7}$$

In Eqs. (5) to (7), $\dot{E}$ and $\dot{E}x$ are energy and exergy rates, respectively. $\dot{E}x_{dest}$ is the rate of exergy destruction, *i* and *o* stand for inlet and outlet of the system, respectively.

By introducing temperature of environment $T_{e,}$ sun surface temperature T_s, energy gained by collector Q_c, work rate $\dot{W}$, and the specific exergy ψ in Eq. (7), the resulting equation becomes:

Eq. (7) can also be expressed in the form of general exergy equation as given below:

$$\sum\left(1-\frac{T_e}{T_s}\right)\dot{Q}_c - \dot{W} + \sum \dot{m}_i \psi_i - \sum \dot{m}_o \psi_o = \sum \dot{E}x_{dest} \tag{8}$$

Where,

$$\psi_i = (h_i - h_e) - T_e(s_i - s_e) \tag{9}$$

$$\psi_o = (h_o - h_e) - T_e(s_o - s_e) \tag{10}$$

In Eqs. (9) and (10), h is enthalpy and s is entropy, suffix *e* stand for environment.

From Eq.(8),(9) and (10), the expression:

$$\left(1-\frac{T_e}{T_s}\right)\dot{Q}_c - \dot{m}\left[(h_o - h_i) - T_e(s_o - s_i)\right] = \sum \dot{E}x_{dest} \tag{11}$$

Where,

$$\dot{Q}_C = IA_C \tag{12}$$

The change in the enthalpy and the entropy of the air

$$\Delta h_{air} = h_o - h_i = C_{pf}(T_{fo} - T_{fi}) \tag{13}$$

$$\Delta s_{air} = s_o - s_i = C_{pf} ln \frac{T_{fo}}{T_{fi}} - R ln \frac{P_o}{P_i} \tag{14}$$

In Eqs. (13) and (14), C_{pf} is specific heat of air (J /kg K), T_{fi} and T_{fo} are inlet and outlet air temperatures, respectively, and R_a is Universal gas constant (J/kg K).

From Eq.(11) to (14) the following expression can be obtained:

$$\left(1-\frac{T_e}{T_s}\right)IA_c - \dot{m}C_{pf}(T_{f_o} - T_{fi}) + \dot{m}T_e\left(C_{pf}\ln\frac{T_{fo}}{T_{fi}} - R_a \ln\frac{P_o}{P_i}\right) = \sum \dot{E}x_{dest} \tag{15}$$

where *P* is the pressure of air.

The Irreversibility/exergy destruction may be expressed as follows:

$$\dot{E}x_{dest} = T_e.\dot{S}_{gen} \tag{16}$$

where $\dot{S}_{gen}$ is the rate of entropy generation.

The exergy efficiency of SAH can be formulated by the ratio of net exergy output of the system to exergy input of the system.

$$\eta_{II} = \frac{\dot{E}x_o}{\dot{E}x_i} = \frac{\dot{m}[(h_o - h_i) - T_e(s_o - s_i)]}{\left(1 - \frac{T_e}{T_S}\right) IA_c} \quad (17)$$

Artificial Neural Network (ANN)

ANN is a complex information processing system, which is structured from interconnected segmental processing elements, called neurons. These neurons find the input information from other sources and perform generally a non-linear operation on the result and then give final results as output. ANN works in two ways, first learning and then storing the knowledge in interconnects called weights. The basic model of ANN is represented in Fig. 6. ANN is a simulation tool in MATLAB which can be used to estimate the values on the basis of input parameters, optimum topology and training processes. In feed forward networks, each product of input elements and weights are fed to summing junctions and is summed with bias of neurons as follows [17, 32, 41]:

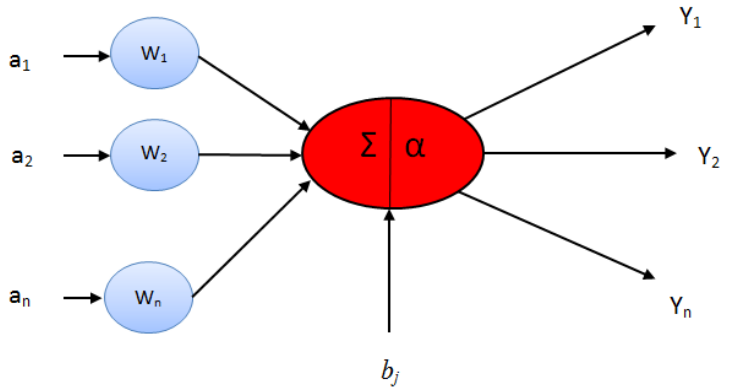

Figure 6. Basic structure of ANN model

$$X = \left(\sum_{i=1}^{n} w_{ij} a_i\right) + b_j \quad (18)$$

Then this sum X passes through transfer function F which generates an output.

$$F(X) = u_j = F\left[\left(\sum_{i=1}^{n} w_{ij} a_i\right) + b_j\right] \quad (19)$$

The most used transfer functions in the hidden layer are *tansig* and *logsig*. The nonlinear activation function, which is widely used, is called as sigmoid function whose output lies in between 0 and 1, and it is given as:

$$F(X) = \frac{1}{1+e^{-X}} \tag{20}$$

The performance index of different training algorithm is mean square error (MSE) and it is formulated as

$$MSE = \frac{1}{n}\sum_{i=1}^{n}(X_{A,i} - X_{P,i})^2 \tag{21}$$

where X_A and X_P are actual value and predicted value, respectively.

Selection Criteria for Optimal ANN Model

The optimal ANN model to predict the exergetic performance is based on the criteria of selection of minimum errors of root mean square error (RMSE), mean absolute error (MAE) and best fit of ANN predicted data with experimental data on the basis of coefficient of determination (COD, R^2).

Root mean square error (RMSE):

$$RMSE = \sqrt{\frac{1}{n}\sum_{i=1}^{n}(X_{A,i} - X_{P,i})^2} \tag{22}$$

Mean absolute error (MAE):

$$MAE = \frac{1}{n}\sum_{i=1}^{n}(X_{A,i} - X_{P,i}) \tag{23}$$

Coefficient of determination (COD):

$$R^2 = 1 - \frac{\sum_{i=1}^{n}(X_{A,i} - X_{P,i})^2}{\sum_{i=1}^{n}X_{P,i}^2} \tag{24}$$

Modeling of ANN Structure

Neural Structure Development

In the present analysis, total 50 sets of experimental data were collected by conducting experiments for 10 days. The proposed MLP ANN model for prediction of energy and exergy analyses is shown in Fig. 7, which was structured with an input layer, hidden layer and output layer. Six parameters in the input layer including time of experiments, mass flow rate of air, atmospheric temperature, air mean temperature, plate temperature and solar intensity, and two parameters of thermal efficiency and exergy efficiency in output layer have been taken. The ranges indicating the minimum and maximum values of input and output parameters are listed in Table 2.

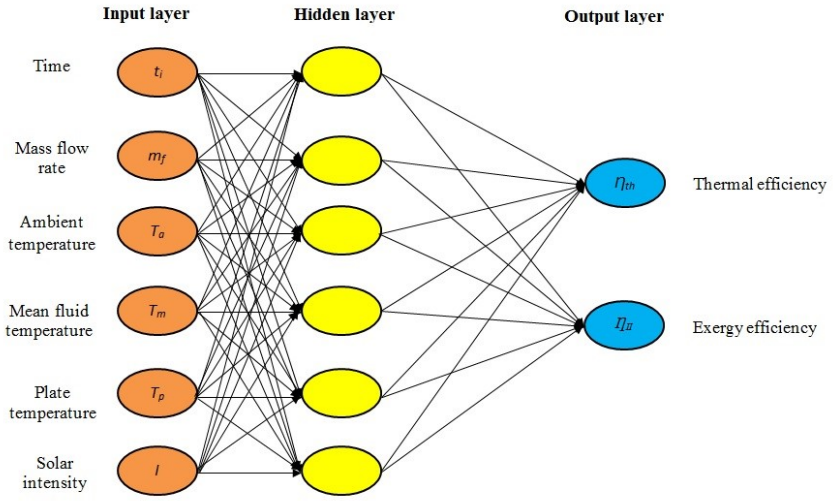

Figure 7. Present ANN model

Table 2. Minimum and maximum values of input and output parameters for ANN Model

Parameters	**Range**	
Input	Minimum value	Maximum value
Mass flow rate of air, m_f(kg/sec)	0.0235	0.0270
Atmospheric temp. T_a (°C)	32	42
Mean temp. of air, T_m (°C)	38	47.5
Absorber Plate temp., T_p (°C)	63.2	73.40
Solar Intensity, I (W/m^2)	833	905
Output		
Thermal efficiency, η_{th}(%)	25.6843	47.9937
Exergy efficiency, η_{II} (%)	0.3829	0.7906

Data Preparation

For this model, 50 data sets have been taken out, in which 70% data is designed for training process and rest of 30% data is taken for testing process. Feed forward back propagation learning algorithm has been applied for learning of present model. Single hidden layer was chosen in this model.

Before developing the ANN model, the input and output sample data must be normalized between -1 and 1 for accuracy of prediction. The following equation is used to normalize data between -1 and 1.

$$Y = \frac{Y_i - Y_{\min}}{Y_{\max} - Y_{\min}} (High_{value} - Low_{value}) + Low_{value} \quad (25)$$

Selection of Learning Algorithm and Transfer Function

For training process, 4-7 neurons have been selected in the hidden layer for the optimal network selection to obtain the best results. The two types of training functions are selected, which are Scaled Conjugate Gradient (SCG) and Levenberg-Marquardt (LM) algorithms. After selecting the training function the adaption learning function was selected (LEARNGDM). *Tansig* transfer function was selected for the hidden layer and linear function (*purelin*) for the output layer. This model is performed in MATLAB software using *nntool* for computation.

Modelling Procedures

In order to find the result, for predicting the performance parameters of SAHs, following steps are followed in MATLAB ANN simulation:

Step 1. Selection of *nntool* command.
The *nntool* for starting the neural network technique in MATLAB software is first selected.

Step 2. Selection of the input and target variables.
For structuring a neural model, mainly, the input and output variables from the experimental data and calculated values of solar air heater have been selected.

Step 3. Selection of training and testing data.
Out of total 50 data sets, 70% data is used for training process and 30% data is used for testing process.

Step 4. Selection of training function and adaption learning function.
In present work, two types of training functions are used such as TRAINLM and TRIANSCG, and the LEARNGDM is selected as adaption learning function.

Step 5. To choose the number of neurons and layers in the hidden layer with transfer functions.
The number of neurons is selected in the hidden layer by trial and error method, accordingly 4-7 number of neurons have been selected to obtain the best model for prediction. Single layer is used in the hidden layer. Tangent sigmoid (*Tansig)* and pure linear (*purlin)* transfer functions are used at hidden and output layer respectively.

Step 6. Training of the ANN model with experimental data.
Different number of neurons using TRAINLM and TRAINSCG for 50 times run for each model is trained.

Step 7. To check and compare the performance of different models.
To obtain the optimal model, different model training performance on the basis of RMSE, MAE and R^2, which are calculated by using Eqs. (22), (23) and (24), respectively, is checked. The performance of training process of different models is shown in Table 3.

Step 8. To select optimal ANN model.
It is found that LM algorithm with six neurons (LM-6) in the hidden layer is optimal model due to the lowest error and the highest value of R^2 for energy and exergy efficiencies.

Step 9. To save the predicted results and to compare with actual available data.
Finally, the predicted results of thermal or energy efficiency and exergy efficiency are saved and compared with actual experimental data. The comparison of predicted results and their statistical error analysis is shown in Table 4.

The flow chart of ANN simulation is shown in Fig. 8, exhibiting all steps undertaken in the analysis.

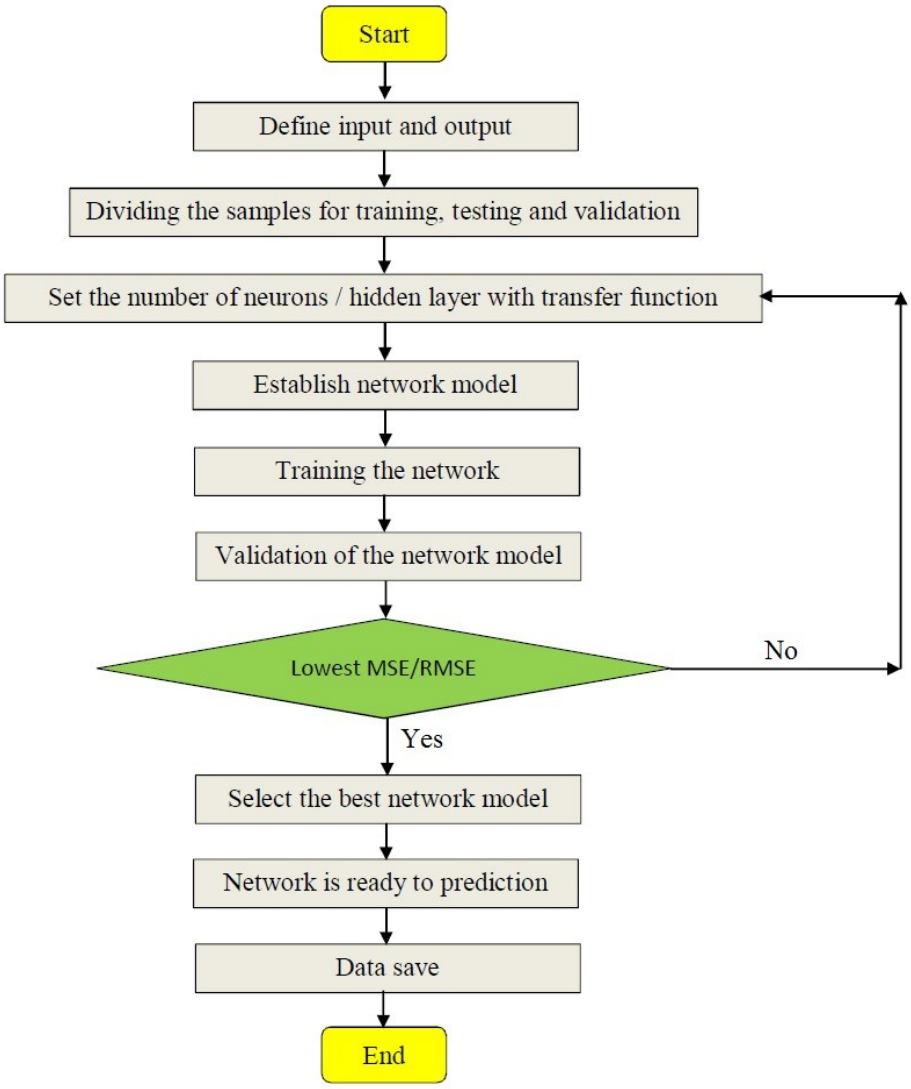

Figure 8. Flow chart of ANN simulation.

Results and Discussion

In the optimal neural model, the training algorithm of LM with 6 neurons adjusted the weights and biases iteratively to minimize the error between actual and predicted values of ANN model.

The values of regression coefficient (R) for training, validation, testing and all process are 1.0, 1.0, 0.99999 and 1.0, respectively (Fig. 9), which gives the accurate result. The best validation performance was found at 4 epoch at which the MSE during validation is found to be 0.022696. Also training process stopped at epoch 54 because the minimum gradient error reached.

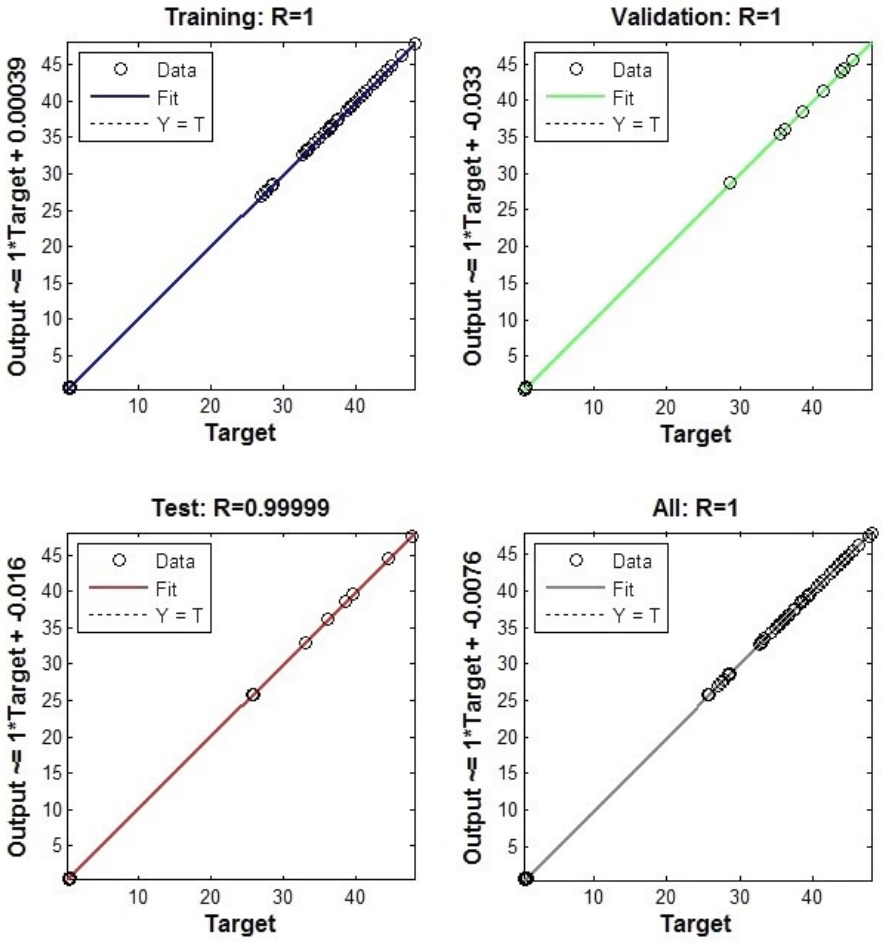

Figure 9. Regression plot of TRAINLM-6

A comparison between actual (experimental) data and predicted data from ANN model is shown in Fig. 10, while the absolute errors are shown in Fig. 11. As from Fig. 11, it has been found that the errors between ANN predicted values and actual experimental values are very small. Table 4 shows the performance of selected LM-6 ANN model for estimating the energy and exergy efficiency on the basis of MAE, sum of square error (SSE), MSE, coefficient of variance (COV) and R^2. The values of MSE,

MAE and R^2 are calculated by Eqs. (21), (23) and (24), respectively. The rest errors are calculated by using following formulas:

Sum of square error (SSE):

$$SSE = \sum_{i=1}^{n} (X_{A,i} - X_{P,i})^2 \tag{26}$$

Coefficient of variance (COV):

$$COV = \frac{RMSE}{\frac{1}{n}\sum_{i=1}^{n} X_{P,i}} \times 100 \tag{27}$$

Table 3. Statistical results of training process

Parameters	Training Function	MAE	R^2	RMSE
Thermal efficiency, η_{th}	LM-4	2.64395	0.99337	3.11437
	SCG-4	2.40804	0.99384	2.99610
	LM-5	1.23885	0.99787	1.77980
	SCG-5	2.45031	0.99382	2.99867
	LM-6	**0.02445**	**0.99999**	**0.04560**
	SCG-6	2.21554	0.99465	2.81480
	LM-7	1.55907	0.99689	2.14564
	SCG-7	1.92430	0.99534	2.62551
Exergy efficiency, η_{II}	LM-4	0.12917	0.93749	0.15481
	SCG-4	0.10456	0.95916	0.13370
	LM-5	0.08096	0.97094	0.09779
	SCG-5	0.13626	0.94039	0.16690
	LM-6	**0.03123**	**0.99509**	**0.03922**
	SCG-6	0.07991	0.96475	0.11359
	LM-7	0.10223	0.95511	0.10032
	SCG-7	0.16794	0.83109	0.20452

From Table 4, it has been found that values of MAE, SSE, MSE and COV are 0.06220, 1.3244, 0.026488 and 0.43471, respectively, for thermal efficiency. Similarly, for exergy efficiency, these values are 0.014689, 0.02257, 4.514E-4 and 0.36241E-1, respectively. Also the values of R^2 are 0.99921 and 0.95737 for thermal efficiency and exergy efficiency, respectively.

The comparison of results of present work and those available in the literature is shown in Table 5. The comparisons are based on the value of R in training, testing, validation and all processes combined. It is clearly observed that the values of R of present work in training, testing, validation and all processes were the highest, as compared to previous work of ANN models based on single and multiple output parameters. The above results reveal that the ANN model accurately predicted the energy and exergy efficiencies of the solar air heater.

Table 4. Performance of proposed MLP ANN model predicting energy and exergy efficiencies.

Parameters	**MAE**	**SSE**	**MSE**	**COV**	**R^2**
Thermal efficiency, η_{th}	0.06220	1.3244	2.648E-2	0.43471	0.99921
Exergy efficiency, η_{II}	0.01468	0.02257	4.514E-4	0.362E-1	0.95737

Table 5. The comparisons of results of present work and those available in the literature.

Authors	**Model Structure**	**Statistical results**			
		Training	**Validation**	**Testing**	**All**
		R1	R2	R3	R
Caner et al. [25]	8-20-1	0.99998	0.99985	0.99995	0.99997
Hamdan et al. [30]	5-20-5	0.99997	0.99998	0.99996	0.99997
Ghritlahre and Prasad [33]	5-5-3	0.99985	0.99991	0.99958	0.9998
Ghritlahre and Prasad [37]	6-6-1	0.99994	0.99943	0.99453	0.99942
Present work	6-6-2	1	1	0.99999	1

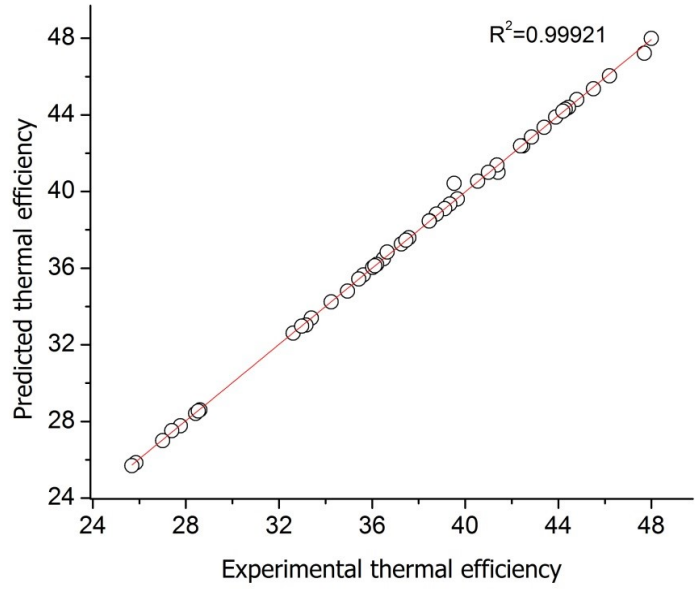

(a)

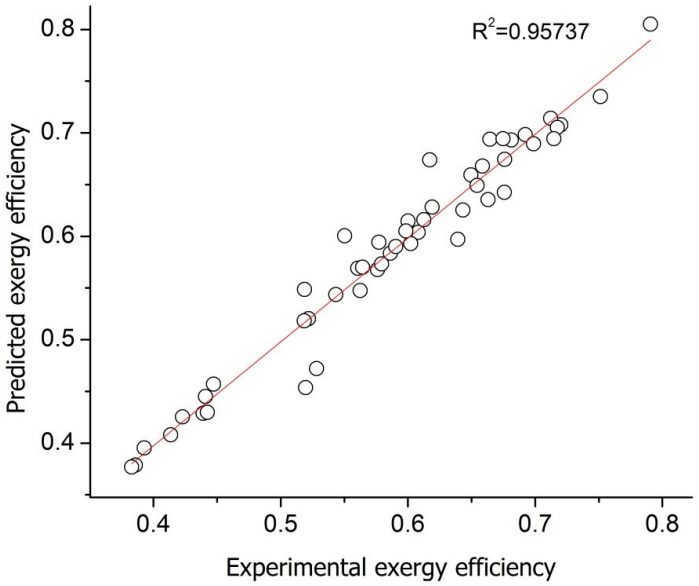

(b)

Figure 10. Comparison of experimental energy and exergy efficiency with ANN predicted energy and exergy efficiency.

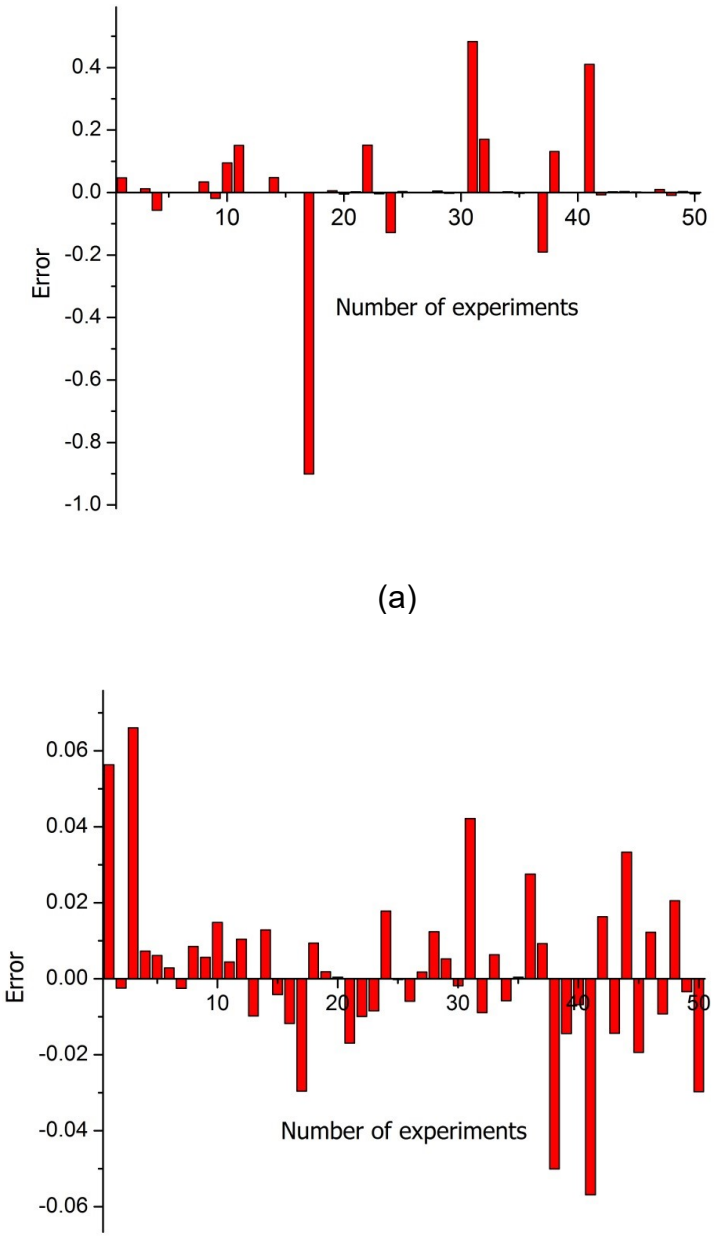

Figure 11. Absolute error for ANN predicted energy and exergy efficiency.

CONCLUSIONS

In this paper, ANN technique has been used to predict the energy and exergy efficiencies of roughened solar air heater. To achieve this objective, total 50 sets of

experimental data and calculated values of energy and exergy efficiencies were collected using traverse wire rib roughened absorber plate. The neural model has been developed with MLP structure using 6 parameters in the input layer and 2 parameters in the output layer. The neural model has been trained with 4 to 7 number of hidden neurons using two different types of learning algorithms, *i.e.*, LM and SCG. The 6-6-2 neural structure with LM learning algorithm is obtained as the optimal neural model for prediction of data. The performance prediction of ANN model has been evaluated on the basis of statistical error analysis. The values of MAE, SSE, MSE and COV for thermal efficiency were obtained as 0.06220, 1.3244, 2.648E-2 and 0.43471, respectively. Similarly, these values for exergy efficiency were found to be 0.01468, 0.02257, 4.514E-4 and 0.362E-1, respectively, which are very low as desired. The values of coefficient of determination (R^2) for energy efficiency and exergy efficiency are 0.99921 and 0.95737, respectively, which are very close to unity and thus perform accurate results of predicted values.

In view of high accuracy obtained in the predicted results of energy and exergy efficiencies of roughened solar air heater, the proposed MLP ANN model is recommended for energetic and exergetic performance analysis of any solar energy systems.

ACKNOWLEDGMENTS

The author gratefully acknowledges Department of Mechanical Engineering, National Institute of Technology, Jamshedpur, Jharkhand, India for their support in research work.

CONFLICTS OF INTEREST

The author declares that there is no conflict of interests regarding the publication of this paper.

REFERENCES

[1] Duffie, J.A., Beckman, W.A. (1991). *Solar Engineering of Thermal Processes*, second ed.,Wiley Publication, New York.

[2] Bhushan, B., Singh, R. (2010). A review on methodology of artificial roughness used in duct of solar air heaters, *Energy,* 35, 202–212. https://doi.org/10.1016/j.energy.2009.09.010

[3] Chamoli, S., Thakur, N.S., Saini,J.S. (2012). A review of turbulence promoters used in solar thermal system. *Renew. Sustain. Energy Rev.,* 16, 3154–3175. https://doi.org/10.1016/j.rser.2012.01.021

[4] Prasad, B.N. (2013). Thermal performance of artificially roughened solar air heaters. *Sol. Energy,* 91, 59–67. https://doi.org/10.1016/j.solener.2013.01.014

[5] Kumar, A., Prasad, B.N., Prasad, L. (2014). Thermal performance of artificially roughened solar air heaters, *M.Tech Thesis,* National Institute of Technology, Jamshedpur, Jharkhand, India.

[6] Mittal, M.K., Varshney, L. (2006). Optimal thermo hydraulic performance of a wire mesh packed solar heater. *Solar Energy,* 80, 1112-1120. https://doi.org/10.1016/j.solener.2005.10.004

[7] Singh, P.L., Deshpandey, B.D., Jena, P.C. (2015). Thermal performance of packed bed heat storage system for solar air heaters. *Energy for sustainable Development*, 29, 112-117. https://doi.org/10.1016/j.esd.2015.10.010

[8] Ajam, H., Farahat, S., Sarhaddi, F. (2005). Exergetic optimization of solar air heaters and comparison with energy analysis. *Int J Thermodyn,* 8(4), 183–190. http://dergipark.gov.tr/download/article-file/65674

[9] Esen, H. (2008). Experimental energy and exergy analysis of a double-flow solar air heater having different obstacles on absorber plates. *Build and Environ,* 43,1046–1054. https://doi.org/10.1016/j.buildenv.2007.02.016

[10] Akpinar, E.K., Koçyigit, F. (2010). Experimental investigation of thermal performance of solar air heater having different obstacles on absorber plates. *Int Commun Heat Mass Transfer,* 37, 416–421. https://doi.org/10.1016/j.icheatmasstransfer.2009.11.007

[11] Alta, D., Bilgili, E., Ertekin, C., Yaldiz, O. (2010). Experimental investigation of three different solar air heaters: Energy and exergy analyses. *Applied Energy,* 87 , 2953–2973 https://doi.org/10.1016/j.apenergy.2010.04.016

[12] Bayrak, F., Oztop, H.F., Hepbasli, A. (2013). Energy and exergy analyses of porous baffles inserted solar air heaters for building applications. *Energy Build,* 57, 338-345. https://doi.org/10.1016/j.enbuild.2012.10.055

[13] Panwar, N., Kaushik, S., Kothari, S. (2012). A review on energy and exergy analysis of solar dying systems. *Renew Sustain Energy Rev,* 16(5), 2812-2819. https://doi.org/10.1016/j.rser.2012.02.053

[14] Saidur, R., BoroumandJazi, G., Mekhlif, S., Jameel, M. (2012). Exergy analysis of solar energy applications. *Renew Sustain Energy Rev,* 16(1), 350-356. https://doi.org/10.1016/j.rser.2011.07.162

[15] Kumar, L., Mukesh Sarvaiya, R.M., Bhagoriya, J.L. (2012). Exergy evaluation of packed bed solar air heater. *Renewable and Sustainable Energy Reviews,* 16, 6262-6267. https://doi.org/10.1016/j.rser.2012.04.024

[16] Park, S., Pandey, A., Tyagi, V., Tyagi, S. (2014). Energy and exergy analysis of typical renewable energy systems, *Renewable and Sustainable Energy Reviews,* 30, 105-123. https://doi.org/10.1016/j.rser.2013.09.011

[17] Kalogirou, S.A. (2000). Applications of artificial neural-networks for energy systems. *Applied Energy,* 67(1-2), 17–35. https://doi.org/10.1016/S0306-2619(00)00005-2

[18] Yang, I.H.,Yeo, M.S., Kim, K.W. (2003). Application of artificial neural network to predict the optimal start time for heating system in building. *Energy Conversion and Management,* 44, 2791–2809. https://doi.org/10.1016/S0196-8904(03)00044-X

[19] Facao, J., Varga, S., Oliveira, A.C. (2004). Evaluation of the Use of Artificial Neural Networks for the Simulation of Hybrid Solar Collectors. *International Journal of Green Energy,* 1(3), 337–352. https://doi.org/10.1081/GE-200033649

[20] Ertunc, H.M., Hosoz, M.(2006). Artificial neural network analysis of a refrigeration system with an evaporative condenser. *Applied Thermal Engineering,* 26, 627–635. https://doi.org/10.1016/j.applthermaleng.2005.06.002

[21] Kalogirou, S.A. (2006). Prediction of flat-plate collector performance parameters using artificial neural networks. *Solar Energy,* 80, 248–259. https://doi.org/10.1016/j.solener.2005.03.003

[22] Yilmaz, S., Atik, K. (2007). Modeling of a mechanical cooling system with variable cooling capacity by using artificial neural network. *Applied Thermal Engineering,* 27, 2308–2313. https://doi.org/10.1016/j.applthermaleng.2007.01.030

[23] Sozen, A., Menlik, T., Unvar, S. (2008). Determination of efficiency of flat-plate solar collectors using neural network approach. *Expert Syst. Appl.,* 35(4), 1533–1539. https://doi.org/10.1016/j.eswa.2007.08.080

[24] Kurt, H., Atik, K., Ozkaymak, M., Recebli, Z. (2008). Thermal performance parameters estimation of hot box type solar cooker by using artificial neural network. *International Journal of Thermal Sciences,* 47, 192–200. https://doi.org/10.1016/j.ijthermalsci.2007.02.007

[25] Caner, M., Gedik, E., Kecebas, A. (2011). Investigation on thermal performance calculation of two type solar air collectors using artificial neural network. *Expert Syst. Appl.,* 38(3), 1668–1674. https://doi.org/10.1016/j.eswa.2010.07.090

[26] Nazghelichi, T., Aghbashlo, M., Kianmehr, M.H., Omid, M. (2011). Prediction of Energy and Exergy of Carrot Cubes in a Fluidized Bed Dryer by Artificial Neural Networks. *Drying Technology: An International Journal,* 29(3), 295-307. https://doi.org/10.1080/07373937.2010.494237

[27] Aghbashlo, M., Mobli, H., Rafiee, S., Madadlou, A. (2012). The use of artificial neural network to predict exergetic performance of spray drying process: A preliminary study. *Computers and Electronics in Agriculture,* 88, 32–43. https://doi.org/10.1016/j.compag.2012.06.007

[28] Benli, H. (2013). Determination of thermal performance calculation of two different types solar air collectors with the use of artificial neural networks. *Int. J. of Heat and Mass Transfer,* 60, 1-7. https://doi.org/10.1016/j.ijheatmasstransfer.2012.12.042

[29] Kalogirou, S.A., Mathioulakis, E., Belessiotis, V. (2014). Artificial neural networks for the performance prediction of large solar systems. *Renewable Energy,* 63 ,90-97. https://doi.org/10.1016/j.renene.2013.08.049

[30] Hamdan, M. A., Abdelhafez, E. A., Hamdan, A. M., and Khalil, R. A. H. (2016). Heat Transfer Analysis of a Flat-Plate Solar Air Collector by Using an Artificial Neural Network. *Journal of Infrastructure Systems*, 22(4), A4014004. DOI: 10.1061/(ASCE)IS.1943-555X.0000213.

[31] Jani, D.B., Mishra, M., Sahoo, P.K. (2016). Performance prediction of solid desiccant – vapor compression hybrid air-conditioning system using artificial neural network. *Energy,* 103, 618-629. http://dx.doi.org/10.1016/j.energy.2016.03.014

[32] Jani, D.B., Mishra, M., Sahoo, P.K. (2016). Performance prediction of rotary solid desiccant dehumidifier in hybrid air-conditioning system using artificial neural network. *Appl Therm Eng,* 98, 1091–1103.

http://dx.doi.org/10.1016/j.applthermaleng.2015.12.112
[33] Ghritlahre, H.K., Prasad, R.K. (2017). Prediction of thermal performance of unidirectional flow porous bed solar air heater with optimal training function using Artificial Neural Network. *Energy Procedia,* 109, 369 – 376. https://doi.org/10.1016/j.egypro.2017.03.033
[34] Ghritlahre, H.K. ,Prasad, R.K. (2017). Energetic and exergetic performance prediction of roughened solar air heater using artificial neural network. *Ciência e Técnica Vitivinícola*, 32 (11), 2-24.
[35] Ghritlahre, H.K. , Prasad, R.K. (2018). Application of ANN technique to predict the performance of solar collector systems - A review. *Renewable and Sustainable Energy Reviews,* 84, 75–88. https://doi.org/10.1016/j.rser.2018.01.001
[36] Ghritlahre, H.K., Prasad, R.K. (2018). Exergetic Performance Prediction of roughened Solar Air Heater Using Artificial Neural Network. *Strojniški vestnik - Journal of Mechanical Engineering,* 64 (3), 195–206. http://dx.doi.org/10.5545/sv-jme.2017.4575
[37] Ghritlahre, H.K., Prasad, R.K. (2018). Development of Optimal ANN Model to Estimate the Thermal Performance of Roughened Solar Air Heater Using Two different Learning Algorithms. *Annals of Data Science,* 5(3),453–467. https://doi.org/10.1007/s40745-018-0146-3
[38] Ghritlahre, H.K., Prasad, R.K. (2018). Investigation on heat transfer characteristics of roughened solar air heater using ANN technique. *International Journal of Heat and Technology,* 36 (1), 102-110. https://doi.org/10.18280/ijht.360114
[39] Ghritlahre, H.K., Prasad, R.K. (2018). Investigation of thermal performance of unidirectional flow porous bed solar air heater using MLP, GRNN, and RBF models of ANN technique. *Thermal Science and Engineering Progress,* 6, 226-235. https://doi.org/10.1016/j.tsep.2018.04.006
[40] Ghritlahre, H.K., Prasad, R.K. (2018). Exergetic performance prediction of solar air heater using MLP, GRNN and RBF models of artificial neural network technique. *Journal of Environmental Management,* 223, 566-575. https://doi.org/10.1016/j.jenvman.2018.06.033
[41] Haykin, S. (1994). *Neural networks, a comprehensive foundation,* New Jersey: Prentice- Hall.
[42] Cengel, Y.A., Boles, M.A. (2006). *Thermodynamics: an engineering approach*. 5th ed. New York: McGraw-Hill.

Trends in Renewable Energy
OPEN ACCESS ISSN:2376-2144
Peer-Reviewed Article futureenergysp.com/index.php/tre

A Global Review of Empirical Models for Estimating Photosynthetically Active Radiation

Samuel Chukwujindu Nwokolo[1],* Solomom Okechukwu Amadi[2]

1: Department of Physics, University of Calabar, Calabar, Nigeria
2: Department of Physics/Geology/Geophysics, Federal University Ndufu-Alike Ikwo, Nigeria

Received August 6, 2018; Accepted August 24, 2018; Published October 4, 2018

A good working knowledge of photosynthetically active radiation (PAR) is of vital requirement for determining the terrestrial photosynthesis, primary productivity calculation, ecosystem-atmosphere carbon dioxide, plant physiology, biomass production, natural illumination in greenhouses, radiation climate, remote sensing of vegetation, and radiation regimes of plant canopy, photosynthesis, productivity models of vegetation, etc. However, routine measurement of PAR is not available in most location of interest across the globe. During the past 77 years in order to estimate PAR on hourly, daily and monthly mean basis, several empirical models have been developed for numerous locations globally. As a result, numerous input parameters have been utilized and different functional forms applied. This study was aim at classifying and reviewing the empirical models employed for estimating PAR across the globe. The empirical models so far utilized were classified into ten main categories and presented base on the input parameters applied. The models were further reclassified into numerous main sub-classes (groups) and finally presented according to their developing year. In general, 757 empirical models, 62 functional forms and 32 groups were reported in literature for estimating PAR across the globe. The empirical models utilized were equally compared with models developed using different artificial neural network (ANN); and the result revealed that ANN models are more suitable for estimating PAR across the globe. Thus, this review would provide solar energy researchers with input parameters and functional forms that have been widely used to up to date, and recognizing their importance in estimating PAR globally.

Keywords: Photosynthetically active radiation; empirical models; classification; functional forms; world review

1. Introduction

Photosynthetically active radiation (PAR) is a component of global solar radiation (H) that covers both photon and energy terms between 400-700 nm waveband incident per unit time on a unit surface. This radiometric flux (PAR) is both photon and energy term capable for driving electron transport within the photosynthetic process used by plants in synthesizing their food as shown by the chemical equation given by Nwokolo [1] and Nwokolo and Ogbuezie [2]:

**Corresponding author:* nwokolosc@stud.unical.edu.ng, sam31628@gmail.com
Tel.: +2348066806702

Tr Ren Energy, 2018, Vol.4, No.2, 236-327. doi: 10.17737/tre.2018.4.2.0079

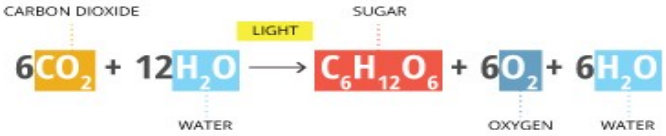

(1)

where the light (PAR) represents light energy wavelength range (400-700 nm) that is the best fit for photosynthesis to occur.

PAR is not only important for single plant leaves, plant communities and modeling vegetation growing due to its relationship with botanical photosynthesis process but a viable irradiance energy needed as a baseline for estimating and understanding PAR parameters such as gross primary productivity (GPP), light use efficiency (LUE) and net ecosystem exchange of carbon dioxide (NEE) for agricultural and ecological studies, etc.

The accurate determination and clear understanding of PAR is needed for many applications such as analyzing terrestrial photosynthesis, primary productivity calculation and ecosystem-atmosphere carbon dioxide [3,4]; plant physiology, biomass production and natural illumination in greenhouses [5]; comprehensive studies of radiation climate, remote sensing of vegetation, radiation regimes of plant canopy, photosynthesis and productivity models of vegetation [6]; carbon dynamic, agricultural productivity, and atmospheric Physics [7-9]; terrestrial photosynthesis modeling [10-12]; radiation forcing effect, energy management, hydrological process and biometeorology [13-14]; studies of crop production, remote sensing of vegetation and carbon cycle modeling [15-16]; evolution of environmental and agricultural fields [17]; agriculture, atmospheric physics, forestry, ecology, energy management and photon science [18-19]; plant physiology, crop growth, biomass production and agricultural meteorology [20-21]; controlling the exchange of carbon between atmosphere, oceans and the terrestrial biosphere [22-25]; radiation intercepted by the canopy, the establishment of leaf photosynthesis and the productivity of agricultural crops and forests [26-27]; and calculating the euphotic depth in the ocean [28].

PAR as a component of solar radiation spectrum is extremely important because it is the solar energy source for vegetative photosynthesis to provide mankind with products such as food and fiber sources, biofuels carriers and additional materials sources that support industrial process. PAR also plays significant roles in plant growth, and it is the principal factor in the rate of solar energy conversion into biological mediated energy.

Therefore, PAR is an indispensable atmospheric radiometric flux nature needed for balance distribution of varieties of plants and perfecting the ecosystem in the horizons across different climatic and geographical regions of the world. The oxygen (O_2) needed by man for respiration is powered by PAR. Thus, the study of PAR is a necessity for understanding how plants, animals and mankind interact and relate with its immediate ecosystem.

Measurement of PAR have been performed in many parts of the world using a variety of instrument such as Eppley precision spectral pyrometer (PSP) and PAR lite. Apart from these radiometric flux instruments, quantum sensor often used for PAR measurement have problems, such as cosine errors, spectral errors, and the lack of a standard absolute PAR value [29-31].

As a result of cost of measuring equipment, its maintenance and calibration requirements, in rural and developing countries in Africa and several places around the

world, a worldwide routine network for the measurement of PAR on like global solar radiation is not yet established. In order to correct these anomalies, different empirical models have been developed [32-34], few of them using satellite data [22, 35]. In another technique, PAR is commonly estimated as a constant ratio of the global solar radiation (H). Numerous authors have studied this ratio [36-43].

Therefore, empirical models that estimate PAR based on global solar radiation (H) are important and are classified into two types. One employed the constant ratio of the global solar radiation (PAR/H). Depending on weather PAR is expressed in energy units (PAR^e Wm^{-2}, MJm^{-2} etc.) or photon units (PAR^P, E/mJ, $\mu Em^{-2}S^{-1}$ etc.), there are two types of ratios:

$$\frac{PAR^e}{H} \text{ (unitless)} \quad (2)$$

$$\frac{PAR^p}{H} \text{ (Unit: } \mu molJ^{-1}\text{, E/mJ, } \mu Em^{-2}S^{-1} \text{ etc.)} \quad (3)$$

According to Walczak *et al.* [44], since the photosynthetic efficiency of green plants is directly proportional to the number of photons absorbed in the spectral range (400-700nm) and not to their energy, therefore, it is more convenient to express PAR using photon number e.g. $\mu Em^{-2}S^{-1}$ (quanta $mol^{-1}s^{-1}$ or $\mu mol^{-1}s^{-1}$) than radiant energy (Wm^{-2}, MJm^{-2}).

In addition to the above mentioned ratio, the following conversion ratio has been employed [4, 45-46]:

$$\frac{PAR^p}{PAR^e} \text{ (Unit: } \mu molJ^{-1}\text{, E/mJ, } \mu Em^{-2}S^{-1} \text{ etc.)} \quad (4)$$

McCree [45] recorded the value of PAR^p/PAR^e as 4.57 $\mu molJ^{-1}$. Assuming this value to be constant, many studies [47-48] have applied it. However, Jacovides *et al.* [46] and Dye [4] reported slightly different values – 4.53 $\mu molJ^{-1}$ and 4.56 $\mu molJ^{-1}$, respectively. Although these values are quite similar, the influence of PAR^p/PAR^e on climatic conditions is not well documented. As a result, Akitsu *et al.* [49] observed that PAR^p/PAR^e may change within 3 % around McCree's constant value (4.57 $\mu molJ^{-1}$) in response to changes in water vapour pressure, solar zenith angle and clearness index. Thus, Akitsu *et al.* [49] recommended the use of McCree's value as it have been accepted by numerous researchers, though the ratio is not strictly constant.

However, numerous researchers have observed that PAR ratio varied according to location [48]; seasons [43, 50]; sky conditions [51-53]; sky clearness, sky brightness and atmospheric depth for the solar beam [54-55]; relative sunshine duration and water vapour pressure [50, 55]; altitude [56]; irradiance intensity [57]; day length [57-58]; Ozone and other atmospheric gases [53, 58-59]; relative humidity [60], minimum and maximum temperature [61]; optical air mass [62-64]; cloud amount and turbidity [55]; global solar radiation [41, 65-67]; clearness index [48, 68-73]; site, season, local time and weather conditions [49]. Thus, each ratio remains incompletely understood as to how it varies with

climatic factors such as water vapour pressure (WVP); solar zenith angle (Θ) and sky cloudiness. Therefore, it is practically difficult to assume reasonable values of these ratio at specific sites and in specific seasons.

For these reasons, numerous studies have employed meteorological parameters, geographical parameters, geometrical factors and astronomical parameters as a single variable or combine parameters to relate with PAR, PAR/H, PAR fraction (PAR/PAR_o) or PAR coefficient (PAR/H_o) etc. (where H_o and PAR_o are the extraterrestrial solar radiation and extraterrestrial PAR respectively) for their estimation [41, 50, 55,61-62, 64-67, 74].

However, solar radiation components have been estimated using different artificial neural network (ANN) techniques in recent decades which constitute a widely accepted method offering an alternative way to synthesize complex problems associated with solar energy estimation such as applying only calculable atmospheric, meteorological, astronomical, geographical, geometrical parameters such as extraterrestrial solar radiation, latitude, altitude, longitude, maximum sunshine duration, azimuth angle, solar declination, cosine of solar zenith angle, and hour angle to estimate PAR. The capacity of ANN technique to accept many input parameters for a particular model which is not possible applying empirical technique that strengthened its reliability is one of highest discoveries and attainment of solar energy researchers in recent times. Moreover, the technique of applying ANN models compared to conventional techniques according to recent studies [75-77] have offer greater accuracy with estimation error in a range (less than 20 %) and could be very good in terms of PAR estimation as much more ANN and other soft computing approaches are demanding in the domain of renewable energy resource estimation.

Therefore, the main purpose of the study was to review empirical models fitted in literature for estimating PAR at numerous geographical locations distributed around the globe and its objectives are identifying several input parameters and functional forms ever applied for estimating PAR across the globe; classify the empirical models commonly employed across the globe according to the main input parameters; compare the performance of empirical and ANN computing models applied and decide the best technique that can yield high accuracies of estimation for future purposes and finally identify the research gap.

Thus, this review would be helpful to solar energy researchers to identify and determine to a large extent the numerous utilized input parameters and functional forms with their corresponding categories ever applied for estimating PAR across the globe and also recognize their significance.

2. Model Parameters

Basic parameters such as maximum sunshine duration, daily and hourly extraterrestrial solar radiation on the horizontal surfaces, hourly and daily PAR, standard atmospheric pressure at sea level (1013 hPa), solar constant, zenith angle, clearness of the sky (ε), and brightness of the skylight (Δ) are significant for the models employed in this

review for estimating PAR. The maximum sunshine duration is expressed mathematically as:

$$S_o = \frac{2}{15}\cos^{-1}\left[-\tan\delta\tan\phi\right] \quad (5)$$

$$\delta = 23.45\sin\left[\frac{360(n+284)}{365}\right] \quad (6)$$

where ϕ is the latitude, δ is the solar declination given by Yaniktepe and Genc [78] and n the number of days of the year starting from first January. The daily extraterrestrial solar radiation is the solar radiation intercepted by horizontal surface during a day without the atmosphere and hourly extraterrestrial radiation has similar definition.

Hourly extraterrestrial solar radiation on the horizontal surface is given by Zhang *et al.* [79] as:

$$I_O = \frac{12\times 3600\times I_{SC}}{\pi}\left(1+0.033\cos\frac{360n}{365}\right)\times\left(\cos\phi\cos\delta(\sin\omega_2-\sin\omega_1)\sin\omega_S+\frac{\pi(\omega_2-\omega_1)}{180}\sin\phi\sin\delta\right) \quad (7)$$

While the daily extraterrestrial solar radiation on the horizontal surface is given by Yaniktepe and Genc [78] as:

$$H_O = \frac{24}{\pi}I_{SC}\left(1+0.033\cos\frac{360n}{365}\right)\times\left(\cos\phi\cos\delta\sin\omega_S+\frac{2\pi\omega_S}{360}\sin\phi\sin\delta\right) \quad (8)$$

Where the mean sunrise hour angle (ω_s) can be evaluated as:

$$\omega_s = \cos^{-1}\left[-\tan\delta\tan\phi\right] \quad (9)$$

I_{SC} is the solar constant, ω_1 and ω_2 are the limit hour angle of an hour, in which ω_2 is the larger, all in degrees and other symbols retain their usual meaning.

Hourly extraterrestrial PAR flux (PAR_o) according to Frouin and Pinker [15] and Hu *et al.* [80] can be estimated from extraterrestrial solar radiation (H_o), with a fraction of 0.5. Therefore, hourly and daily PAR_o can be calculated by multiplying the ratio 4.57 of the energy flux density to photosynthetic photon flux density as suggested by Dye [4]. Thus, the hourly PAR_o can be expressed as:

$$PAR_O = 0.5\times 4.57(I_O) \quad (10)$$

And daily PAR_o can be calculated as:

$$PAR_O = 0.5\times 4.57(H_O) \quad (11)$$

The sky clearness (ε) and brightness of the skylight (Δ) can be evaluated as proposed by Wang *et al.* [71]:

$$\varepsilon = \frac{H_d+H_b}{H_d} \quad (12)$$

$$\Delta = \frac{H_d}{H_b\cos(\theta)} \quad (13)$$

The cosine of sun zenith angle (θ) is expressed as:

$$\cos(\theta) = \left(\cos\delta\cos\phi\cos\omega+\sin\delta\sin\phi\right) \quad (14)$$

While the relative optical mass (m) can be calculated as proposed by Wang *et al.* [71]:

$$m = \frac{1}{\cos(\theta) + 0.15(93.885 - \theta)^{-1.253}} \quad (15)$$

Where H_d and H_b are the diffuse and direct radiation on the earth horizontal surface and other symbols retain their usual meaning.

3. Evaluation Metrics

Evaluation, principally, compares how good the observed and estimated fit each other. This evaluation is applied at numerous steps of the computing model development as for instance during the evaluation of the estimation model itself (during the training of a statistical model for instance), for judging the improvement of the computing model after some modifications and for comparing numerous computing models. As previously mentioned, this performance comparison is not easy for numerous reasons such as different estimated time horizons, numerous time scale of the estimated data and variability of the meteorological conditions from one site to another one. It works by comparing the estimated outputs $\hat{y}$) with observed data y which are also measured data themselves linked to an error (or precision) of a measure.

Graphic tools are available for estimating the adequacy of the computing model with the experimental measurements via:

1. Time series of estimated global radiation in comparison with measured global radiation which allows to visualize easily the prediction quality. In Fig. 1a, for instance, a high estimate accuracy in clear-sky conditions and a low one in partly cloudy conditions can be seen.
2. Scatter plots of estimated over measured global radiation (as shown in Fig. 1b) which can reveal systematic bias and deviations depending on the global radiation conditions and show the range of deviations that are related to the estimates.
3. Receiver Operating Characteristic (ROC) curves which compare the rates of true positives and false positive.

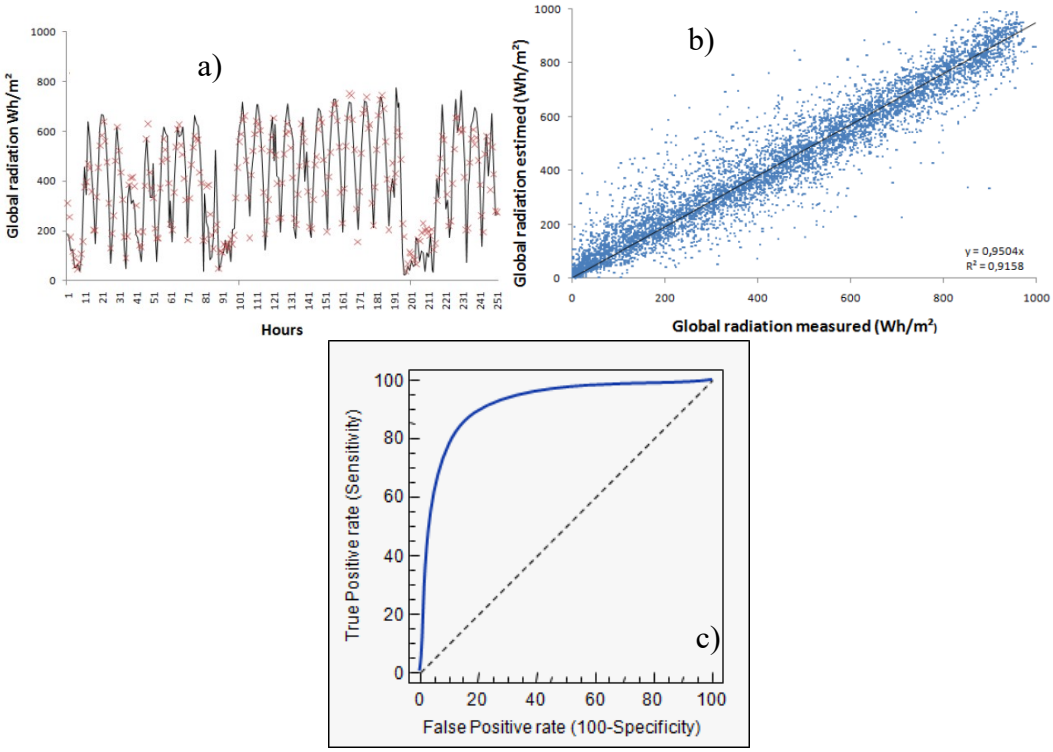

Figure 1: a) Time series of predicted and measured global radiation for 2008 in Ajaccio (France); b) Scatter plot of predicted vs. measured global radiation in Ajaccio (France); c) Example of ROC curve (an ideal ROC curve is near the upper left corner) Lauret *et al.* [81].

Up till now, there is no standard evaluation measures accepted for photosynthetically active radiation measurement, which makes the comparison of the estimating methods difficult. Sperati *et al.* [82] presented a benchmarking exercise within the framework of the European Actions Weather Intelligence for Renewable Energies (WIRE) with the purpose of evaluating the performance of state of the art computing models for short term renewable energy estimation or forecasting. This research is a very good example of reliability parameter utilization. They concluded that: "More work using more test cases, data and computing models needs to be performed in order to achieve a global overview of all possible conditions. They also pointed out that test cases located all over Europe, the US and other relevant countries should be considered, in an effort to represent most of the possible meteorological conditions". This study therefore illustrates very well the difficulties of performance comparisons encountered for photosynthetically active radiation estimation.

The commonly applied statistics for photosynthetically active radiation estimation include the following:

The mean bias error (MBE) represents the mean bias of the estimation:

$$MBE = \frac{1}{N} \times \sum_{i=1}^{N} \left(\hat{y}(i) - y(i) \right) \quad (16)$$

with $\hat{y}$ is the estimated photosynthetically active radiation, y the measured photosynthetically active radiation and N the number of observations. The estimation will under-estimate or over-estimate the observations. Thus, MBE is not a good statistical indicator for the relatability of a computing model because the errors compensate each other but it allows to see how much it overestimates or underestimates.

The mean absolute error (MAE) is appropriate for comparing photosynthetically active radiation estimation with linear cost functions, i.e., where the costs resulting from a poor estimation are proportional to the estimation error:

$$MAE = \frac{1}{N} \times \sum_{i=1}^{N} \left| \hat{y}(i) - y(i) \right| \quad (17)$$

The mean square error (MSE) applies the squared of the difference between observed and predicted data. This statistical indicator penalizes the highest gaps:

$$MSE = \frac{1}{N} \times \sum_{i=1}^{N} \left(\hat{y}(i) - y(i) \right)^2 \quad (18)$$

MSE is principally the statistical parameter which is minimized by the training algorithm.

The root mean square error (RMSE) is more sensitive to big estimation errors, and thus is good for applications where small errors are more tolerable and larger errors cause disproportionately high costs, as in the case of utility applications [83]. It is probably the reliability parameter that is most appreciated and employed:

$$RMSE = \sqrt{MSE} = \sqrt{\frac{1}{N} \times \sum_{i=1}^{N} \left(\hat{y}(i) - y(i) \right)^2} \quad (19)$$

The mean absolute percentage error (MAPE) is close to the MAE but each gap between observed and predicted value is divided by the observed value so as to consider the relative gap.

$$MAPE = \frac{1}{N} \times \sum_{i=1}^{N} \left| \frac{\hat{y}(i) - y(i)}{y(i)} \right| \quad (20)$$

This statistical indicator has a challenge that it is unstable when y(i) is near zero and it cannot be defined for y(i)=0.

Of recent, these errors are normalized particularly for the RMSE; as reference the mean value of global radiation is generally employed but other definitions can be applied:

$$nRMSE = \frac{\sqrt{\frac{1}{N} \times \sum_{i=1}^{N} \left(\hat{y}(i) - y(i) \right)^2}}{\bar{y}} \quad (21)$$

with $\bar{y}$ is the mean value of y. Other statistical indicators exist and can be employed as the correlation coefficient (R), coefficient of determination (R^2), or the index of agreement (d) which are normalized between 0 and 1.

As the estimation accuracy strongly depends on the location and time period applied for evaluation and on other parameters, it is difficult to evaluate the quality of an estimation from accuracy metrics alone. Then, it is the best to compare the accuracy of different estimations against a common set of test data Pelland *et al.* [84]. "Trivial" estimation approach can be applied as a reference [83], the most common one is the

persistence model ("things stay the same", Trapero *et al.* [85] where the estimation is always equal to the last known data point. The photosynthetically active radiation has a deterministic component due to the geometrical path of the sun. This characteristic may be included as a constraint to the simplest form of persistence in considering as an example, the measured data of the previous day or the previous hour at the same time as an estimation value. Other common reference forecasts include those based on climate constants and simple autoregressive methods. Such comparison with referenced NWP computing model is shown in Figure 2. Generally, after 1 hour the forecast is better than persistence. For forecast horizons of more than two days, climate averages show lower errors and should be preferred for photosynthetically active radiation estimation.

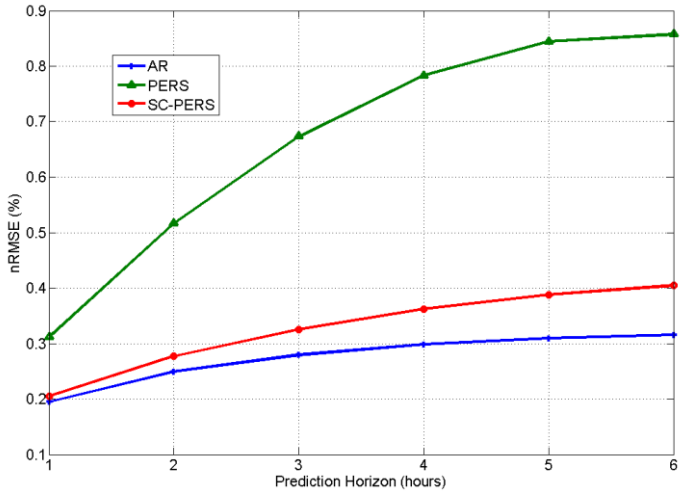

Figure 2: Relative RMSE of forecasts (persistence, auto regression, and scaled persistence) and of reference models depending on the forecast horizon Lauret *et al.* [81].

Classically, a comparison of performance is performed with a reference computing model and to do it, a skill factor is employed. The skill factor or skill score defines the difference between the forecast and the reference forecast normalized by the difference between a perfect and the reference forecast Lauret *et al.* [81]:

$$SkillScore = \frac{Metric_{forecasted} - Metric_{reference}}{Metric_{perfectfoecast} - Metric_{reference}} = 1 - \frac{MSE_{forecatd}}{MSE_{reference}} \quad (22)$$

Its value thus ranges between 1 (perfect forecast) and 0 (reference forecast). A negative value indicates a performance which is even worse compared to the reference (observed data). Skill scores can be adopted not only for comparison between observed and estimated PAR values but also for inter-comparisons of different photosynthetically active radiation estimation techniques.

4. Empirical Models

An empirical model correlates PAR, PAR/H, PAR/PAR_o and PAR/H_o with other easily measureable and calculable parameters such as clearness index, global solar radiation, relative humidity, minimum and maximum temperature, optical air mass, cloud amount, water vapour pressure, turbidity, sunshine duration and combination of the above parameters by employing concise mathematical functions. Numerous empirical models have been reported in literature for estimating PAR on the horizontal surface either on hourly mean basis (HB) or daily mean basis (DB) or monthly mean daily basis (MB) across the globe. In this review, the PAR models are classified according to the basis of their input parameters applied in correlating with PAR, PAR/H, PAR/PAR_o and PAR/H_o. it has been established that PAR is relatively influenced by meteorological parameters, astronomical factors, geographical factors, and geometrical factors. This could be attributed to the uniqueness of local climate in determining the atmospheric and meteorological parameters that best fit that particular locality. This also depends on the availability of input meteorological/atmospheric parameters that a given radiometric station or an individual is capable of measuring or calculating routinely which finally turned out to be the best input parameter at the disposal of the researcher for estimating PAR in that locality. Thus, in this review, the empirical models for estimating PAR can be classified into ten (10) following categories based on the applied meteorological and atmospheric parameters via:

1. Global solar radiation-based models
2. Relative humidity-based models
3. Temperature-based models
4. Optical air mass-based models
5. Cloud amount-based models
6. Water vapour pressure-based models
7. Turbidity-based models
8. Sunshine duration-based models
9. Clearness index-based models
10. Hybrid parameter-based models

4.1 Global Solar Radiation-Based Models

Since PAR is a component of global solar radiation (H) on the horizontal surface, solar radiation researcher applied it for estimating PAR and the ratio of PAR/H as a result of its great important and influence for determining the PAR striking a particular location at the top of the atmosphere and its comprehensive impact on PAR on the horizontal surface. Thus, the functional forms and models employed across the globe are presented in this section.

4.1.1 Group 1

Empirical models from this group are parameterized as the ratio of photosynthetically active radiation $\left(PAR^{p}\right)$ to global solar radiation $\left(H\right)$ expressed in photon

units (μmolJ^{-1}, E MJ^{-1} etc.) according to their developing year. The functional form is given as:

$$PAR^p = a(H) \quad (23)$$

Where a is the regression coefficient

McCree [36] developed the following MB model for New Zealand as:

$$PAR^p = 2.70(H) \quad (24)$$

Monteith [86] developed the following DB model for the tropics under clear sky as:

$$PAR^p = 2.23(H) \quad (25)$$

Szeicz [57] proposed the following DB model from January-December for Cambridge, UK as:

$$PAR^p = 2.33(H) \quad (26)$$

Britton and Dodd [56] developed the following DB model for January-December in College Station, TX, USA as:

$$PAR^p = 2.17(H) \quad (27)$$

Hodges and Kanemasu [87] proposed the following DB model for Manhattan, Kanas as:

$$PAR^p = 2.17(H) \quad (28)$$

Stanhill and Fuchs [88] obtained the following HB models for numerous locations. For Rockeville, MD, USA (January-December)

$$PAR^p = 2.24(H) \quad (29a)$$

For Washington DC (January-December)

$$PAR^p = 2.23(H) \quad (29b)$$

For Jerusalem, Isreal (January-December)

$$PAR^p = 2.19(H) \quad (29c)$$

For Dar es Salaan, Tanzania (October-January)

$$PAR^p = 2.33(H) \quad (29d)$$

For Washington, Rockville and Jerusalem

$$PAR^p = 2.24(H) \quad (29e)$$

Arkin *et al.* [89] stimulated the following DB model for Temple, Texas as:

$$PAR^p = 2.89(H) \quad (30)$$

Hodges *et al.* [90] reported the following DB model for Manhattan, Kanas as:

$$PAR^p = 2.55(H) \quad (31)$$

Howell *et al.* [91] proposed the following DB models for University of California USA as:

$$PAR^p = 2.058(H) \quad (32)$$

Kvifte *et al.* [92] established the following DB models for several locations as follows:

For Copenhagen, Denmark

$$PAR^p = 2.239(H) \quad (33a)$$

For Aas, Norway

$$PAR^p = 2.194(H) \quad (33b)$$

For Ultuna, Sweden (May-October)

$$PAR^p = 2.102(H) \quad (33c)$$

For Reykjavik, Iceland (May-October)

$$PAR^p = 2.102(H) \quad (33d)$$

For Sodankyla, Finland (May-October)

$$PAR^p = 2.194(H) \quad (33e)$$

For Tromso, Norway (May-October)

$$PAR^p = 2.056(H) \quad (33f)$$

Rodskjer [93] established the following DB model for Ultuna, Sweden as:

$$PAR^p = 2.125(H) \quad (34)$$

Meek *et al.* [41] obtained the following MB mo (42m)

Finch *et al.* [43] obtained thee following DB models under various sky conditions for Lusaka, Zambia as follows:

For clear sky

$$PAR^p = 1.914(H) \quad (43a)$$

For cloudy sky

$$PAR^p = 2.111(H) \quad (43b)$$

Wang *et al.* [54] reported the following MB model for Naeba Mountain in China as:

$$PAR^p = 1.94(H) \quad (43c)$$

Wang *et al.* [71] recorded the following MB models in Wuhan, China

For January

$$PAR^p = 1.70(H) \quad (44a)$$

For February

$$PAR^p = 1.73(H) \quad (44b)$$

For March

$$PAR^p = 1.78(H) \quad (44c)$$

For April

$$PAR^p = 1.87(H) \quad (44d)$$

For May

$$PAR^p = 1.92(H) \quad (44e)$$

For June

$$PAR^{p} = 1.97(H) \quad (44f)$$

For July

$$PAR^{p} = 2.00(H) \quad (44g)$$

For August

$$PAR^{p} = 2.06(H) \quad (44h)$$

For September

$$PAR^{p} = 1.96(H) \quad (44i)$$

For October

$$PAR^{p} = 1.92(H) \quad (44j)$$

For November

$$PAR^{p} = 1.83(H) \quad (44k)$$

For December

$$PAR^{p} = 1.75(H) \quad (44L)$$

For January-December

$$PAR^{p} = 1.93(H) \quad (44m)$$

For Dry Seasons

$$PAR^{p} = 1.78(H) \quad (44n)$$

For Humid season

$$PAR^{p} = 1.95(H) \quad (44o)$$

For clear sky

$$PAR^{p} = 1.78(H) \quad (44p)$$

For intermediate

$$PAR^{p} = 1.94(H) \quad (44q)$$

For cloudy

$$PAR^{p} = 2.01(H) \quad (44r)$$

Wang *et al.* [98] reported the following MB models for Wuhan in Central China.

For January

$$PAR^{p} = 1.81(H) \quad (45a)$$

For July

$$PAR^{p} = 2.0(H) \quad (45b)$$

For December

$$PAR^{p} = 1.83(H) \quad (45c)$$

For January-December

$$PAR^{p} = 1.90(H) \quad (45d)$$

Anjorin *et al.* [99] fitted the following HB models for Jos, Nigeria as follows:

For January

$$PAR^p = 1.92(H) \quad (46a)$$

For February

$$PAR^p = 2.06(H) \quad (46b)$$

For March

$$PAR^p = 2.10(H) \quad (46c)$$

For April

$$PAR^p = 2.14(H) \quad (46d)$$

For May

$$PAR^p = 2.15(H) \quad (46e)$$

For June

$$PAR^p = 2.14(H) \quad (46f)$$

For July

$$PAR^p = 2.11(H) \quad (46g)$$

For August

$$PAR^p = 2.09(H) \quad (46h)$$

For September

$$PAR^p = 2.11(H) \quad (46i)$$

For October

$$PAR^p = 2.13(H) \quad (46j)$$

For November

$$PAR^p = 2.06(H) \quad (46k)$$

For December

$$PAR^p = 1.96(H) \quad (46L)$$

For January-December

$$PAR^p = 2.08(H) \quad (46m)$$

Hu and Wang [62] estimated the following MB models for Sangjiang, Hailun and Changbai Mountain in Northeast China.

For Sangjiang

For January

$$PAR^p = 1.83(H) \quad (47a)$$

For February

$$PAR^p = 1.82(H) \quad (47b)$$

For March

$$PAR^p = 1.83(H) \quad (47c)$$

For April

$$PAR^{p} = 1.89(H) \quad (47d)$$

For May

$$PAR^{p} = 1.97(H) \quad (47e)$$

For June

$$PAR^{p} = 1.99(H) \quad (47f)$$

For July

$$PAR^{p} = 2.01(H) \quad (47g)$$

For August

$$PAR^{p} = 1.97(H) \quad (47h)$$

For September

$$PAR^{p} = 1.96(H) \quad (47i)$$

For October1

$$PAR^{p} = 1.91(H) \quad (47j)$$

For November

$$PAR^{p} = 1.85(H) \quad (47k)$$

For December

$$PAR^{p} = 1.86(H) \quad (47L)$$

For HB

$$PAR^{p} = 1.81(H) \quad (47m)$$

For Hailun

For January

$$PAR^{p} = 1.73(H) \quad (47n)$$

For February

$$PAR^{p} = 1.74(H) \quad (47o)$$

For March

$$PAR^{p} = 1.79(H) \quad (47p)$$

For April

$$PAR^{p} = 1.93(H) \quad (47q)$$

For May

$$PAR^{p} = 1.92(H) \quad (47r)$$

For June

$$PAR^{p} = 1.98(H) \quad (47s)$$

For July

$$PAR^{p} = 2.00(H) \quad (47t)$$

For August

$$PAR^p = 1.93(H) \quad (47u)$$

For September

$$PAR^p = 1.87(H) \quad (47v)$$

For October

$$PAR^p = 1.92(H) \quad (47w)$$

For November

$$PAR^p = 1.84(H) \quad (47x)$$

For December

$$PAR^p = 1.81(H) \quad (47y)$$

For Changbai Mountain

For January

$$PAR^p = 1.84(H) \quad (47z)$$

For February

$$PAR^p = 1.89(H) \quad (47aa)$$

For March

$$PAR^p = 1.90(H) \quad (47ab)$$

For April

$$PAR^p = 2.01(H) \quad (47ac)$$

For May

$$PAR^p = 2.01(H) \quad (47ad)$$

For June

$$PAR^p = 2.04(H) \quad (47ae)$$

For July

$$PAR^p = 2.04(H) \quad (47af)$$

For August

$$PAR^p = 2.01(H) \quad (47ag)$$

For September

$$PAR^p = 1.98(H) \quad (47ah)$$

For October

$$PAR^p = 1.93(H) \quad (47ai)$$

For November

$$PAR^p = 1.92(H) \quad (47aj)$$

For December

$$PAR^p = 1.92(H) \quad (47ak)$$

Pankoew *et al.* [100] obtained the following HB model across UK using MSG SEVIRI data as:

$$PAR^p = 1.9455(H) \quad (48)$$

Wang *et al.* [63] obtained the following HB and DB models for Inner Mongolia, China from 1990 to 2012

Hourly basis (HB)

For January

$$PAR^p = 1.78(H) \quad (49a)$$

For February

$$PAR^p = 1.84(H) \quad (49b)$$

For March

$$PAR^p = 1.80(H) \quad (49c)$$

For April

$$PAR^p = 1.74(H) \quad (49d)$$

For May

$$PAR^p = 1.76(H) \quad (49e)$$

For June

$$PAR^p = 1.83(H) \quad (49f)$$

For July

$$PAR^p = 1.86(H) \quad (49g)$$

For August

$$PAR^p = 1.89(H) \quad (49h)$$

For September

$$PAR^p = 1.88(H) \quad (49i)$$

For October

$$PAR^p = 1.87(H) \quad (49j)$$

For November

$$PAR^p = 1.80(H) \quad (49k)$$

For December

$$PAR^p = 1.69(H) \quad (49L)$$

For January-December

$$PAR^p = 1.80(H) \quad (49m)$$

Daily basis (DB)

For January

$$PAR^p = 1.73(H) \quad (49n)$$

For February

$$PAR^p = 1.79(H) \quad (49o)$$

For March

$$PAR^p = 1.79(H) \quad (49p)$$

For April

$$PAR^p = 1.70(H) \quad (49q)$$

For May

$$PAR^p = 1.76(H) \quad (49r)$$

For June

$$PAR^p = 1.83(H) \quad (49s)$$

For July

$$PAR^p = 1.86(H) \quad (49t)$$

For August

$$PAR^p = 1.89(H) \quad (49u)$$

For September

$$PAR^p = 1.88(H) \quad (49v)$$

For October

$$PAR^p = 1.85(H) \quad (49w)$$

For November

$$PAR^p = 1.80(H) \quad (49x)$$

For December

$$PAR^p = 1.68(H) \quad (49y)$$

For January-December

$$PAR^p = 1.80(H) \quad (49z)$$

Akitsu *et al.* [49] stimulated the following MB models for Tsukuba, Japan.

For Summer period (a wet season):

$$PAR^p = 2.12(H) \quad (50a)$$

For Winter (a dry season)

$$PAR^p = 1.92(H) \quad (50b)$$

Peng *et al.* [101] proposed the following MB models for Lhasa located on the Tibetan Plateau in China as follows:

For January

$$PAR^p = 1.81(H) \quad (51a)$$

For July

$$PAR^p = 2.0(H) \quad (51b)$$

For December

$$PAR^p = 1.83(H) \quad (51c)$$

For January-December

$$PAR^p = 1.84(H) \quad (51d)$$

Hu *et al.* [64] fitted the following HB models for several stations in Beijing site as follows:

For Beijing

$$PAR^p = 1.88(H) \quad (52a)$$

For Luancheng

$$PAR^p = 1.80(H) \quad (52b)$$

For Yuchen

$$PAR^p = 1.87(H) \quad (52c)$$

For Jiaozhouwan

$$PAR^p = 1.95(H) \quad (52d)$$

For Changwu

$$PAR^p = 1.89(H) \quad (52e)$$

For Fengqin

$$PAR^p = 1.85(H) \quad (52f)$$

Nwokolo and Ogbulezie [70] calibrated the following MB models for several locations in Nigeria.

Gusau

For January

$$PAR^p = 1.921(H) \quad (53a)$$

For February

$$PAR^p = 1.908(H) \quad (53b)$$

For March

$$PAR^p = 1.923(H) \quad (53c)$$

For April

$$PAR^p = 1.933(H) \quad (53d)$$

For May

$$PAR^p = 1.968(H) \quad (53e)$$

For June

$$PAR^p = 1.954(H) \quad (53f)$$

For July

$$PAR^p = 1.984(H) \quad (53g)$$

For August

$$PAR^{p} = 1.982(H) \quad (53h)$$

For September

$$PAR^{p} = 1.946(H) \quad (53i)$$

For October

$$PAR^{p} = 1.928(H) \quad (53j)$$

For November

$$PAR^{p} = 1.890(H) \quad (53k)$$

For December

$$PAR^{p} = 1.889(H) \quad (53l)$$

For January-December

$$PAR^{p} = 1.936(H) \quad (53m)$$

For Rainy Seasons

$$PAR^{p} = 1.956(H) \quad (53n)$$

For Dry season

$$PAR^{p} = 1.909(H) \quad (53o)$$

Port Harcourt

For January

$$PAR^{p} = 1.950(H) \quad (53p)$$

For February

$$PAR^{p} = 1.955(H) \quad (53q)$$

For March

$$PAR^{p} = 1.980(H) \quad (53r)$$

For April

$$PAR^{p} = 1.987(H) \quad (53s)$$

For May

$$PAR^{p} = 2.010(H) \quad (53t)$$

For June

$$PAR^{p} = 2.052(H) \quad (53u)$$

For July

$$PAR^{p} = 2.060(H) \quad (53v)$$

For August

$$PAR^{p} = 2.044(H) \quad (53w)$$

For September

$$PAR^{p} = 2.054(H) \quad (53x)$$

For October

$$PAR^{p} = 2.038(H) \quad (53y)$$

For November

$$PAR^{p} = 1.999(H) \quad (53z)$$

For December

$$PAR^{p} = 1.960(H) \quad (53aa)$$

For January-December

$$PAR^{p} = 2.007(H) \quad (53ab)$$

For Rainy Seasons

$$PAR^{p} = 2.027(H) \quad (53ac)$$

For Dry season

$$PAR^{p} = 1.980(H) \quad (53ad)$$

Enugu

For January

$$PAR^{p} = 1.985(H) \quad (53ae)$$

For February

$$PAR^{p} = 1.973(H) \quad (53af)$$

For March

$$PAR^{p} = 1.972(H) \quad (53ag)$$

For April

$$PAR^{p} = 1.961(H) \quad (53ah)$$

For May

$$PAR^{p} = 1.966(H) \quad (53ai)$$

For June

$$PAR^{p} = 1.976(H) \quad (53aj)$$

For July

$$PAR^{p} = 2.003(H) \quad (53ak)$$

For August

$$PAR^{p} = 2.005(H) \quad (53aL)$$

For September

$$PAR^{p} = 2.001(H) \quad (53am)$$

For October

$$PAR^{p} = 2.041(H) \quad (53an)$$

For November

$$PAR^{p} = 1.971(H) \quad (53ao)$$

For December

$$PAR^{p} = 1.977(H) \quad (53ap)$$

For January-December

$$PAR^{p} = 1.986(H) \quad (53aq)$$

For Rainy Seasons

$$PAR^{p} = 1.983(H) \quad (53aw)$$

For Dry season

$$PAR^{p} = 1.989(H) \quad (53ax)$$

Abeokuta

For January

$$PAR^{p} = 1.938(H) \quad (53ay)$$

For February

$$PAR^{p} = 1.936(H) \quad (53az)$$

For March

$$PAR^{p} = 1.944(H) \quad (53aaa)$$

For April

$$PAR^{p} = 1.968(H) \quad (53aab)$$

For May

$$PAR^{p} = 1.975(H) \quad (53aac)$$

For June

$$PAR^{p} = 1.997(H) \quad (53aad)$$

For July

$$PAR^{p} = 2.025(H) \quad (53aae)$$

For August

$$PAR^{p} = 2.011(H) \quad (53aaf)$$

For September

$$PAR^{p} = 2.039(H) \quad (53aag)$$

For October

$$PAR^{p} = 1.981(H) \quad (53aah)$$

For November

$$PAR^{p} = 1.952(H) \quad (53aai)$$

For December

$$PAR^{p} = 1.927(H) \quad (53aaj)$$

For January-December

$$PAR^{p} = 1.975(H) \quad (53aak)$$

For Rainy Seasons

$$PAR^{p} = 1.995(H) \quad (53aaL)$$

For Dry season

$$PAR^{p} = 1.947(H) \quad (53aam)$$

Ilorin

For January

$$PAR^{p} = 1.917(H) \quad (53aan)$$

For February

$$PAR^{p} = 1.922(H) \quad (53aao)$$

For March

$$PAR^{p} = 1.923(H) \quad (53aap)$$

For April

$$PAR^{p} = 1.934(H) \quad (53aaq)$$

For May

$$PAR^{p} = 1.946(H) \quad (53aar)$$

For June

$$PAR^{p} = 1.966(H) \quad (53aas)$$

For July

$$PAR^{p} = 1.989(H) \quad (53aat)$$

For August

$$PAR^{p} = 2.005(H) \quad (53aau)$$

For September

$$PAR^{p} = 2.004(H) \quad (53aav)$$

For October

$$PAR^{p} = 1.946(H) \quad (53aaw)$$

For November

$$PAR^{p} = 1.918(H) \quad (53aax)$$

For December

$$PAR^{p} = 1.906(H) \quad (53aay)$$

For January-December

$$PAR^{p} = 1.943(H) \quad (53aaz)$$

For Rainy Seasons

$$PAR^{p} = 1.967(H) \quad (53aaaa)$$

For Dry season

$$PAR^{p} = 1.922(H) \quad (53aaab)$$

Sokoto

For January

$$PAR^{p} = 1.917(H) \quad (53aaac)$$

For February

$$PAR^{p} = 1.907(H) \quad (53aaad)$$

For March

$$PAR^{p} = 1.905(H) \quad (53aaae)$$

For April

$$PAR^{p} = 1.915(H) \quad (53aaaf)$$

For May

$$PAR^{p} = 1.909(H) \quad (53aaag)$$

For June

$$PAR^{p} = 1.919(H) \quad (53aaah)$$

For July

$$PAR^{p} = 1.935(H) \quad (53aaai)$$

For August

$$PAR^{p} = 1.955(H) \quad (53aaaj)$$

For September

$$PAR^{p} = 1.934(H) \quad (53aaak)$$

For October

$$PAR^{p} = 1.926(H) \quad (53aaaL)$$

For November

$$PAR^{p} = 1.911(H) \quad (53aaam)$$

For December

$$PAR^{p} = 1.916(H) \quad (53aaan)$$

For January-December

$$PAR^{p} = 1.921(H) \quad (53aaao)$$

For Rainy Seasons

$$PAR^{p} = 1.931(H) \quad (53aaap)$$

For Dry season

$$PAR^{p} = 1.914(H) \quad (53aaaq)$$

4.1.2 Group 2

Empirical models from this group are parameterized as the ratio of photosynthetically active radiation $\left(PAR^{e}\right)$ to global solar radiation $\left(H\right)$ expressed in energy (unitless) according to their developing year. The functional form is given as:

$$PAR^e = a(H) \quad (54)$$

where a is the regression coefficient

Moon [36] computed spectral distribution of direct sunlight for sea level and suggested the ratio of PAR to H as:

$$PAR^e = 0.44(H) \quad (55)$$

Yocum *et al.* [102] established the following MB model for Ithaca, NY, USA in the month of August as:

$$PAR^e = 0.47(H) \quad (56)$$

Williams [103] obtained the following MB model for a wide variety of climatic conditions as:

$$PAR^e = 0.45(H)$$

Goldberg and Klein [104] fitted the following DB model between January-December for Jerusalem, Israel and Rockeville, MD, USA.

For Jerusalem, Israel

$$PAR^e = 0.45(H) \quad (57a)$$

For Rockeville, MD, USA

$$PAR^e = 0.45(H) \quad (57b)$$

Stigter and Musabilha [105] established the following HB models for Dar es Salaam, Tanzania under various sky conditions

For clear sky

$$PAR^e = 0.510(H) \quad (58a)$$

For cloudy sky

$$PAR^e = 0.630(H) \quad (58b)$$

Rao [51] developed the following HB model for Corvallis, Oregon, USA under various sky conditions and from January-December.

For January-December

$$PAR^e = 0.46(H) \quad (59a)$$

For clear sky

$$PAR^e = 0.443(H) \quad (59b)$$

For partially cloudy sky

$$PAR^e = 0.447(H) \quad (59c)$$

For cloudy sky

$$PAR^e = 0.483(H) \quad (59d)$$

Hansen [106] reported the following DB model for Aas, Norway (May-August) as:

$$PAR^e = 0.44(H) \quad (60)$$

Papaioannou *et al.* [52] reported the following DB and HB models for Anthens, Greece under various sky conditions

Hourly Basis (HB)

For clear sky

$$PAR^e = 0.480(H) \quad (61a)$$

For cloudy sky

$$PAR^e = 0.490(H) \quad (61b)$$

Daily Basis (DB)

For clear sky

$$PAR^e = 0.463(H) \quad (61c)$$

For cloudy sky

$$PAR^e = 0.472(H) \quad (61d)$$

Papaioannou *et al.* [107] reported the following MB model for Anthens, Greece as:

$$PAR^e = 0.43(H) \quad (62)$$

Zhou *et al.* [108] fitted the following HB models for Yucheng, China under varying local standard time (hours).

For January, 1992 (08:00)

$$PAR^e = 0.39(H) \quad (63a)$$

For January, 1992 (09:00)

$$PAR^e = 0.42(H) \quad (63b)$$

For January, 1992 (10:00)

$$PAR^e = 0.43(H) \quad (63c)$$

For January, 1992 (11:00)

$$PAR^e = 0.42(H) \quad (63d)$$

For January, 1992 (12:00)

$$PAR^e = 0.43(H) \quad (63e)$$

For January, 1992 (13:00)

$$PAR^e = 0.43(H) \quad (63f)$$

For January, 1992 (14:00)

$$PAR^e = 0.43(H) \quad (63g)$$

For January, 1992 (15:00)

$$PAR^e = 0.42(H) \quad (63h)$$

For January, 1992 (16:00)

$$PAR^e = 0.42(H) \quad (63i)$$

For July, 1991 (07:00)

$$PAR^e = 0.47(H) \quad (63j)$$

For July, 1991 (08:00)

$$PAR^e = 0.50(H) \quad (63k)$$

For July, 1991 (09:00)

$$PAR^e = 0.51(H) \quad (63L)$$

For July, 1991 (10:00)

$$PAR^e = 0.52(H) \quad (63m)$$

For July, 1991 (11:00)

$$PAR^e = 0.53(H) \quad (63n)$$

For July, 1991 (12:00)

$$PAR^e = 0.51(H) \quad (63o)$$

For July, 1991 (13:00)

$$PAR^e = 0.51(H) \quad (63p)$$

For July, 1991 (14:00)

$$PAR^e = 0.51(H) \quad (63q)$$

For July, 1991 (15:00)

$$PAR^e = 0.52(H) \quad (63r)$$

For July, 1991 (16:00)

$$PAR^e = 0.51(H) \quad (63s)$$

For July, 1991 (17:00)

$$PAR^e = 0.49(H) \quad (63t)$$

For July, 1991 (18:00)

$$PAR^e = 0.45(H) \quad (63u)$$

Jacovides *et al.* [53] stimulated the following DB and HB models for Athalassa, Cyprus under various sky conditions

Hourly Basis (HB)

For Cloudy Sky

$$PAR^e = 0.411(H) \quad (64a)$$

For cloudy sky

$$PAR^e = 0.440(H) \quad (64b)$$

Daily Basis (DB)

For Clear sky

$$PAR^e = 0.408(H) \quad (64c)$$

For intermediate sky

$$PAR^e = 0.421(H) \quad (64d)$$

For Overcast

$$PAR^e = 0.440(H) \quad (64e)$$

Tsubo and Walker [48] established the following HB and DB models for Bloemfontein, South Africa.

For Daily Basis (DB)

$$PAR^e = 0.48(H) \quad (65a)$$

For Hourly Basis (HB)

$$PAR^e = 0.49(H) \quad (65b)$$

Aguiar *et al.* [66] proposed the following MB models for Fazenda Noosa Sen hora in Rondonia.

For January

$$PAR^e = 0.48(H) \quad (66a)$$

For February

$$PAR^e = 0.48(H) \quad (66b)$$

For March

$$PAR^e = 0.48(H) \quad (66c)$$

For April

$$PAR^e = 0.47(H) \quad (66d)$$

For May

$$PAR^e = 0.47(H) \quad (66e)$$

For June

$$PAR^e = 0.46(H) \quad (66f)$$

For July

$$PAR^e = 0.46(H) \quad (66g)$$

For August

$$PAR^e = 0.44(H) \quad (66h)$$

For September

$$PAR^e = 0.43(H) \quad (66i)$$

For October

$$PAR^e = 0.46(H) \quad (66j)$$

For November

$$PAR^e = 0.47(H) \quad (66k)$$

For December

$$PAR^e = 0.47(H) \quad (66L)$$

For Dry Season

$$PAR^e = 0.43(H) \quad (66m)$$

For Rainy Season

$$PAR^e = 0.48(H) \quad (66n)$$

Jacovides *et al.* [109] developed the following HB models for Athens, Greece under various sky conditions

For clear sky

$$PAR^e = 0.434(H) \quad (67a)$$

For intermediate sky

$$PAR^e = 0.442(H) \quad (67b)$$

For cloudy sky

$$PAR^e = 0.461(H) \quad (67c)$$

Escobedo *et al.* [110] developed the following DB and HB under various sky conditions at Botucatu, Brazil.

Hourly Basis (HB)

$$PAR^e = 0.501(H) \quad H/H_o \le 0.35 \quad (68a)$$

$$PAR^e = 0.495(H) \quad 0.35 < H/H_o \le 0.55 \quad (68b)$$

$$PAR^e = 0.490(H) \quad 0.55 < H/H_o \le 0.65 \quad (68c)$$

$$PAR^e = 0.489(H) \quad H/H_o > 0.63 \quad (68d)$$

$$PAR^e = 0.491(H) \quad 0 \le H/H_o \le 1 \quad (68e)$$

For clear sky

$$PAR^e = 0.489(H) \quad (68f)$$

For cloudy sky

$$PAR^e = 0.501(H) \quad (68g)$$

Daily Basis (DB)

$$PAR^e = 0.512(H) \quad H/H_o \le 0.35 \quad (68h)$$

$$PAR^e = 0.496(H) \quad 0.35 < H/H_o \le 0.55 \quad (68i)$$

$$PAR^e = 0.490(H) \quad 0.55 < H/H_o \le 0.65 \quad (68j)$$

$$PAR^e = 0.485(H) \quad H/H_o > 0.63 \quad (68k)$$

$$PAR^e = 0.489(H) \quad 0 \le H/H_o \le 1 \quad (68L)$$

For clear sky

$$PAR^e = 0.481(H) \quad (68m)$$

For cloudy sky

$$PAR^e = 0.512(H) \quad (68n)$$

Li *et al.* [55] stimulated the following HB models for Wuhaoliang site in Northern Tibetan Plateau, China under various local standard time (hours).

For January, 1994-1997 (08:00)

$$PAR^{e} = 0.50(H) \quad (69a)$$

For January, 1994-1997 (09:00)

$$PAR^{e} = 0.46(H) \quad (69b)$$

For January, 1994-1997 (10:00)

$$PAR^{e} = 0.44(H) \quad (69c)$$

For January, 1994-1997 (11:00)

$$PAR^{e} = 0.43(H) \quad (69d)$$

For January, 1994-1997 (12:00)

$$PAR^{e} = 0.42(H) \quad (69e)$$

For January, 1994-1997 (13:00)

$$PAR^{e} = 0.42(H) \quad (69f)$$

For January, 1994-1997 (14:00)

$$PAR^{e} = 0.41(H) \quad (69g)$$

For January, 1994-1997 (15:00)

$$PAR^{e} = 0.40(H) \quad (69h)$$

For January, 1994-1997 (16:00)

$$PAR^{e} = 0.39(H) \quad (69i)$$

For January, 1994-1997 (17:00)

$$PAR^{e} = 0.49(H) \quad (69j)$$

For July, 1994-1997 (07:00)

$$PAR^{e} = 0.50(H) \quad (69k)$$

For July, 1994-1997 (08:00)

$$PAR^{e} = 0.48(H) \quad (69L)$$

For July, 1994-1997 (09:00)

$$PAR^{e} = 0.46(H) \quad (69m)$$

For July, 1994-1997 (10:00)

$$PAR^{e} = 0.45(H) \quad (69n)$$

For July, 1994-1997 (11:00)

$$PAR^{e} = 0.44(H) \quad (69o)$$

For July, 1994-1997 (12:00)

$$PAR^{e} = 0.43(H) \quad (69p)$$

For July, 1994-1997 (13:00)

$$PAR^e = 0.43(H) \quad (69q)$$

For July, 1994-1997 (14:00)

$$PAR^e = 0.43(H) \quad (69r)$$

For July, 1994-1997 (15:00)

$$PAR^e = 0.42(H) \quad (69s)$$

For July, 1994-1997 (16:00)

$$PAR^e = 0.41(H) \quad (69t)$$

For July, 1994-1997 (17:00)

$$PAR^e = 0.38(H) \quad (69u)$$

For July, 1994-1997 (18:00)

$$PAR^e = 0.36(H) \quad (69v)$$

Guefeng *et al.* [111] fitted the following DB model within the Poyang Lake National Nature Reserve, China as:

$$PAR^e = 0.45(H) \quad (70)$$

Escobedo *et al.* [112] fitted the following HB and DB models for Botucatu, Brazil

Hourly Basis (HB)

For 2001

$$PAR^e = 0.4896(H) \quad (71a)$$

For 2002

$$PAR^e = 0.4892(H) \quad (71b)$$

For 2003

$$PAR^e = 0.4866(H) \quad (71c)$$

For 2004

$$PAR^e = 0.5000(H) \quad (71d)$$

For 2001-2004

$$PAR^e = 0.491(H) \quad (71e)$$

Daily Basis (DB)

For 2001

$$PAR^e = 0.4919(H) \quad (71f)$$

For 2002

$$PAR^e = 0.4887(H) \quad (71g)$$

For 2003

$$PAR^e = 0.4893(H) \quad (71h)$$

For 2004

$$PAR^e = 0.4926(H) \quad (71i)$$

For 2001-2004

$$PAR^e = 0.489(H) \quad (71j)$$

Wang *et al.* [9] stimulated the following MB models under different sky conditions in Wuhan, Central China

For January

$$PAR^e = 0.3940(H) \quad H/H_o \le 0.35 \quad (72a)$$

$$PAR^e = 0.3787(H) \quad 0.35 \le H/H_o < 0.65 \quad (72b)$$

$$PAR^e = 0.3764(H) \quad H/H_o \ge 0.65 \quad (72c)$$

For February

$$PAR^e = 0.3997(H) \quad H/H_o \le 0.35 \quad (72d)$$

$$PAR^e = 0.3631(H) \quad 0.35 \le H/H_o < 0.65 \quad (72e)$$

For March

$$PAR^e = 0.3985(H) \quad H/H_o \le 0.35 \quad (72f)$$

$$PAR^e = 0.3751(H) \quad 0.35 \le H/H_o < 0.65 \quad (72g)$$

$$PAR^e = 0.3745(H) \quad H/H_o \ge 0.65 \quad (72h)$$

For April

$$PAR^e = 0.41(H) \quad H/H_o \le 0.35 \quad (72i)$$

$$PAR^e = 0.3848(H) \quad 0.35 \le H/H_o < 0.65 \quad (72j)$$

$$PAR^e = 0.3832(H) \quad H/H_o \ge 0.65 \quad (72k)$$

For May

$$PAR^e = 0.4156(H) \quad H/H_o \le 0.35 \quad (72L)$$

$$PAR^e = 0.3919(H) \quad 0.35 \le H/H_o < 0.65 \quad (72m)$$

$$PAR^e = 0.3877(H) \quad H/H_o \ge 0.65 \quad (72n)$$

For June

$$PAR^e = 0.4217(H) \quad H/H_o \le 0.35 \quad (72o)$$

$$PAR^e = 0.3947(H) \quad 0.35 \le H/H_o < 0.65 \quad (72p)$$

For July

$$PAR^e = 0.4377(H) \quad H/H_o \le 0.35 \quad (72q)$$

$$PAR^e = 0.4114(H) \quad 0.35 \le H/H_o < 0.65 \quad (72r)$$

$$PAR^e = 0.4011(H) \quad H/H_o \ge 0.65 \quad (72s)$$

For August

$$PAR^e = 0.4236(H) \qquad H/H_o \le 0.35 \qquad (72t)$$

$$PAR^e = 0.4107(H) \qquad 0.35 \le H/H_o < 0.65 \qquad (72u)$$

$$PAR^e = 0.4146(H) \qquad H/H_o \ge 0.65 \qquad (72v)$$

For September

$$PAR^e = 0.4313(H) \qquad H/H_o \le 0.35 \qquad (72w)$$

$$PAR^e = 0.3994(H) \qquad 0.35 \le H/H_o < 0.65 \qquad (72x)$$

$$PAR^e = 0.3838(H) \qquad H/H_o \ge 0.65 \qquad (72y)$$

For October

$$PAR^e = 0.4245(H) \qquad H/H_o \le 0.35 \qquad (72z)$$

$$PAR^e = 0.3847(H) \qquad 0.35 \le H/H_o < 0.65 \qquad (72aa)$$

$$PAR^e = 0.3771(H) \qquad H/H_o \ge 0.65 \qquad (72ab)$$

For November

$$PAR^e = 0.4173(H) \qquad H/H_o \le 0.35 \qquad (72ac)$$

$$PAR^e = 0.3751(H) \qquad 0.35 \le H/H_o < 0.65 \qquad (72ad)$$

$$PAR^e = 0.3885(H) \qquad H/H_o \ge 0.65 \qquad (72ae)$$

For December

$$PAR^e = 0.3966(H) \qquad H/H_o \le 0.35 \qquad (72af)$$

$$PAR^e = 0.3639(H) \qquad 0.35 \le H/H_o < 0.65 \qquad (72ag)$$

Bat-Oyun *et al.* [59] reported the following MB models for Mongolian grassland.

For January

$$PAR^e = 0.425(H) \qquad (73a)$$

For February

$$PAR^e = 0.437(H) \qquad (73b)$$

For March

$$PAR^e = 0.427(H) \qquad (73c)$$

For April

$$PAR^e = 0.420(H) \qquad (73d)$$

For May

$$PAR^e = 0.421(H) \qquad (73e)$$

For June

$$PAR^e = 0.448(H) \qquad (73f)$$

For July

$$PAR^e = 0.459(H) \quad (73g)$$

For August

$$PAR^e = 0.439(H) \quad (73h)$$

For September

$$PAR^e = 0.438(H) \quad (73i)$$

For October

$$PAR^e = 0.449(H) \quad (73j)$$

For November

$$PAR^e = 0.429(H) \quad (73k)$$

For December

$$PAR^e = 0.423(H) \quad (73L)$$

For January-December

$$PAR^e = 0.435(H) \quad (73m)$$

For Growing Seasons (May-August)

$$PAR^e = 0.442(H) \quad (73n)$$

For cloudy sky

$$PAR^e = 0.456(H) \qquad H/H_o < 0.33 \quad (73o)$$

For partly cloudy sky

$$PAR^e = 0.439(H) \qquad 0.33 < H/H_o \le 0.67 \quad (73p)$$

For clear sky

$$PAR^e = 0.430(H) \qquad H/H_o > 0.67 \quad (73q)$$

For All sky

$$PAR^e = 0.434(H) \qquad 0 \le H/H_o \le 1 \quad (73r)$$

Abolfazi [61] obtained the following MB model for Southern Iran (January-December) as:

$$PAR^e = 0.584(H) \quad (74a)$$

Yu and Guo [76] fitted the following HB models for Bonville, Illinois and Sioux Falls, South Dakota in Midwestern United States under various sky conditions.

For Bonville, Illinois

$$PAR^e = 0.463(H) \qquad H/H_o \le 0.35 \quad (75a)$$

$$PAR^e = 0.429(H) \qquad 0.35 \le H/H_o < 0.65 \quad (75b)$$

$$PAR^e = 0.416(H) \qquad H/H_o \ge 0.65 \quad (75c)$$

$$PAR^e = 0.422(H) \qquad 0 \le H/H_o \le 1 \quad (75d)$$

For Sioux Falls, South Dakota

$$PAR^e = 0.475(H) \qquad H/H_o \le 0.35 \qquad (75e)$$

$$PAR^e = 0.446(H) \qquad 0.35 \le H/H_o < 0.65 \qquad (75f)$$

$$PAR^e = 0.433(H) \qquad H/H_o \ge 0.65 \qquad (75g)$$

$$PAR^e = 0.438(H) \qquad 0 \le H/H_o \le 1 \qquad (75h)$$

Akitsu *et al.* [49] recorded the following MB models for Tsukuba, Japan.

For Summer Period (a wet season)

$$PAR^e = 0.465(H) \qquad (76a)$$

For Winter Period (a dry season)

$$PAR^e = 0.420(H) \qquad (76b)$$

Yu *et al.* [113] established the DB model for several locations in the contiguous United States under various sky conditions.

For Bonville, Illinois

$$PAR^e = 0.4642(H) \qquad H/H_o \le 0.3 \qquad (77a)$$

$$PAR^e = 0.4271(H) \qquad 0.3 < H/H_o < 0.7 \qquad (77b)$$

$$PAR^e = 0.4169(H) \qquad H/H_o \ge 0.7 \qquad (77c)$$

$$PAR^e = 0.4169(H) \qquad \text{All Sky} \qquad (77d)$$

For Desert Rock, Nevada

$$PAR^e = 0.4906(H) \qquad H/H_o \le 0.3 \qquad (77e)$$

$$PAR^e = 0.4486(H) \qquad 0.3 < H/H_o < 0.7 \qquad (77f)$$

$$PAR^e = 0.4346(H) \qquad H/H_o \ge 0.7 \qquad (77g)$$

$$PAR^e = 0.4371(H) \qquad \text{All Sky} \qquad (77h)$$

For Fort Pecks, Montana

$$PAR^e = 0.4767(H) \qquad H/H_o \le 0.3 \qquad (77i)$$

$$PAR^e = 0.4447(H) \qquad 0.3 < H/H_o < 0.7 \qquad (77j)$$

$$PAR^e = 0.4360(H) \qquad H/H_o \ge 0.7 \qquad (77k)$$

$$PAR^e = 0.4415(H) \qquad \text{All Sky} \qquad (77L)$$

For Goodwin Creek/Mississippi

$$PAR^e = 0.4623(H) \qquad H/H_o \le 0.3 \qquad (77m)$$

$$PAR^e = 0.4317(H) \qquad 0.3 < H/H_o < 0.7 \qquad (77n)$$

$$PAR^e = 0.4220(H) \qquad H/H_o \ge 0.7 \qquad (77o)$$

$$PAR^e = 0.4284(H) \qquad \text{All Sky} \qquad (77p)$$

For Penn, State University, Pennsylvania

$$PAR^e = 0.4519(H) \qquad H/H_o \le 0.3 \qquad (77q)$$

$$PAR^e = 0.4221(H) \qquad 0.3 < H/H_o < 0.7 \qquad (77r)$$

$$PAR^e = 0.4116(H) \qquad H/H_o \ge 0.7 \qquad (77s)$$

$$PAR^e = 0.4196(H) \qquad \text{All Sky} \qquad (77t)$$

For Sioux Falls, South Dakota

$$PAR^e = 0.4714(H) \qquad H/H_o \le 0.3 \qquad (77u)$$

$$PAR^e = 0.4452(H) \qquad 0.3 < H/H_o < 0.7 \qquad (77v)$$

$$PAR^e = 0.4370(H) \qquad H/H_o \ge 0.7 \qquad (77w)$$

$$PAR^e = 0.4409(H) \qquad \text{All Sky} \qquad (77x)$$

For Table Mountain, Boulder, Colorado

$$PAR^e = 0.4626(H) \qquad H/H_o \le 0.3 \qquad (77y)$$

$$PAR^e = 0.4301(H) \qquad 0.3 < H/H_o < 0.7 \qquad (77z)$$

$$PAR^e = 0.4231(H) \qquad H/H_o \ge 0.7 \qquad (77aa)$$

$$PAR^e = 0.4266(H) \qquad \text{All Sky} \qquad (77ab)$$

For All Sites

$$PAR^e = 0.4638(H) \qquad H/H_o \le 0.3 \qquad (77ac)$$

$$PAR^e = 0.4342(H) \qquad 0.3 < H/H_o < 0.7 \qquad (77ad)$$

$$PAR^e = 0.4286(H) \qquad H/H_o \ge 0.7 \qquad (77ae)$$

$$PAR^e = 0.4381(H) \qquad \text{All Sky} \qquad (77af)$$

Nwokolo *et al.* [70] calibrated the following MB models for several locations in Nigeria.

Port Harcourt

For January

$$PAR^e = 0.4682(H) \qquad (78a)$$

For February

$$PAR^e = 0.4712(H) \qquad (78b)$$

For March

$$PAR^e = 0.4838(H) \qquad (78c)$$

For April

$$PAR^e = 0.4886(H) \qquad (78d)$$

For May

$$PAR^e = 0.4983(H) \quad (78e)$$

For June

$$PAR^e = 0.5199(H) \quad (78f)$$

For July

$$PAR^e = 0.5231(H) \quad (78g)$$

For August

$$PAR^e = 0.5127(H) \quad (78h)$$

For September

$$PAR^e = 0.5204(H) \quad (78i)$$

For October

$$PAR^e = 0.5134(H) \quad (78j)$$

For November

$$PAR^e = 0.4949(H) \quad (78k)$$

For December

$$PAR^e = 0.4738(H) \quad (78L)$$

For January-December

$$PAR^e = 0.4974(H) \quad (78m)$$

For Dry Season

$$PAR^e = 0.4843(H) \quad (78n)$$

For Rainy Season

$$PAR^e = 0.5064(H) \quad (78o)$$

Enugu

For January

$$PAR^e = 0.4880(H) \quad (78p)$$

For February

$$PAR^e = 0.4820(H) \quad (78q)$$

For March

$$PAR^e = 0.4811(H) \quad (78r)$$

For April

$$PAR^e = 0.4751(H) \quad (78s)$$

For May

$$PAR^e = 0.4726(H) \quad (78t)$$

For June

$$PAR^e = 0.4833(H) \quad (78u)$$

For July

$$PAR^e = 0.4974(H) \quad (78v)$$

For August

$$PAR^e = 0.4982(H) \quad (78w)$$

For September

$$PAR^e = 0.4965(H) \quad (78x)$$

For October

$$PAR^e = 0.5027(H) \quad (78y)$$

For November

$$PAR^e = 0.4807(H) \quad (78z)$$

For December

$$PAR^e = 0.4841(H) \quad (78aa)$$

For January-December

$$PAR^e = 0.4868(H) \quad (78ab)$$

For Dry Season

$$PAR^e = 0.4875(H) \quad (78ac)$$

For Rainy Season

$$PAR^e = 0.4863(H) \quad (78ad)$$

Abeokuta

For January

$$PAR^e = 0.4542(H) \quad (78ae)$$

For February

$$PAR^e = 0.4601(H) \quad (78af)$$

For March

$$PAR^e = 0.4640(H) \quad (78ag)$$

For April

$$PAR^e = 0.4780(H) \quad (78ah)$$

For May

$$PAR^e = 0.4814(H) \quad (78ai)$$

For June

$$PAR^e = 0.4925(H) \quad (78aj)$$

For July

$$PAR^e = 0.5047(H) \quad (78ak)$$

For August

$$PAR^e = 0.5103(H) \quad (78aL)$$

For September

$$PAR^e = 0.5032(H) \quad (78am)$$

For October

$$PAR^e = 0.4877(H) \quad (78an)$$

For November

$$PAR^e = 0.4643(H) \quad (78ao)$$

For December

$$PAR^e = 0.4542(H) \quad (78ap)$$

For January-December

$$PAR^e = 0.4798(H) \quad (78aq)$$

For Dry Season

$$PAR^e = 0.4641(H) \quad (78ar)$$

For Rainy Season

$$PAR^e = 0.4906(H) \quad (78as)$$

Ilorin

For January

$$PAR^e = 0.4486(H) \quad (78at)$$

For February

$$PAR^e = 0.4520(H) \quad (78au)$$

For March

$$PAR^e = 0.4559(H) \quad (78av)$$

For April

$$PAR^e = 0.4614(H) \quad (78aw)$$

For May

$$PAR^e = 0.4663(H) \quad (78ax)$$

For June

$$PAR^e = 0.4713(H) \quad (78ay)$$

For July

$$PAR^e = 0.4884(H) \quad (78az)$$

For August

$$PAR^e = 0.4953(H) \quad (78aaa)$$

For September

$$PAR^e = 0.4796(H) \quad (78aab)$$

For October

$$PAR^e = 0.4665(H) \quad (78aac)$$

For November

$$PAR^e = 0.4433(H) \quad (78aad)$$

For December

$$PAR^e = 0.4414(H) \quad (78aae)$$

For January-December

$$PAR^e = 0.4647(H) \quad (78aaf)$$

For Dry Season

$$PAR^e = 0.4504(H) \quad (78aag)$$

For Rainy Season

$$PAR^e = 0.4740(H) \quad (78aah)$$

Sokoto

For January

$$PAR^e = 0.4492(H) \quad (78aai)$$

For February

$$PAR^e = 0.4438(H) \quad (78aaj)$$

For March

$$PAR^e = 0.4419(H) \quad (78aak)$$

For April

$$PAR^e = 0.4430(H) \quad (78aaL)$$

For May

$$PAR^e = 0.4444(H) \quad (78aam)$$

For June

$$PAR^e = 0.4500(H) \quad (78aan)$$

For July

$$PAR^e = 0.4596(H) \quad (78aao)$$

For August

$$PAR^e = 0.4715(H) \quad (78aap)$$

For September

$$PAR^e = 0.4595(H) \quad (78aaq)$$

For October

$$PAR^e = 0.4545(H) \quad (78aar)$$

For November

$$PAR^e = 0.4453(H) \quad (78aas)$$

For December

$$PAR^e = 0.4483(H) \quad (78aat)$$

For January-December

$$PAR^e = 0.4535(H) \quad (78aau)$$

For Dry Season

$$PAR^e = 0.4480(H) \quad (78aav)$$

For Rainy Season

$$PAR^e = 0.5580(H) \quad (78aaw)$$

Bauchi

For January

$$PAR^e = 0.4489(H) \quad (78aax)$$

For February

$$PAR^e = 0.4481(H) \quad (78aay)$$

For March

$$PAR^e = 0.4523(H) \quad (78aaz)$$

For April

$$PAR^e = 0.4566(H) \quad (78aaaa)$$

For May

$$PAR^e = 0.4535(H) \quad (78aaab)$$

For June

$$PAR^e = 0.4534(H) \quad (78aaac)$$

For July

$$PAR^e = 0.4636(H) \quad (78aaad)$$

For August

$$PAR^e = 0.4625(H) \quad (78aaae)$$

For September

$$PAR^e = 0.4596(H) \quad (78aaaf)$$

For October

$$PAR^e = 0.4502(H) \quad (78aaag)$$

For November

$$PAR^e = 0.4466(H) \quad (78aaah)$$

For December

$$PAR^e = 0.4463(H) \quad (78aaai)$$

For January-December

$$PAR^e = 0.4974(H) \quad (78aaaj)$$

For Dry Season

$$PAR^e = 0.4482(H) \quad (78aaak)$$

For Rainy Season

$$PAR^{e} = 0.4528(H) \quad \text{(78aaaL)}$$

4.1.3 Group 3

Empirical models from this group are parameterized as the first-order polynomial function of the global solar radiation where photosynthetically active radiation $\left(PAR^{p}\right)$ is expressed in photon units (μmolJ^{-1}, E MJ^{-1} etc.) and photosynthetically active radiation $\left(PAR^{e}\right)$ is expressed in energy terms as shown below in the following forms:

$$PAR^{p} = a(H) + b \quad (79)$$

$$PAR^{e} = a(H) + b \quad (80)$$

where a and b are the regression coefficients and other symbols retain their usual meaning.

Meek *et al.* [41] fitted the following MB model for Fresno-West side located at the University of California, USA as:

$$PAR^{p} = 2.017(H) + 0.163 \quad (81)$$

Aguiar *et al.* [66] obtained the following HB and DB models for Fazenda Nossa Senhora in Rondonia.

For Hour Basis, HB

$$PAR^{e} = 0.478(H) + 0.747 \quad \text{(wet season)} \quad (82a)$$

$$PAR^{e} = 0.471(H) - 1.0689 \quad \text{(wet-dry season)} \quad (82b)$$

$$PAR^{e} = 0.452(H) - 4.578 \quad \text{(dry season)} \quad (82c)$$

$$PAR^{e} = 0.466(H) - 0.877 \quad \text{(dry-wet season)} \quad (82d)$$

For Daily Basis, DB

$$PAR^{e} = 0.466(H) + 4.956 \quad \text{(wet season)} \quad (82e)$$

$$PAR^{e} = 0.466(H) + 0.735 \quad \text{(wet-dry season)} \quad (82f)$$

$$PAR^{e} = 0.457(H) - 6.762 \quad \text{(dry season)} \quad (82g)$$

$$PAR^{e} = 0.452(H) + 4.244 \quad \text{(dry-wet season)} \quad (82h)$$

Finch *et al.* [67] obtained the following MB model for Zambia as:

$$PAR^{p} = 1.8807(H) + 1.9749 \quad (83)$$

Aguiar *et al.* [65] fitted the following HB and DB models for pasture and forest sites in South West Amazonia.

For Pasture Site (Hourly Basis, HB)

$$PAR^{e} = 0.283(H) + 0.474 \quad \text{(wet season)} \quad (84a)$$

$$PAR^{e} = -0.88818(H) + 0.467 \quad \text{(wet-dry season)} \quad (84b)$$

$$PAR^{e} = -4.192(H) + 0.449 \quad \text{(dry season)} \quad (84c)$$

$$PAR^{e} = -1.160(H) + 0.464 \quad \text{(dry-wet season)} \quad (84d)$$

$PAR^e = -1.162(H) + 0.462$ (Annual) (84e)

For Forest Site (Hourly Basis, HB)

$PAR^e = -0.407(H) + 0.423$ (wet season) (84f)

$PAR^e = 0.766(H) + 0.420$ (wet-dry season) (84g)

$PAR^e = -3.444(H) + 0.432$ (dry season) (84h)

$PAR^e = 0.594(H) + 0.427$ (dry-wet season) (84i)

$PAR^e = -0.482(H) + 0.425$ (Annual) (84j)

For Pasture Site (Daily Basis, DB)

$PAR^e = 3.847(H) + 0.464$ (wet season) (84k)

$PAR^e = 2.363(H) + 0.459$ (wet-dry season) (84L)

$PAR^e = -4.044(H) + 0.449$ (dry season) (84m)

$PAR^e = 5.389(H) + 0.447$ (dry-wet season) (84n)

$PAR^e = 6.254(H) + 0.443$ (Annual) (84o)

For Forest Site (Daily Basis, DB)

$PAR^e = 1.881(H) + 0.416$ (wet season) (84p)

$PAR^e = -0.154(H) + 0.422$ (wet-dry season) (84q)

$PAR^e = -4.017(H) + 0.433$ (dry season) (84r)

$PAR^e = 2.672(H) + 0.422$ (dry-wet season) (84s)

$PAR^e = 0.795(H) + 0.421$ (Annual) (84t)

Melina-Maria *et al.* [77] stimulated the following HB model for Greece as:

$$PAR^e = 0.457(H) - 7.424 \quad (85)$$

4.2 Relative Humidity-Based Models

Relative humidity-based computing models are often employed for estimating PAR in that it has been observed that when the total energy in the near infrared (NIR) portion of the solar spectrum greatly reduced, relative humidity is almost transparent to PAR wavelength. Thus, increasing global solar radiation in the NIR range will culminate into a lower PAR clearness index in the coastal region and higher PAR clearness index in the interior region. On this ground, it can be inferred that relative humidity can be employed for estimating PAR in geographical regions where relative humidity is greater than 64% annually. Hence, solar energy researchers have applied this meteorological parameter to stimulate computing models for estimating PAR as presented in this section. Therefore, empirical models from this group are parameterized as the first-order polynomial function

of the relative humidity (RH) where photosynthetically active radiation $\left(PAR^{e}\right)$ is expressed in energy terms as shown below in the following form:

$$\frac{PAR^{e}}{PAR_{o}} = a + b\left(\frac{RH}{100}\right) \tag{86}$$

where a and b are the regression coefficients and other symbols retain their usual meaning.

Nwokolo *et al.* [60] developed the following MB models for several locations in Nigeria under various seasons and all sky conditions.

For Port Harcourt

$$\frac{PAR^{e}}{PAR_{o}} = 2.300 - 2.209\left(\frac{RH}{100}\right) \quad \text{(All sky conditions)} \tag{87a}$$

$$\frac{PAR^{e}}{PAR_{o}} = 0.118 + 0.354\left(\frac{RH}{100}\right) \quad \text{(Rainy season)} \tag{87b}$$

$$\frac{PAR^{e}}{PAR_{o}} = 1.597 - 1.293\left(\frac{RH}{100}\right) \quad \text{(Dry season)} \tag{87c}$$

For Owerri

$$\frac{PAR^{e}}{PAR_{o}} = 1.484 - 1.167\left(\frac{RH}{100}\right) \quad \text{(All sky conditions)} \tag{87d}$$

$$\frac{PAR^{e}}{PAR_{o}} = 1.277 - 0.941\left(\frac{RH}{100}\right) \quad \text{(Rainy season)} \tag{87e}$$

$$\frac{PAR^{e}}{PAR_{o}} = 1.074 - 0.603\left(\frac{RH}{100}\right) \quad \text{(Dry season)} \tag{87f}$$

For Ikeja

$$\frac{PAR^{e}}{PAR_{o}} = 1.651 - 1.364\left(\frac{RH}{100}\right) \quad \text{(All sky conditions)} \tag{87g}$$

$$\frac{PAR^{e}}{PAR_{o}} = 0.990 - 0.600\left(\frac{RH}{100}\right) \quad \text{(Rainy season)} \tag{87h}$$

$$\frac{PAR^{e}}{PAR_{o}} = 0.997 - 0.491\left(\frac{RH}{100}\right) \quad \text{(Dry season)} \tag{87i}$$

For Abuja

$$\frac{PAR^{e}}{PAR_{o}} = 0.866 - 0.369\left(\frac{RH}{100}\right) \quad \text{(All sky conditions)} \tag{87j}$$

$$\frac{PAR^e}{PAR_o} = 2.111 - 1.875\left(\frac{RH}{100}\right) \quad \text{(Rainy season)} \quad (87k)$$

$$\frac{PAR^e}{PAR_o} = 0.763 - 0.095\left(\frac{RH}{100}\right) \quad \text{(Dry season)} \quad (87L)$$

For Maiduguri

$$\frac{PAR^e}{PAR_o} = 0.790 - 0.247\left(\frac{RH}{100}\right) \quad \text{(All sky conditions)} \quad (87m)$$

$$\frac{PAR^e}{PAR_o} = 0.661 + 0.049\left(\frac{RH}{100}\right) \quad \text{(Rainy season)} \quad (87n)$$

$$\frac{PAR^e}{PAR_o} = 0.816 - 0.406\left(\frac{RH}{100}\right) \quad \text{(Dry season)} \quad (87o)$$

For Sokoto

$$\frac{PAR^e}{PAR_o} = 0.779 - 0.141\left(\frac{RH}{100}\right) \quad \text{(All sky conditions)} \quad (87p)$$

$$\frac{PAR^e}{PAR_o} = 0.835 - 0.224\left(\frac{RH}{100}\right) \quad \text{(Rainy season)} \quad (87q)$$

$$\frac{PAR^e}{PAR_o} = 0.796 - 0.300\left(\frac{RH}{100}\right) \quad \text{(Dry season)} \quad (87r)$$

4.3 Temperature-Based Models

Temperature-based model is an adaptation of Hargreaves-Samani [114] type computing model for estimating Photosynthetically Active Radiation (PAR) especially where sunshine hour, global solar radiation, data, etc. are not readily available. This could be attributed to the availability of daily mean minimum and maximum temperature in most standard stations around the location of interest; hence, researchers employed this meteorological parameter for estimating PAR on the horizontal surface. The basis of temperature-based computing models is that the differences between the maximum and minimum temperature is directly proportional to the fraction of extraterrestrial PAR received at the surface of the earth. However, other factors that affect temperature difference include cloudiness, relative humidity, elevation, topography, latitude and proximity to a large body of water. In this temperature-based computing model, PAR clearness index is a function of maximum and minimum temperature as show in this section. Therefore, empirical models from this group were calibrated from Hargreaves and Samani [114] computing model where photosynthetically active radiation $\left(PAR^e\right)$ is expressed in energy terms as shown below in the following form:

$$PAR = aH\sqrt{(T_{\max} - T_{\min})} \quad (88)$$

where a being the regression coefficient and T_{max} and T_{min} are the maximum and minimum temperature and other symbols retain their usual meaning.

Abolfazi [61] calibrated the following MB model for Shiraz University in South Iran as:

$$PAR = 0.0993H\sqrt{(T_{\max} - T_{\min})} \quad (89)$$

4.4 Optical Air Mass-Based Models

Optical air mass-based models have been employed by solar energy researchers for estimating PAR on hourly, daily and monthly time scales as a result of its observable influence on it. PAR changes as atmospheric parameters fluctuate. Experimental reports have revealed that PAR generally decrease with increasing optical air mass and the maxima were achieved when the sky conditions were cloudless. Meanwhile, PAR under clear skies decreased exponentially with optical air mass and the dispersion was much smaller than that under all sky conditions, which implies that PAR can be modelled using an exponential function of optical air mass in any region of the world as presented in these functional forms:

$$PAR^{e} = a(m)^{-b} \quad (90)$$

$$PAR^{p} = a(m)^{-b} \quad (91)$$

where m being the optical air mass, a and b are the regression coefficients and symbols retain their usual meaning.

Wang *et al.* [9] stimulated the following DB model for Central China as:

$$PAR^{e} = 1721(m)^{-1.06} \quad (92)$$

Hu and Wang [62] developed the following MB model for Sanjiang in Northeast China under clear sky condition as:

$$PAR^{p} = 2253.7(m)^{-1.3} \quad (93)$$

Wang *et al.* [63] established the following MB model for Inner Mongolia, China as:

$$PAR^{p} = 1524.3(m)^{-0.98} \quad (94)$$

Hu *et al.* [64] fitted the following MB model for North China Plain as:

$$PAR^{p} = 1886.1(m)^{-1.1} \quad (95)$$

4.5 Cloud Amount-Based Models

Cloud amount as a climate variable is the fraction of the sky obscured by clouds when observed from a given locality. Cloud amount data are periodically obtained from meteorological stations or satellites-derived and are expressed in percent (%) of the maximum cloud amount. Cloud amount is mostly classified into several categories of 0 – 24%, 25 – 49%, 50 – 74% and 75 – 100%. The implication is that zero percent implies no visible cloud in the sky while hundred percent cloud amount indicates no clear sky is visible. Researchers in the domain of renewable energy in the past have investigated and

simulated empirical computing models to relate cloud amount conditions and PAR owing to the fact that as PAR/H increases, cloud amount increases as well. This is because of the absorption of water vapour's waveband selective in the solar spectrum that is, in cloudy and humid conditions, the absorption of solar radiation in the infrared portion of the solar spectrum is enhanced whereas absorption in the PAR waveband does not vary significantly as shown in the relations below.

$$\frac{PAR^e}{H} = a + b(C) \tag{96}$$

where a and b are the regression coefficients, C is the cloud amount and other symbols retain their usual meaning.

Li *et al.* [55] obtained the following MB model for Northern Tibetan Plateau, China as:

$$\frac{PAR^e}{H} = 0.4315 + 0.04581(C) \tag{97}$$

4.6 Water Vapour Pressure-Based Models

Water vapour pressure-based models have been applied by researchers in the domain of renewable energy for estimating PAR in that it causes observable influence on the ratio of PAR/H. PAR/H fluctuates with changes in the atmospheric parameters. Experimental reports have shown that PAR/H increases with the increase in water vapour pressure. This could be attributed to the absorption of water vapour's waveband selective in the solar spectrum. That is, in cloudy and humid conditions, the absorption of solar radiation in the near infrared (NIR) portion of the solar spectrum is not vary significantly, hence, an increase in the PAR/H ratio occur under cloudy and humid conditions. Thus, in this section, water vapour is related to PAR/H as shown below.

$$\frac{PAR^e}{H} = a + bIn\left(E^*\right) \tag{98}$$

where $E^* = E \times P / P_0$. E is the monthly average value of water vapour pressure at the site. P_o is the standard atmospheric pressure at the sea level (1013hPa). P is the monthly average atmospheric pressure at the site. Where a and b are the regression coefficients and other symbols retain their usual meaning.

Li *et al.* [55] fitted the following model for Northern Tibetan Plateau, China as:

$$\frac{PAR^e}{H} = 0.4345 + 0.0087In\left(E^*\right) \tag{99}$$

4.7 Turbidity-Based Models

Observable influence of turbidity (βc) on the ratio of PAR/H in recent experimental report have culminated into development of empirical computing models for relating turbidity to ratio of PAR/H. This could be attributed to the absorption of water vapour pressure and cloud amount waveband selective in the solar spectrum. In cloudy and

humid conditions, the absorption of solar radiation in the near infrared (NIR) portion of the solar spectrum is enhanced, whereas absorption in the PAR waveband does not vary significantly, thus, an increase in the PAR/H ratio is found under cloudy and humid conditions. Therefore, in this section, turbidity is related to PAR/H as presented in the functional form below.

$$\frac{PAR^e}{H} = a + b(\beta c) \tag{100}$$

where a and b are the regression coefficients, (βc) being turbidity and other symbols retain their usual meaning.

Li *et al.* [55] fitted the following MB model for Northern Tibetan Plateau, China as:

$$\frac{PAR^e}{H} = 0.4547 - 0.247(\beta c) \tag{101}$$

4.8 Sunshine-Based models

The relative sunshine duration is one of the most commonly employed meteorological parameter for estimating PAR globally since sunshine duration is measured routinely at numerous meteorological stations across the globe, researchers in the domain of renewable energy often apply this parameter for PAR estimating worldwide as presented in this section.

4.8.1 Group 1

Empirical models from this group are parameterized as the first-order polynomial function of the sunshine where photosynthetically active radiation $\left(PAR^p\right)$ is expressed in photon units (μmolJ^{-1}, E MJ^{-1} etc.) and photosynthetically active radiation $\left(PAR^e\right)$ is expressed in energy terms as shown below in the following forms:

$$\frac{PAR^e}{H} = a + b\left(\frac{S}{S_o}\right) \tag{102}$$

$$\frac{PAR^p}{H} = a + b\left(\frac{S}{S_o}\right) \tag{103}$$

$$\frac{PAR^e}{PAR_o} = a + b\left(\frac{S}{S_o}\right) \tag{104}$$

$$\frac{PAR^p}{PAR_o} = a + b\left(\frac{S}{S_o}\right) \tag{105}$$

where a and b are the regression coefficients, $\left(\frac{S}{S_o}\right)$ being sunshine fraction and other symbols retain their usual meaning.

Udo and Aro [74] established the following MB models for Ilorin, Nigeria between 1993-1994.

For data obtained in 1993

$$\frac{PAR^p}{PAR_o} = 0.41 + 1.06\left(\frac{S}{S_o}\right) \quad (106a)$$

For data recorded in 1994

$$\frac{PAR^p}{PAR_o} = 0.53 + 0.89\left(\frac{S}{S_o}\right) \quad (106b)$$

For 1993-1994 data

$$\frac{PAR^p}{PAR_o} = 0.47 + 0.99\left(\frac{S}{S_o}\right) \quad (106c)$$

For dry season

$$\frac{PAR^p}{PAR_o} = 0.59 + 0.76\left(\frac{S}{S_o}\right) \quad (106d)$$

For rainy season

$$\frac{PAR^p}{PAR_o} = 0.39 + 1.18\left(\frac{S}{S_o}\right) \quad (106e)$$

For 1993-1994 data

$$\frac{PAR^e}{PAR_o} = 0.11 + 0.22\left(\frac{S}{S_o}\right) \quad (106f)$$

Li *et al.* [55] stimulated the following MB model for Northern Tibetan Plateau, China as:

$$\frac{PAR^e}{H} = 0.4861 - 0.0591\left(\frac{S}{S_o}\right) \quad (107)$$

Abolfazi [61] obtained the following MB model for Shiraz University in South Iran as:

$$\frac{PAR^e}{PAR_o} = 0.188 + 0.338\left(\frac{S}{S_o}\right) \quad (108)$$

4.8.2 Group 2

Empirical models from this group are parameterized as the second-order polynomial function of the sunshine where photosynthetically active radiation $\left(PAR^p\right)$ is expressed in photon units (μmolJ^{-1}, E MJ^{-1} etc.) as shown below in the following form:

$$\frac{PAR^p}{PAR_o} = a + b\left(\frac{S}{S_o}\right) + c\left(\frac{S}{S_o}\right)^2 \quad (109)$$

where a, b and c are the regression coefficients, $\left(\frac{S}{S_o}\right)$ being sunshine fraction and other symbols retain their usual meaning.

Udo and Aro [74] established the following MB models for Ilorin, Nigeria between 1993-1994.

$$\frac{PAR^p}{PAR_o} = 0.07 + 2.76\left(\frac{S}{S_o}\right) - 1.85\left(\frac{S}{S_o}\right)^2 \quad (110)$$

4.8.3 Group 3

Empirical models from this group are parameterized as logarithmic fit of the sunshine where photosynthetically active radiation $\left(PAR^p\right)$ is expressed in photon units ($\mu molJ^{-1}$, E MJ^{-1} etc.) as shown below in the following form:

$$\frac{PAR^p}{PAR_o} = a + bIn\left(\frac{S}{S_o}\right) \quad (111)$$

where a and b are the regression coefficients, $\left(\frac{S}{S_o}\right)$ being sunshine fraction and other symbols retain their usual meaning.

Udo and Aro [74] established the following MB models for Ilorin, Nigeria between 1993-1994.

$$\frac{PAR^p}{PAR_o} = 1.29 + 0.46In\left(\frac{S}{S_o}\right) \quad (112)$$

4.9 Clearness Index-Based Models

Clearness index (K_t) indicates that percentage depletion by the sky of the incoming solar variation and therefore gives both the level of availability of solar radiation and changes in the atmospheric condition in a given environment [1-2]. for this purpose, clearness index is closely related to PAR. Thus, clearness index has been known as a keynote determinant parameter for estimating PAR across the globe. One of the greatest characteristics of the model from this class is their convenient application in that utilizing them involve only measured global solar radiation data. Several functional forms and computing models have been employed for estimating PAR applying this parameter on HB, DB and MB across the globe as outline in this section according to their developing year.

4.9.1 Group 1

Empirical models from this group are parameterized as the first-order polynomial function of the clearness index where photosynthetically active radiation $\left(PAR^e\right)$ is expressed in energy terms as shown below in the following forms:

$$\frac{PAR^e}{PAR_o} = a + b\left(\frac{H}{H_o}\right) \quad (113)$$

$$\frac{PAR^e}{H_o} = a + b\left(\frac{H}{H_o}\right) \quad (114)$$

$$\frac{PAR^e}{H} = a + bIn\left(\frac{H}{H_o}\right) \quad (115)$$

Yu *et al.* [72] fitted the following MB model for contiguous United States as:

$$\frac{PAR^e}{H} = 0.4180 - 0.04095In\left(\frac{H}{H_o}\right) \quad (116)$$

Etuk *et al.* [68] establish the following MB models for Calabar, Nigeria as follows:

$$\frac{PAR^e}{H_o} = 0.001 + 0.448\left(\frac{H}{H_o}\right) \quad (117a)$$

$$\frac{PAR^e}{PAR_o} = 0.002 + 1.119\left(\frac{H}{H_o}\right) \quad (117b)$$

4.9.2 Group 2

Empirical models from this group are parameterized as the second-order polynomial function of the sunshine where photosynthetically active radiation $\left(PAR^p\right)$ is expressed in photon units (μmolJ^{-1}, E MJ^{-1} etc.) and photosynthetically active radiation $\left(PAR^e\right)$ is expressed in energy terms as shown below in the following forms:

$$\frac{PAR^e}{H} = a + b\left(\frac{H}{H_o}\right) + c\left(\frac{H}{H_o}\right)^2 \quad (118)$$

$$\frac{PAR^p}{H} = a + b\left(\frac{H}{H_o}\right) + c\left(\frac{H}{H_o}\right)^2 \quad (119)$$

$$\frac{PAR^e}{H_o} = a + b\left(\frac{H}{H_o}\right) + c\left(\frac{H}{H_o}\right)^2 \quad (120)$$

$$\frac{PAR^e}{PAR_o} = a + b\left(\frac{H}{H_o}\right) + c\left(\frac{H}{H_o}\right)^2 \quad (121)$$

$$\frac{PAR^e}{H} = a + bIn\left(\frac{H}{H_o}\right) + cIn\left(\frac{H}{H_o}\right)^2 \quad (122)$$

Tsubo and Walker [48] fitted the following MB and HB models for Bloemfontein, South Africa.

For Daily Basis (DB)

$$\frac{PAR^p}{H} = 0.635 - 0.401\left(\frac{H}{H_o}\right) + 0.150\left(\frac{H}{H_o}\right)^2 \quad (123a)$$

For Hourly Basis (HB)

$$\frac{PAR^p}{H} = 0.613 - 0.334\left(\frac{H}{H_o}\right) + 0.121\left(\frac{H}{H_o}\right)^2 \quad (123b)$$

Wang *et al.* [71] established the following HB model for Central China as:

$$\frac{PAR^p}{H} = 0.567 - 0.625\left(\frac{H}{H_o}\right) - 0.659\left(\frac{H}{H_o}\right)^2 \quad (124)$$

Yu *et al.* [72] fitted the following MB model for contiguous United States as:

$$\frac{PAR^e}{H} = 0.4287 + 0.012238In\left(\frac{H}{H_o}\right) - 0.01223In\left(\frac{H}{H_o}\right)^2 \quad (125)$$

Etuk *et al.* [69] calibrated the following MB models for several locations in Nigeria.

For Port Harcourt

$$\frac{PAR^e}{PAR_o} = 0.001 + 1.126\left(\frac{H}{H_o}\right) - 0.001\left(\frac{H}{H_o}\right)^2 \quad (126a)$$

For Enugu

$$\frac{PAR^e}{PAR_o} = 0.005 + 1.101\left(\frac{H}{H_o}\right) - 0.027\left(\frac{H}{H_o}\right)^2 \quad (126b)$$

For Abeokuta

$$\frac{PAR^e}{PAR_o} = -0.001 + 1.128\left(\frac{H}{H_o}\right) - 0.003\left(\frac{H}{H_o}\right)^2 \quad (126c)$$

For Ilorin

$$\frac{PAR^e}{PAR_o} = 0.053 + 0.919\left(\frac{H}{H_o}\right) - 0.192\left(\frac{H}{H_o}\right)^2 \quad (126d)$$

For Bauchi

$$\frac{PAR^e}{PAR_o} = 0.028 + 1.032\left(\frac{H}{H_o}\right) + 0.076\left(\frac{H}{H_o}\right)^2 \quad (126e)$$

For Sokoto

$$\frac{PAR^e}{PAR_o} = -0.018 + 1.186\left(\frac{H}{H_o}\right) - 0.051\left(\frac{H}{H_o}\right)^2 \quad (126f)$$

Etuk *et al.* [68] proposed the following MB models for Calabar, Nigeria as follows:

$$\frac{PAR^e}{PAR_o} = 0.020 + 1.034\left(\frac{H}{H_o}\right) + 0.103\left(\frac{H}{H_o}\right)^2 \quad (127a)$$

$$\frac{PAR^e}{H_o} = 0.009 + 0.406\left(\frac{H}{H_o}\right) + 0.050\left(\frac{H}{H_o}\right)^2 \quad (127b)$$

Nwokolo *et al.* [70] calibrated the following MB models for numerous locations in Nigeria.

For Port Harcourt

$$\frac{PAR^e}{H} = 0.614 - 0.338\left(\frac{H}{H_o}\right) + 0.126\left(\frac{H}{H_o}\right)^2 \quad (128a)$$

For Enugu

$$\frac{PAR^e}{H} = 0.616 - 0.345\left(\frac{H}{H_o}\right) + 0.134\left(\frac{H}{H_o}\right)^2 \quad (128b)$$

For Abeokuta

$$\frac{PAR^e}{H} = 0.557 - 0.088\left(\frac{H}{H_o}\right) - 0.142\left(\frac{H}{H_o}\right)^2 \quad (128c)$$

For Ilorin

$$\frac{PAR^e}{H} = 0.576 - 0.201\left(\frac{H}{H_o}\right) + 0.007\left(\frac{H}{H_o}\right)^2 \quad (128d)$$

For Sokoto

$$\frac{PAR^e}{H} = 0.616 - 0.343\left(\frac{H}{H_o}\right) + 0.129\left(\frac{H}{H_o}\right)^2 \quad (128e)$$

For Bauchi

$$\frac{PAR^e}{H} = 0.615 - 0.341\left(\frac{H}{H_o}\right) + 0.127\left(\frac{H}{H_o}\right)^2 \quad (128f)$$

4.9.3 Group 3

Empirical models from this group are parameterized as the third-order polynomial function of the sunshine where photosynthetically active radiation $\left(PAR^p\right)$ is expressed in photon units (μmolJ^{-1}, E MJ^{-1} etc.) as shown below in the form:

$$PAR^p = a + b\left(\frac{H}{H_o}\right) + c\left(\frac{H}{H_o}\right)^2 + d\left(\frac{H}{H_o}\right)^3 \quad (129)$$

Wang *et al.* [98] obtained the following MB model for Wuhan, Central China as:

$$PAR^p = 28.4 + 3130.2\left(\frac{H}{H_o}\right) - 2210.3\left(\frac{H}{H_o}\right)^2 + 1926.4\left(\frac{H}{H_o}\right)^3 \quad (130)$$

Wang *et al.* [63] developed the following MB model for Inner Mongolia, China from 1990 to 2012 as:

$$PAR^p = 110.488 + 1185.2\left(\frac{H}{H_o}\right) + 1823.3\left(\frac{H}{H_o}\right)^2 - 1470.0\left(\frac{H}{H_o}\right)^3 \quad (131)$$

Wang *et al.* [115] proposed the following MB model in China as:

$$PAR^p = 58.4 + 1771.2\left(\frac{H}{H_o}\right) + 791.3\left(\frac{H}{H_o}\right)^2 - 734.4\left(\frac{H}{H_o}\right)^3 \quad (132)$$

Peng *et al.* [73] fitted the following MB model for Tibatan Plateau, Lhasa, China as:

$$PAR^p = 88.98 + 1486.1\left(\frac{H}{H_o}\right) + 1094.6\left(\frac{H}{H_o}\right)^2 - 846.33\left(\frac{H}{H_o}\right)^3 \quad (133)$$

Hu *et al.* [116] stimulated the following model for Tibetan Plateau, China as:

$$PAR^p = 73.5 + 2256.9\left(\frac{H}{H_o}\right) + 1246.7\left(\frac{H}{H_o}\right)^2 - 1182.8\left(\frac{H}{H_o}\right)^3 \quad (134)$$

4.10 Hybrid Parameter-Based Models

In as much as input parameters for estimating PAR on the horizontal surface varies periodically with the local climate in a given geographical location, it therefore indicates that to accurately stimulate a computing model that can fit a specific geographical area, solar energy researchers must test the local climate with various input parameters depending on the availability of the measurable metrological parameters and atmospheric variables at the disposal of the researcher. Numerous solar energy researchers across the globe have observed that hybrid parameter-based computing models fit local climate more than one variable-global solar radiation-based models, relative humidity-based models, temperature-based models, relative humidity-based models, temperature-based models, optical air mass-based models, cloud amount-based models, water vapour pressure-based models, turbidity-based models, sunshine-based models and clearness index-based models employed for estimating PAR. In this section, several hybrid parameter-based models are presented and classified based on their input parameters and developing year.

4.10.1 Group 1

In this group, global solar radiation and clearness index were incorporated with PAR in the forms:

$$PAR^p = a(H) + b\left(\frac{H}{H_o}\right) + c \quad (135)$$

$$PAR^e = a(H) + b\left(\frac{H}{H_o}\right) + c \quad (136)$$

Aguiar *et al.* [65] established the following HB models for pasture and forest sites in South Amazonia under hourly and daily time scales.

For Pasture site (Hourly Basis, HB)

$$PAR^e = 1.146(H) + 0.478\left(\frac{H}{H_o}\right) - 5.547 \quad \text{(wet season)} \quad (137a)$$

$$PAR^e = 1.336(H) + 0.471\left(\frac{H}{H_o}\right) - 6.911 \quad \text{(wet-dry season)} \quad (137b)$$

$$PAR^e = -6.633(H) + 0.445\left(\frac{H}{H_o}\right) + 7.669 \quad \text{(dry season)} \quad (137c)$$

$$PAR^e = 3.904(H) + 0.480\left(\frac{H}{H_o}\right) - 27.641 \quad \text{(dry-wet season)} \quad (137d)$$

$$PAR^e = 1.612(H) + 0.469\left(\frac{H}{H_o}\right) - 11.761 \quad \text{(Annual)} \quad (137e)$$

For Forest Site (Hourly Basis, HB)

$$PAR^e = 3.074(H) + 0.437\left(\frac{H}{H_o}\right) - 22.882 \quad \text{(wet season)} \quad (137f)$$

$$PAR^e = 3.121(H) + 0.424\left(\frac{H}{H_o}\right) - 8.042 \quad \text{(wet-8dry season)} \quad (137g)$$

$$PAR^e = -0.8017(H) + 0.436\left(\frac{H}{H_o}\right) - 9.302 \quad \text{(dry season)} \quad (137h)$$

$$PAR^e = 5.544(H) + 0.447\left(\frac{H}{H_o}\right) - 32.168 \quad \text{(dry-wet season)} \quad (137i)$$

$$PAR^e = 2.939(H) + 0.434\left(\frac{H}{H_o}\right) - 16.509 \quad \text{(Annual)} \quad (137j)$$

For Pasture Site (Daily Basis, DB)

$$PAR^e = 3.847(H) + 0.466\left(\frac{H}{H_o}\right) - 1.516 \quad \text{(wet season)} \quad (137k)$$

$$PAR^e = 2.737(H) + 0.513\left(\frac{H}{H_o}\right) - 39.827 \quad \text{(wet-dry season)} \quad (137L)$$

$$PAR^e = -0.946(H) + 0.335\left(\frac{H}{H_o}\right) + 79.082 \quad \text{(dry season)} \quad (137m)$$

$$PAR^e = 4.109(H) + 0.709\left(\frac{H}{H_o}\right) - 234.374 \quad \text{(dry-wet season)} \quad (137n)$$

$$PAR^e = 5.257(H) + 0.479\left(\frac{H}{H_O}\right) - 27.375 \text{ (Annual)} \quad (137o)$$

For Forest Site (Daily Basis, DB)

$$PAR^e = 2.738(H) + 0.457\left(\frac{H}{H_O}\right) - 41.467 \text{ (wet season)} \quad (137p)$$

$$PAR^e = -0.339(H) + 0.410\left(\frac{H}{H_O}\right) + 9.599 \text{ (wet-dry season)} \quad (137q)$$

$$PAR^e = -4.142(H) + 0.431\left(\frac{H}{H_O}\right) + 1.893 \quad \text{(dry season)} \quad (137r)$$

$$PAR^e = 2.128(H) + 0.384\left(\frac{H}{H_O}\right) + 39.020 \text{ (dry-wet season)} \quad (137s)$$

$$PAR^e = 0.925(H) + 0.426\left(\frac{H}{H_O}\right) - 4.352 \quad \text{(Annual)} \quad (137t)$$

Hu and Wang [62] reported the following HB model for Northern China as:

$$PAR^p = 61.9(H) + 2.0\left(\frac{H}{H_O}\right) + 209.0 \quad (138)$$

Hu *et al.* [64] developed the following HB models for Beijing site in North China Plain as:

$$PAR^p = 1.92(H) - 242.7\left(\frac{H}{H_O}\right) + 42.8 \quad (139)$$

4.10.2 Group 2

In this group, clearness index, daytime length (L_D) and solar zenith angle (θ_z) were incorporated with PAR in the forms:

$$PAR^p = \left(a + b\left(\frac{H}{H_o}\right) + c\left(\frac{H}{H_o}\right)^2 + d\left(\frac{H}{H_o}\right)^3\right) \times \theta_z^e \times L_D \quad (140)$$

$$PAR^p = \left(a + b\left(\frac{H}{H_o}\right) + c\left(\frac{H}{H_o}\right)^2 + d\left(\frac{H}{H_o}\right)^3\right) \times \theta_z^e \quad (141)$$

$$PAR^e = \left(a + b\left(\frac{H}{H_o}\right) + c\left(\frac{H}{H_o}\right)^2 + d\left(\frac{H}{H_o}\right)^3\right) \times \theta_z^e \times L_D \quad (142)$$

$$PAR^e = \left(a + b\left(\frac{H}{H_o}\right) + c\left(\frac{H}{H_o}\right)^2 + d\left(\frac{H}{H_o}\right)^3\right) \times \theta_z^e \quad (143)$$

Wang *et al.* [98] developed the following DB and I minute models for Wuhan, Central China.

For I minute Basis

$$PAR^p = \left(28.4 + 3130.2\left(\frac{H}{H_o}\right) - 2210.3\left(\frac{H}{H_o}\right)^2 + 1926.4\left(\frac{H}{H_o}\right)^3 \right) \times \theta_z^{1.045} \quad (144a)$$

For Daily Basis (DB)

$$PAR^p = \left(6.21 + 684.9\left(\frac{H}{H_o}\right) - 483.7\left(\frac{H}{H_o}\right)^2 + 421.5\left(\frac{H}{H_o}\right)^3 \right) \times \theta_z^{1.045} \times L_D \quad (144b)$$

Wang *et al.* [63] fitted the following HB models for Inner Mongolia, China.

For Hourly Basis (HB)

$$PAR^e = \left(110.48 + 1185.2\left(\frac{H}{H_o}\right) + 1833.3\left(\frac{H}{H_o}\right)^2 - 1470\left(\frac{H}{H_o}\right)^3 \right) \times \theta_z^{0.941} \quad (145a)$$

For Daily Basis (DB)

$$PAR^p = \left(7.57 + 30.39\left(\frac{H}{H_o}\right) + 126.64\left(\frac{H}{H_o}\right)^2 - 100.39\left(\frac{H}{H_o}\right)^3 \right) \times \theta_z^{1.47} \quad (145b)$$

Peng *et al.* [73] fitted the following DB and I minute models for Lhasa (Tibetan Plateau) in China.

For Daily Basis (DB)

$$PAR^p = \left(16.587 - 15.909\left(\frac{H}{H_o}\right) + 182.544\left(\frac{H}{H_o}\right)^2 - 117.93\left(\frac{H}{H_o}\right)^3 \right) \times \theta_z^{1.621} \times L_D \quad (146a)$$

For I minute Basis

$$PAR^p = \left(88.98 - 1486.1\left(\frac{H}{H_o}\right) + 1094.6\left(\frac{H}{H_o}\right)^2 - 846.33\left(\frac{H}{H_o}\right)^3 \right) \times \theta_z^{1.027} \quad (146b)$$

Wang *et al.* [115] developed the following HB and DB model for LZ station, China.

For Hourly Basis (HB)

$$PAR^e = \left(58.4 + 1771.2\left(\frac{H}{H_o}\right) + 791.3\left(\frac{H}{H_o}\right)^2 - 734.4\left(\frac{H}{H_o}\right)^3 \right) \times \theta_z^{1.045} \quad (147a)$$

For Daily Basis (DB)

$$PAR^p = \left(3.75 + 67.22\left(\frac{H}{H_o}\right) + 42.29\left(\frac{H}{H_o}\right)^2 - 35.77\left(\frac{H}{H_o}\right)^3 \right) \times \theta_z^{1.622} \quad (147b)$$

Hu *et al.* [116] established the following HB and DB models for Lhasa and Huaibei, Tibetan Plateau, China as follows:

For Hourly Basis (HB)

$$PAR^e = \left(73.5 + 2256.9\left(\frac{H}{H_o}\right) + 1246.7\left(\frac{H}{H_o}\right)^2 - 1182.8\left(\frac{H}{H_o}\right)^3 \right) \times \theta_z^{1.09} \quad (148a)$$

For Daily Basis (DB)

$$PAR^e = \left(2.1 - 2.4\left(\frac{H}{H_o}\right) + 23.9\left(\frac{H}{H_o}\right)^2 - 15.5\left(\frac{H}{H_o}\right)^3\right) \times \theta_z^{1.13} \times L_D \quad (148b)$$

4.10.3 Group 3

In this group, the attenuation factor in clear skies (AF_C, ratio of measured to extraterrestrial (PAR_o) under clear skies), the attenuation factor with clouds, which can be expressed as H/H_o were incorporated with PAR fraction in the form:

$$\frac{PAR^e}{PAR_o} = aAF_C^b\left(\frac{H}{H_o}\right)^c \quad (149)$$

where a, b and c are the regression coefficients and other symbols retain their usual meaning.

Wang *et al.* [63] stimulated the HB model for Inner Mongolia, China as:

$$\frac{PAR^e}{PAR_o} = 1.06AF_C^{0.34}\left(\frac{H}{H_o}\right)^{0.88} \quad (150)$$

4.10.4 Group 4

In this group, clearness index and optical air mass (m) were incorporated with PAR clearness index in the form:

$$\frac{PAR^p}{PAR_o} = a\left(\frac{H}{H_o}\right)^b m^c \quad (151)$$

where a, b and c are the regression coefficients and other symbols retain their usual meaning.

Hu and Wang [62] developed the HB model for Northern China under all sky conditions as:

$$\frac{PAR^p}{PAR_o} = 0.92\left(\frac{H}{H_o}\right)^{-0.0012} m^{0.7925} \quad (152)$$

Hu *et al.* [64] fitted the following HB model for Beijing site as:

$$\frac{PAR^p}{PAR_o} = 0.80\left(\frac{H}{H_o}\right)^{0.84} m^{0.09} \quad (153)$$

4.10.5 Group 5

In this group, global solar radiation (H), solar zenith angle (θ_z), columnar perceptible water vapour (wv), and aerosol optical depth (AOD) were incorporated with PAR in the form:

$$PAR^e = a(\theta_z) + b(H) + c(wv) + d(AOD) + e \quad (154)$$

Melina-Maria *et al.* [77] stimulated the following HB model for Greece as:

$$PAR^e = -0.375(\theta_z) + 0.431(H) + 3.673(wv) - 3.447(AOD) + 19.940 \quad (155)$$

4.10.6 Group 6

In this group, water vapour pressure and relative sunshine duration were incorporated with ratio of PAR/H in the form:

$$\frac{PAR^e}{H} = a + b(E^*) + c\left(\frac{S}{S_O}\right) \quad (156)$$

where $E^* = E \times P/P_0$. E is the monthly average value of water vapour pressure at the site. P_o is the standard atmospheric pressure at the sea level (1013hPa). P is the monthly average atmospheric pressure at the site, while a, b and c are the regression coefficients and other symbols retain their usual meaning.

Li *et al.* [55] obtained the following MB model for Northern Tibetan Plateau, China as:

$$\frac{PAR^e}{H} = 0.453 + 0.0161(E^*) - 0.024\left(\frac{S}{S_O}\right) \quad (157)$$

4.10.7 Group 7

In this group, clearness of the sky (ε), brightness of the skylight (Δ), solar zenith angle (θ_z), clearness index, site elevation (h) and perceptible water (wv) were incorporated with PAR/H ratio in the forms:

$$\frac{PAR^p}{H} = a + b(In\Delta) + c(In\varepsilon) + d(Inwv) + e(\sinh) \quad (158)$$

$$\frac{PAR^p}{H} = a + b\left(In\frac{H}{H_O}\right) + c(\sinh) + d(Inwv) \quad (159)$$

Wang *et al.* [71] fitted the following HB models for Wuhan, Central China as:

$$\frac{PAR^p}{H} = 0.444 - 0.054(In\Delta) - 0.05(In\varepsilon) + 0.029(Inwv) + 0.1(\sinh) \quad (160a)$$

$$\frac{PAR^p}{H} = 0.33 - 0.058\left(In\frac{H}{H_O}\right) + 0.027(\sinh) + 0.025(Inwv) \quad (160b)$$

4.10.8 Group 8

In this group, water vapour pressure, global solar radiation and clearness index were incorporated with PAR in the form:

$$PAR^e = a(H) + b\left(\frac{H}{H_O}\right) + c(E) + d \quad (161)$$

Aguiar *et al.* [65] developed the following DB and HB models for Pasture and Forest Sites in South West Amazonia

For Pasture Site (Hourly Basis)

$$PAR^e = 11.196(H) + 0.478\left(\frac{H}{H_o}\right) - 6.088(E) + 0.385 \quad \text{(wet season)} \quad (162a)$$

$$PAR^e = -4.534(H) + 0.470\left(\frac{H}{H_o}\right) - 6.511(E) + 0.246 \quad \text{(wet-dry season)} \quad (162b)$$

$$PAR^e = -14.164(H) + 0.444\left(\frac{H}{H_o}\right) + 10.533(E) + 0.339 \quad \text{(dry season)} \quad (162c)$$

$$PAR^e = 7.102(H) + 0.480\left(\frac{H}{H_o}\right) - 27.739(E) - 0.127 \quad \text{(dry-wet season)} \quad (162d)$$

$$PAR^e = -26.505(H) + 0.464\left(\frac{H}{H_o}\right) - 3.210(E) + 1.105 \quad \text{(Annual)} \quad (162e)$$

For Forest Site (Hourly Basis)

$$PAR^e = -12.054(H) + 0.441\left(\frac{H}{H_o}\right) - 27.446(E) + 0.686 \quad \text{(wet season)} \quad (162f)$$

$$PAR^e = -6.610(H) + 0.425\left(\frac{H}{H_o}\right) - 8.972(E) + 0.436 \quad \text{(wet-dry season)} \quad (162g)$$

$$PAR^e = -15.891(H) + 0.435\left(\frac{H}{H_o}\right) - 4.325(E) + 0.606 \quad \text{(dry season)} \quad (162h)$$

$$PAR^e = 0.518(H) + 0.447\left(\frac{H}{H_o}\right) - 34.066(E) + 0.274 \quad \text{(dry-wet season)} \quad (162i)$$

$$PAR^e = -7.072(H) + 0.435\left(\frac{H}{H_o}\right) - 18.125(E) + 0.467 \quad \text{(Annual)} \quad (162j)$$

For Pasture Site (Daily Basis)

$$PAR^e = 4.447(H) + 0.466\left(\frac{H}{H_o}\right) - 1.362(E) - 0.023 \quad \text{(wet season)} \quad (162k)$$

$$PAR^e = -8.390(H) + 0.487\left(\frac{H}{H_o}\right) - 22.223(E) + 0.499 \quad \text{(wet-dry season)} \quad (162L)$$

$$PAR^e = -27.462(H) + 0.347\left(\frac{H}{H_o}\right) + 86.718(E) + 0.927 \quad \text{(dry season)} \quad (162m)$$

$$PAR^e = 20.423(H) + 0.766\left(\frac{H}{H_o}\right) - 286.430(E) - 0.629 \quad \text{(dry-wet season)} \quad (162n)$$

$$PAR^e = -34.302(H) + 0.435\left(\frac{H}{H_o}\right) + 17.944(E) + 1.495 \quad \text{(Annual)} \quad (162o)$$

For Forest Site (Daily Basis)

$$PAR^e = -16.421(H) + 0.453\left(\frac{H}{H_o}\right) - 40.867(E) + 0.903 \quad \text{(wet season)} \quad (162p)$$

$$PAR^e = -8.834(H) + 0.418\left(\frac{H}{H_o}\right) + 3.108(E) + 0.396 \quad \text{(wet-dry season)} \quad (162q)$$

$$PAR^e = -35.878(H) + 0.442\left(\frac{H}{H_o}\right) + 9.893(E) + 1.069 \quad \text{(dry season)} \quad (162r)$$

$$PAR^e = -10.179(H) + 0.398\left(\frac{H}{H_o}\right) + 17.392(E) + 0.773 \quad \text{(dry-wet season)} \quad (162s)$$

$$PAR^e = -13.566(H) + 0.426\left(\frac{H}{H_o}\right) - 6.702(E) + 0.703 \quad \text{(Annual)} \quad (162t)$$

4.10.9 Group 9

In this group, solar zenith angle (θ_z), solar elevation angle (β), clearness of the sky (ε), brightness of skylight (Δ) and dew temperature (T_d) were incorporated with ratio of PAR with H in the form:

$$\frac{PAR^p}{H} = a + b(In\varepsilon) + c(In\Delta) + d(T_d) + e(\sin^2\beta) \quad (163)$$

$$\frac{PAR^p}{H} = a + b(In\varepsilon) + c(In\Delta) + d(T_d) + e(\cos^2\theta) \quad (164)$$

Alados *et al.* [5] developed the following HB model at the University of Almeria site as:

$$\frac{PAR^p}{H} = 1.786 - 0.192(In\varepsilon) - 0.202(In\Delta) + 0.005(T_d) + 0.032(\sin^2\beta) \quad (165)$$

Alados and Alados-Arboledas [117] calibrated the following HB model at the University of Almeria site as:

$$\frac{PAR^p}{H} = 1.786 - 0.192(In\varepsilon) - 0.202(In\Delta) + 0.005(T_d) + 0.032(\cos^2\theta) \quad (166)$$

Wang *et al.* [9] developed the following HB models for Wuhan, Central China as:

$$\frac{PAR^p}{H} = 0.454 - 0.052(In\Delta) - 0.064(In\varepsilon) + 0.072(\sin^2\theta) \quad (167)$$

4.10.10 Group 10

In this group, clearness of the solar zenith angle (θ_z), solar elevation angle (β), clearness of the sky (ε) and brightness of skylight (Δ) were incorporated with ratio of PAR with H in the form:

$$\frac{PAR^p}{H} = a + b\left(In\varepsilon\right) + c\left(In\Delta\right) + d\left(\sin^2\beta\right) \quad (168)$$

$$\frac{PAR^p}{H} = a + b\left(In\varepsilon\right) + c\left(In\Delta\right) + d\left(\cos^2\beta\right) \quad (169)$$

Alados *et al.* [5] fitted the following HB model for University of Almeria site as:

$$\frac{PAR^p}{H} = 1.854 - 0.194\left(In\varepsilon\right) - 0.19\left(In\Delta\right) + 0.076\left(\sin^2\beta\right) \quad (170)$$

Alados and Alados-Arboledas [117] calibrated the following HB model for University of Almeria site as:

$$\frac{PAR^p}{H} = 1.854 - 0.194\left(In\varepsilon\right) - 0.195\left(In\Delta\right) + 0.076\left(\cos^2\beta\right) \quad (171)$$

4.10.11 Group 11

In this group, clearness index (H/H_o), dew point temperature (T_d), solar zenith angle (θ_z) or solar elevation angle (β) were incorporated with ratio of PAR with H in the form:

$$\frac{PAR^p}{H} = a + b\left(In\frac{H}{H_o}\right) + c\left(T_d\right) + d\left(\sin\beta\right) \quad (172)$$

$$\frac{PAR^p}{H} = a + b\left(In\frac{H}{H_o}\right) + c\left(T_d\right) + d\left(\cos\theta\right) \quad (173)$$

Alados *et al.* [5] developed the following HB model for University of Almeria site as:

$$\frac{PAR^p}{H} = 1.791 - 0.190\left(In\frac{H}{H_o}\right) + 0.005\left(T_d\right) + 0.049\left(\sin\beta\right) \quad (174)$$

Alados and Alados-Arboledas [117] calibrated the following HB model for University of Almeria site as:

$$\frac{PAR^p}{H} = 1.791 - 0.190\left(In\frac{H}{H_o}\right) + 0.005\left(T_d\right) + 0.049\left(\cos\theta\right) \quad (175)$$

Yu *et al.* [72] fitted the following HB models for contiguous United States as:

$$\frac{PAR^e}{H} = 0.0138\left(In\frac{H}{H_o}\right)^2 - 0.005396\left(In\frac{H}{H_o}\right) + 0.0001159\left(T_d\right) - 0.049\left(\cos\theta_z\right) + 0.4680 \quad (176)$$

$$\frac{PAR^p}{H} = 0.45 - 0.0385\left(In\frac{H}{H_o}\right) - 0.0001166\left(T_d\right) - 0.06031\left(\cos\theta\right) \quad (177)$$

4.10.12 Group 12

In this group, clearness index, solar elevation angle (β) or solar zenith angle (θ_z) were incorporated with PAR to H ratio in the form:

$$\frac{PAR^p}{H} = a + b\left(In\frac{H}{H_o}\right) + c\left(\sin\beta\right) \quad (178)$$

$$\frac{PAR^p}{H} = a + b\left(In\frac{H}{H_o}\right) + c(\cos\theta_z) \quad (179)$$

Alados *et al.* [5] fitted the following HB model for University of Almeria site as:

$$\frac{PAR^p}{H} = 1.832 - 0.191\left(In\frac{H}{H_O}\right) + 0.099(\sin\beta) \quad (180)$$

Alados and Alados-Arboledas [117] calibrated the following HB model for University of Almeria site as:

$$\frac{PAR^p}{H} = 1.832 - 0.191\left(In\frac{H}{H_o}\right) + 0.099(\cos\theta_z) \quad (181)$$

Wang *et al.* [71] reported the following HB model for Wuhan, Central China as:

$$\frac{PAR^e}{H} = 0.336 - 0.061\left(In\frac{H}{H_o}\right) + 0.045(\sin\beta) \quad (182)$$

Yu *et al.* [72] developed the following HB models for Contiguous United States as:

$$\frac{PAR^e}{H} = 0.4511178 - 0.03853\left(In\frac{H}{H_o}\right) - 0.06099(\cos\theta_z) \quad (183a)$$

$$\frac{PAR^e}{H} = 0.4641 + 0.01344\left(In\frac{H}{H_o}\right)^2 - 0.006911\left(In\frac{H}{H_o}\right) - 0.0631(\cos\theta_z) \quad (183b)$$

4.10.13 Group 13

In this group, clearness index and dew point temperature were incorporated to PAR to H ratio, PAR to H_o ratio, and PAR fraction in the forms:

$$\frac{PAR^e}{H_o} = a + b\left(\frac{T_d}{100}\right) + c\left(\frac{H}{H_o}\right) \quad (184)$$

$$\frac{PAR^e}{PAR_o} = a + b\left(\frac{T_d}{100}\right) + c\left(\frac{H}{H_o}\right) \quad (185)$$

$$\frac{PAR^e}{H} = a\left(In\frac{H}{H_o}\right)^2 + b\left(In\frac{H}{H_o}\right) + c(T_d) + d \quad (186)$$

Yu *et al.* [72] developed the following HB model for Contiguous United States as:

$$\frac{PAR^e}{H} = 0.01102\left(In\frac{H}{H_o}\right)^2 - 0.01632\left(In\frac{H}{H_o}\right) + 0.0005011(T_d) + 0.4283 \quad (187)$$

Etuk *et al.* [68] fitted the following MB models for Calabar, Nigeria as:

$$\frac{PAR^e}{H_o} = 0.001 + 0.001\left(\frac{T_d}{100}\right) + 0.009\left(\frac{H}{H_o}\right) \quad (188a)$$

$$\frac{PAR^e}{PAR_o} = 0.002 + 0.003\left(\frac{T_d}{100}\right) + 1.120\left(\frac{H}{H_o}\right) \quad (188b)$$

4.10.14 Group 14

In this group, diffuse fraction (H_d/H), brightness of the skylight ($_\Delta$), or solar zenith angle θ_z or dew point temperature (T_d) were incorporated with PAR and H ratio in the forms:

$$\frac{PAR^e}{H} = a\left(In\frac{H_d}{H}\right) + b\left(In\Delta\right) + c\left(T_d\right) + d\left(\cos^2\theta_z\right) + e \quad (189)$$

$$\frac{PAR^e}{H} = a\left(In\frac{H_d}{H}\right) + b\left(In\Delta\right) + c\left(\cos^2\theta_z\right) + d \quad (190)$$

$$\frac{PAR^e}{H} = a\left(In\frac{H_d}{H}\right) + b\left(In\Delta\right) + c \quad (191)$$

Yu *et al.* [72] obtained the following HB models for Contiguous United State as:

$$\frac{PAR^e}{H} = 0.039\left(In\frac{H_d}{H}\right) - 0.041\left(In\Delta\right) - 0.000089\left(T_d\right) - 0.0521\left(\cos^2\theta_z\right) + 0.4318 \quad (192)$$

$$\frac{PAR^e}{H} = 0.0387\left(In\frac{H_d}{H}\right) - 0.041\left(In\Delta\right) - 0.05728\left(\cos^2\theta_z\right) + 0.4332 \quad (193)$$

$$\frac{PAR^e}{H} = 0.04094\left(In\frac{H_d}{H}\right) - 0.040\left(In\Delta\right) + 0.4186 \quad (194)$$

4.10.15 Group 15

In this group, clearness index and sunshine fraction were incorporated with PAR fraction or PAR to H_o in the forms:

$$\frac{PAR^e}{H_o} = a + b\left(\frac{H}{H_o}\right) + c\left(\frac{S}{S_o}\right) \quad (195)$$

$$\frac{PAR^e}{PAR_o} = a + b\left(\frac{H}{H_o}\right) + c\left(\frac{S}{S_o}\right) \quad (196)$$

Etuk *et al.* [68] recorded the following MB models for Calabar, Nigeria as:

$$\frac{PAR^e}{H_o} = -0.002 + 0.448\left(\frac{H}{H_o}\right) + 0.004\left(\frac{S}{S_o}\right) \quad (197a)$$

$$\frac{PAR^e}{PAR_o} = -0.003 + 1.120\left(\frac{H}{H_o}\right) + 0.007\left(\frac{S}{S_o}\right) \quad (197b)$$

4.10.16 Group 16

In this group, relative humidity (RH) or sunshine fraction, clearness index was incorporated to PAR fraction in the forms:

$$\frac{PAR^e}{PAR_o} = a + b\left(\frac{R}{100}\right) + c\left(\frac{H}{H_o}\right) \quad (198)$$

$$\frac{PAR^e}{PAR_o} = a + b\left(\frac{R}{100}\right) + c\left(\frac{H}{H_o}\right) + d\left(\frac{H}{H_o}\right)^2 \quad (199)$$

$$\frac{PAR^e}{PAR_o} = a + b\left(\frac{R}{100}\right) + c\left(\frac{H}{H_o}\right)^2 \quad (200)$$

$$\frac{PAR^e}{PAR_o} = a + b\left(\frac{R}{100}\right) + c\left(\frac{S}{S_o}\right) + d\left(\frac{H}{H_o}\right) \quad (201)$$

Etuk *et al.* [68] reported the following MB models for Calabar, Nigeria as:

$$\frac{PAR^e}{PAR_o} = 0.005 - 0.02\left(\frac{R}{100}\right) + 1.118\left(\frac{H}{H_o}\right) \quad (202a)$$

$$\frac{PAR^e}{PAR_o} = 0.025 - 0.003\left(\frac{R}{100}\right) + 1.025\left(\frac{H}{H_o}\right) + 0.111\left(\frac{H}{H_o}\right)^2 \quad (202b)$$

$$\frac{PAR^e}{PAR_o} = 0.253 - 0.022\left(\frac{R}{100}\right) + 1.326\left(\frac{H}{H_o}\right)^2 \quad (202c)$$

$$\frac{PAR^e}{PAR_o} = 0.001 - 0.008\left(\frac{R}{100}\right) + 0.014\left(\frac{S}{S_o}\right) + 1.114\left(\frac{H}{H_o}\right) \quad (202d)$$

4.10.17 Group 17

In this group, dew point temperature, sunshine fraction, clearness index and ratio of minimum and maximum temperature were incorporated to PAR fraction and PAR to H_o ratio in the forms:

$$\frac{PAR^e}{PAR_o} = a + b\left(\frac{T_d}{100}\right) + c\left(\frac{S}{S_o}\right) + d\left(\frac{H}{H_o}\right) \quad (203)$$

$$\frac{PAR^e}{PAR_o} = a + b\left(T_R\right) + c\left(\frac{H}{H_o}\right) + d\left(\frac{S}{S_o}\right) \quad (204)$$

$$\frac{PAR^e}{H_o} = a + b\left(T_R\right) + c\left(\frac{H}{H_o}\right) + d\left(\frac{H}{H_o}\right)^2 \quad (205)$$

Etuk *et al.* [68] proposed the following MB models for Calabar, Nigeria as:

$$\frac{PAR^e}{PAR_o} = -0.008 + 0.016\left(\frac{T_d}{100}\right) + 0.009\left(\frac{S}{S_o}\right) + 1.121\left(\frac{H}{H_o}\right) \quad (206a)$$

$$\frac{PAR^e}{PAR_o} = -0.001 - 0.003\left(T_R\right) + 0.448\left(\frac{H}{H_o}\right) + 0.005\left(\frac{S}{S_o}\right) \quad (206b)$$

$$\frac{PAR^e}{H_o} = 0.011 - 0.002\left(T_R\right) + 0.402\left(\frac{H}{H_o}\right) + 0.055\left(\frac{H}{H_o}\right)^2 \quad (206c)$$

5. Discussion

As a result of the various empirical computing models reported by peers and researchers for estimating photosynthetically active radiation (PAR) applying astronomical parameters, meteorological parameters, geographical parameters, geometrical factors and atmospheric parameters resulting in a rigorous task for introducing a set input parameter with a particular functional form for optimal estimation PAR across the globe because of the nature of PAR and PAR/H dependence on latitude and altitude of the site and movement of the earth culminating in variations of local climate.

For this purpose, the author has classified numerous PAR and PAR/H computing models into ten (10) categories based on their dependence on atmospheric parameters, meteorological parameters, geometrical factors, geographical parameters, astronomical factors etc. via: global solar radiation-based models, relative humidity-based models, temperature-based models, optical air mass-based models, clouds, cloud amount-based models, water vapour pressure-based models, turbidity-based models, sunshine-based models, cleanness index-based models and hybrid parameter-based models as mentioned earlier.

The influence of water vapour pressure on PAR/H has been roughly reported in literature in season variations such as the higher in summer (wet season) and lower in winter (dry season) [51, 59, 107]. This report is in agreement with recent report of dependence of PAR/H on water vapour pressure by Akitsu *et al.* [49] who observed that the monthly mean PAR/H recorded higher values (0.465) in summer and lower value (0.420) in winter as shown in Fig. 3. In another study, Li *et al.* [55] observed that PAR^e/H increases with the increase in water vapour pressure and low-level cloud amount. According to the authors, this could be attributed to the absorptions of water vapour's waveband selective in the solar spectrum. That is, in cloudy and humid conditions, the absorption of solar radiation in the near infrared (NIR) portion of the solar spectrum is enhanced, whereas absorption in the PAR waveband does not vary significantly.

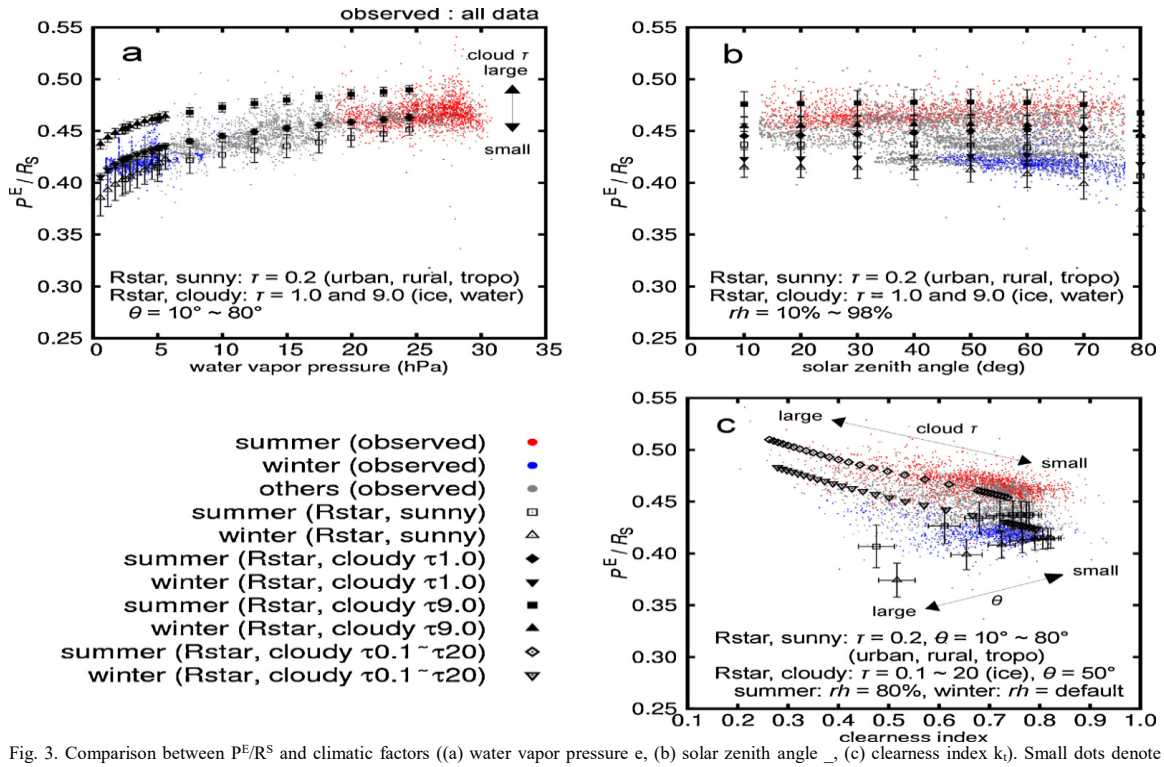

Fig. 3. Comparison between P^E/R^S and climatic factors ((a) water vapor pressure e, (b) solar zenith angle _, (c) clearness index k_t). Small dots denote observed data, while symbol marks denote mean value of simulation output (Rstar). Error bars denote the std. (For interpretation of the references to color in this figure text, the reader is referred to the web version of this article.) Akitsu *et al.* [55]

Moreover, Bat-Oyun *et al.* [59] equally observed that increases in PAR^e/H were found under cloudy and humid conditions. The authors equally recorded a significant correlation between PAR^e/H and water vapour pressure ($r = 0.49$, $P < 0.001$) for day time (08:00 – 17:00, local time). However, the correlation was stronger during April – September ($r = 0.70$, $P < 0.001$) compared to the rest of the study period, i.e. October – March ($r = 0.26$, $P < 0.001$). McCree [37] recorded that during cloudy skies the energy in the PAR region formed a greater part of global solar radiation than on clear days. Another researcher, Hu *et al.* [118] observe similar seasonal variations in PAR/H for Beijing where lower PAR/H was observed during the dry season and higher PAR/H recorded in the wet season.

Since water vapour pressure, relative humidity and cloud amount are similar in atmospheric behaviour, it can be inferred that increases in PAR/H or PAR culminate in a corresponding increase in water vapour pressure [37, 49, 51, 55, 59, 64, 107, 118], low level cloud amount [55] and relative humidity [60].

Considering clearness index, optical air mass, Angstrom turbidity coefficient and relative sunshine, these four factors (classes) increases with decreasing PAR/H. Li *et al.* [55] observed that the correlations between PAR^e/H and relative sunshine and clearness index are relatively good to some degree with the coefficient of correlation (R) value of 0.65 and 0.69 respectively. According to the authors, compared with relative sunshine and clearness index, the correlation coefficient between PAR/H and Angstrom turbidity coefficient is relatively poor (0.38). They equally stated that the reason for poor relation

between PAR/H and Angstrom turbidity coefficient (β) is that the (β) values are determined under the clear sky conditions; they influence PAR significantly with clear sky conditions, whereas the PAR/H values are under the real sky conditions.

Wang *et al.* [63] observed the dependence of hourly PAR on optical air mass defined by Kasten and Young [119] as a measure of length of the path through the atmosphere to earth surface, under several sky conditions in inner Mongolia, China that PAR generally decreased with increasing optical air mass and the maxima were achieved when sky conditions were cloudless as shown in Fig. 4. The same trend was observed by other researchers [9, 62, 64].

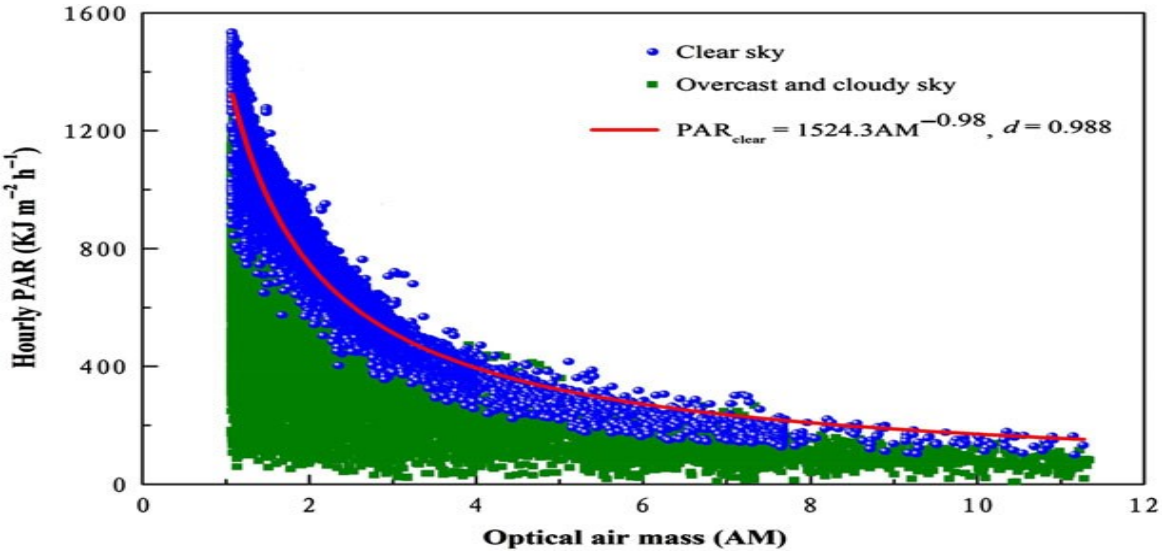

Figure 4. Dependence of hourly PAR on optical air mass under different sky conditions in Inner Mongolia (NMG) Wang *et al.* [63].

In as much as clearness index, optical air mass, Angstrom turbidity coefficient and relative sunshine possessed similar characteristics of atmospheric trend, it can be stated that increases in PAR/H or PAR brings about a corresponding decrease in clearness index [48, 55, 59, 68, 72]; Angstrom turbidity coefficient [55]; relative sunshine [55, 61, 74]; optical air mass [62-63, 80].

Generally, it is impossible to introduce a set of input parameter with a singular functional form for optimal estimation of photosynthetically active radiation. In fact, the tendency of enhancing the accuracy of estimation by combing some sets of input parameters is solely dependent on local climate and regional geography etc. To restate this, a brief review of the qualitative effort of solar energy researchers to enhance the accuracy of estimation of photosynthetically active radiation computing models by employing varieties of influencing factors are as represented in the following.

Wang *et al.* [63] calibrated hybrid empirical consist of the attenuation factor in clear skies (AF_c, ratio of measured to extraterrestrial PAR under clear skies); attenuation factor with clouds, which can be expressed as H/H_o with PAR coefficient (PAR/PAR_o) under hourly time scale (model 1) parameters. The authors equally fitted another hybrid model comprises clearness index (H/H_o) – attenuation factor with clouds and cosine of solar zenith angle (θ_z) under hourly and daily time scales (model 2). From the statistical indices, model

2 was chosen for reconstructing hourly and daily time scales PAR records in Inner Mongolia, China. This indicates that cosine of zenith angle (θ_z) and clearness index is more suitable compared to attenuation factor in clear skies, extraterrestrial PAR and clearness index in Inner Mongolia under clear skies in China as shown in Fig. 5 and 6.

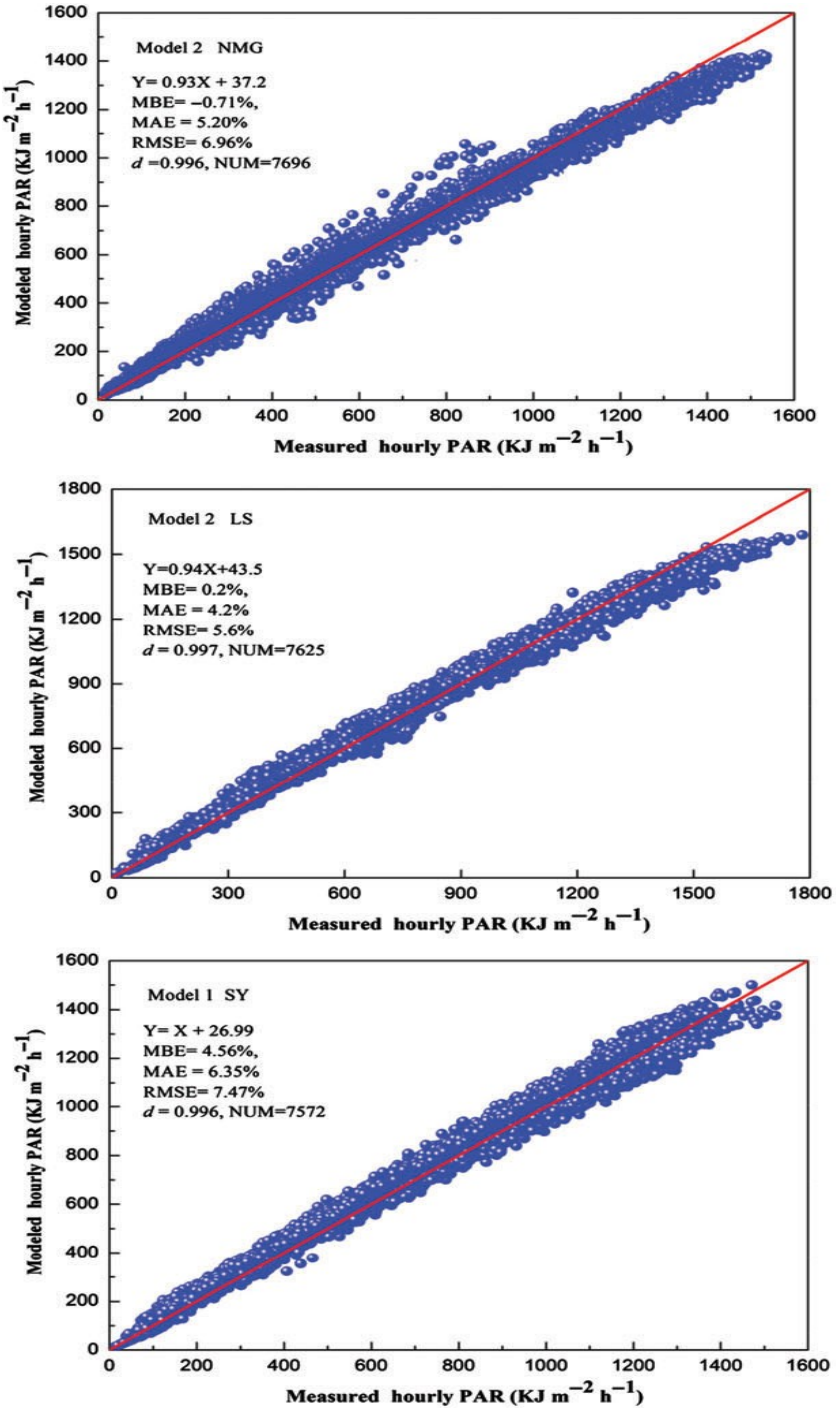

Figure 5. Scatterplot of hourly measured PAR and estimates in Inner Mongolia (NMG) using model 2 (grey line means 1 : 1 relationship) Wang *et al.* [63]

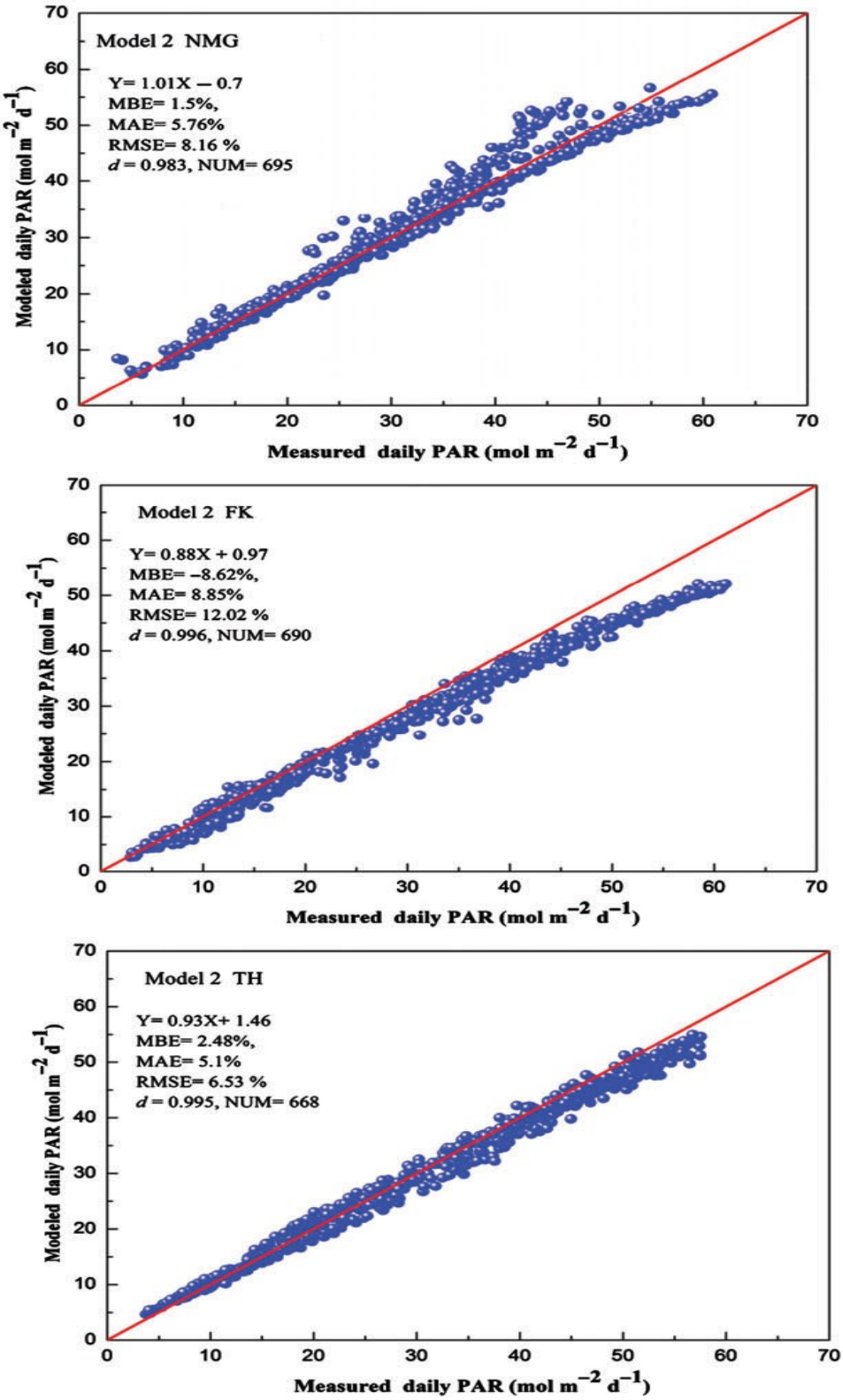

Figure 6. Scatterplot of daily measured PAR and estimates in Inner Mongolia (NMG) using model 2 (grey line means 1 : 1 relationship) Wang *et al.* [63]

Yu and Guo [76] calibrated Alados *et al.* [5] computing models to generate the relationship between PAR fraction and model parameters for Bondville station (BON) and Sioux Falls Station (SXF) in Midwestern United States using data from 2009 – 2011. The authors employed diffuse fraction (Hd/H), the sky brightness (Δ), the dew point temperature and cosine of sun zenith angle ($\cos\theta_z$) as model 1 input parameters; diffuse fraction, the sky brightness and the cosine of sun zenith angle as model 2 input parameters; clearness index, dew point temperature and the cosine of sun zenith angle as model 4 input parameters under several sky conditions. From the statistical indices, it was discovered that model 1 was more suitable for estimating PAR in Midwestern United States followed by model 3 next by model 2 and model 4 recorded the least performance under Overcast Sky (OS). Under partially cloudy sky (PS), model 3 was most suitable, followed by model 2, next by model 3 and model 4 was the least suitable empirical model for estimation of PAR in Midwestern United States. Whereas, under Clear Sky (CS) model 3 recorded the most suitable, followed by model 4, next by model 3 and lastly by model 4 for PAR estimation in Midwestern United States. Under all sky conditions, model 2 recorded the best, followed by model 3, next by model 1 and model 4 reported the least computing model for PAR estimation in Midwestern United States as shown in Table 2.

Yu *et al.* [72] synthesized ten (10) empirical computing models from previous studies to compare with their measure PAR in the contiguous United States. Model 1 – 4 were purposed by Alados *et al.* [5]. Model 5 – 6 were suggested by Zhang *et al.* [97]. Model 7 – 10 were obtained from previous studies [55, 109, 120-121]. From the statistical indices, the ten synthetized computing models for estimating PAR from H show that the quadratic function model taking ($\ln H/H_o$) as main parameter plus $\cos\theta_z$ has the best performance. According to the authors, the results equally show that clearness index (H/H_o) is capable to be the indicator for estimating PAR from H as one substitute of the combination of diffuse fraction (Hd/H) and the skylight brightness (Δ). They also observed that the role of dew point temperature in the models is not significant to improve the overall performance.

Yu and Wang [62] employed only ratio of PAR/H as input parameter for model 1; global solar radiation (H) and clearness index as input parameter for model 2; and clearness index and optical air as input parameter for model 3 for estimation of PAR in Sanjiang site, Northeast China for hourly time scale under all sky conditions. The statistical indicators revealed that model 3 is the most suitable computing model for PAR estimation in Sanjiang site as shown in Table 1.

Table 1: Comparison results of empirical estimation model for hourly PAR at Sanjiang site Yu and Wang [62].

Models	Slope (a)	Intercept (b)	Coefficient of Determination (R^2)	MBE ($\mu molm^{-2}s^{-1}$)	RMSE ($\mu molm^{-2}s^{-1}$)	RE (%)
A	1.03	5.6	0.98	35	75.5	10.7
B	1.01	4.2	0.97	15.3	76.7	11.4
C	1.01	1.5	0.97	19.5	67.8	9.4

Wang *et al.* [71] employed sky clearness (ε), sky brightness (Δ), precipitate water (w), and sin of solar elevation angle (h) as an input parameter for model 1; clearness index, sin of solar elevation angle (h) and perceptible water (wv) as input parameter for model 2;

only clearness index as input parameter for model 3; sky clearness (k_t), sky brightness (Δ), and sin of solar elevation angle for input parameter for model 4; and clearness index and sin of solar elevation angle as input parameter for Sanya station (SY), Lasa Station (LS), Yingtan station (YT), Fergqiv station (FQ), Changshu Station (CS), and other stations in central China for estimating PAR under hourly time scale. According to the authors, as shown in Fig. 7. the slopes of all the models were higher than expected and the estimated values were slightly smaller than the observed results. This reveals that there are some influencing factors on PAR/H not being taken into consideration, for example, the influence of ozone absorption and surface albedo. The authors equally stated that model 2 and 3 may be better for calculating PAR from measurement in Wuhan. In order to check the level of reliability of the models (2 and 3), the author tested the two models (model 2 and 3) at seven (7) stations in Central China. The authors revealed that the two models work well in most stations in that the relative error in DH station was about 5.9%, which produced a better result than that in other stations in China. For instance, Hu *et al.* [118] reported relative error between measured and estimated PAR as about 20% in Beijing. On the whole, the statistical results revealed that PAR could be estimated with a high level of precision using global solar radiation and a variable that accounts for the sky condition dependence of PAR/H in Central China. However, a larger derivation was still found at Huitong Station (HS), Taoyuan station (TY), and Qianyanzhou station (QYS), with relative error higher than 10%. This according to the authors may be attributed to the higher absorption effects for extraterrestrial solar radiation in the above three sites (clouds and water vapour), which lie south of Wuhau and close to the tropical regions.

Li *et al.* [55] employed water vapour pressure-based model, cloud amount-based models, relative sunshine-based models, clearness index-based models and hybrid model consisting of relative sunshine and water vapour pressure input parameters to estimate PAR in Northern Tibetan Plateau (NTP). From the statistical indices, the hybrid model performed better than other four models mentioned above. To check the applicability of the model, the authors tested the models in five stations outside the location the models were fitted (Wudaoliang, WDL) since PAR is local climate and geographical site dependent. The result revealed that the model is practicable for Tibetan Plateau, and Southeast of China. They further stated that the model is considered acceptable for Northwest of China; but for the East of China, the model is not applicable.

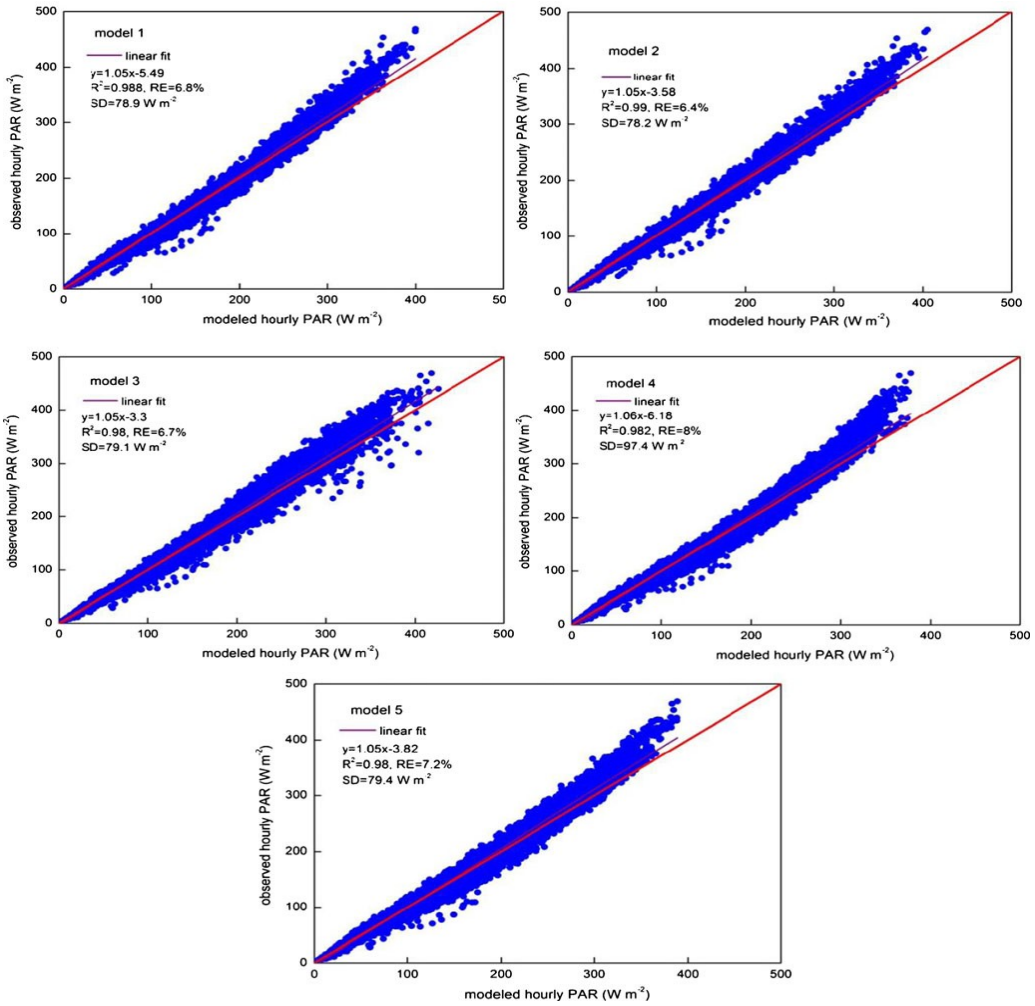

Fig. 7. Linear regression between hourly observed and modeled PAR in Wuhan (red line 1:1 relationship) Wang *et al.* [71].

Aguiar *et al.* [65] developed three empirical models for estimating PAR in South West Amazonia both hourly and daily time scale. The authors employed global solar radiation as the only input parameter to develop model 1. Model 2 was fitted by applying global solar radiation and clearness index as input parameter while global solar radiation, cleanness index and water vapour pressure was employed as input parameter for simulating model 3. From the statistical indices on both hourly and daily time scale, the authors reported that the least accurate estimates were usually obtained by model 3 for seasonal models as well as annual models, which employed solar radiation, clearness index and water vapour as input parameters. The exception to this general trend was during the transition between the dry and the wet seasons on the pasture site, whereas model 1 (hourly time scale) and 2 (daily time scale) reported the worst performance respectively. The authors stressed that the relative inferior performance of model 3 is probably due to lack of a clear relationship between the ratio of PAR/H and water vapour pressure. However, the researchers stated that the models showed no significant differences among themselves. That is, significantly, no single model was superior throughout the year, with the best fit

alternating between model 1 (global solar radiation as input parameter) and model 2 (global solar radiation and cleanness index as input parameters). The authors concluded that the results suggest that simple models of PAR based on one or two parameters are robust and may provide a strong basis for regionally or ecosystem-based Ecophysiological models in this ecologically important part of Brazil. This finding is similar to report found in literature. Yu and Guo [76] in an attempt to identify the most relevant input parameter for estimating PAR in Midwestern United States excluded relative humidity, dew point temperature and perceptible water related to water vapour pressure indicating that water vapour pressure is not a key factor for hourly PAR estimation compared with other parameters. Lopez *et al.* [122] suggested that input parameters related to water vapour are less important than other sky condition parameters for PAR estimation.

Also, Wang *et al.* [63] discovered that employing global solar variation, clearness index and cosine of solar zenith angle are sufficient for PAR estimation. However, Jacovides *et al.* (2015) recommended that only the combination of sunshine fraction and global solar radiation can estimate the daily PAR with reasonable accuracy.

In general, out of the ten (10) different classes of empirical models for estimation PAR across the globe identified in this paper, seven hundred and fifty-seven (757) theoretical models were reported with 62 functional forms and 32 groups (sub-class). Five hundred and seventy (570) models with the corresponding 4 functional forms and 3 groups were recorded from global solar radiation-based models representing 75.29 %; 18 models with the corresponding 1 functional form and 1 group resulting to 2.37 % were applied for relative humidity-based models; 1 model with 1 functional form and 1 group amounting to 0.13 % for temperature-based model; 1 model with 1 functional form and 1 group yielding to 0.13 % for cloud amount-based model; 1 model with 1 functional form and 1 group yielding to 0.13 % for water vapour pressure-based model; 1 model with 1 functional form and 1 group yielding to 0.13 % for turbidity-based model; 4 models with 2 functional forms and 1 group yielding to 0.52 % for optical air mass-based models; 10 models with 6 functional forms and 3 groups yielding to 1.32 % for sunshine-based models; 27 models with 9 functional forms and 3 group yielding to 3.56 % for clearness index-based models; and 91 models with 36 functional functions and 17 groups resulting to 12.02 % for hybrid parameter-based models as presented in Fig 8.

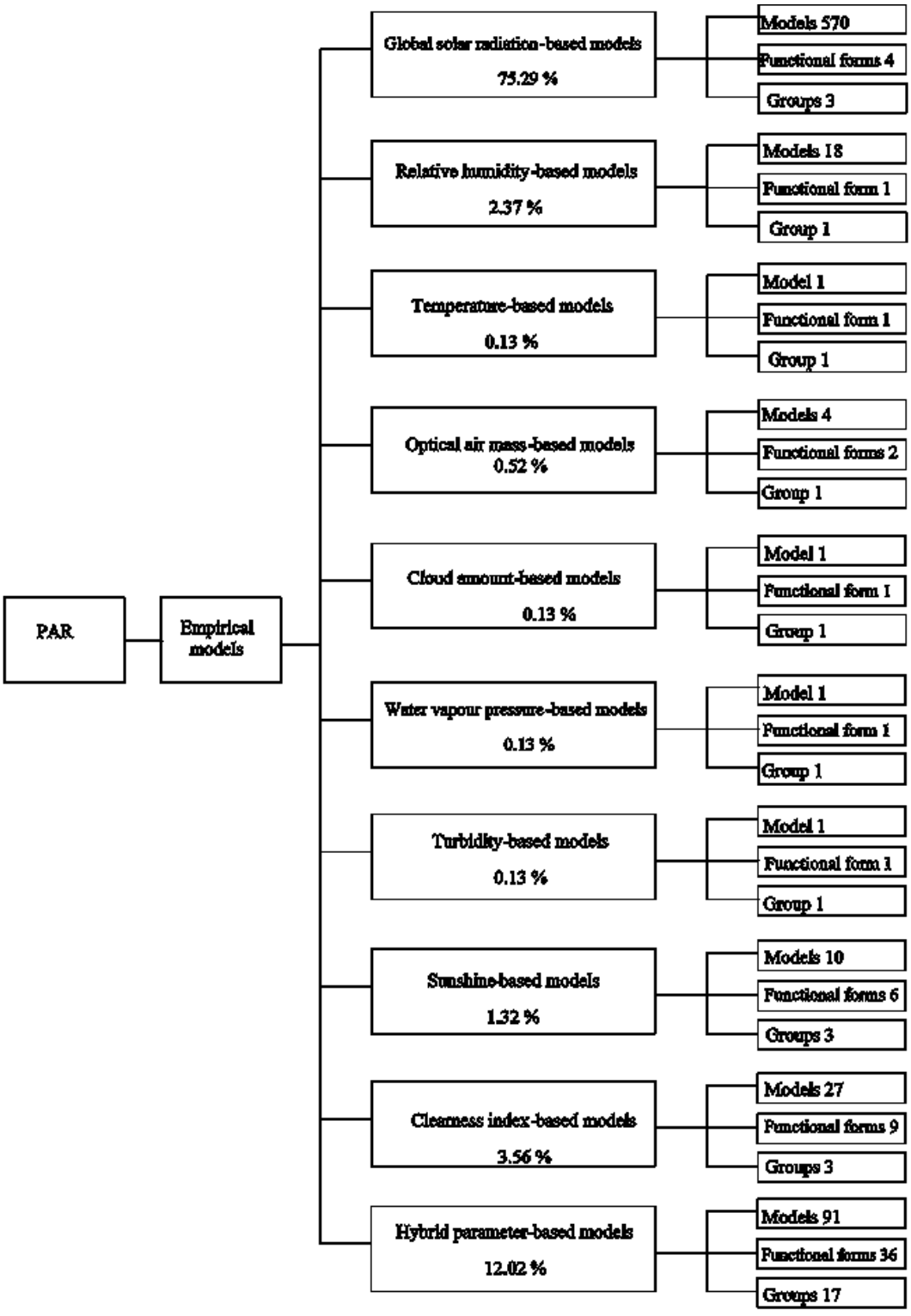

Fig. 8: Classification of photosynthetically active radiation (PAR) and corresponding values of models, functional forms and groups

It is clear that from above literature that introducing an appropriate set of input that is hybrid model for photosynthetically active radiation estimation in any site of interest is not a viable work. This could be attributed to its complexity involved because of using numerous numbers of required input parameters, inaccuracies associated with irrelevant parameters, difficulty in explaining the model and time consuming task for selecting the required parameter and its inability to accept many input parameters.

The artificial neutral network (ANN) and other soft computer techniques often applied for estimating other component of solar radiation such as diffuse solar radiation, direct normal irradiance and global solar radiation etc. can be adopted for estimating PAR or PAR/H. Several applications of artificial neural networks are reported in numerous fields such image impression, defense, mathematics, character recognition, aerospace, neurology, meteorology and engineering [1-2]. These techniques have been employed for prediction and empirical analysis in market trend forecasting, solar and weather.

For instance, Yu and Guo [76] applied artificial neural networks (multiple layers' perception, MLP) and conventional Multiple Linear Regression (MLP) models for estimating PAR on hourly time scale under different sky conditions in Midwestern United States. The result from the statistical indices revealed that ANN models show higher accuracy than the Multiple Linear Regression (MLR) models especially for overcast sky and clear sky as shown in Table 2. The authors also commented that using water vapour parameters (relative humidity, dew point temperature and precipitable water) do not improve the accuracy significantly. They equally concluded that ANN model that combine the sky clearness, the cosine of sun zenith angle and the hourly global solar radiation as inputs estimated PAR most accurately. This report is in line with findings in literature [63, 75, 122].

Wang *et al.* [75] applied ANN models (multi-layer perception, MLP; Radial Basis Neural Network, RBNN; and Generalized Regression Neural Networks, GRNN) and all-sky regression PAR model (ALSKY) to estimate hourly PAR under ecosystem such as farmland, forest, lake, desert, grassland, bay and wetland. Global solar radiation (H) was applied as the only input parameter; combination of H and air pressure (PA); combination of H and dew point temperature (T_d); combination of H and relative humidity (RH); combination of H and Water Vapour Pressure (E^*); combination of H and air temperature (T); combination of H, T and RH; finally, combination of H, T, RH, T_d, E^* and PA as input parameters for PAR estimation. From the statistical indicators, MLP and RBNN models perform better than GRNN and ALSYK models and the combinations of air temperature and air pressure parameters recorded more effects on hourly PAR compared with relative humidity, dew point temperature and water vapour pressure parameters under agricultural farmland ecosystem stations. This report is in line with the findings in literature that water vapour parameters are less important than other sky condition parameters for PAR estimation [76, 122]. The author also pointed that under forest ecosystem stations, the GRNN model produces the lowest root mean square error and mean absolute error by combining global solar radiation and air pressure variables inputs at HLF station while MLP, BNN and ALSKY models perform better than the GRNN model. It is also indicated that relative humidity is not a key parameter influencing the hourly PAR parameter as reported by other researchers [76, 122]. Moreover, under the

Bay ecosystem, the ANN models generally provide better estimates than the ALSKY model, and MLP and GRNN models significantly overestimate low PAR values while the RBNN and the ALSKY model slightly overestimates and underestimates respectively. For the grassland stations, the researcher recorded that the MLP and AKSKY model yielded more accurate hourly PAR estimates compared with the GRNN and RBNN models at NMG ecosystem station, while GRNN model with global solar radiation input parameter provides the lowest statistical indices at HBG station whereas for the wetland ecosystem SJM ecosystem station, the GRNN model comprising global solar radiation input parameter produces slightly lower RMSE values. Under the desert ecosystem stations, the MLP model performs better than the GRNN, RBNN and ALSKY models at FKD station, and the dew temperature parameter generally has more effect on hourly PAR estimates compared with air temperature, relative humidity, air pressure and water vapour pressure. While under lake ecosystem stations, the GRNN model yielded better estimates than other models at DHI station and the water vapour pressure is the most important parameter influencing the hourly PAR fluctuations. The researcher finally concluded that the MLP and RBNN models are more accurate in estimating hourly PAR at different ecosystems in China compared with GRNN and ALSKY models, which will be of vital importance for terrestrial photosynthesis modeling and surface energy budget as shown in Fig. 9 – 15.

Table 2: Statistical comparison between observed hourly PAR and modeled PAR from ANN and conventional regression models Yu and Guo [76]

		$k_t \leq 0.35$(OS)				$0.35 < k_t < 0.65$(PS)				$k_t \geq 0.35$(CS)				$0 < k_t < 1$			
		R^2	NRMSE	MPE	RSD	R^2	NRMSE	MPE	RSD	R^2	NRMSE	MPE	RSD	R^2	NRMSE	MPE	RSD
ANN1	BON	0.999	3.32	3.26	4.36	0.998	2.75	0.23	1.98	0.996	4.17	−4.30	6.15	0.996	3.98	−1.23	6.43
	SXF	0.999	2.93	2.74	3.36	0.999	1.98	−1.32	2.36	0.997	4.56	−3.73	4.96	0.997	3.73	0.96	4.71
	ALL	0.999	3.17	3.01	3.98	0.999	2.53	−0.71	2.05	0.997	4.43	−3.96	5.61	0.996	3.86	−0.15	5.96
ANN2	BON	0.999	3.12	1.29	4.36	0.997	3.03	1.06	3.77	0.993	3.92	−2.23	3.16	0.996	3.46	0.12	5.11
	SXF	0.998	2.79	−2.28	3.78	0.999	2.64	−1.38	3.39	0.999	3.78	−3.72	4.35	0.997	3.11	−2.78	3.95
	ALL	0.999	2.94	−1.07	4.01	0.998	2.88	−0.33	3.51	0.995	3.89	−2.98	3.83	0.997	3.27	1.45	4.87
ANN3	BON	0.996	4.03	2.10	3.02	0.999	3.79	0.36	2.73	0.996	3.99	−5.37	7.21	0.999	4.01	−3.23	6.98
	SXF	0.997	3.72	0.76	2.99	0.996	3.31	−0.23	2.85	0.995	4.21	−6.02	6.99	0.998	3.85	−3.36	5.84
	ALL	0.996	3.85	1.79	3.01	0.997	3.56	0.24	2.79	0.996	4.06	−5.77	7.08	0.998	3.68	−3.27	6.03
ANN4	BON	0.993	2.96	0.33	3.71	0.999	2.81	0.32	3.68	0.998	5.12	−3.98	5.36	0.995	3.81	−1.32	4.69
	SXF	0.996	3.51	3.56	4.58	0.999	3.13	−2.09	4.36	0.999	4.23	−4.76	5.99	0.997	3.67	−0.98	5.77
	ALL	0.995	3.32	2.75	4.17	0.999	2.94	−1.78	4.07	0.999	4.76	−4.58	5.71	0.996	3.79	−1.17	5.21
ANN5	BON	0.998	4.20	3.38	5.12	0.993	3.77	1.88	4.76	0.982	5.79	0.23	1.07	0.993	4.42	1.96	5.04
	SXF	0.996	4.10	4.01	5.69	0.995	3.96	−2.02	4.35	0.973	4.73	−4.29	6.02	0.989	4.28	−0.39	5.67
	ALL	0.998	4.13	3.77	5.41	0.994	3.95	−0.17	4.43	0.979	5.16	−2.17	3.51	0.990	4.37	0.75	5.52
ANN6	BON	0.997	3.67	2.96	4.35	0.996	3.50	−0.39	3.56	0.999	4.23	−3.76	4.97	0.998	3.69	−0.36	4.23
	SXF	0.999	3.56	−1.97	3.96	0.998	3.47	1.96	3.76	0.979	3.99	0.11	1.21	0.999	3.61	0.03	3.97
	ALL	0.998	3.47	0.58	4.07	0.998	3.48	0.72	3.63	0.981	4.02	−2.88	3.09	0.999	3.72	−0.12	4.16
Model 1	BON	0.996	4.53	6.75	7.07	0.969	2.88	2.36	3.65	0.965	5.32	−5.59	7.05	0.996	4.43	1.17	6.71
	SXF	0.993	3.76	5.32	6.81	0.978	3.46	−0.70	1.24	0.962	6.01	−2.37	3.56	0.993	4.63	0.75	5.32
	ALL	0.994	4.29	6.01	6.98	0.972	3.23	0.90	2.46	0.963	5.80	−3.93	5.21	0.994	4.57	0.91	6.01
Model 2	BON	0.995	5.61	2.10	3.53	0.998	4.02	−2.33	4.05	0.943	4.33	−4.79	5.98	0.989	4.32	−1.67	5.92
	SXF	0.996	4.96	1.37	1.99	0.995	3.17	1.91	3.01	0.986	5.17	−5.01	6.76	0.977	4.45	−0.76	6.07
	ALL	0.995	5.30	1.77	2.78	0.996	3.59	0.23	3.56	0.963	4.71	−4.87	6.33	0.980	4.41	−1.21	5.98
Model 3	BON	0.983	4.99	−0.32	1.07	0.956	2.98	2.79	4.43	0.997	3.76	1.36	2.49	0.969	4.93	1.35	4.79
	SXF	0.979	4.78	2.30	3.33	0.969	3.01	1.31	2.19	0.965	4.09	−4.03	6.70	0.956	4.01	0.59	5.98
	ALL	0.980	4.85	1.19	2.17	0.962	2.99	2.03	3.37	0.979	3.98	−1.43	4.23	0.963	4.51	0.98	5.63
Model 4	BON	0.967	6.01	2.38	3.96	0.997	4.10	3.14	5.01	0.959	4.98	−2.77	3.98	0.960	4.71	0.93	4.39
	SXF	0.976	5.72	3.06	4.59	0.992	3.77	−1.29	2.79	0.963	5.07	−1.76	2.99	0.972	5.05	0.10	5.76
	ALL	0.977	5.91	2.66	4.23	0.995	3.92	0.93	3.59	0.960	5.01	−2.20	3.61	0.965	4.88	0.58	5.08

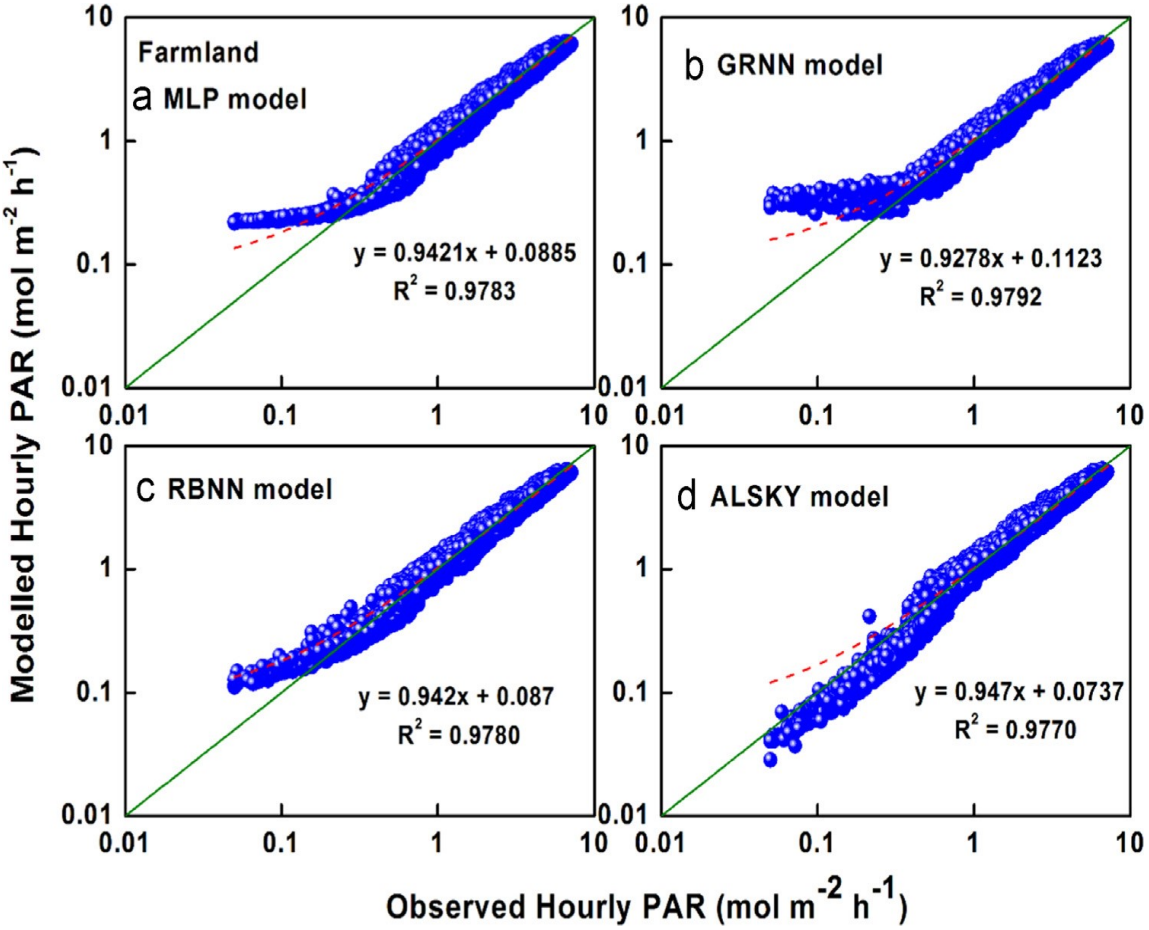

Fig. 9. The PAR estimates of the optimal models for the FQA station in farm land ecosystem Wang *et al.* [75].

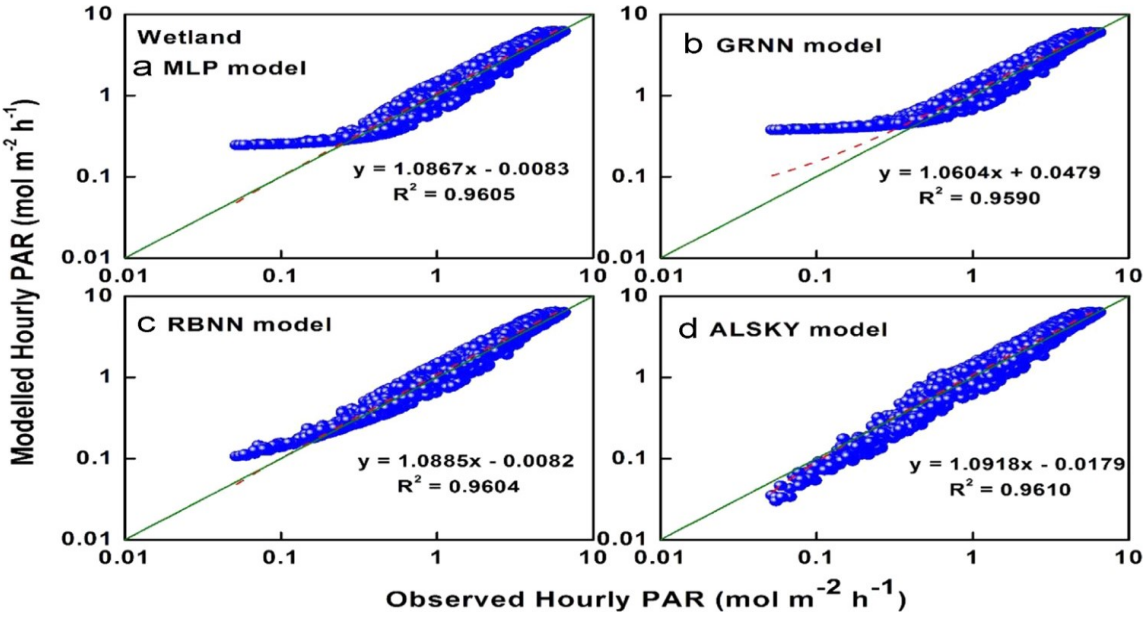

Fig. 10. The PAR estimates of the optimal models for the SJM station in wetland ecosystem Wang *et al.* [75].

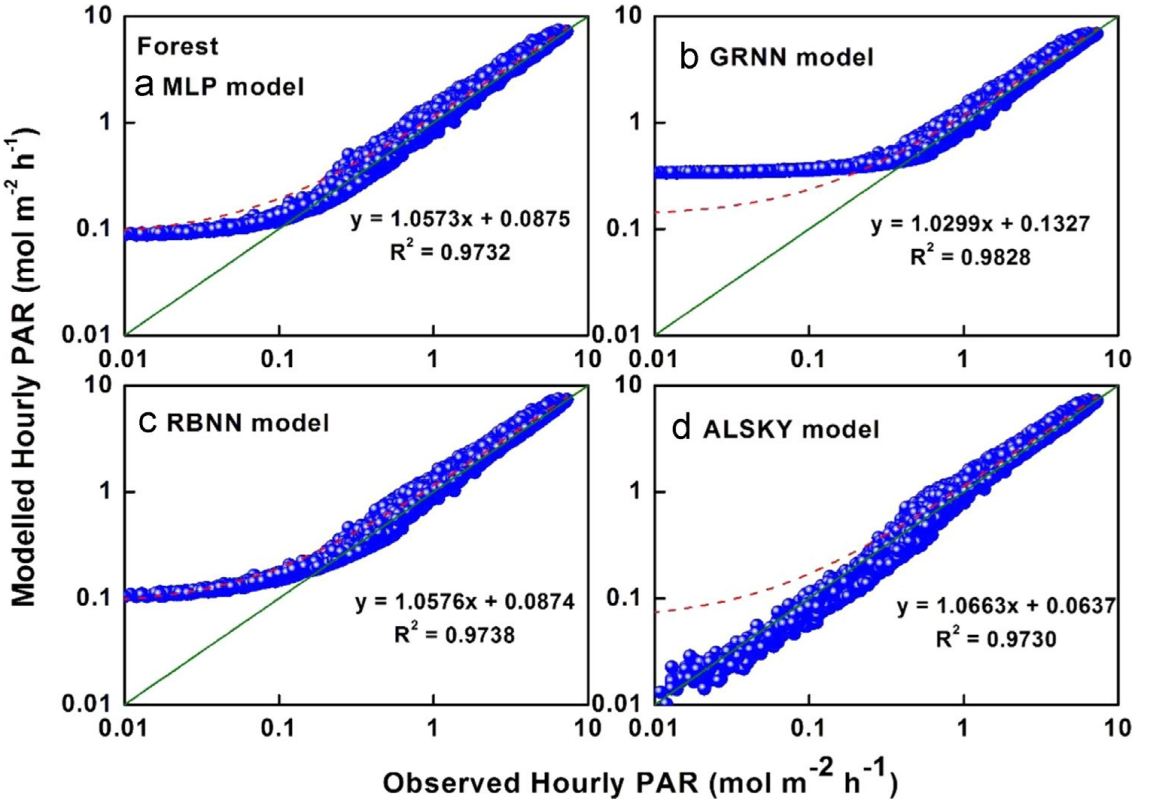

Fig. 11. The PAR estimates of the optimal models for the ALF Station in forest ecosystem Wang *et al.* [75].

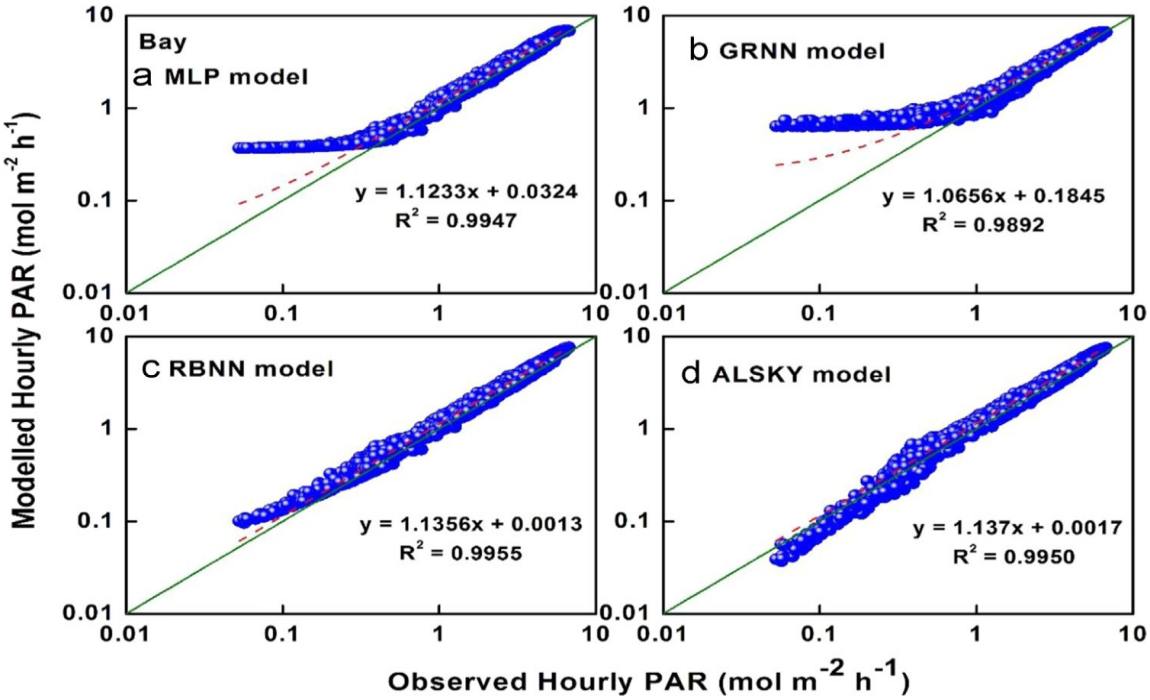

Fig. 12. The PAR estimates of the optimal models for the SYB station in bay ecosystem Wang *et al.* [75].

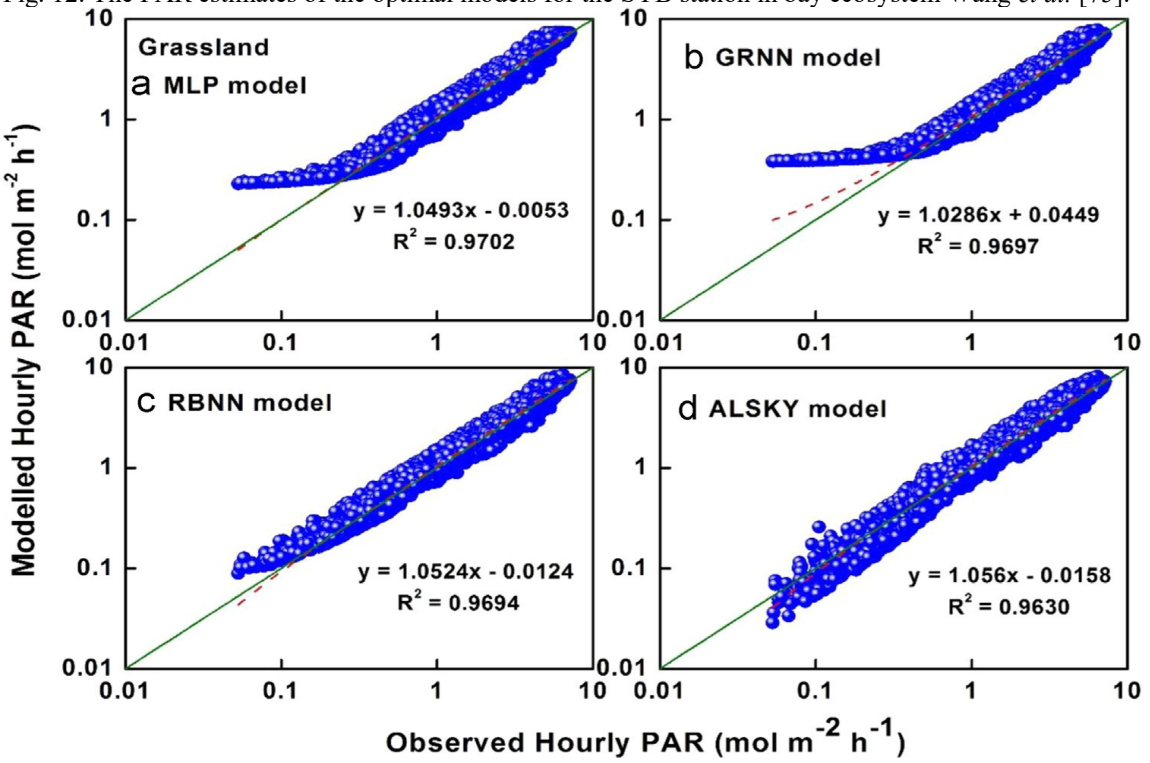

Fig. 13. The PAR estimates of the optimal models for the HBG station in grassland ecosystem Wang *et al.* [75].

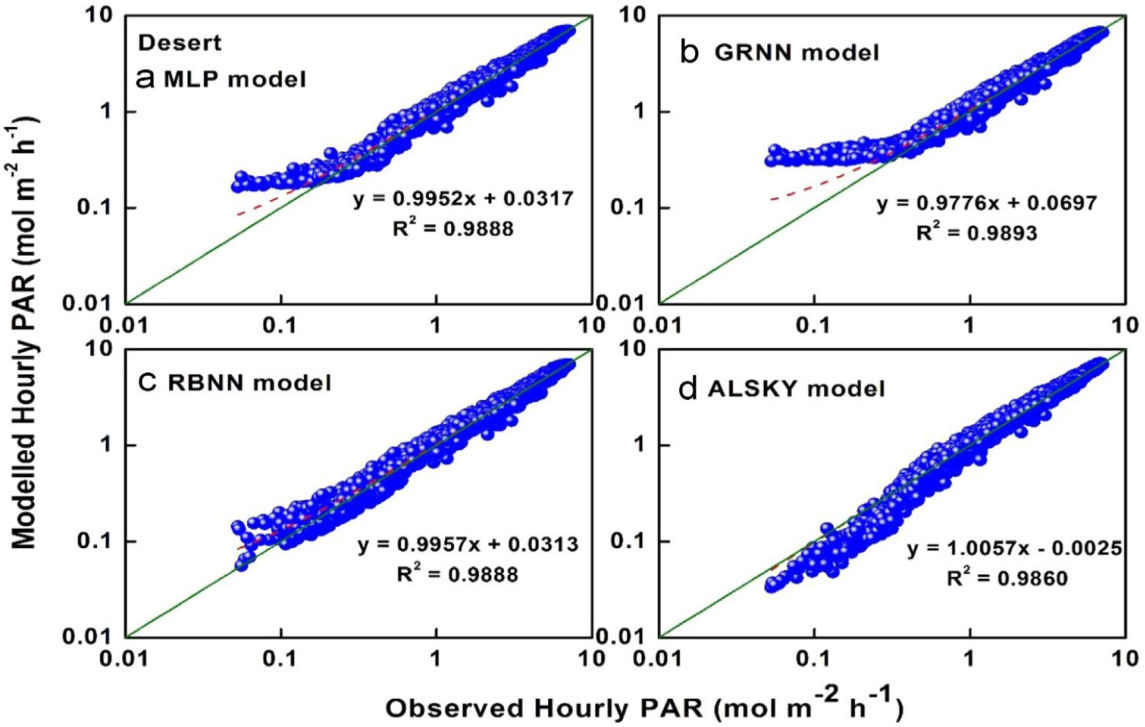

Fig. 14. The PAR estimates of the optimal models for the SPD station in desert ecosystem Wang *et al.* [75].

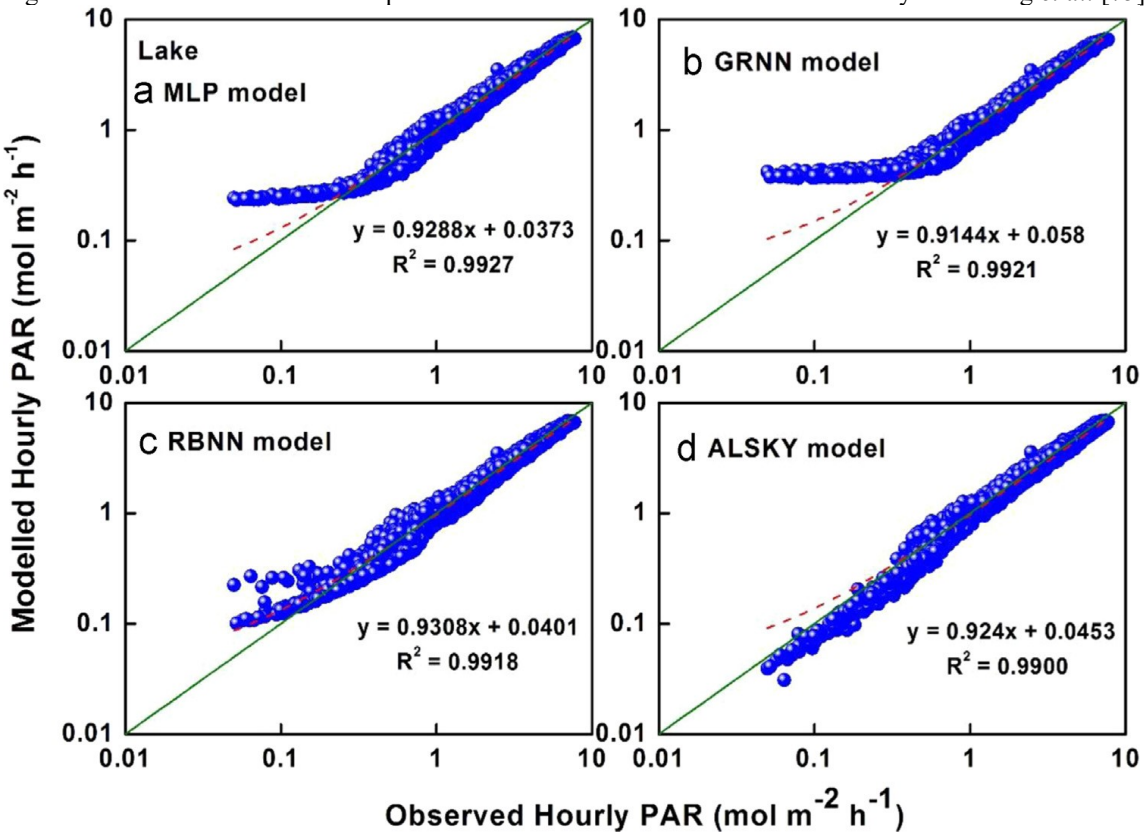

Fig. 15. The PAR estimates of the optimal models for the THL station in lake ecosystem Wang *et al.* [75].

6. Research Gaps

The photosynthetically active radiation (PAR) empirical models examine in this paper is distinctive and provide valuable outcome for numerous circumstances. The models regarded as capable and convenient for hourly models, temperature-based models, optical air mass-based models, relative humidity-based models, cloud amount-based models, water vapour pressure-based models, turbidity-based models, sunshine-based models, clearness index-based models and hybrid parameter-based models. A number of essential areas identified in literature as well as shortcomings with solutions recommended in this paper are summed up subsequently below.

1. In previous studies, authors employed one, two, three, or more years of photosynthetically active radiation data as available to build ANN models is not a viable work. Thus, employing training and testing data of minimum three years and one year respectively can be adopted to estimate photosynthetically active radiation accurately; however, further comparative analysis on the aspect can be under taken also.
2. During the development of ANN models, the neurons in ANN hidden layer are changed one by one and mean absolute percentage error (MAPE) are calculated which is time consuming. Therefore, considerable techniques should be developed to find out hidden layer neurons at which estimation error is minimum.
3. Different artificial neural networks models need to be stimulated employing latitude, longitude, altitude, extraterrestrial solar radiation, solar declination, cosine of solar zenith angle, optical air mass and other atmospheric and meteorological input parameters that can be calculated with standardized formulas and checked for accuracy. The goal is that, if an appropriate modelling of this radiometric flux (PAR) could be developed, a large data resource of it will be created without the substantial cost of the instrumentation network that would otherwise be needed thereby meeting the needed meteorological stations and countries (Africa) that cannot measure PAR routinely.
4. Comparison of Niching genetic algorithm, automatic relevance determination methodology need to be employed in selecting most relevant input parameters in addition with ANN models for estimation
5. Additional studies are needed for the estimation of beam and diffuse photosynthetically active radiation (PAR) using ANN and other soft computing models
6. Drawing from findings in literature, a single model based on the variations of the ratio photosynthetically active radiation to global solar radiation under different sky conditions, ecosystem, local climate and geographical regions over several sites employing empirical models so as to developed weather-dependent functions of this ratio should been considered and emerged. The goal is to develop a model transferable to these locations that routinely measured the broadband solar radiation for appropriation calibration of the model using their measured meteorological data to generate and probably recommend a model transferable to other sites, ecosystem, local climate and geographical areas as in what was obtainable in Food and

Agriculture Organization (FAO) Penman-Monteith model recommended for estimating reference evapotranspiration developed by Allen *et al.* [123] without local calibration globally.

7. It is also essential to mention that soft computing models has newly been initiated for estimating renewable energy resources (e.g. PAR), but additional work is necessary to increase solar radiation or PAR estimation accuracy pertaining to numerous seasons, climate change to supply increasingly reliable efficient solar systems on the market.

7. Concluding Remarks

This review paper presents a comprehensive review of literature on photosynthetically active radiation across the globe. 757 empirical models, 62 functional forms, and 32 groups were identified employing global solar radiation-based models, relative humidity-based models, temperature-based models, optical air mass-based models, cloud amount-based models, water vapour pressure-based models, turbidity-based models, sunshine-based models, clearness index-based models, and hybrid parameter-based models. The findings in this paper provide future dimension to industry and research practitioners for further studies on solar system and photosynthetically active radiation estimation in particular.

From this review, ANN models are found to estimate PAR accurately in different climate conditions and ecosystem across the globe. This could be attributed to the fact that these models can accept many input parameters as compared with empirical models that strengthen its reliability. Moreover, it can also be concluded that ANN models estimations offer greater accuracy as compared with empirical models, e.g. Tables 2 and Fig. 9 – 15 show estimation error in a range (less than 20%) and this could be very good in terms of PAR estimation. Therefore, ANN and other soft computing models are much more demanding in the domain of renewable energy (e.g PAR) estimation and solar system design. It is finally recommended that future studies on PAR estimation should consider employing both empirical and soft computing models in order to observe the research gap between the two techniques in sites where PAR estimation has not been carried out before particularly in Africa continent where few meteorological station are capable of measuring this radiometric flux.

Acknowledgements:

Our thanks go to all the authors cited in this paper for their research works that has made this research possible.

Funding

This research did not receive any specific grant from funding agencies in the public, commercial, or not-for-profit sectors.

CONFLICTS OF INTEREST

The authors declare that there is no conflict of interests regarding the publication of this paper.

References

[1] Nwokolo SC. A comprehensive review of empirical models for estimating global solar radiation in Africa. Renewable and sustainable energy reviews, 2017, 78: 955 – 995.

[2] Nwokolo SC, Ogbulezie JC. A single hybrid parameter-based model for calibrating hargreaves-samani coefficient in Nigeria. International Journal of Physical Research, 2017, 5(2): 49-59

[3] Pohlert T. Use of empirical global radiation models for maize growth simulator. Agricultural and Forest Meteorology, 2004, 126 (1): 47 – 58.

[4] Dye DG. Spectral composition and quanta-to-energy ratio of diffuse photosynthetically active radiation under diverse clouds condition. J. Geophys Res: Atmos, 2004. DOI:10.1029/2003JD 004251

[5] Alados I, Foyo-Moreno I, Alados–Arboledas L. Photosynthetically active radiation. Measurements and Modeling. Agricultural and Forest Meteorology, 1996, 78: 121 – 131.

[6] Dye DG, Shibasaki R. Intercomparison of Global PAR data set. Geophy Res Lett, 1995, 22: 2013 – 2016.

[7] Zhao MS, Running SW. Drought-induced reduction in global territorial net primary production from 2000 through 2009. Science, 2010, 329: 940 – 943.

[8] Asaf D, Rotenberg E, Tatarinor F, Dicken U, Montzka SA, Yakir D. Ecosystem Photosynthesis inferred from measurements of carbonyl sulphide flux. Nat Geosci, 2013, 6:186 – 190.

[9] Wang L. Gong W, Lin A, Hu B. Analysis of photosynthetically active radiation under various sky conditions in Wuhan, Central China. Int J. Biometeorol., 2013. DOI:1007/500484-013-0775-3

[10] Cooter EJ, Dhakhua GB. A solar radiation model for use in biological applications in the south and southeastern USA. Agricultural and Forest Meteorology, 1995, 78: 31 – 51.

[11] Hunt LA, Kuchar L, Swanto CJ. Estimation of solar radiation for use in crop modeling. Agricultural and Forest Meteorology, 1998, 91: 293 – 300.

[12] Hoogenboom G. Contribution of agrio meteorology to the simulation of crop production and its applications. Agricultural and Forest Meteorology, 2000, 103: 137 – 157.

[13] Loutzenhiser PG, Manz H, Felsmann C, Stranchan PA, Frank T. Empirical Validation of models to compute solar irradiance on inclined surfaces for building energy simulation. Solar Energy, 2007, 81: 254 – 267.

[14] Holyle CR, Myher G, Isaksen I. Present – day contribution of anthropogenic emissions from China to the global burden and radiative forcing of aerosol and Ozone. Tellus B, 2009, 61: 618 – 624.
[15] Frouin R, Pinker RT. Estimating photosynthetically active radiation (PAR) at the earth's surface from satellite observations. Remote Sensing Environ, 1995, 51: 98 – 107.
[16] Wang LC, Gong W. Ma YY, Zhang M. Modeling regional vegetation NPP variations and their relationships with climatic parameters in Wuhan, China. Earth Interaction, 2013, 17: 1 – 20.
[17] Wang Q, Tenhunen J, Schmidt M, Otieno D, Kolcuu O. Diffuse Par irradiance under clear skies in complex alpine tenain. Agricultural and Forest Meteorology, 2005, 128: 1 – 15.
[18] Zarzo M, Marti P. Modeling the variability of solar radiation doctor among weather station by means of principal component analysis. Applied Energy, 2011, 88: 2775 – 2784.
[19] Cao MK, Prince SD, Tao B, Li KK. Regional Pattern and international variations in global terrestrial carbon intake in response to changes in climate and atmospheric Co_2. Tellus B, 2005, 57: 210 – 217.
[20] Gallo KP, Daughtry CST, Bauer ME. Spectral estimation of absorbed photosynthetically active radiation in corn canopies. Remote Sens. Environ., 1985, 17: 221-232.
[21] Beer C, Reichstein M, Tomelleri E, Ciais P. Terrestrial gross carbon dioxide uptake: global distribution and covariation with climate. Science, 2010, 329: 834-838.
[22] Pinker RT, Laszlo I. Global distribution of photosynthetically active radiation as observed from satellites. J. Chem., 1992, 5: 56 – 65.
[23] Knorr W. Annual and Internal Co_2 exchanges of the terrestrial biosphere: process-based stimulations and uncertainties. Glob. Ecol. Biogeogr., 2000, 9: 225 – 252.
[24] Trenberth KE, Fasullo JT, Kiehl J. Earth's global energy budget. Bull. Am. Meteorol. Soc., 2009, 90: 311 – 323.
[25] Garnaud C, Sushama L, Arora VK. The effect of driving climate data on the simulated terrestrial carbon pools and fluxes over North America. International Journal of Climatology, 2014, 34:1098 – 1110.
[26] Jonathan AP, Colin P, Navin R, Samuel L, David P. An Integrated biosphere model of band surface process, territorial carbon balance, and vegetation dynamics – Global Biogeochem. Cycles, 1996, 10:603 – 628.
[27] Van RL, Sanchez GA. Mapping PAR using MODIS atmospheric products. Remote Sens. Environ., 2005, 94; 554 – 563.
[28] Nwokolo SC, Ogbulezie JC. Relationship between photosynthetically active radiation with global solar radiation using empirical model over selected climatic zones in Nigeria. Journal of Scientific Research in Allied Sciences, 2017, 3(3): 1-17.
[29] Mizoguchi Y, Ohtani Y, Aoshima T, Hirakata A, Yuta S, Takanashi S, Iwata H, Nakai Comparison of the characteristics of five quantum sensors. Bull. FFPRI, 2010, 9(3): 113 – 120.

[30] Mizoguchi Y, Yasuda Y, Ohtani Y, Watanabe T, Komianami Y, Yamanoi K. A practical model to estimate photosynthetically active radiation using general meteorological elements in a temperate humid area and comparison among models. Theor. Appl Chimatol, 2014, 15: 583 – 589.
[31] Ross J, Sulvev M. Sources of errors in measurements of PAR. Agricultural and Forest Meteorology, 2000, 100:103 – 125.
[32] Gueymard C. An atmospheric transmittance model for the clear sky beam, diffuse and global photosynthetically active radiation. Agricultural and Forest Meteorology, 1989, 45: 215 – 229.
[33] Gueymard C. A two-band model for the calculation of clear sky solar irradiance, illuminance, and photosynthetically active radiation at the Earth's surface. Solar Energy, 1989, 43: 253 – 265.
[34] Olseth JA, Skartvert A. Luminous efficacy models and their application for calculation of photosynthetically active radiation. Solar Energy, 1993, 52: 391 – 399.
[35] Eck TF, Dye DG. Satellite estimation of incident photosynthetically active radiation using ultraviolet reflectance. Remote Sens. Environ., 1991, 38: 135 – 146.
[36] Moon P. Proposed standard solar – radiation curves for engineering use. J Franklin Inst, 1940, 230: 583 – 618.
[37] McCree KJ. A solarimeter for measuring photosynthetically active radiation. Agricultural and Forest Meteorology, 1966, 3: 353 – 366.
[38] McCartney HA. Spectral distribution of solar radiation. Part II: Global and diffuse. Q.J.R. Meteorol. Soc., 1978, 104; 911 – 926.
[39] Karalis JD. Characteristic of direct photosynthetically active radiation. Agricultural and Forest Meteorology, 1989, 48: 225 – 234.
[40] Escobedo JF, Gomes EN, Oliveirol AP, Soares J. Modeling hourly and daily fraction of UV, PAR and NIR to global solar radiation under various sky conditions at Botucoctu, Brazil. Applied Energy, 2009, 86: 299 – 309.
[41] Meek DW, Hatfied JL, Howell TA, Idso SB, Reginato RJ. A generalized relationship between photosynthetically active radiation and solar radiation. Agronomy Journal, 1983, 76: 939 – 945.
[42] Finch DA, Bailey WG, McArthur LJB, Nasitivitwi M. Photosynthetically active radiation in Zambia. 2004. https://www.researchgate.net/publication/238088149_Photosynthetically_active_radiation_in_Zambia (accessed on 10/4/2018)
[43] Finch DA, Bailey WG, McArthur LJB, Nasitivitivi M. Photosynthetically active radiation regimes in a southern African Savanna environment. Agricultural and Forest Meteorology, 2004, 122: 229 – 238.
[44] Walczak T, Maczek W, Czainowsk M. Quantum radiometer for measurement of photosynthetically active radiation. Zesz. Probl. Post. Nauk. Rol., 1989, 263 – 265.
[45] McCree KJ. Test of current definition of measuring photosynthetically active radiation against leaf photosynthesis data. Agricultural and Forest Meteorology, 1972, 10: 441 – 453.

[46] Jacovides CP, Timbios FS, Asimakopoulos DN, Steven MD. Urban aerosol and clear skies spectra for global and diffuse photosynthetically active radiation. Agricultural and Forest Meteorology, 1997, 87: 91-104
[47] Mizoguchi Y, Yasuda Y, Ohtani Y, Watanabe T, Komianami Y, Yamanoi K. A practical model to estimate photosynthetically active radiation using general meteorological elements in a temperate humid area and comparison among models. Theor. Appl Chimatol, 2014, 15: 583 – 589.
[48] Tsubo M, Walker S. Relationship between photosynthetically active radiation and clearness index in Bloemfontein, South Africa. Theor. Appl. Climatol, 2005, 80:17 – 25.
[49] Akitsu T, Kume A, Hirose Y, Ijima O, Nasahara KN. On the stability of radiometric of photosynthetically active radiation to global solar radiation in Tsukuba, Japan. Agricultural and Forest Meteorology, 2015, 209: 59-68.
[50] Udo SO, Aro TO. Calobal PAR related to global solar radiation for central Nigeria. Agricultural and Forest Meteorology, 1999, 97: 21 – 31.
[51] Rao CR. Photosynthetically active components of global solar radiation: measurements and model computations. Arch meteorol. Geophys. Bioclim. Ser. B, 1984, 34: 353 – 364.
[52] Papaioannou G, Papanikolaou N, Retalis D. Relationships of Photosynthetically active radiation and shortwave irradiance. Theor Appl Climatol, 1993, 48: 23 – 27.
[53] Jacovides CP, Tymrios FS, Papaioannou G, Assimakopoulos DN, Theofilou CM. Ratios of PAR to broadband solar radiation measured in Cyprus. Agricultural and Forest Meteorology, 2004, 121: 134 – 140.
[54] Wang Q, Kakabari Y, Kubota M, Tenhunen J. Variation of PAR to global solar radiations ratio along altitude gradient in Naeba Mountain. Theor Appl Climatol, 2007, 87: 239-253.
[55] Li R, Zhao, L, Ding Y, Wang S, Ji G, Xiao Y, Liu G, Sun L. Monthly ratios of PAR to global solar radiation measured of northern Tibetan Plateau, China. Solar Energy, 2010, 84: 964-973.
[56] Britton CM, Dodd JD. Relationships of Photosynthetically active radiation and structure irradiance. Agricultural and Forest Meteorology, 1976, 17: 1 – 7.
[57] Szeicz G. Solar radiation for plant growth. J Appl Ecol., 1984, 11: 617 – 636.
[58] Monteith JL, Unsworth M. Principle of environmental physics, second ed. Edward Armold, London: 1990.
[59] Bat-Oyun T, Shinoda M, Tsubo M. Effects of Cloud, Atmospheric water vapor, dust on photosynthetically active radiation and total solar radiation in a Mongolian grassland. Journal of Arid Land, 2012, 4(4): 349 – 356.
[60] Nwokolo SC, Ogbulezie JC. Modeling the influence of relative humidity on photosynthetically active radiation from global horizontal irradiation in six tropical ecological zones in Nigeria. New York Science Journal, 2016, 9(11): 40-55.
[61] Abolfazi MH. Estimating Photosynthetically active radiation (PAR) using air temperature and sunshine duration. Journal of Biodiversity and Environmental Sciences, 2014, 5(4): 371 – 377.

[62] Hu B, Wang Y, Comparison of multi-empirical estimation models of photosynthetically active radiation under all sky conditions in Northeast China. Theor Appl Climatol, 2014, 116: 119-129.
[63] Wang L, Gong W, Feng L, Lin A, Hu B, Zhou M. Estimation of hourly and daily photosynthetically active radiation in Inner Mongolia, China, from 1990 to 2012. International Journal of Climatology, 2014. DOI: 10:1002/joc.4197
[64] Hu B, Yu Y, Lin Z, Wang Y. Analysis of photosynthetically active radiation and applied parameterization model for estimating of PAR in the North China plain. J. Atoms Chem, 2016. DOI:10.1007/510874-016-9330-2
[65] Aguiar LJG, Fischer GR, Ladle RJ, Malhado ACM, Justino FB, Aguiar RG, Da Costa JMN. Modeling the photosynthetically active radiation in South West Amazonia under all sky conditions. Theor Appl. Climatol, 2011. DOI:10.1007/s00704-011-0556-2
[66] Aguiar LJG, Da Costa JMN, Aguiar RG, Fischer GR. Estimates and measurements of photosynthetically active radiation and global solar irradiance in Rondonia. 2006. DOI: 10.1063/1.3117013
[67] Finch DA, Bailey WG, McArthur LJB, Nasitivitivi M. Photosynthetically active radiation regimes in a southern African Savanna environment. Agricultural and Forest Meteorology, 2004, 122: 229 – 238.
[68] Etuk SE, Okechukwu AE, Nwokolo SC. Modelling and estimating pohotosynthetically active radiation over six tropical ecological zones in Nigeria. Journal of Geography, Environment and Earth Science International, 2016, 12(2): 1-12.
[69] Etuk SE, Nwokolo SC, Okechukwu AE, John-Jaja SA. Analysis of photosynthetically active radiation over six tropical ecological zones in Nigeria. Journal of Geography, Environment and Earth Science Internal, 2016, 7(4): 1 – 15.
[70] Nwokolo SC, Ogbulezie JC, Toge CK, John-Jaja SA. Photosynthetically active radiation estimation and modeling over different climatic zone in Nigeria. 2017, DOI:10.9734/JAERI/2017/30000
[71] Wang L, Gong W, Ma Y, Hu B. Photosynthetically active radiation and its relationship with global solar radiation in Central China. Int J Biometeorol, 2013. DOI:10.1007/s00484-013-0690-7
[72] Yu X, Wu Z, Jiang W, Guo X. Predicting daily photosynthetically active radiation from global solar radiation in the contiguous United States. Energy Conversion and Management, 2015, 89: 71-82.
[73] Peng S, Du, Lin A, Hu B, Xiao K, Xi Y. Observation and estimation of photosynthetically active radiation in Lhasa (Tibetan Plateau). Advances in space research, 2015, 55: 1604-1612.
[74] Udo SO, Aro TO, New medical relationships for determining global PAR from measurement of global solar radiation, infrared radiation or sunshine duration. International Journal of Climatology, 2000, 20: 1265-1274.
[75] Wang L, Kisi O, Zounemat-Kermani M, Hu B, Gong W. Modeling and Comparison of hourly photosynthetically active radiation in different ecosystems. Renewable and sustainable energy reviews, 2016, 56: 436 – 453.

[76] Yu X, Guo X. Hourly photosynthetically active radiation estimation Midwestern United States from artificial neural networks and conventional regression models. Int J. Biometeorol, 2016, 60(8):1247-59. DOI: 10.1007/s00484-015-1120-9
[77] Melina-Maria Z, Michael T, Alkiviadis B, Stelios K. Modeling the relationship between photosynthetically active radiation and global horizontal irradiance using singular spectrum analysis. Journal of Qualitative Spectroscopy and Radiative Transfer, 2016, 182: 240-263.
[78] Yaniktepe B, Genc YA. New Model for predicting the global solar radiation on horizontal surface. International Journal of Hydrogen, 2015, 40: 15278 – 15283.
[79] Zhang J, Zhao L, Deng S, Xn W, Zhang Y. A Critical review of models used to estimate solar radiation. Renewable and sustainable Energy Reviews, 2017, 70: 314 – 329.
[80] Yu, Y, Chen HB, Xia XA. Significant variation of surface Albedo during a snow period at Xiaughe observatory China. Adv. Atmos Sci., 2010, 27: 80 – 86.
[81] Lauret P, Voyant C, Soubdhan T, David M, Poggi P. A benchmarking of machine learning techniques for solar radiation forecasting in an insular context. Solar Energy, 2015, 112: 446–457.
[82] Sperati S, Alessandrini S, Pinson P, Kariniotakis G. The "Weather Intelligence for Renewable Energies" Benchmarking Exercise on Short-Term Forecasting of Wind and Solar Power Generation. Energies, 2015, 8:9594–9619. DOI:10.3390/en8099594.
[83] COST | About COST, (n.d.). http://www.cost.eu/about_cost (accessed on June 31, 2017).
[84] Pelland S, Galanis G, Kallos G. Solar and photovoltaic forecasting through post-processing of the Global Environmental Multiscale numerical weather prediction model, Prog. Photovolt. Res. Appl., 2013, 21: 284–296. DOI:10.1002/pip.1180.
[85] Trapero JR, Kourentzes N, Martin A. Short-term solar irradiation forecasting based on Dynamic Harmonic Regression. Energy, 2015, 84: 289–295.
[86] Monteith JL. Solar radiation and productivity in tropical ecosystems. J. Appl. Ecol., 1972, 9: 747 – 766.
[87] Hodges T, Kanemasu E. Modeling daily dry matter production of winter wheat. Agronomy Journal, 1977, 69: 974 – 978.
[88] Stanhill G, Fuchs M. The relative flux density of photosynthetically active radiation. J Appl Ecol, 1977, 14: 317 – 322.
[90] Hodges T, Kanemasu E, Teare I. Modeling dry matter accumulating and yield of grain soighum. Can. J. Plant Sci., 1979, 59: 803 – 818.
[91] Howell TA, Meek DW, Hatfield JL. Relationship of photosynthetically active radiation to shortwave radiation in the San Joaquin Valley. Agricultural and Forest Meteorology, 1983, 28: 157 – 175.
[92] Kvifte G, Hegg K, Hansen V. Spectral distribution and characteristics distribution of solar radiation in the Nordic countries. J. Climate Appl Meteorol, 1983, 22: 143 – 152.
[93] Rodskjer N. Spectral daily insolation at Uppsala, Sweden. Arch meteorol Geophys Bioclim Ser B, 1983, 33: 89 – 98.

[94] Blackbum WJ, Proctor JTA. Estimating photosynthetically active radiation from measured solar irradiance. Solar Energy, 1983, 31: 233 – 234.
[95] Weiss A Norman JM. Partitioning solar radiation into direct and diffuse, visible and near – infrared components. Agricultural and Forest Meteorology, 1985, 34: 205 – 213.
[96] Slomka J. photosynthetic photon inflow in relation to sunshine duration of Belsk. Inst. Geophys. Pol. Acad. Sci., 1977, D-32 (230): 85 – 87.
[97] Zhang X, Zhang Y. Zhou Y. Measuring and Modelling photosynthetically active radiation in Tibet Plateau during April – October. Agricultural and Forest Meteorology, 2000, 102: 207 – 212.
[98] Wang L. Gong W, Li C, Lin A, Hu B, Ma Y. Measurement and estimation of photosynthetically active radiation from 1961 to 2011 in Central China. Applied Energy, 2013, 111: 1010-1017.
[99] Anjorin OF, Utah EU, Likita MS. Estimation of hourly photosynthetically Active radiation (PAR) from hourly global solar radiation (GSR) in Jos, Nigeria. Asian Review of Environmental and Earth Sciences, 2014, 1 (2): 43 – 50.
[100] Pankaew P, Milton EJ, Dash J. Estimating hourly variation in photosynthetically active radiation across the UK using MSG SEVIRI data. 35th International Symposium on Remote Sensing of Environment (ISRSE35); IOP Conference Series: Earth and Environmental Science, 2015, 17: 012069, DOI: 10.1088/1755-1315/17/1/012069
[101] Peng S, Du O, Lin A, Hu B, Xiao K, Xi Y. Observation and estimation of photosynthetically active radiation in Lhasa Tibetean Plateau. Advances in Space Research, 2015, 55: 1604-1612.
[102] Yocum CS, Allen LH, Lemon ER. Photosynthesis under field conditions. VI. Solar radiation balance and photosynthesis efficiency. Agronomy Journal, 1964, 56: 249 – 253.
[103] Williams JG. Small variation in the photosynthetically active fraction of solar radiation on clear days. Arch Meteorol Geophys Bioclim Ser B, 1976, 33: 89 – 98.
[104] Goldberg B, Klein WH. Variation in the spectral distribution of daylight as various geographical locations on the earth's surface. Solar Energy, 1977, 19: 3 – 13.
[105] Stigter CJ, Musabillia MM. The conservative ratio of photosynthetically active radiation to total radiation in the tropics. J. Appl Ecol, 1982, 19:853 – 858.
[106] Hansen V. spectral distribution of solar radiation on clear days. A comparison between measurements and model estimates. J. Climate Appl Meteorol, 1984, 23: 772 – 780.
[107] Papaioannou G, Nikolidakis G, Asimakopoulos D, Retalis D. Photosynthetically active radiation in Athens. Agricultural and Forest Meteorology, 1996, 81: 287 – 298.
[108] Zhou Y, Xiang Y, Luan L. Climatological estimation of photosynthetically active quantity flux. Acta Meteol. Sinica, 1996, 54(4): 447-454.
[109] Jacovides CP, Tymuios FS, Assimakopoulos VD, Kaltsounides NA. The dependence of global and diffuse PAR radiation components on sky condition at Athens, Greece. Agricultural and Forest Meteorology, 2007, 143: 277 – 287.

[110] Escobedo JF, Gomes EN, Oliveira AP, Soares J. Ratios of UV, PAR and NIR components to global solar radiation measured at Botucatu site in Brazil. Renewable Energy, 2011, 36:169 – 178.
[111] Guefeng W, De Leeuw J, Skidmore AK, Yaolin L, Prins HHT. Comparison of extrapolation and interpolation methods for estimating daily photosynthetically active radiation (PAR). Geo-spatial Information Science, 2010, 13(4): 235-242.
[112] Escobedo JF, Gomes EN, Oliveirol AP, Soares J. Modeling hourly and daily fraction of UV, PAR and NIR to global solar radiation under various sky conditions at Botucoctu, Brazil. Applied Energy, 2009, 86: 299 – 309.
[113] Yu X, Wu Z, Jiang W, Guo X. Predicting daily photosynthetically active radiation from global solar radiation in the Contiguous United States. Energy Conversion and management, 2015, 89: 71-882
[114] Hargreaves GH, Samani ZA. Estimating potential evaporation. Journal of Irrigation and Drainage Engineering, 1982, 108: 223-230.
[115] Wang L, Gong W, Hu B, Lin A, Li H, Zou. Modeling and analysis of the spatiotemporal variations of photosynthetically active radiation in China during 1961 – 2012. Renewable and sustainable energy reviews, 2015, 49: 1019 – 1032.
[116] Hu B, Liu H, Wang Y. Investigation of the Variability of photosynthetically active radiation in the Tibetan Plateau, China. Renewable and Sustainable Energy Reviews, 2016, 55: 210 – 248.
[117] Alados I, Alados-Arboledas L. Validation of an empirical model for photosynthetically active radiation. International Journal of Climatology, 1999, 19: 1145 – 1152.
[118] Hu B, Wang YS, Liu GR. Measurements and estimation of photosynthesis active radiation in Beijing. Atmospheric Research, 2007, 85: 361 – 371.
[119] Kasten F, Young AT. Revised optical air mass tables and approximation formula. Appl Opt, 1989, 28: 4735 – 4738.
[120] Al-Shooshan AA. Estimations of photosynthetically active radiation under an arid climate. J. Agric Eng Res., 1997, 66: 9 – 13.
[121] Alados I, Olmo FJ, Foyo-Moreno I, Alados-Arboledas L. Estimation of photosynthetically active radiation under cloudy conditions Agricultural and forest meteorology, 2000, 102: 39 – 50.
[122] Lopez G, Rubio MA, Martinez M, Batlles FJ. Estimation of hourly global photosynthetically active radiation using artificial neural network models. Agricultural and Forest Meteorology, 2001, 107: 279 – 291.
[123] Allen RG, Pereina LS, Raes D, Smith M. Crop evapotranspiration guideline for computing croup matter requirement. FAO Imitation and Drainage Paper, Rome, Italy. 1998, 56: 290.

CALL FOR PAPERS

Trends in Renewable Energy

ISSN Print: 2376-2136 ISSN online: 2376-2144

http://futureenergysp.com/index.php/tre/

Trends in Renewable Energy (TRE) is an open accessed, peer-reviewed semi-annual journal publishing reviews and research papers in the field of renewable energy technology and science. The aim of this journal is to provide a communication platform that is run exclusively by scientists. This journal publishes original papers including but not limited to the following fields:

- ✧ Renewable energy technologies
- ✧ Catalysis for energy generation, Green chemistry, Green energy
- ✧ Bioenergy: Biofuel, Biomass, Biorefinery, Bioprocessing, Feedstock utilization, Biological waste treatment,
- ✧ Energy issues: Energy conservation, Energy delivery, Energy resources, Energy storage, Energy transformation, Smart Grid
- ✧ Environmental issues: Environmental impacts, Pollution
- ✧ Bioproducts
- ✧ Policy, etc.

We publish the following article types: peer-reviewed reviews, mini-reviews, technical notes, short-form research papers, and original research papers.

The article processing charge (APC), also known as a publication fee, is fully waived for the Trends in Renewable Energy.

Call for Editorial Board Members

We are seeking scholars active in a field of renewable energy interested in serving as volunteer Editorial Board Members.

Qualifications

Ph.D. degree in related areas, or Master's degree with a minimum of 5 years of experience. All members must have a strong record of publications or other proofs to show activities in the energy related field.

If you are interested in serving on the editorial board, please email CV to editor@futureenergysp.com.